

Cavity-Enhanced Detection of Biologically Relevant Magnetic Field Effects

Dean M. W. Sheppard

New College

A thesis submitted for the degree of

Doctor of Philosophy

Physical & Theoretical Chemistry Laboratory

University of Oxford

Trinity 2016

Cavity-Enhanced Detection of Biologically Relevant Magnetic Field Effects

Dean M. W. Sheppard, New College
Trinity 2016

A thesis submitted for the degree of
Doctor of Philosophy

Abstract

Magnetoreception is the ability of some animals to use the weak magnetic field of the Earth for navigation over long-distance migrations. It is a well-known phenomenon, but its underlying biophysical mechanisms remain poorly understood. One proposal involves light-induced, magnetically sensitive chemical reactions occurring within cryptochrome proteins, rationalised via the radical pair mechanism (Chapter 1). The absence of evidence in support of this hypothesis is in part due to the lack of sufficiently sensitive techniques to measure magnetic field effects (MFEs) in biological samples.

Cavity-enhanced detection, most commonly in the form of cavity ring-down spectroscopy (CRDS) or cavity-enhanced absorption spectroscopy (CEAS), is widely used in the gas phase to provide significant sensitivity gains over traditional single-pass measurements (Chapter 2). However, successful studies in the condensed phase are less prevalent due to the additional background losses inherent to the sample.

This thesis reports on the application of broadband (i.e. monitoring $> 100\,\text{nm}$) variants of CRDS and CEAS to the study of MFEs on the radical recombination reactions of flavin-based systems in solution. The broadband CRDS (BBCRDS) instrument employed in Chapter 4 is able to monitor the spectral changes induced by magnetic fields with submicrosecond time resolution. However, the need to scan both the probe wavelength and time delay to construct time-resolved spectra leads to prohibitively long acquisition times, and hence exposure of sensitive samples to high numbers of photons. The broadband CEAS (BBCEAS) studies reported in Chapter 5 combine the high irradiance and spectral coverage of a supercontinuum radiation (SCR) source with a CCD detector to simultaneously acquire absorption spectra across the visible region (480–700 nm). The CW nature of this technique precludes the possibility of following radical pair kinetics in real time.

In an effort to combine the respective advantages of these two instruments, which individually have represented powerful advances in capability, a new cavity-enhanced technique is reported for the first time (Chapter 6). The result, optical cavity-enhanced transient absorption spectroscopy (OCTAS), is able to simultaneously monitor spectral evolution and associated MFEs on the microsecond timescale, with comparable sensitivity to the existing techniques.

Magnetic responses in animal cryptochrome proteins have successfully been recorded using all three techniques, lending considerable weight to the hypothesis that these molecules are at the heart of the magnetic sense in animals.

Acknowledgements

My biggest thanks go to my supervisor, Prof. Stuart Mackenzie, who has taught me all the Physical Chemistry I know (and lots more that I don't any more), for his continued support both of my research and teaching interests. I have enjoyed many great experiences over the years of working with you, and I am grateful for all the opportunities you have given me. Also, of course, thanks go to Prof. Christiane Timmel, the better half of the double act, for your enthusiasm, advice and guidance. Getting to know you has been a particular highlight of my research career. Along with Prof. Peter Hore, whose insightful comments have always been very helpful, I would like to thank all of you for the brilliant project I have been entrusted with. It has been a pleasure working with you.

Particular thanks go to Dr Kiminori Maeda, who taught me about CRDS and came up with the initial concept for the OCTAS technique. I hope it has lived up to expectations. Your great ideas for experiments and creative explanations of strange results have been sorely missed. I immensely enjoyed our time in the lab together and it is a real shame it was cut short. Japan is lucky to have you back! Thanks also to Dr Kevin Henbest for explaining cryptochrome photochemistry to me.

I'd like to thank all members of the Mackenzie and Timmel groups, past and present for all the fun we've had together. In particular, Dr Simon Neil, who introduced me to the world of cavities a long time ago and taught me all that I know. A special mention has to go to (Dr!) Emrys Evans, a great friend both in and out of the lab. Thank you for all the help you have given me in interpreting my pretty pictures with your immense knowledge of spin chemistry. Thanks for all the great memories, Berlin and India are particular highlights (Fatehpur Sikri!).

I owe a large debt of gratitude to Dr Jon Storey for all the time he spent developing the fantastic data acquisition and analysis software for both BBCEAS and OCTAS. Much of this thesis would not have been possible without your help. Tilo, congratulations on taking my poor tutorial on CRDS and running so far with it. Thanks for letting me play with it again recently and reminding me of the ropes, and for your help with the tricky deconvolution. Marcin, thanks for explaining global analysis to me. I'm glad to be leaving things in such capable hands, I can't wait to see what you do with it.

Thank you to all the staff at New College School for your welcome and friendliness throughout my time with you, especially Harriet Cawood and Sandie Capel for all of your advice and guidance (I finally understand Year 8 geometry!). Particular thanks are due to Robert Gullifer for letting me loose in your classrooms, and your flexibility when I had to travel away for conferences.

I have been lucky to meet some excellent support staff in the department, and I'd like to thank Neville Baker and John Adams in particular for all of their help with magnetic fields, impedances and lasers.

Zala, thank you for everything over the past six years. I am so glad I met you. Thank you for the cultural education and the proof-reading – your written English is much better than mine!

Finally, to my family, for giving me everything I could ever need.

Abbreviations

AOM	Acousto-optic modulator
AOTF	Acousto-optic tunable filter
$AscH_2$	Ascorbic acid
BBCEAS	Broadband CEAS
BBCRDS	Broadband CRDS
BET	Back electron transfer
CCD	Charge coupled device
CEAS	Cavity enhanced absorption spectroscopy
CEF	Cavity enhancement factor
CRDS	Cavity ring-down spectroscopy
CW	Continuous wave
DASH	*Drosophila*, *Arabidopsis*, *Synechocystis* and Human
*Dm*Cry	*Drosophila melanogaster* cryptochrome
*Ec*PL	*Escherichia coli* photolyase
EPR	Electron paramagnetic resonance
ET	Electron transfer
FAD	Flavin adenine dinucleotide
FBG	Fibre Bragg grating
FMN	Flavin mononucleotide
F-pair	Freely-diffusing pair
FSR	Free spectral range
G-pair	Geminate pair
HEWL	Hen egg white lysozyme
HPLC	High performance liquid chromatography
ICOS	Integrated cavity output spectroscopy
IR	Infrared
ISC	Intersystem crossing
LED	Light emitting diode
LFE	Low field effect
MARY	Magnetically altered reaction yield

MFE	Magnetic field effect
MTHF	Methenyltetrahydrofolate
ND	Neutral density
NICE-OHMS	Noise immune cavity enhanced optical heterodyne molecular spectroscopy
NMR	Nuclear magnetic resonance
OPO	Optical parametric oscillator
PC	Personal computer
PCF	Photonic crystal fibre
PMT	Photomultiplier tube
PT	Proton transfer
RP	Radical pair
RPM	Radical pair mechanism
SEM	Standard error of the mean
SNR	Signal-to-noise ratio
SCR	Supercontinuum radiation
SCRP	Spin correlated radical pair
S-T	Singlet-triplet
TA	Transient absorption
TrpH (or W)	Tryptophan
T-T	Triplet-triplet
TTL	Transistor-transistor logic
UV	Ultra violet
UV-Vis	Ultraviolet-visible
*Xl*Cry	*Xenopus laevis* cryptochrome

Contents

1 Introduction: Spin Chemistry, Magnetic Field Effects and Cryptochromes 1

1.1 Motivation . . . 1

1.2 Spin Chemistry . . . 3

1.3 The Zeeman Effect . . . 4

1.4 Coupled Spins . . . 7

1.4.1 Exchange interaction . . . 11

1.4.2 Dipolar interaction . . . 11

1.4.3 Hyperfine interaction . . . 12

1.5 The Radical Pair Mechanism . . . 14

1.6 Spin Mixing . . . 17

1.6.1 Δg mechanism . . . 18

1.6.2 Hyperfine mechanism . . . 19

1.6.3 Low-field effects . . . 20

1.6.4 Spin relaxation . . . 22

1.7 Biological Magnetic Field Effects . . . 23

1.7.1 Magnetoreception . . . 24

1.7.2 Cryptochromes and photolyases . . . 25

1.8 Measuring MFEs . . . 27

1.8.1 Magnetically Altered Reaction Yield (MARY) plots . . . 28

1.8.2 Biological MFE detection . . . 31

1.9 Scope of the Thesis 31

2 Cavity Enhanced Spectroscopy **33**

2.1 The Beer-Lambert Law 34

2.2 Multipass Techniques 36

2.3 Optical Cavities 38

2.3.1 Cavity mode structure and stability 38

2.4 Cavity Ring-Down Spectroscopy (CRDS) 42

2.4.1 CRDS sensitivity 45

2.5 Cavity-Enhanced Absorption Spectroscopy (CEAS) 46

2.5.1 Broadband CEAS (BBCEAS) 50

2.5.2 CEAS sensitivity 51

2.5.3 Origin of sensitivity 54

2.6 Light Sources 57

2.6.1 Pulsed vs continuous wave (CW) light sources 57

2.6.2 Broadband light sources 59

2.7 Cavity Enhancement in the Condensed Phase 61

2.7.1 CRDS in the condensed phase 62

2.7.2 CEAS and BBCEAS in the condensed phase 64

3 Experimental Characterisation **67**

3.1 Introduction 67

3.2 Materials: Preparation and Characterisation 67

3.3 Photochemical Schemes 72

3.3.1 FMN/HEWL 72

3.3.2 FAD 73

3.3.3 FAD/W 74

3.3.4 Cryptochromes and photolyase 75

3.4 Light Sources . . . 77
3.4.1 Probe light sources . . . 77
3.4.2 Photoexcitation light sources . . . 79
3.5 Photodetectors . . . 80
3.6 Sample Cell . . . 81
3.7 Cavity Mirrors . . . 82
3.7.1 CEF calibration . . . 83
3.7.2 Mirror reflectivity profile . . . 86
3.8 Instrument Stability . . . 88
3.8.1 Supercontinuum stability . . . 88
3.8.2 Allan deviation . . . 89
3.8.3 Additional sources of uncertainty . . . 92
3.9 Conclusions . . . 94

4 BBCRDS Studies of MFEs in Biologically Relevant Systems 97
4.1 Introduction . . . 97
4.2 Experimental . . . 99
4.2.1 BBCRDS experimental set-up . . . 99
4.2.2 Measuring MFEs . . . 101
4.3 Results and Discussion . . . 104
4.3.1 BBCRDS MFE study of FMN/HEWL . . . 104
4.3.2 Comparative BBCRDS MFE study of FAD and FAD/W . . . 109
4.3.3 BBCRDS cryptochrome MFE studies . . . 117
4.3.4 Deconvolution of the ring-down time and spectral decay . . . 120
4.4 Conclusions and Future Directions . . . 127

5 BBCEAS Studies of MFEs in Biologically Relevant Systems 129
5.1 Introduction . . . 129

5.2 Experimental . . . 131
5.2.1 BBCEAS experimental set-up . . . 131
5.2.2 Measuring MFEs . . . 134
5.3 BBCEAS Study of the FMN/HEWL Model System . . . 140
5.3.1 Absorbances . . . 140
5.3.2 MFE action spectrum . . . 143
5.3.3 Percentage MFE spectrum . . . 144
5.3.4 Spectrally-resolved MFE surface plots . . . 146
5.3.5 MARY plots . . . 147
5.4 Power Dependence of the MFE in FMN/HEWL . . . 149
5.4.1 Experimental results . . . 149
5.4.2 Photochemical simulation . . . 153
5.5 Coulombic and Diffusive Effects . . . 158
5.6 BBCEAS MFE Studies of FAD and FAD/W . . . 160
5.7 Cavity-Enhanced Detection of Low-Field Effects . . . 165
5.8 BBCEAS MFE Studies of Cryptochrome and Photolyase . . . 168
5.8.1 BBCEAS MFE study of *Ec*PL . . . 169
5.8.2 BBCEAS MFE study of *Dm*Cry . . . 170
5.8.3 Comparison of *Ec*PL and *Dm*Cry . . . 173
5.9 Pump-Beam Modulated BBCEAS . . . 174
5.9.1 The establishment of photochemical equilibrium . . . 175
5.9.2 Data collection and analysis . . . 178
5.9.3 Modulated BBCEAS results . . . 182
5.10 Conclusions and Future Directions . . . 186

6 Optical Cavity-Enhanced Transient Absorption Spectroscopy (OCTAS) 189
6.1 Introduction . . . 189
6.2 Experimental . . . 190

6.2.1 The OCTAS instrument 190
6.2.2 Detection wavelength characterisation 193
6.2.3 Impedance and time-response 194
6.2.4 Measuring MFEs 196
6.3 OCTAS Studies of FMN/HEWL 201
6.3.1 OCTAS detection of MFEs 201
6.3.2 Global analysis 207
6.3.3 OCTAS MARY demonstration 210
6.3.4 Power dependence of the FMN/HEWL MFE 213
6.4 OCTAS MFE Studies of FAD and FAD/W 216
6.5 OCTAS MFE Study of *Xenopus laevis* Cryptochrome 223
6.6 Conclusions and Future Directions 227

7 Summary and Outlook **229**

8 Bibliography **239**

Chapter 1

Introduction: Spin Chemistry, Magnetic Field Effects and Cryptochromes

1.1 Motivation

For decades, scientists have been fascinated by the phenomenon of magnetoreception, the ability of some animals, birds in particular, to sense the Earth's weak magnetic field and use the information to perform impressive feats of navigation over thousands of kilometres. That they use the Earth's field alongside alternative sun and star compasses for directional cues is not in doubt, but the biophysical mechanisms underlying their magnetic sense are still not understood.[1–5]

The impact of weak magnetic fields on biological systems is also of potential concern to human health, particularly with the prevalence of high power electricity lines in close proximity to populated areas in industrial nations. The associated extremely low frequency (ELF) radiation has been linked with increased incidences of various forms of cancer, childhood leukaemia in particular,[6] and is listed as potentially carcinogenic by the World

Health Organisation.[7,8] The origin of any effect due to such non-ionizing radiation is unclear, but if shown to exist the underlying cause may share similarities with those mechanisms governing the more beneficial outcome harnessed by migrating animals.

Currently, two plausible hypotheses for magnetoreception are backed up by experimental evidence and observations. The magnetite hypothesis,[9–12] which suggests magnetically sensitive iron mineral deposits in the bodies of animals, might at first glance seem the most intuitive, as these crystals would align with an external magnetic field in much the same way as a traditional compass needle.

The alternative proposal, of relevance to this work, is based around the radical pair mechanism (RPM), involving the interconversion of quantum mechanical spin states of reactive intermediates.[13–17] It is suggested that the yield of chemical reactions in light-sensitive proteins can be directly affected by the application of weak magnetic fields. On first consideration, this seems highly improbable as the interaction energy of an isolated electron with an Earth-strength magnetic field ($\sim 50\,\mu T$) is several orders of magnitude smaller than the background thermal energy of molecular rotations and vibrations at room temperature. However, the understanding is framed within the radical pair mechanism (Section 1.5), where the field interacts with the system in a highly non-equilibrium state, and thermodynamic considerations hold little relevance. It is therefore a kinetic effect and requires the competition between fast photochemical reactions, the relative yields of which can be altered by a magnetic field.

While magnetic fields may be expected to affect the yield of a chemical reaction within the framework of the radical pair mechanism, the predicted effects are still very small. This thesis reports on recent developments of highly sensitive absorption techniques, harnessing optical cavities for signal enhancement. The use of existing approaches to monitor the small effect of magnetic fields on the photochemistry of biological samples has proved challenging. Previous work in this group has resulted in a step change in detection sensitivity via the use of optical cavities,[18,19] and it is this early success that is continued and

further developed in this work.

1.2 Spin Chemistry

Spin is an intrinsic angular momentum possessed by some particles, quantum mechanical in origin with no classical analogue, which plays a crucial role in the relativistic quantum mechanics developed by Dirac.[20,21] It is distinct from the orbital angular momentum and a characteristic of each elementary particle, more analogous to mass or charge. The spin angular momentum is a vector, $\boldsymbol{s}$, and its associated quantum number is denoted s. Particles with half-integer spins, such as electrons, protons and neutrons ($s = 1/2$), are known as fermions, and those with integral spins, such as photons ($s = 1$) are called bosons.[22–25]

Its existence was first proposed following the observed splitting of a beam of silver atoms into two components by an inhomogeneous magnetic field,[26] despite the lack of any orbital component of angular momentum (silver has one unpaired s-electron and so $L = 0$).

The magnitude of $\boldsymbol{s}$ is quantised, and is given in terms of its corresponding quantum number as:

$$|\boldsymbol{s}| = \hbar\sqrt{s(s+1)}. \tag{1.1}$$

Its vector projections onto a space-fixed axis (the z-axis by convention) are represented by s_z, which can take $2s+1$ values corresponding to the allowed values of the spin angular momentum projection quantum number, m_s, given by:

$$m_s = s, s-1, ..., -s. \tag{1.2}$$

The z-component, s_z is restricted to the values $m_s\hbar$, and so the spatial components of the spin angular momentum are also quantized, along with its magnitude. An electron, with its characteristic value of $s = 1/2$, can therefore adopt two orientations, corresponding to

either $m_s = 1/2$ (often known as the α or spin up state, $\uparrow$) or $m_s = -1/2$ (denoted the β or spin down state, $\downarrow$), which are degenerate in the absence of an external field.

The charge on the electron results in a spin angular momentum, $\boldsymbol{s}$, giving rise to an associated magnetic moment $\boldsymbol{\mu_s}$:

$$\boldsymbol{\mu_s} = -\frac{g_e \mu_B \boldsymbol{s}}{\hbar}, \tag{1.3}$$

where the dimensionless proportionality constant g_e (= 2.002319304) is the g-value for a free electron, and μ_B is the Bohr magneton, the fundamental quantum of magnetic moment:

$$\mu_B = -\gamma_e \hbar = \frac{e\hbar}{2m_e}. \tag{1.4}$$

Here, γ_e is the gyromagnetic ratio of the electron ($-e/2m_e$, the ratio of its magnetic momentum to its angular momentum), e is the elementary charge, and m_e is the mass of the electron.

As the projection of the spin angular momentum vector onto the z-axis is given by $m_s\hbar$, it follows from Equation 1.3 that the z-component of the spin magnetic moment is itself quantized according to:

$$\mu_z = -g_e \mu_B m_s. \tag{1.5}$$

This magnetic moment can interact with an external field via the Zeeman interaction and lift the degeneracy of the two m_s substates.

1.3 The Zeeman Effect

In the absence of an external magnetic field the two m_s states (α and β) are degenerate i.e. there is no energetic advantage from the electron spin taking either of the available orientations. However, upon application of an external magnetic field the spin states are split in energy via its interaction with the spin magnetic moment.

For a classical magnetic moment, $\boldsymbol{\mu}$, interacting with an external static field, $\boldsymbol{B}$, the interaction energy is given by:

$$E = -\boldsymbol{\mu} \cdot \boldsymbol{B}. \tag{1.6}$$

In a quantum mechanical treatment, the Hamiltonian for the same system may be written as:

$$\hat{H} = -\hat{\boldsymbol{\mu}} \cdot \boldsymbol{B}, \tag{1.7}$$

where $\hat{\boldsymbol{\mu}}$ is the quantum mechanical operator for the magnetic moment. If the system under consideration is an electron then the interaction is between the electron spin angular momentum and the external field. From Equations 1.3 and 1.4:

$$\hat{H} = -\hat{\boldsymbol{\mu}}_{\boldsymbol{s}} \cdot \boldsymbol{B} = -g_e \gamma_e \hat{\boldsymbol{s}} \cdot \boldsymbol{B}, \tag{1.8}$$

where $\hat{\boldsymbol{s}}$ is the operator corresponding to electron spin angular momentum.

If the applied magnetic field is sufficiently strong, the system aligns with the field direction and its energy is quantized along the z-axis. In this situation, $\hat{\boldsymbol{\mu}}_{\boldsymbol{s}}$ can be replaced by the operator for the z-component of the spin magnetic moment, $\hat{\mu}_z$. If the strength of the applied field is denoted B, and $\hat{s}_z$ is the operator for the z-component of the spin, the Hamiltonian for the system becomes:

$$\hat{H} = -\hat{\mu}_z B = -g_e \gamma_e \hat{s}_z B. \tag{1.9}$$

As the eigenvalues of $\hat{s}_z$ are known ($m_s \hbar$), the energies of the state (Zeeman energies) are given by:

$$E_{m_s} = -g_e \gamma_e m_s \hbar B = g_e \mu_B m_s B, \tag{1.10}$$

and therefore the energies corresponding to the α ($m_s = +1/2$) and β ($m_s = -1/2$) spin states are:

$$E_\alpha = +\frac{1}{2} g_e \mu_B B, \tag{1.11}$$

$$E_\beta = -\frac{1}{2} g_e \mu_B B. \tag{1.12}$$

The difference in energy levels due to the interaction of different spin projections with the applied magnetic field is known as the Zeeman splitting:

$$\Delta E_{\text{zee}} = g_e \mu_B B. \tag{1.13}$$

The resulting Zeeman interaction is shown in Figure 1.1. This is valid for free electrons in a vacuum, which only experience the external magnetic field.

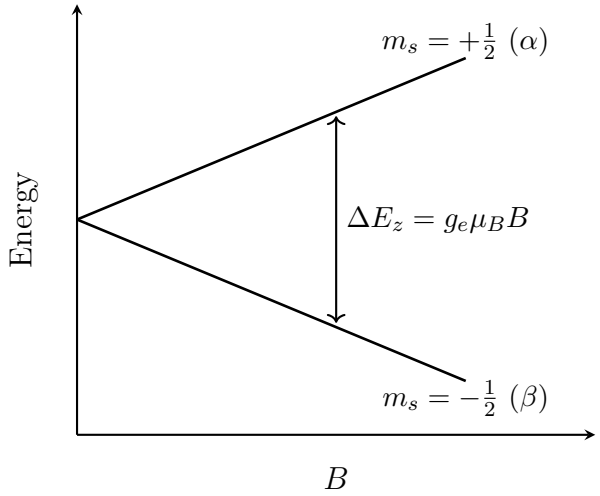


Figure 1.1: The energetic splitting of the two different spin orientations (α and β) of a single isolated electron in the presence of a magnetic field, B. At zero-field both orientations are degenerate.

For an unpaired electron in an atom or molecule, there is also a contribution to the field it experiences from its local magnetic environment (B_{loc}), which arises from both spin-orbit coupling and the Zeeman interaction between its orbital magnetic moment and the applied field. The result is an effective magnetic field, B_{eff}, comprised of both external and local components.

Due to the difficulties in calculating the local contributions to the overall field experienced by the electron, deviations from B are accounted for by replacing the free electron

g-factor, g_e, with an effective g-factor, g, which compensates for these effects. To account for this (in isotropic solution) Equation 1.13 is expressed as:

$$\begin{aligned} \Delta E_z &= g_e \mu_B B_{\text{eff}} \\ &= g_e \mu_B (B + B_{\text{loc}}) \\ &= g \mu_B B \end{aligned} \tag{1.14}$$

For the majority of organic radicals, including those studied in this work, g varies little from g_e.

1.4 Coupled Spins

The system considered so far only contains a single unpaired electron. However, as will become apparent, two radical species in a spin-correlated radical pair (SCRP) are required for a magnetic field effect to be observed in a chemical reaction.

Spin correlation is a property describing the relative mutual orientation of the two spins in a pair of radicals. The spins may be completely randomly oriented with respect to one another, in which case the radical pair is described as uncorrelated. This is the most common form of radical pairs, and arises in situations such as random encounter of radicals in bulk solution, forming a so-called freely-diffusing pair (F-pair). Alternatively, if the radicals are both formed at the same instant, for example by an electron transfer, the process occurs with conservation of spin angular momentum and the spins are formed with a fixed orientation with respect to each other. These are spin-correlated radical pairs (SCRPs) and comprise the crucial reactive intermediate in the radical pair mechanism. Due to their importance, future reference to radical pairs (RPs) in this work should be assumed to be the correlated form, unless specifically stated otherwise.

For a system comprising two electrons, the total spin angular momentum, $\boldsymbol{S}$, is given by the vector sum of the individual spins, $\boldsymbol{S} = \boldsymbol{s_1} + \boldsymbol{s_2}$. A corresponding overall spin

quantum number, S, can be defined and it can take the values based on a Clebsch-Gordan series:

$$S = (s_1 + s_2), (s_1 + s_2 - 1), \ldots, |s_1 - s_2|. \tag{1.15}$$

For a two-electron system, the only possibilities are 0 or 1 ($s_1 = s_2 = 1/2$). As for the single electron case, these spin states have associated projections onto the z-axis, represented here by M_s. For $S = 1$, there are three possible values (0, ± 1), corresponding to three possible magnetic quantum states. These are known as the triplet states and are labelled as T_0, T_+ and T_- to match the respective M_s values. For the $S = 0$ case there is only one possibility for the value of M_s (zero), so this is known as the singlet state and labelled as S.

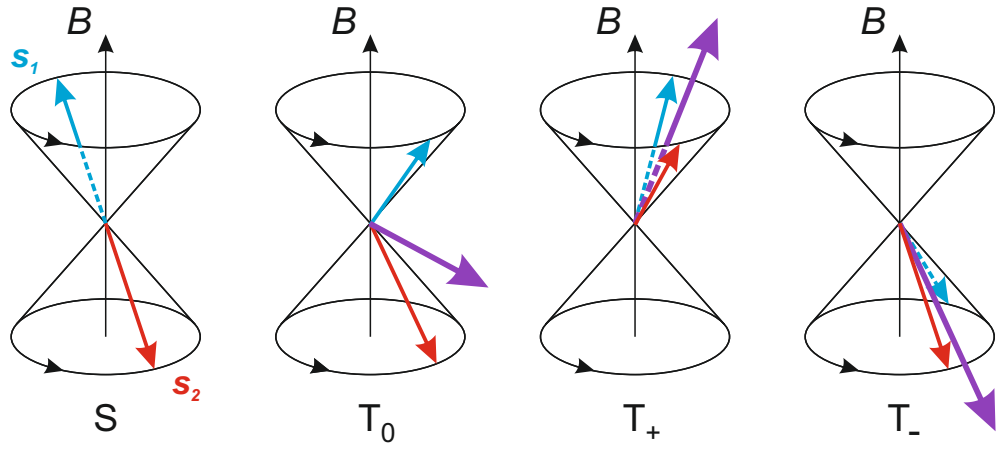


Figure 1.2: Simplified vector model of the singlet (S) and triplet (T_0,T_+,T_-) spin states of a radical pair. The spin vectors of the individual electrons are represented by the blue ($\boldsymbol{s_1}$) and red ($\boldsymbol{s_2}$) arrows, respectively. Their resultant, $\boldsymbol{S}$, is shown as the thick purple arrow. Each spin vector precesses around the field direction at its Larmor frequency (Equation 1.17). The direction of the arrows represent the α and β states of the individual electron spins, i.e. up and down, respectively.

These four spin states available to a pair of radicals are shown in simplified vector form[27] in Figure 1.2. The two vectors $\boldsymbol{s_1}$ and $\boldsymbol{s_2}$ represent the spin angular momenta of electrons 1 and 2, together comprising the radical pair. Each vector has a length $\hbar\sqrt{3}/2$ (obtained by substituting $s = 1/2$ into Equation 1.1). As a result of the commutation

relations of angular momenta, the precise magnitudes and orientations of $\boldsymbol{s_1}$ and $\boldsymbol{s_2}$ cannot be known simultaneously. Consequently, they must be considered to precess around the quantization axis (the field direction if B is sufficiently strong), sweeping out a cone of all possible orientations with the same projection onto the z-axis.

The rate of this precession is dependent on the strength of the applied field and can be considered as the frequency of radiation required to match the Zeeman splitting energy:

$$\Delta E_z = \hbar\omega_L = g\mu_B B \tag{1.16}$$

$$\omega_L = \frac{g\mu_B B}{\hbar} \tag{1.17}$$

where ω_L is the Larmor frequency of precession around the applied field axis.

In the singlet (S) state, $\boldsymbol{s_1}$ and $\boldsymbol{s_2}$ lie antiparallel to one another, so their resultant spin angular momentum and their net projection are both zero. The individual spin vectors in the triplet arrangements lie at $\sim 70.5°$ with respect to one other on average. A range of values is possible but they cannot all lie precisely in the same orientation as then their resultant would have magnitude $\hbar\sqrt{3}$ rather than the $\hbar\sqrt{2}$ required by $\hbar\sqrt{S(S+1)}$.[5] For the T_0 state, the projections of $\boldsymbol{s_1}$ and $\boldsymbol{s_2}$ onto the z-axis (field axis) are opposite to give a resultant of zero ($M_s = 0$), while for T_+ and T_- they lie in same direction ($M_s = \pm 1$). The projection of $\boldsymbol{S}$ is given by $S_z = M_s\hbar$, and has the values 0 and $\pm\hbar$ for T_0 and $T_\pm$, respectively.

At this point it is worth noting that, while overly simplified, the vector model shown in Figure 1.2 provides insight into the mechanisms which would allow interconversion between the spin states. The S and T_0 states are only distinguished by the relative phases of the two electrons. Any process that causes a variation in the precession rate of one of the spins by changing its Larmor frequency can cause them to interconvert. On the other hand, processes which lead to a change in the m_s value of either electron (a spin-flip) will lead to interconversion of the S and T_0 with the $T_\pm$ states. Several processes that can

induce spin-mixing are described in Section 1.6.

The Zeeman energy of a radical pair spin state in a magnetic field is given by an analogous expression to that for a single electron (Equation 1.14) with the overall magnetic quantum number, M_s, in place of that of an individual spin:

$$E_{M_s} = g\mu_B M_s B. \tag{1.18}$$

It is clear from this expression that only those spin states with non-zero M_s will be affected by the application of a magnetic field. The result is the energetic separation of the T_+ and T_- states ($M_s = \pm 1$) from the S and T_0 states (with $M_s = 0$), which have no spin angular momentum component along the field axis. The overall splitting between the T_+ and T_- is therefore $2g\mu_B B$, and the field dependence of the energy levels is shown schematically in Figure 1.3a).

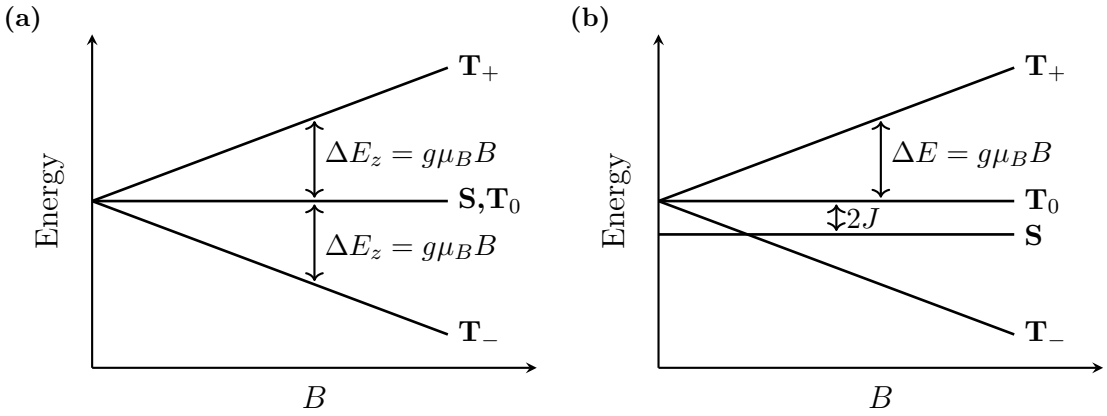


Figure 1.3: a) the Zeeman splitting for the spin states of a pair of electron spins, with magnitude given by Equation 1.16. b) the additional effects of the exchange interaction, which lifts the degeneracy of the singlet state S from the three triplet levels at zero field (see Section 1.4.1). The exchange energy, $2J$, can be positive or negative.[28]

In addition to the Zeeman interaction with an external field, there are also interactions between the spins that comprise the radical pair themselves, which are crucial to its formation and behaviour. These interactions can lead to changes in the energy levels of the overall spin states and are involved in the spin-mixing processes alluded to above.

1.4.1 Exchange interaction

The exchange interaction is a consequence of the Pauli exclusion principle, and is purely quantum mechanical in origin. It lifts the degeneracy of the singlet and triplet radical pairs, even at zero-field. In solution, the interaction parameter may be treated as isotropic due to the rapid molecular tumbling.

The Hamiltonian representing the effects of exchange may be written as:[29,30]

$$\hat{H}_{\text{ex}} = -2J(r)\hat{\boldsymbol{s}}_{\mathbf{1}} \cdot \hat{\boldsymbol{s}}_{\mathbf{2}}, \tag{1.19}$$

where $2J$ is the exchange energy as a function of the radical-radical separation, r, and $\hat{\boldsymbol{s}}_{\mathbf{1}}$ and $\hat{\boldsymbol{s}}_{\mathbf{2}}$ represent the spin angular momentum operators for electrons 1 and 2. The combined effects of the exchange interaction and Zeeman splitting on the spin state energy levels in shown in Figure 1.3b) for $J < 0$. J can be positive or negative, leading to the triplet state or singlet state being lower in energy, respectively.

The exchange energy has a strong distance dependence, decreasing exponentially with inter-radical distance,[31] and can be considered negligible for separations greater than $\sim 1\,\text{nm}$.[32] In the strong exchange regime, the S and T states are stationary states (eigenstates) of the Hamiltonian, and therefore radicals need to diffuse apart for spin mixing to occur and the various spin states to interconvert. In the radical pair systems studied in this thesis, the required separation ($r \geq 1\,\text{nm}$) occurs within a few hundred picoseconds, so the exchange interaction can be treated as having almost no effect for the majority of the RP lifetime.

1.4.2 Dipolar interaction

The dipolar interaction describes the interaction between the magnetic dipoles associated with the unpaired electrons in a radical pair. The weak local magnetic field created can lift the degeneracy of the triplet states in the absence of an external field. This type of

self-induced Zeeman interaction is referred to as zero-field splitting.

The dipolar Hamiltonian can be written as:

$$\hat{H}_{\text{dip}} = \hat{\boldsymbol{s}}_{\mathbf{1}} \cdot \boldsymbol{D} \cdot \hat{\boldsymbol{s}}_{\mathbf{2}}, \tag{1.20}$$

where D is the dipolar tensor describing the direction and magnitude of the interaction. To a first approximation, the magnitude of the dipolar interaction is inversely proportional to r^3 and is therefore expected to act over a longer range than the exponentially decaying exchange interaction. However, because it is anisotropic, it can be assumed that in solution it is effectively averaged out by rapid molecular motion to the extent where its impact is negligible.

1.4.3 Hyperfine interaction

The exchange and dipolar interactions describe effects between the unpaired electrons in the radical pair. If the RP components contain atoms with magnetic nuclei (those with non-zero nuclear spin angular momentum, I), then the unpaired electrons will also interact with their associated nuclear magnetic moments.

The hyperfine interaction has both an electric and magnetic component. The electric hyperfine interaction occurs with nuclei possessing at least a quadrupolar electric moment, and its $1/r^5$ distance dependence renders it negligible at typical electron-nuclear separations in radicals. As a result, only the magnetic hyperfine interaction is relevant and will be discussed in detail.

The nuclear spin angular momentum, I, is subject to the same quantum mechanical treatment as all angular momenta. It has magnitude $\hbar\sqrt{I(I+1)}$ and $2I+1$ sublevels corresponding to the permitted values of the nuclear magnetic quantum number, m_I:

$$m_I = I, I-1, \ldots, -I. \tag{1.21}$$

In general, only nuclei with even numbers of protons and neutrons (both spin-1/2 particles) have no spin. The most important nuclei for biologically relevant radical pairs are ^{1}H and ^{14}N, which have significant magnetic moments and near 100% natural abundance. At least one magnetically active nucleus is required in a radical pair to provide the hyperfine interaction needed to allow singlet-triplet mixing (ST-mixing) to occur. For non-zero values of m_I, the nuclear magnetic moment generates a weak local field which may interact with an unpaired electron via two coupling mechanisms.

The dipole-dipole interaction between the magnetic dipole moments of the nucleus and electron is analogous to the electron-electron dipolar interaction described previously (Section 1.4.2). As such, its anisotropic nature results in it being averaged out to zero net contribution in solution due to rapid molecular tumbling.

The second mechanism is the Fermi contact interaction, which is dependent on the electron spin density at the nucleus, and hence the amount of s-character in the molecular orbital. The isotropic nature of the interaction means that there is no averaging out in solution, as it only depends on the relative orientation of the electron and nuclear spins.[33]

The resulting magnetic hyperfine interaction produces a local contribution, B_{hf}, to the effective magnetic field experienced by the electron in addition to the applied field, B:

$$\begin{aligned} B_{\mathrm{eff}} &= B + B_{\mathrm{hf}} \\ &= B + m_I a. \end{aligned} \tag{1.22}$$

The hyperfine contribution, B_{hf}, is given by the product of the nuclear magnetic quantum number, m_I, and the isotropic hyperfine coupling constant, a. Unless the hyperfine couplings experienced by both electrons are exactly identical, this extra contribution to the effective magnetic field will result in the spins precessing at different Larmor frequencies. This is the basis of the hyperfine spin-mixing mechanism explained in Section 1.6.2.

1.5 The Radical Pair Mechanism

The radical pair mechanism provides the framework within which the surprising observation that a magnetic field can influence the outcome of chemical reactions can be understood. It was discovered independently by Kaptein and Oosterhoff,[13] and by Closs,[14] (both in 1969) and is responsible for the majority of magnetic responses exhibited by radical recombination reactions.[15,32,34] As mentioned in the introduction, the energies associated with the Zeeman interaction of an isolated electron with a magnetic field are orders of magnitude smaller than the thermal energy at room temperature, and so the idea that a magnetic field could have an impact on the bond making and breaking processes involved in chemical reactions seems highly unlikely.

However, the existence of spin-correlated radical pairs indicates one plausible mechanism, whereby an external magnetic field can influence the extent of spin-mixing, and thereby the relative proportions of singlet and triplet radical pair states present at a given time. If the spin states have different reaction pathways available then a magnetic field effect on the overall system can result. This can either be as a result of the singlet and triplet states forming different products (e.g. because only the singlet state can undergo spin-allowed recombination), or reacting at different rates.

A simplified general reaction scheme relevant to the studies of flavin-based photochemistry in this thesis is shown in Figure 1.4. The flavin (F) and electron donor (D) could be separate molecules, or two parts of the same molecule. An electronically excited state of the flavin is formed (here via photoexcitation but thermal initiation is also possible) with the same spin multiplicity as the ground state, due to the conservation of spin angular momentum. This is usually the singlet state, corresponding to a flavin ground state in which all the electrons are paired. The excited state can either return to the ground state through radiative decay (fluorescence) or follow a non-radiative pathway, such as intersystem crossing (ISC) to a state of different spin multiplicity.

The excited state of the flavin can also accept an electron from a donor (D) to form a

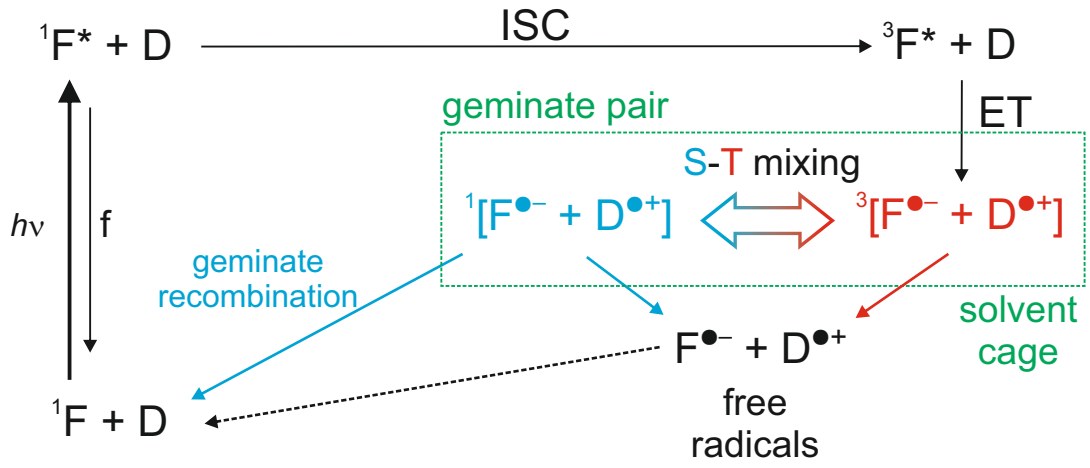


Figure 1.4: A simplified schematic representation of the radical pair mechanism (colour), embedded in a photochemical cycle. The magnetic sensitivity arises from the ST-mixing processes, which are external field dependent, and spin-selective geminate recombination to form the ground state precursors, the latter being only available to the singlet state. A triplet-born radical pair is formed when intersystem crossing (ISC) occurs faster than electron transfer (ET). The radiative fluorescence pathway is also shown (f). This scheme is representative of the chemical model systems studied in this thesis. The details of reaction schemes for specific systems used in this project are given in Chapter 3.

radical pair, in which the two components have opposite charges and correlated electron spins. This radical pair also forms under conservation of spin angular momentum, and its spin state therefore depends on the relative rates of electron transfer (ET) and intersystem crossing (ISC). In the example shown here, ISC outcompetes the rate of electron transfer and the radical pair is formed from the triplet excited state (i.e. a triplet-born RP). This behaviour is characteristic of the chemical systems studied in this work. However, in the biological systems of interest the RP is formed in the singlet state (i.e. singlet-born), due to the optimised ET pathway available in proteins (see Section 1.7.2). Singlet- and triplet-born RPs therefore exhibit opposite responses to a magnetic field, and this will be noted where relevant.

Initially, the two radicals comprising the radical pair are formed in close proximity

to one another, trapped within a solvent cage (indicated in Figure 1.4 by the dashed green box), and known as a 'geminate pair' (G-pair). At the very small initial radical separation, the exchange and dipolar interactions dominate and the RPs are locked into the (stationary) spin states (S, T_0, $T_\pm$). Interconversion between the spin states is therefore precluded.[35,36] To permit ST-mixing, the radicals must diffuse apart a short distance ($r \geq 1\,\mathrm{nm}$) to where the exchange and dipolar interactions are negligible. It is the ST-mixing processes described in the following sections that are magnetically sensitive and a crucial aspect of the radical pair mechanism (RPM).

Crucially, recombination on re-encounter requires the radicals to be in the singlet state to be spin-allowed. If a reactive re-encounter does not occur in the geminate pair, due to the RP being in the triplet state for instance, the radicals may eventually escape the solvent cage forming free radicals. The proportion of geminate recombination and escape therefore reflects the time-dependent probability of the SCRP being in a singlet or triplet state, respectively. The free radicals formed by diffusion may encounter one another in solution to form a 'freely-diffusing' pair (F-pair), in which spin correlation is re-established by overlap of molecular orbitals on the radicals. In this case, however, a statistical distribution of the S and T states will be produced (1/4 population in each). As for the G-pair, recombination at the F-pair stage is also subject to spin selection rules. Free radicals may also return to the ground state separately via other processes, or react with other species to form different products.[37]

Any process that changes the relative proportions of S and T states present can affect the relative yields of the ground state and free radicals. In the case of a triplet-born radical pair, a reduction in ST-mixing efficiency would lead to a reduction in singlet recombination product and an increase in the number of radicals escaping the G-pair to form free radicals. This could be achieved by energetic isolation of the $T_\pm$ states via the Zeeman interaction with an external magnetic field. For a singlet-born radical pair, the effect would be reversed and there would be an increased likelihood of recombination,

reducing the free radical yield. The external field dependence of the ST-mixing rate endows the RPM with magnetic sensitivity, and the details of these mixing mechanisms are discussed in the following section.

1.6 Spin Mixing

For a magnetic field to have an effect on a radical recombination proceeding via a SCRP, the radical spin states must be able to interconvert by singlet-triplet mixing (ST-mixing). This ensures that the time dependent probability of a SCRP being found in a singlet or triplet state is constantly evolving. If the number of states involved in the interconversion can be reduced by the Zeeman splitting on application of a magnetic field, then the probability of being found in any individual state will be affected. The resulting effects on the proportion of recombination product can be detected as a magnetic field effect (MFE). If the spin states were permanently stationary states (due to high exchange and dipolar interactions), then the splitting of energy levels by a magnetic field would have no effect on the outcome of the reaction. The same number of molecules would proceed by the same paths regardless. For a triplet-born RP there would be no geminate recombination and for a singlet-born RP no free radicals would form.

After the initial diffusion apart to allow interconversion, the RPs also need to re-encounter otherwise no geminate product could be formed. This requires them to be kept in reasonably close proximity while spin mixing occurs, which can be achieved by the use of a viscous solution (reducing the escape yield from the solvent cage), attractive electrostatic (Coulombic) interactions between the RP partners, or biradicals in which both components are covalently linked regions of the same molecule.

The most important ST-mixing mechanisms for the field strengths performed in this work are the hyperfine and low-field hyperfine mechanisms. While less relevant, the Δg and relaxation mechanisms are also outlined for completeness.

1.6.1 Δg mechanism

The rate of precession of an electron spin in the presence of an external magnetic field, the Larmor frequency (Equation 1.17), is dependent on the g-value of the electron, which in turn is dependent on its particular local magnetic environment (Equation 1.14). It is unlikely that the electrons on two different radical pair partners have identical magnetic environments, and therefore identical g values, and so there will be a difference in Larmor frequency between the two electrons:

$$\Delta\omega_L = \frac{\Delta g \mu_B B}{\hbar}. \tag{1.23}$$

The difference in precession frequencies, $\Delta\omega_L$, will alter the relative phase of the two electron spins comprising the RP, and hence can lead to interconversion between the S and T_0 states, which are related by a phase difference of π.

The difference in frequency is also proportional to the external magnetic field, B, and so the interconversion rate, and the S-T_0 mixing efficiency, will increase in the presence of very strong fields. If B is sufficiently high, the S-T_0 interconversion can occur on a timescale which competes with the formation of singlet and/or triplet products, rendering the yields magnetic field dependent. In this work the singlet product refers to the ground state, and the triplet 'product' is diffusion apart to form long-lived free radical species. The effect is not on the overall yield of reaction, as eventually everything returns to the ground state, but on the proportion of molecules trapped in a long-lived radical intermediate i.e. it is a kinetic effect.

For the organic (carbon-centred) radicals of interest here, differences in g values are very small, and for the low field strengths employed in these studies ($B \leq 20\,\mathrm{mT}$) the contribution of the Δg mechanism is negligible.

1.6.2 Hyperfine mechanism

The hyperfine mechanism is most easily understood by considering a radical pair in which both electrons have identical g values, but only $\boldsymbol{s_1}$ is coupled to a magnetic nucleus with $I = 1/2$ e.g. a single proton. The coupling is governed by the isotropic hyperfine interaction (Section 1.4.3). For high external fields ($B >> a$) the magnetic moment of the nucleus contributes to the effective field experienced by $\boldsymbol{s_1}$ according to Equation 1.22 with $m_I = \pm 1/2$:

$$B_{\text{eff}} = B \pm \frac{a}{2}, \tag{1.24}$$

where the sign of m_I depends on the orientation of the nuclear spin with respect to the external field. Both magnetic moments of the electron and nucleus are aligned with and precess around the external field direction. The field at $\boldsymbol{s_1}$ therefore differs from that experienced by $\boldsymbol{s_2}$, which has no such hyperfine interaction and is only affected by B. As a result the electron spins $\boldsymbol{s_1}$ and $\boldsymbol{s_2}$ precess with Larmor frequencies differing by:

$$\Delta\omega_L = \frac{g\mu_B \Delta B}{\hbar} = \pm\frac{g\mu_B a}{2\hbar}, \tag{1.25}$$

where ΔB is the difference in magnetic field strengths experienced by the two electrons ($B_{\text{eff}} - B = \pm\frac{a}{2}$). The difference in precession frequencies is field independent (in contrast to the Δg mechanism), and leads to S-T_0 interconversion as the relative phases of the two electrons change, in a similar fashion to the Δg mechanism.

If the external field strength is weak ($B \leq a$), the spins are no longer quantized along the external field axis, instead aligned around their resultant $\boldsymbol{J} = \boldsymbol{s} + \boldsymbol{I}$, which in turn precesses around B. If $\boldsymbol{s_1}$ is the only electron spin hyperfine coupled to a nuclear spin, its projection onto the external field axis can change in time while the projection of $\boldsymbol{s_2}$ remains constant. This effectively leads to a spin-flip transition, and therefore interconversion between S and all three T states can be achieved.

This is shown by Figure 1.5, in a reference frame rotating at the Larmor frequency of

$\boldsymbol{s_2}$. Initially the mutual arrangement of spins is S but in time $\boldsymbol{s_1}$ precesses around the $\boldsymbol{J}$ resultant, so its z-projection matches that of $\boldsymbol{s_2}$ and a T$_-$ state is formed ($M_s = -1$).

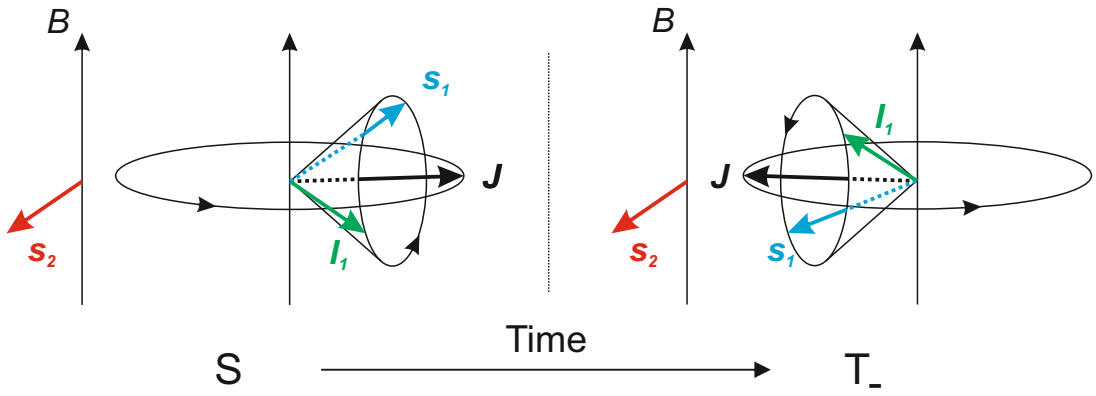


Figure 1.5: A simplified version of the hyperfine spin mixing mechanism at weak external fields ($B \leq a$), demonstrating S-T$_-$ mixing due to the change in relative orientation of $\boldsymbol{s_1}$ and $\boldsymbol{s_2}$. Electron and nuclear spins are represented by $\boldsymbol{s}$ and $\boldsymbol{I}$ respectively. $\boldsymbol{J}$ is the resultant of $\boldsymbol{s_1}$ and $\boldsymbol{I_1}$. This scenario is pictured in the rotating reference frame corresponding to the Larmor frequency of $\boldsymbol{s_2}$ precession around B.

1.6.3 Low-field effects

The existence of low-field effects was first predicted by Brocklehurst in 1976,[38] characterised by their opposite phase to the normal hyperfine-induced MFE when the system is exposed to weak magnetic fields ($0 < B < \frac{a\hbar}{2g\mu_B}$).[36,39] This is indicative of an increase in S-T mixing efficiency before the Zeeman splitting becomes dominant. LFEs are most easily understood by considering a one proton radical pair ($I = 1/2$).

The total spin angular momentum of the system, $\boldsymbol{F}$, is given by:

$$\boldsymbol{F} = \boldsymbol{S} + \boldsymbol{I}, \tag{1.26}$$

where $\boldsymbol{S}$ and $\boldsymbol{I}$ have their usual meanings of electron and nuclear spin, respectively. As for all angular momenta, the projection of the total spin angular momentum onto the static

field axis is given by M_F, which can take the values F, $F-1,\ldots,-F$. The eight possible total spin states for the RP are listed in Table 1.1.

State	Sα	Sβ	T$_0\alpha$	T$_0\beta$	T$_+\alpha$	T$_+\beta$	T$_-\alpha$	T$_-\beta$
F	$+\frac{1}{2}$	$+\frac{1}{2}$	$+\frac{1}{2}$	$+\frac{1}{2}$	$+\frac{3}{2}$	$+\frac{3}{2}$	$+\frac{3}{2}$	$+\frac{3}{2}$
M_F	$+\frac{1}{2}$	$-\frac{1}{2}$	$+\frac{1}{2}$	$-\frac{1}{2}$	$+\frac{3}{2}$	$+\frac{1}{2}$	$-\frac{1}{2}$	$-\frac{3}{2}$

Table 1.1: The total spin states of a one proton RP. S, T$_0$, T$_+$ and T$_-$ represent the electron spin states, while α and β denote the nuclear spin ($M_I = \pm 1/2$).

The LFE can be considered to arise from a relaxation in angular momentum selection rules on application of a weak field. In zero-field, both F and M_F are subject to the selection rules $\Delta F = 0$ and $\Delta M_F = 0$, whereas in the presence of a field only M_F must be conserved.

For the one proton case shown in Table 1.1, the result is an increase in the number of allowed transitions when $B \neq 0$. At zero-field there are only two allowed transitions which satisfy the selection rules: S$\alpha \leftrightarrow$ T$_0\alpha$ and S$\beta \leftrightarrow$ T$_0\beta$. When $B > 0$, F is allowed to vary and so two additional transitions from S$\alpha \leftrightarrow$ T$_+\beta$ and S$\beta \leftrightarrow$ T$_-\alpha$ are permitted. Compared to zero-field, the ST-mixing efficiency increases on application of a weak magnetic field. On increasing the strength of the field further the energetic separation of the T$_\pm$ levels due to the Zeeman effect starts to dominate and ST-mixing efficiency is reduced.

This overly simplified model gives a basic explanation of the origin of the LFE but offers no quantitative insight. The Hamiltonian of the LFE has been calculated to give an analytical solution and suitable characteristics of a RP to exhibit a significant LFE have been suggested.[39–41] These include a long geminate pair lifetime, weak exchange interactions compared to the hyperfine coupling, and a slow relaxation rate.

1.6.4 Spin relaxation

Relaxation is the term used to describe incoherent spin mixing mechanisms that act to destroy the spin polarization created upon RP formation. The (coherent) Δg and hyperfine mechanisms are based on the different magnetic environments of the radical pair electrons and interconvert spin states with a periodic oscillation at a well-defined rate. In contrast, relaxation is the result of random fluctuations in the local fields experienced by the electrons, which act to restore a Boltzmann distribution of spin states.[42]

Spin-lattice relaxation occurs due to the wide range of frequencies in the fluctuating local magnetic field due to rapid molecular motion and tumbling. If one of the component frequencies matches the energy separation between S/T_0 and $T_\pm$ states due to the Zeeman interaction (Figure 1.3a), then it can induce a spin-flip to interconvert between the states.

The effect of spin-spin relaxation is very similar to the Δg and hyperfine mechanisms, and causes $S\text{-}T_0$ interconversion by altering the Larmor frequencies of the electrons to destroy the phase coherence. In the case of relaxation, this is due to oscillations in the local field with very low frequencies, which appear virtually static on the timescale of the RP lifetime and act as an additional contribution to the local field. In contrast with the coherent mixing mechanisms, the rate of $S\text{-}T_0$ interconversion is randomised.

Were relaxation processes to be dominant, they would obscure the effects of coherent spin mixing and hence reduce the MFE of the system. For most organic radical systems they can be ignored as they act over a timescale ($10^{-6} - 10^{-4}$ s)[34] far longer than both typical SCRP lifetimes ($10^{-10} - 10^{-7}$ s) and the timescales for coherent spin mixing processes ($10^{-9} - 10^{-8}$ s).[43] However, some of the biological systems studied in this thesis, have geminate RP lifetimes on the order of microseconds, and so relaxation can cause significant challenges in the measurement of MFEs.

1.7 Biological Magnetic Field Effects

The possible interaction of magnetic fields with radical pair recombination reactions occurring in biological systems has taken on new significance in recent years, driven by interest in two main areas.

Weak environmental electromagnetic fields ($<< 1\,\mathrm{mT}$), such as those associated with high voltage power lines, have been suggested to adversely affect human health,[44–47] notably being linked to an increased incidence of the development of childhood leukaemia.[48,49] As the radical pair mechanism is the only current theory that could explain any adverse effects on human health due to such small interactions, this has led to the investigation of extremely low frequency (ELF) magnetic fields (μT, 50 Hz). However, the only existing evidence to date indicates that fields less than $0.4\,\mu\mathrm{T}$ have no such effect.[6,49]

More recently, interest has been focused on the phenomenon of magnetoreception, whereby a wide variety of animals can sense the very weak magnetic field of the Earth and use it for directional information when migrating over long distances.[2,3] Few *in vitro* studies existed[50] before the suggestion that the cryptochrome flavoprotein could be involved as the primary magnetic sensory molecule in those animals which exhibit magnetoreception.[16] Cryptochromes, are blue-light receptor proteins found in a wide range of organisms including plants, insects, birds and humans.[51,52] Radical pair reactions are also implicated in the highly efficient electron transfer steps in the initial stages of photosynthesis, and previous biological MFE studies had focused on these systems.[53–55]

If the radical pair mechanism were to be the basis of a magnetic compass sense in animals, the molecular detection system must be anisotropic (i.e. direction dependent). To act as a navigational cue, the outcome of a chemical reaction must be sensitive to the direction of an external field, as well as its magnitude.[16] There must also, of course, be a signalling mechanism which converts the chemical MFE into an electronic neuronal response for transmission to and interpretation by the animal's brain. While a magnetic sense has been claimed in plants[56] (and discredited)[57] and animals,[2] the majority of

interest has been focussed on avian magnetoreception.[1,4,5,58–65] Due to its popularity, a short introduction to this phenomenon is provided in the next section.

1.7.1 Magnetoreception

The ability of some animals to orient themselves within the weak magnetic field of the Earth is known as the phenomenon of magnetoreception. It is observed in the behaviour of a wide variety of animals including fish,[66,67] reptiles,[68] amphibians,[69] insects,[70,71] mammals,[72,73] and of course birds.[62] However, despite long-standing interest, the underlying biophysical mechanisms remain poorly understood.[17]

Currently, two proposed mechanisms to explain this behaviour in birds are under discussion.[74] A third, much more recent proposal involves the inner ear lagena,[75–77] but it remains unclear whether the input is magnetic or gravitational.[78]

The magnetite hypothesis[9,79] is based on deposits of magnetic iron-containing minerals within the body, with the crystals aligning themselves in an external magnetic field, acting like a traditional compass needle. In birds, these are proposed to be located in the upper beak and associated with the ophthalmic branch of the trigeminal nerve (V1).[11,80–82] However, there are conflicting reports in this area and the transmission of magnetic information to the brain via V1 is believed to be either important[83,84] or 'neither necessary nor sufficient'.[85] More recent work indicates that the iron-mineral deposits are macrophages and not magnetosensitive neurons.[86] The magnetite mechanism is strongly suspected to operate in fish[87,88] and rodents,[89] but there are aspects of the avian magnetic sense that indicates the involvement of radical pairs.[16,33,85,89–96]

European robins are known to exhibit a light-activated magnetic compass sense,[63,90] which also depends on the wavelength of light, with more reliable orientation performed under blue and green light conditions.[97–99] They are also disoriented under a range of oscillating magnetic fields (with frequencies from 50 kHz to 5 MHz) close to the Larmor frequency of an electron in the Earth's field,[94,100–102] and exhibit sensitivity to the incli-

nation (the angle the field makes with the ground) but not the polarity of the magnetic field.[62] These observations are strongly indicative of the involvement of a spin-correlated radical pair as part of the magnetic sense, as first suggested in a far-sighted prediction by Schulten et al.[103]

The radical pair hypothesis of magnetoreception involves the light dependent formation of an equilibrium of singlet and triplet states, the position of which can be perturbed by the Earth's magnetic field and lead to a neuronal signal. In order to act as a compass sense and provide directional information, the molecules involved in RP formation would need to be immobilised e.g. membrane bound, so that the anisotropic hyperfine interactions could lead to different responses.[5,59] Interest in this area was ignited by the proposal of cryptochrome proteins as the candidate magnetoreceptor molecule,[16] and their suitability for the role is outlined in the next section.

1.7.2 Cryptochromes and photolyases

Intense interest has been focused on the viability of cryptochrome proteins as the magnetosensitive molecule at the heart of the RPM hypothesis since 2000,[16] and four types of cryptochromes have since been found in the eyes of migratory birds.[91,104–106]

Cryptochromes are 55 kDa blue-light receptor flavoproteins, with a plethora of functions including control of growth and development in plants and entrainment of circadian rhythms in animals.[52,107–110] Now, they are also proposed to be involved in magnetoreception. They are closely related to the photolyase proteins, which are widely considered to be their evolutionary ancestors,[105,108] and with which they share high sequence and structural homology.[111–113] This includes a flavin adenine dinucleotide (FAD) cofactor, located within the protein structure in close proximity to a highly conserved chain of three tryptophan residues in a fixed spatial orientation. This has become known as the "tryptophan triad" and acts as an electron transfer chain.[114] It facilitates rapid electron transfer and provides the electrons required for photolyase to perform its function in re-

pairing UV damage to DNA.[110] Recent attention has been focused on the presence of a nearby fourth tryptophan residue in animal cryptochrome proteins, and its implications for cryptochrome magnetoreception.[115,116]

In cryptochrome, it is suggested that this mediates the transfer of an electron in a stepwise cascade process to form a spin-correlated radical pair between the fully oxidized FAD and the terminal (surface-exposed) tryptophan residue.[114,117,118] It is this flavosemiquinone/tryptophan (W) radical pair that acts as the magnetically sensitive species in the cryptochrome-centred radical pair hypothesis of magnetoreception. These radical pairs have already been demonstrated to possess the microsecond lifetime spin correlation required to exhibit magnetic field sensitivity.[117–121] If the reaction yields of the FAD/W radical pair were influenced by the direction of Earth's magnetic field vector (according to the RPM), then cryptochromes could act as a form of molecular compass providing directional information.[16,33,122,123]

Assuming cryptochromes are bound to membranes in an ordered array around the retina of migratory birds (where light activation would readily occur), the varying reaction yields at different points could be interpreted to provide directional information. This would subsequently need to be converted into a neuronal response by signal transduction, and the resulting impulse carried along the optic nerve to the cluster N forebrain via the visual thalamus.[5,59]

Much of the existing evidence for radical pair magnetoreception is circumstantial, including the wavelength dependence and disorientation effects described above.[59] Behavioural experiments on the *Drosophila melanogaster* fruit fly indicate that cryptochromes are crucial to the magnetosensitivity of these insects,[71,124] although whether they are the primary magnetosensitive species or just involved downstream as part of the signalling process is unclear. Interestingly, it has been shown that cryptochrome extracted from the retina of humans (*Hs*Cry) can reinstate the light-dependent magnetic sense in a Cry-deficient mutant fruit fly.[125]

Very recently a system has been discovered which combines the attributes of both Cry and magnetite based systems, the so-called "Mag-R" protein, which exhibits spontaneous alignment in magnetic fields.[126] There is no existing evidence that this new complex is involved in magnetoreception. To date, there remain no other candidate molecules apart from cryptochrome itself,[30,105,127] but no studies exist which provide irrefutable evidence in support of the cryptochrome RPM hypothesis.

Experiments where cryptochromes and photolyases exhibit *in vitro* responses to magnetic fields provide some of the most compelling evidence. Studies on photoactivated *Escherichia coli* photolyase have confirmed the existence of a long-lived (microsecond) FAD/W radical pair, which exhibits a magnetic response to an applied magnetic field, albeit much stronger than that of the Earth's.[19,128] Cryptochrome from the plant *Arabidopsis thaliana* (*At*Cry) has also been shown to be sensitive to magnetic fields *in vitro*, via the photoinduced formation of FAD/W radical pairs.[96] These promising results are built upon in this work with the observation of magnetic field effects in the animal cryptochromes from the *Drosophila melanogaster* fruit fly and the African clawed toad (*Xenopus laevis*).

To date, no biological protein system has been shown to respond to an Earth-strength field. Only a model system composed of covalently linked carotenoid, porphyrin and fullerene (a CPF triad) has been shown to be sensitive to such a weak field.[93] At higher fields, this system also exhibits a directional dependence in its response to the field, a crucial characteristic that must be shared by any biological chemical compass molecule.

1.8 Measuring MFEs

The effect of a magnetic field on a chemical reaction can either be detected by monitoring a change in kinetics or product yield compared with the zero-field case. The effects of both static and oscillating magnetic fields have been measured in a wide range of chemical systems that involve RP intermediates,[15,129–133] while due to their challenging nature, successful studies on biological systems are not widely reported. With the exception of

a small number using photoconductivity or HPLC techniques, the vast majority of the existing literature is based around optical detection methods.

Fluorescence detection can be a powerful tool due its zero-background nature. Its already high sensitivity can be improved still further by straightforward combination with modulation techniques and lock-in detection. However, it is of course limited to systems with sufficiently high fluorescence quantum yields, which can reduce its suitability for the study of biological molecules.[134]

The remainder of studies have been performed almost exclusively using techniques with absorption detection, the most prevalent of which is transient absorption (TA). These detection methods typically suffer from low sensitivity as the absorbance signal is detected as a small change in intensity against a large, noisy background. Flash photolysis techniques, such as TA, benefit from the intense pulse of radiation used to initiate the reaction producing a high instantaneous concentration of radical pair species. The magnetic field dependent yield of free radicals (triplet products) or ground state molecules (singlet recombination products) is measured as a function of time to monitor the time-dependent behaviour of the MFE.[93,96,128,135,136]

1.8.1 Magnetically Altered Reaction Yield (MARY) plots

To allow valid comparison between different detection methods, a standardised magnetic field effect (MFE) is defined. The change in sample absorbance upon photoexcitation, and therefore generation of radical species, is labelled ΔA. This differential absorbance can be measured in both the presence, ΔA_B, and absence, ΔA, of a magnetic field, allowing a percentage MFE to be defined as:

$$\begin{aligned} \text{MFE} &= \frac{\Delta A_B - \Delta A}{\Delta A} \times 100 \\ &= \frac{\Delta\Delta A}{\Delta A} \times 100, \end{aligned} \tag{1.27}$$

which is independent of the size of the absorbance signal.

A common approach is to record the MFE as a function of applied field strength, to produce what is known as a magnetically altered reaction yield (MARY) plot.

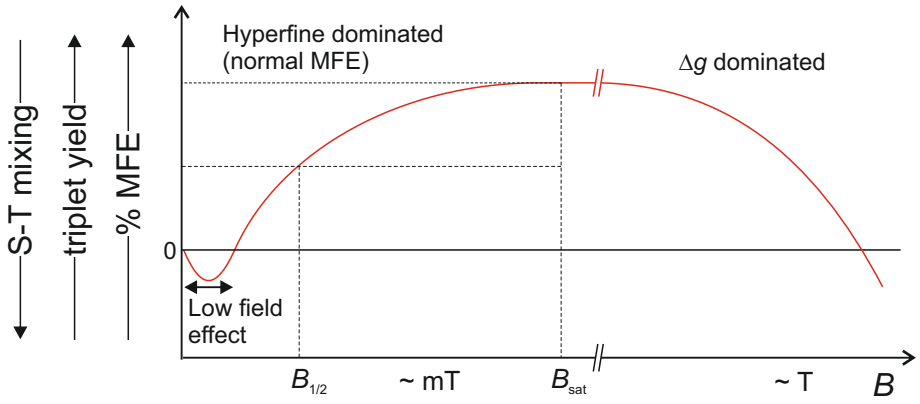


Figure 1.6: A schematic representation of a magnetically altered reaction yield (MARY) plot for the free radical yield of a triplet-born radical pair. An increase in applied magnetic field, B, affects the ST-mixing to different extents, depending on the dominant mechanism (see Section 1.6 for details). The width of the curve is characterised by the $B_{1/2}$ parameter, the field at which the hyperfine-dominated MFE reaches half its saturated value, B_{sat}.

A schematic MARY spectrum for the free radical yield of a triplet-born RP is shown in Figure 1.6 (consistent with the photochemical scheme in Figure 1.4). The labelled features arise from the dominant regimes of the various ST-mixing mechanisms described in Section 1.6. This behaviour is exhibited by the chemical model systems studied throughout this thesis. It is only the cryptochrome and photolyase proteins, with their highly efficient electron transfer, that form singlet-born RPs. To envisage the MARY spectrum for a given singlet-born RP product yield (geminate recombination or triplet escape), the phase of the corresponding triplet-born curve is simply inverted.

At low fields, a relaxation of the selection rules leads to an initial increase in the ST-mixing efficiency (the low-field effect, Section 1.6.3). As a result, more RP singlet spin state is formed and there is a higher chance of spin-allowed recombination, reducing the triplet (free radical) yield compared to the zero-field case (MFE < 0). As the strength of the applied field is increased to exceed the average hyperfine coupling ($B > a$), the

Zeeman splitting begins to dominate, separating the $T_{\pm}$ levels in energy from S-T_0. The maximum of the LFE is determined by the competition between these effects.[137]

With further increase in magnetic field, the ST-mixing efficiency drops relative to the zero-field case. Radicals formed in the $T_{\pm}$ states are now trapped and the chance of spin-allowed recombination decreases, leading to a higher free radical yield. This region is known as the 'normal' MFE. S-T_0 mixing is the only interconversion possible, and this occurs at frequencies determined by the (B-independent) hyperfine coupling constant (Section 1.6.2), indicated by the eventual plateauing of the MARY response. At high enough fields, much higher than those used in this work, the field-dependent Δg mechanism begins to dominate, which increases the rate of S-T_0 interconversion and therefore the overall rate of spin mixing, reducing the free radical yield.

The width of the MARY profile can be used to characterise MFEs. It is quantified via the $B_{1/2}$ parameter, defined as the field at which the MFE reaches half of its saturated value. Throughout this thesis, the value is extracted from a Lorentzian fit to the experimentally measured MARY curves. It can also be predicted theoretically, using the empirically derived Weller equation:[138]

$$B_{1/2} = \sqrt{3}\frac{\langle a_F\rangle^2 + \langle a_D\rangle^2}{\langle a_F\rangle + \langle a_D\rangle}, \tag{1.28}$$

where F and D label the individual radical components comprising the radical pair and $\langle a_X\rangle$ is the effective hyperfine coupling constant for each radical:[139]

$$\langle a_X\rangle = \sqrt{\frac{4}{3}\sum_i a_{iX}^2 I_{iX}(I_{iX}+1)}. \tag{1.29}$$

Here, I_{iX} is the nuclear spin quantum number and a_{iX} is the hyperfine coupling constant for nucleus i in radical X. The value obtained for the flavin/tryptophan radical pair relevant to this work is $B_{1/2} = 3.3\,\mathrm{mT}$, calculated from the isotropic hyperfine coupling constants.[140,141]

1.8.2 Biological MFE detection

In an effort to compensate for the low sensitivity of traditional absorption measurements, high concentrations (mM) and long sample pathlengths, requiring high sample volumes (mL), are used. Extensive signal averaging extends the typical experiment duration to several hours, which would cause excessive photodegradation of the sample, requiring even larger volumes to permit replenishment of the sample by solution flow.

These demands on the systems of interest are particularly problematic for the precious biological protein samples proposed to be at the heart of radical pair magnetoreception. Typically, cryptochrome proteins are difficult (and therefore expensive) to express, and can only be produced in low volumes. High concentrations of protein in solution leads to precipitation and aggregation, which causes issues of light scatter as well as the formation of less biologically relevant entities. They are often very sensitive to photodegradation which also precludes the long signal averaging permitted on less precious chemical systems. This combination of factors makes it challenging to successfully detect MFEs in biological samples using existing approaches.

Previously, our group has reported the development of a range of cavity-based optical techniques, optimised for study in the liquid phase to offer substantial improvements in sensitivity for such applications. These have comprised monochromatic and broadband variants of cavity ring-down spectroscopy (CRDS)[19] and cavity-enhanced absorption spectroscopy (CEAS).[18,142]

1.9 Scope of the Thesis

This thesis is concerned with the further development and application of these existing techniques to provide greater insight and understanding into a selection of biologically relevant chemical and protein systems. The next chapter introduces optical cavities, sets out the various experimental methodologies implemented in this work, and gives a brief

overview of other condensed-phase applications in which they have found success. Chapter 3 gives a brief overview of the experimental hardware, and characterises the instrumentation and the photochemistry of the radical pair systems studied.

Chapter 4 reports on the results of broadband-CRDS (BBCRDS) studies of chemical model systems and the *Xl*Cry animal protein. Broadband-CEAS (BBCEAS) studies of a similar range of photochemical systems are reported in Chapter 5. The basic model system studies in the first sections of this chapter were the subject of a recent publication,[142] while the field effect detected in the *Dm*Cry protein using this technique was the first such measurement recorded and is currently awaiting publication.

The culmination of this work is reported in Chapter 6, where the microsecond time-resolution of BBCRDS is combined with the spectral multiplexing advantage of BBCEAS to produce a powerful new instrument, known as optical cavity-enhanced transient absorption spectroscopy (OCTAS). This new technique has been successful in detecting temporally and spectrally resolved magnetic responses of both model systems and cryptochromes with high sensitivity.

The final chapter summarises the achievements and continuing challenges of the project, and suggests some areas that could hold interest in future.

Chapter 2

Cavity Enhanced Spectroscopy

Spectroscopy is the study of light's interaction with matter, from which a range of important atomic and molecular properties can be extracted. The lines observed comprise a spectrum, corresponding to allowed transitions between the various quantum states of a molecule. These can include electronic transitions studied by simple UV-Vis spectroscopy, as well as vibrational and rotational transitions probed by infrared (IR), microwave and Raman spectroscopy. The nuclear and electronic spins of molecules introduced in the previous chapter can be studied by NMR and EPR techniques, respectively, the former being particularly powerful and ubiquitous in synthetic chemistry and medical applications, while the latter is limited to the characterisation of paramagnetic species.

The use of spectroscopy has permitted the detailed study of our atmosphere, as well as those of distant planets. The interaction of matter with a photon travelling light years across the universe provides clues to the composition of interstellar space, which would otherwise be completely inaccessible. Spectroscopy led to the discovery and identification of the element Helium in the sun before it was detected on Earth,[143] and is widely used in the hunt for exoplanets by monitoring the dip in light intensity as they pass in front of a more distant star. The modification of the transmitted light permits the characterisation of their atmosphere and allows us to assess the possibility of the existence of life in the

farthest reaches of the universe.

This chapter introduces the fundamentals of single-pass electronic spectroscopy, described by the Beer-Lambert law. The major shortcoming of this technique is identified as low sensitivity. Multipass arrangements, and their natural extension optical cavities, are presented as a solution in which the sample is surrounded by two highly reflective mirrors to increase the effective pathlength. A brief introduction to the theory of optical cavities is provided, followed by a description of two of the most prevalent techniques currently used for spectroscopic measurements, cavity ring-down spectroscopy (CRDS) and cavity-enhanced absorption spectroscopy (CEAS). The discussion is extended to the broadband variant of CEAS (BBCEAS) of most relevance to this work, and a consideration of suitable light sources is provided. Finally, existing work applying optical cavity enhancement to condensed phase spectroscopy is summarised.

2.1 The Beer-Lambert Law

The simplest kind of spectroscopy involves measurement of the reduction in light intensity following a single-pass through a sample, represented in Figure 2.1. The incident light intensity on the sample, I_{in}, and the transmitted light intensity through the sample, I, are related by the Beer-Lambert law:[144–146]

$$I = I_{\text{in}} 10^{-\epsilon C l}, \tag{2.1}$$

in which ϵ is known as the molar attenuation coefficient, C is the concentration of the absorbing species, and l is the pathlength the light travels through the sample. The characteristic absorbance, A, of the sample is defined as:

$$A = -\log_{10} \frac{I}{I_{\text{in}}} = \epsilon C l. \tag{2.2}$$

While the analytical chemistry community base measurements of absorbance around

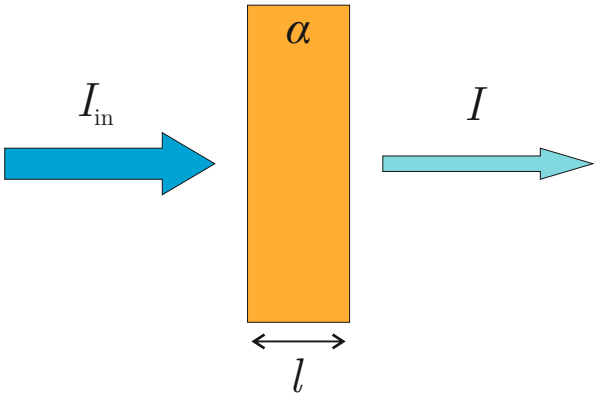


Figure 2.1: A simple schematic representation of a single-pass direct absorption measurement of a sample with attenuation coefficient, α, and optical pathlength, l. The incident and transmitted light intensities are represented by I_{in} and I, respectively.

the decadic (base-10) scale, gas phase spectroscopists conventionally use natural logarithms to characterise absorption and scattering losses:

$$A' = -\ln \frac{I}{I_{\text{in}}} = \alpha l, \tag{2.3}$$

where α is known as the attenuation coefficient of the sample. These two expressions can be related, and therefore easily interconverted, by:

$$A = \epsilon C l = \frac{\alpha l}{\ln(10)}. \tag{2.4}$$

For a well-known optical pathlength, l, and attenuation coefficient, α, an unknown concentration can be determined conveniently without requiring independent calibration. In general, α has a wavelength dependence, and therefore the full absorption spectrum of a sample can be obtained by scanning the frequency of the incident light beam across the absorption feature.

Direct absorption spectroscopy is a powerful tool due to its near universal applicability, and its experimental simplicity. However, single-pass variants are limited in their

sensitivity when the sample has a small intrinsic attenuation coefficient, is present in low concentrations, or if only a small sample volume is available for study (as this reduces the optical pathlength).

The minimum detectable absorbance in such a single-pass experiment is defined as:

$$A_{\min} \ln(10) = \alpha_{\min} l = \frac{\Delta I_{\min}}{I_{\text{in}}}, \tag{2.5}$$

and is determined by minimum detectable reduction in light intensity, $\Delta I_{\min}$, caused by sample absorption. For high sensitivity, a very small attenuation in light level must be distinguished against a large (and typically noisy) background. Even for modern instruments, utilising stabilised light sources and dual-beam arrangements to provide a reference for background correction, this proves challenging, and typically absorbances less than 1×10^{-3} are undetectable except with prolonged averaging.

2.2 Multipass Techniques

One common approach utilised to increase the sensitivity of a direct absorption measurement is to artificially increase the optical pathlength, l, through the sample with multiple passes. This is achieved by reflecting the beam between two mirrors, increasing the interaction of light with the sample and leading to a larger absorbance signal, as shown by Equation 2.4.

Two so-called multipass arrangements are shown in Figure 2.2, for a) a White cell[147] and b) a Herriott cell,[148] with high reflectivity mirrors in two different configurations around the sample. Light is injected at an angle, either adjacent to a mirror or via an aperture drilled through its centre. The non-zero incident angle on the mirrors results in the spatial distribution of the beam on each reflection and the multiple passes take different optical paths, avoiding interference effects. While the increased number of passes can lead to an increase in pathlength, and therefore A, of one or even two orders of magnitude,

the distribution of the beam paths reduces spatial resolution, requiring large mirrors and large sample volumes.

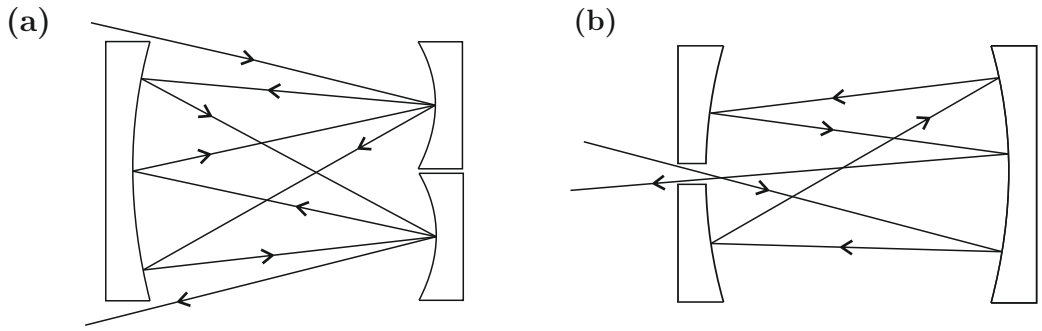


Figure 2.2: A schematic representation of two traditional multipass arrangements: a) a White cell and b) a Herriott cell. The large beam spread between the mirrors precludes the study of small sample volumes.

The multipass arrangement can be extended to its natural extreme by making the incidence angle equal to zero, and coupling the light through the back of the input mirror without the need for an aperture. This is the basis of optical cavity techniques. The spatial overlap of the multiple passes made within the cavity ensures that the same volume of sample is probed on each round trip. In theory, this limits the required minimum sample volume to the product of the beam diameter and the pathlength of the sample cell. In the gas phase, the pathlength is often equal to the length of the cavity as the mirrors are used as the ends of the sample tube. In the condensed phase, however, due to the liquid nature of the sample, an additional element such as a cuvette is usually required and the pathlength can be controlled. The resulting high number of optical passes is determined by the losses due to mirror transmission and the sample on each pass, and is normally beyond the reach of the multipass arrangements shown in Figure 2.2.

In very recent work, of only tangential relevance but which garnered widespread attention, two extremely long (i.e. 4 km) mutually perpendicular optical cavities were used to detect gravitational waves, first predicted by Einstein exactly 100 years ago as a consequence of his newly developed theory of general relativity.[149,150]

2.3 Optical Cavities

2.3.1 Cavity mode structure and stability

The spatial overlap of multiple passes of light results in the formation of an optical cavity (also known as a resonator), with an associated interference pattern that only permits transmission of light of certain frequencies.[151]

The simplest variant of an optical resonator, known as the Fabry-Perot interferometer, consists of two flat surfaces that repeatedly reflect and refocus an optical beam. The transmission spectrum of the interferometer exhibits maxima and minima, corresponding to constructive and destructive interference between the partial waves supported by the cavity, respectively.

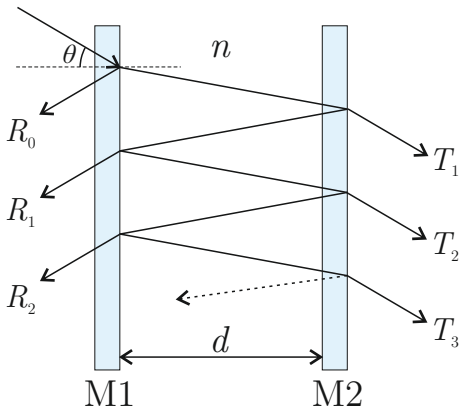


Figure 2.3: A Fabry-Perot interferometer formed between two reflective surfaces, M1 and M2, the simplest implementation of an optical cavity. The standing wave solutions (mode structure), and therefore the transmission profile, depend on the incident angle of the input light, θ, the reflectivity of the surfaces, R, and their separation, d, and the refractive index of the material between the surfaces, n.

An optical cavity is the result of taking the number of passes achieved by this arrangement to the extreme, by reducing incidence angle, θ, to zero. The exact spatial overlap of the multiple passes of light creates interference patterns, known as cavity modes. For a fixed mirror separation (cavity length), d, and input angle, θ, the separation between

adjacent transmission peaks is known as the free spectral range, $\Delta\nu_{\mathrm{FSR}}$. This is indicated in Figure 2.4, which shows the mode structure for two cavities of fixed length but different values of the mirror reflectivity, R.

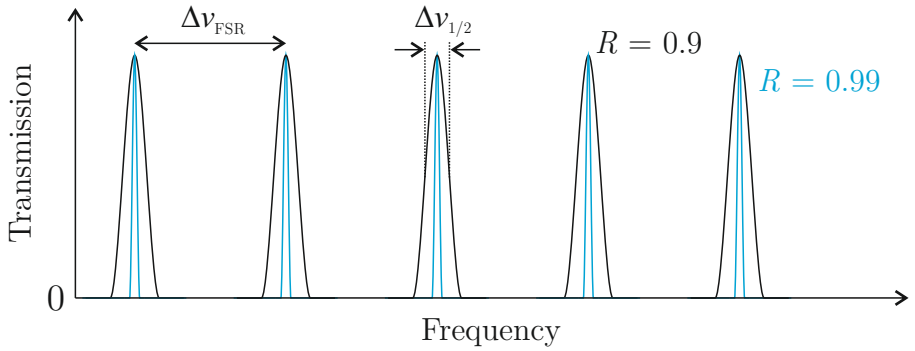


Figure 2.4: A schematic representation of the mode structure of an optical cavity. The free spectral range, $\Delta\nu_{\mathrm{FSR}}$, is the frequency spacing between adjacent cavity modes, and is typically on the order of hundreds of MHz. The full width at half maximum (FWHM), $\Delta\nu_{1/2}$, is reduced by increasing mirror reflectivity, which results in an increase in the ratio of the FSR to the $\Delta\nu_{1/2}$, also known as the cavity finesse.

Increasing R narrows the transmission peak, leading to a smaller full-width-at-half-maximum (FWHM), $\Delta\nu_{1/2}$. The finesse, F, of an optical cavity is widely used to characterise its resolution and sensitivity. It is defined as the ratio of the separation of the transmission features ($\Delta\nu_{\mathrm{FSR}}$) to their width ($\Delta\nu_{1/2}$):[152]

$$F = \frac{\Delta\nu_{\mathrm{FSR}}}{\Delta\nu_{1/2}} = \frac{\pi\sqrt{R}}{1-R}. \tag{2.6}$$

A higher mirror reflectivity therefore leads to a higher finesse, and the sharper transmission peaks result in higher frequency resolution. However, it is consequently more challenging experimentally to couple light from a narrow bandwidth light source into a cavity of higher finesse.

In addition to longitudinal modes the cavity also supports transverse modes, which differ in their spatial profile of the beam in the direction of cavity propagation. The most important of these is the TEM_{00} mode as it is Gaussian in shape, and can therefore

be coupled into most efficiently by a propagating laser pulse. It also has the smallest divergence of all transverse modes, and can therefore be focused to the smallest spot size within the cavity. Great effort is taken to couple into this mode as efficiently as possible as a result, usually requiring pre-cavity lenses.

Once light is injected into the cavity by mode matching of the input light source, either by scanning the laser frequency or the cavity length, it must be contained within it for a large number of passes in order to benefit from the increased sensitivity. If the constrained beam is not successively refocused, then it can spread and diffraction losses can occur where light is lost outside the edge of the cavity mirrors. This depends on the relative values of the cavity length, d, and the radii of curvature of the cavity mirrors, r. The criterion of cavity stability is given by:[153]

$$0 < g_1 g_2 < 1, \tag{2.7}$$

where, for the ith cavity mirror,

$$g_i = \left(1 - \frac{d}{r_i}\right). \tag{2.8}$$

Values that satisfy this condition are shown as unshaded regions in Figure 2.5, where the axes represent the g-values of the two mirrors. Three examples of special cases of cavity configurations are also shown, along with their respective stabilities.

In all examples, the cavities are only marginally stable and any slight misalignment will result in large diffraction losses. The plane parallel arrangement ($r_1 = r_2 = \infty$) between two flat surfaces is the archetypal Fabry-Perot interferometer, and is unpopular due to the difficult nature of alignment. Practical cavities incorporate at least one concave element for this reason. The concentric arrangement ($2r_1 = 2r_2 = d$) is popular in some applications as it guarantees the smallest beam waist at the centre of the cavity and therefore the smallest probed volume of sample.

A stable cavity is one for which light is refocused after each round trip between the

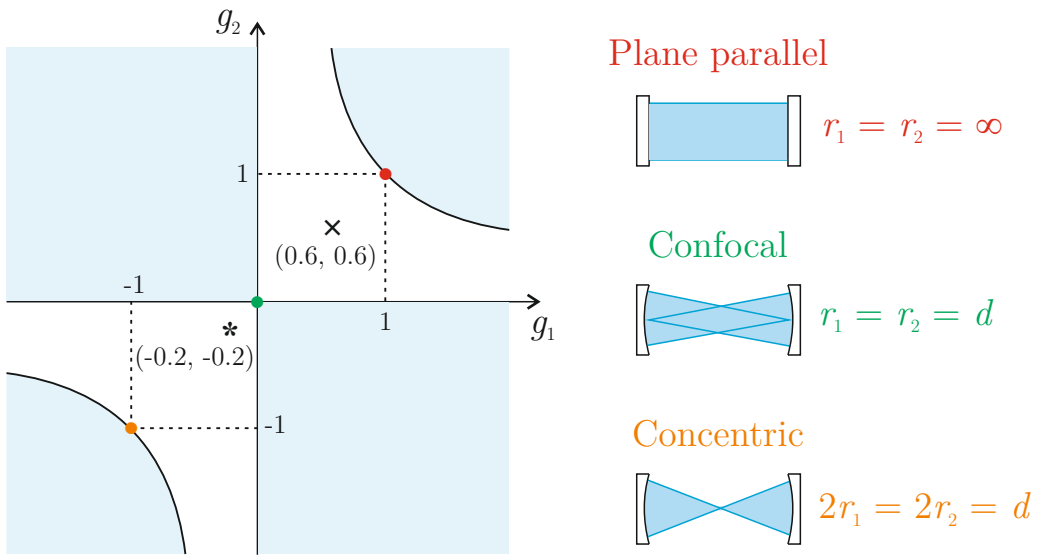


Figure 2.5: The conditions for cavity stability illustrated graphically as a function of the g values for each mirror (see text). Only the unshaded regions of the plot lead to the successive refocusing of light and thus the formation of a stable cavity, without huge diffractive losses due to beam spread. Three special cases with only marginal stability are plotted. The stability of the cavities used in this project are indicated with a cross (BBCEAS and OCTAS, Chapters 5 and 6: $d = 0.2\,\text{m}$, $r_1 = r_2 = 0.5\,\text{m}$), and a star (CRDS, Chapter 4: $d = 0.6\,\text{m}$, $r_1 = r_2 = 0.5\,\text{m}$).

mirrors. For extremely high finesse cavities excited by narrowband laser sources (with bandwidths less than the FSR), the chosen geometry can be vital in minimising diffraction losses or the excitation of higher order transverse modes.

The majority of condensed phase applications do not employ narrowband lasers as light sources due to the broad nature of the absorption features in solution Diffraction losses are typically minimal compared to the contributions from the mirrors, sample and any intracavity elements present. As long as the fundamental condition for stability is fulfilled, the choice of geometric arrangement in most condensed phase experiments is instead governed by the consideration of available sample volume and method of constraint.

Optical cavities can be used to great effect in enhancing the signal of direct absorption measurements. Introductions to the two most popular and widely used variants, CRDS

and CEAS, are given in the following sections.

2.4 Cavity Ring-Down Spectroscopy (CRDS)

Cavity ring-down spectroscopy (CRDS) was initially discovered as a by-product of a technique developed to measure the reflectivity of high quality optical mirrors.[154,155] O'Keefe and Deacon were able to assign a feature in their data to the weak absorption band of a forbidden transition in molecular oxygen.[156] Subsequently, CRDS has found most application and success in the gas phase, where the use of a high finesse optical cavity can lead to major gains in sensitivity. The low per-pass background losses due to scattering by the gaseous sample, and the lack of requirement for additional intracavity optical elements such as a sample cell for confinement, can lead to ring-down times approaching milliseconds, depending on the length of the cavity.

More recently, CRDS has found increasing application in the liquid phase, where its enhancement is not as dramatic, but still significant. It now exists in a range of guises, finding application in a wide range of areas.[152,157–160]

To provide an introduction to the technique, the simplest form of pulsed CRDS using a linear cavity is considered here, shown in Figure 2.6. A pulse of laser light with intensity I_{in} is injected into a high finesse optical cavity through the back of the input mirror, M1. The circulating light intensity decays exponentially due to a combination of loss processes, including transmission through the cavity mirrors and absorption and scattering within the cavity. The small amount of light transmitted through the rear cavity mirror, M2, on each round trip is recorded as a function of time using a sensitive detector, and is fitted to extract the ring-down time, τ.

Assuming the duration of the laser pulse is shorter than the round trip time of the cavity, the detected signal is a train of pulses with exponentially decaying intensity. For the simple case shown in Figure 2.6, the two cavity mirrors have identical reflectivity, R. If I_{in} is the light intensity incident on the rear of M1, then the light intensity after the

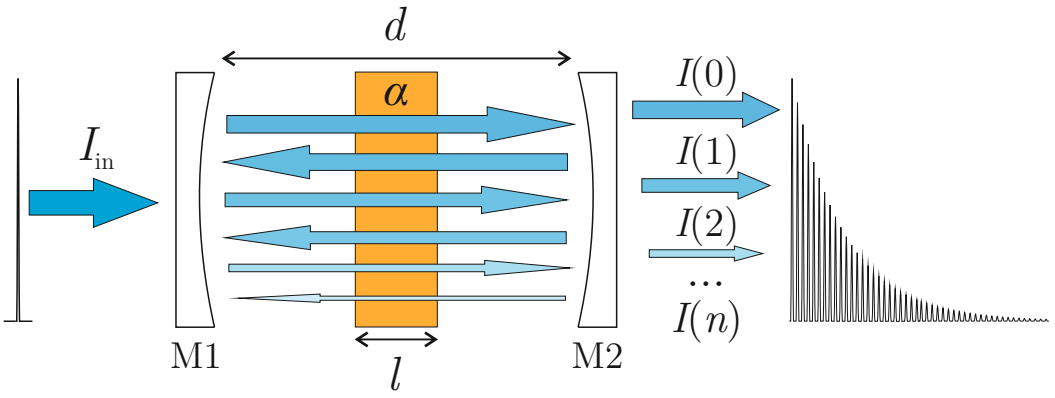


Figure 2.6: A simple schematic of the CRDS experiment, showing the series of reflections the incident light, I_{in}, undergoes on insertion into the cavity. The intensity detected after n round trips through a cavity of length d, containing a sample of pathlength l and attenuation coefficient α, is shown as a resolved pulse train, $I(n)$. The spatial position of the arrows is not indicative of the behaviour of the intracavity light, which retraces the same path through the sample on each pass.

first pass through the cavity, $I(0)$, is given by:

$$I(0) = I_{\text{in}} T^2 \mathrm{e}^{-\alpha l}, \tag{2.9}$$

where $e^{-\alpha l}$ is the fraction of incident light transmitted after a single-pass through the sample (assuming the Beer-Lambert law), and the mirrors are assumed to be ideal ($T = 1 - R$, where T is the mirror transmission).

For each subsequent round trip that the surviving intracavity intensity makes, it is further attenuated by a factor of $R^2 e^{-\alpha l}$. After a given number, n, of such round trips the detected intensity is:

$$I(n) = I(0) \left(R \mathrm{e}^{-\alpha l} \right)^{2n} = I(0) \exp \Big(2n (\ln R - \alpha l) \Big). \tag{2.10}$$

The detector is usually chosen to be unable to resolve the pulse train, and so the output signal appears as a smooth monoexponential decay. Consequently, the discrete variable n

can be changed to the continuous time variable t, given by:

$$t = n\frac{2d}{c}, \tag{2.11}$$

where d is the mirror separation (often equal to l in gas phase measurements), and $2dn$ is the total distance travelled by the light pulse. Therefore, the time-dependent light intensity escaping the cavity can be expressed as:

$$I(t) = I(0)\exp\left(\frac{ct}{d}\left(\ln R - \alpha l\right)\right). \tag{2.12}$$

As the reflectivity of cavity mirrors is normally chosen to be close to 1 in order to achieve a high effective pathlength, the approximation $\ln R = -(1-R)$ is valid and so the expression can be re-written as:

$$I(t) = I(0)\exp\left(-\frac{ct}{d}\left(1 - R + \alpha l\right)\right). \tag{2.13}$$

The ring-down time, τ, is defined as the time taken for the detected intensity to reach $1/e$ of its initial value, $I(0)$:

$$\tau = \frac{d}{c\left(1 - R + \alpha l\right)}. \tag{2.14}$$

In the case of an empty cavity (i.e. one with no absorber present), $\alpha = 0$ and the ring-down time, τ_0, is simply given by:

$$\tau_0 = \frac{d}{c\left(1 - R\right)}. \tag{2.15}$$

The absorbance, αl, can therefore be calculated by simple rearrangement of the expressions for the ring-down times with and without the absorbing species present:

$$A\ln(10) = \alpha l = \frac{d}{c}\left(\frac{1}{\tau} - \frac{1}{\tau_0}\right) = \frac{d}{c}\frac{\Delta\tau}{\tau_0\tau}, \tag{2.16}$$

where $\Delta\tau = \tau_0 - \tau$. If a tunable laser is available, the full absorption spectrum can be obtained by measuring τ and τ_0 as a function of wavelength.

The benefits of CRDS are clear from Equation 2.16. As in conventional absorption spectroscopy, the technique is self-calibrating, and provides absolute absorbance values without the need for an additional calibration step beyond the measurement of τ_0. In addition, the measurement is based around the rate of the decay of light intensity, rather than the absolute intensity itself, and so the technique is relatively insensitive to shot-to-shot intensity fluctuations in the probe beam.

2.4.1 CRDS sensitivity

The consequence of measuring in the time domain is that instead of distinguishing a small difference in two large intensity signals, the sensitivity of CRDS is determined by how accurately a small change in ring-down times can be measured. The minimum detectable absorbance is therefore given by:[152]

$$A_{\min} \ln(10) = \frac{d}{c} \frac{\Delta\tau_{\min}}{\tau_0^2} = (1 - R) \left(\frac{\Delta\tau}{\tau_0} \right)_{\min}, \tag{2.17}$$

where $\Delta\tau_{\min}$ is the smallest detectable change in the ring-down time, and for very similar ring-down times $\tau_0\tau \approx \tau_0^2$ has been assumed.

In the condensed phase applications described in this thesis, background losses due to scattering and/or absorption increase with optical pathlength. Consequently, a straightforward increase in mirror reflectivity, R, or τ_0 (e.g. by increasing cavity length, d) does not necessarily lead to an increase in the sensitivity of a CRDS measurement, as might be inferred from Equation 2.17. The use of a high resolution digitiser for the detected signal can help, as improved time and intensity information can lead to more accurate fits, particularly for the fast decays commonly seen in condensed phase applications.

2.5 Cavity-Enhanced Absorption Spectroscopy (CEAS)

Cavity Enhanced Absorption Spectroscopy (CEAS),[161] also known as integrated cavity output spectroscopy (ICOS),[162] has long been used to provide sensitive gas phase measurements. Experimentally simpler than CRDS, the cavity is continually pumped with probe light and its integrated intensity is monitored, which is proportional to the absorbance of any sample within the cavity. In contrast to CRDS, the fractional change in light intensity is measured in CEAS, akin to conventional direct absorption techniques. The lack of necessity for detectors with a fast time response leads to a decrease in cost and the complexity of data acquisition and analysis. A wide range of variants exists,[160] and their basis is described in great detail elsewhere.[152] A brief overview is given here.

In CEAS, light is continually pumped into the high finesse optical cavity formed between two highly reflective mirrors. The light intensity inside the cavity rapidly reaches a steady state corresponding to equal rates of injection and loss due to absorption, scattering and mirror transmission. The light intensity escaping the rear cavity mirror is monitored to determine the sample absorbance, as described below.

Figure 2.7 shows a simple schematic representation of the circulating and measured intensities of light in a CEAS experiment. The measured intensity can be modelled as a superposition of photons having made differing numbers of round trips in the cavity. Each mirror is treated as ideal, with reflectivity R and transmission $T = 1 - R$. Assuming Beer-Lambert behaviour, the per-pass transmission through the sample is $e^{-\alpha l}$. The total time-integrated intensity transmitted through the rear cavity mirror and incident on the detector is given by the sum of the transmitted light intensities after n round trips.

After the first pass through the cavity, the intensity is given by:

$$I(0) = I_{\text{in}}(1 - R)^2 \text{e}^{-\alpha l}. \tag{2.18}$$

The light must make complete round trips before it is detected again. On each one its

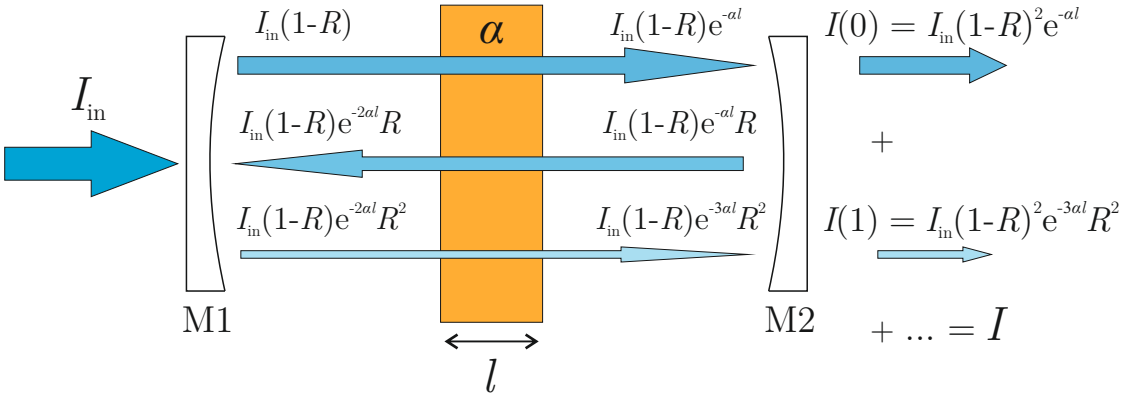


Figure 2.7: A simple schematic of the CEAS experiment showing the behaviour of the incident light, I_{in}, on insertion into the cavity. The intensity detected from a cavity comprising two mirrors of reflectivity R, and containing a sample of pathlength l and attenuation coefficient α, is given by the sum of the individual intensities after n round trips. The spatial position of the arrows is not indicative of the behaviour of the intracavity light, which retraces the same path through the sample on each pass.

intensity is reduced by a factor $R^2e^{-2\alpha l}$, and so the total detected intensity after the light has made n round trips is given by the expression:

$$I = I_{\text{in}}(1-R)^2\text{e}^{-\alpha l}\sum_{n=0}^{\infty} R^{2n}\text{e}^{-2n\alpha l}. \tag{2.19}$$

As both R and $e^{-\alpha l}$ are less than one, the infinite geometric series in the summation term converges and can be written as:

$$I = I_{\text{in}}\frac{(1-R)^2\text{e}^{-\alpha l}}{1-R^2\text{e}^{-2\alpha l}}. \tag{2.20}$$

For an empty cavity (i.e. $\alpha = 0$), the transmitted intensity, I_0, is:

$$I_0 = I_{\text{in}}\frac{(1-R)^2}{1-R^2}, \tag{2.21}$$

and the ratio of Equations 2.21 and 2.20 gives:

$$\frac{I_0}{I} = \frac{1 - R^2 \mathrm{e}^{-2\alpha l}}{(1 - R^2)\mathrm{e}^{-\alpha l}}. \tag{2.22}$$

As has been shown by Fiedler et al.,[163] this can be rewritten to give the intracavity absorbance:

$$A \ln(10) = \alpha l = \left| \ln \left[\frac{1}{2R^2} \left(\sqrt{4R^2 + \left(\frac{I_0}{I}(1 - R^2) \right)^2} - \frac{I_0}{I}(1 - R^2) \right) \right] \right|. \tag{2.23}$$

Assuming $\alpha \to 0$ and $R \to 1$, which is reasonable in most CEAS applications when high reflectivity mirrors are used to monitor low absorbances, Equations 2.22 and 2.23 both simplify to:

$$A \ln(10) = \alpha l = \left(\frac{I_0}{I} - 1 \right) (1 - R_{\mathrm{eff}}), \tag{2.24}$$

where $\left(\frac{I_0}{I} - 1\right)$ represents the experimental observable which is proportional to sample absorbance. The constant of proportionality, $(1 - R_{\mathrm{eff}})^{-1}$ is known as the cavity enhancement factor (CEF), and can be interpreted as the number of passes the light makes through the sample.

At this stage it is important to realise that on incorporation into an optical cavity, the measured mirror reflectivity, R, will be reduced to an effective mirror reflectivity, R_{eff}, due to scattering and absorptive losses characteristic of the particular cavity set-up These overall background losses, L_{b}, are then folded into the mirror reflectivity, related to the original value by:[164]

$$R_{\mathrm{eff}} = R(1 - L_{\mathrm{b}}). \tag{2.25}$$

It is important to consider the conditions under which the approximations that lead to Equation 2.24 are valid.[152] The absorbances calculated for various values of $\frac{I_0}{I}$ from Equation 2.23 (exact) and Equation 2.24 (approximated) are shown in Figure 2.8 as solid lines and open circles, respectively. They are shown for a range of mirror reflectivities

relevant to study in the condensed phase.

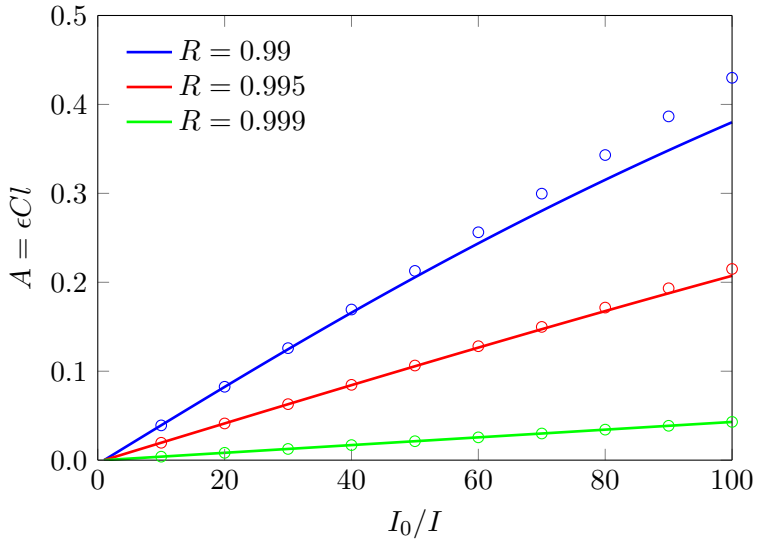


Figure 2.8: The relationship between absorbance ($l = 1\,\text{mm}$) and the CEAS measured ratio I_0/I, based on Equation 2.23 (solid lines) and Equation 2.24 (open circles). The approximations of $R \to 1$ and $\alpha \to 0$ which lead to the linear relationship, break down for low reflectivities ($R = 0.99$, blue) and high absorbance values ($A \geq 0.2$).

At high levels of light attenuation $\left(\frac{I_0}{I}\right)$ and low values of R, there is a significant deviation between the two expressions due to a breakdown in the approximations made (blue line and circles, $R = 0.99$). Even in this case, it is evident from the figure that the agreement only breaks down for absorbances that are sufficiently high to be detectable by single pass experiments, and so optical cavities would generally not be required. It is important to note that under the typical conditions used in this work ($R = 0.998$, $\frac{I_0}{I} \leq 10$) the agreement is excellent and Equation 2.24 is appropriate. The maximum value of $\frac{I_0}{I}$ in a CEAS experiment is generally limited by the dynamic range of the detector, and in our instrument it varies between 30 and 100 dependent on wavelength.

A significant disadvantage of CEAS, compared with single-pass measurements or CRDS, is the need to accurately know the value of R_{eff} (or equivalently the CEF) via a prior calibration step before absolute absorbance values can be obtained. This can be performed either by measurement of τ_0 using CRDS, or by use of a calibrant species with a well-

known single-pass absorbance. Any error in determining R_{eff} reduces the accuracy of any absorbance value subsequently measured. The calibration procedure for the CEAS-based techniques used in this thesis, employing a calibrant dye solution, is reported in detail in the next chapter (Section 3.7.1). Another drawback to CEAS detection is its sensitivity to probe beam fluctuation, a problem which it shares with conventional single-pass methods but to which CRDS is relatively immune.

In some applications, however, it does hold some advantages over CRDS. Any sample with high absorbance or scatter (such as condensed phase samples for instance) dramatically reduces the ring-down time of an optical cavity, reducing the sensitivity of CRDS in these studies. CEAS therefore enjoys a larger dynamic range than CRDS in such situations. For similar reasons, CEAS is more suitable for miniaturisation as the short ring-down times resulting from small cavity length result in no loss of sensitivity. The experimental demands of CRDS are relatively high, requiring short light pulses and detectors with fast time resolution, in contrast to the much simpler integrating detectors used for CEAS. Frequency modulation of the probe light intensity, coupled with lock-in detection, can also be combined with CEAS detection for a further increase in sensitivity, although this negates the advantage of simplicity a basic implementation holds over CRDS.

2.5.1 Broadband CEAS (BBCEAS)

CEAS was initially conceived and developed in the gas phase, using light sources with narrow spectral linewidths. However, in the condensed phase, absorption features are typically broad and featureless and time consuming scanning of the probe frequency is required to obtain spectral information. To increase the suitability of CEAS to condensed phase study a broadband probe beam can be used. A spectral output covering hundreds of nanometres is wide enough to record condensed phase absorption spectra simultaneously without the need for laser scanning. The result, broadband CEAS (BBCEAS) was initially conceived in the gas phase by Fiedler et al.[163] In this work, broadband is used to describe

spectral coverage of hundreds of nanometres. The choice of light source is covered in more detail in Section 2.6.

The treatment above can easily be extended to a broadband variant, where the light intensity exiting the cavity is measured at all wavelengths simultaneously. The wavelength dependent absorbance, $A(\lambda)$, is now given by a wavelength dependent version of Equation 2.24:

$$A(\lambda)\ln(10) = \alpha(\lambda)d = \left(\frac{I_0(\lambda)}{I(\lambda)} - 1\right)(1 - R_{\text{eff}}(\lambda)). \tag{2.26}$$

The light intensity transmitted by the cavity will have a wavelength dependence according to the spectral profile of the probe beam, and the mirror reflectivity will also vary (significantly) as a function of wavelength, particularly in the case of the broadband dielectric mirrors used in this project (see Chapter 3).

2.5.2 CEAS sensitivity

The minimum detectable absorbance of CEAS is given by:

$$A_{\text{min}}\ln(10) = \alpha_{\text{min}}d = \left(\frac{\Delta I}{I_0}\right)_{\text{min}}(1 - R_{\text{eff}}), \tag{2.27}$$

assuming $I \approx I_0$. This a very similar expression to the single pass case in Equation 2.5, with the additional $(1 - R_{\text{eff}})$ term. Hence the CEF, $(1 - R_{\text{eff}})^{-1}$, can be thought of as the reduction in the minimum detectable absorbance measurable by CEAS compared to a single-pass experiment. This implies that using higher and higher values of R would increase the sensitivity of a CEAS instrument. However, this fails to take into consideration the lower light level reaching the detector due to the accompanying reduction in transmission through the highly reflective mirrors.

The signal-to-noise ratio (SNR) of the detected intensity for a CEAS experiment will be *lower* than that of a corresponding single pass experiment.[164] Assuming the noise is only due to ideal quantum noise i.e. shot-to-shot fluctuations in the probe beam, then the

SNR is given by $N/\Delta N$, where $\Delta N = \sqrt{N}$, and N is the number of detected photons. The SNR can also be expressed in terms of the intensity, I (photons per time). The subsequent derivations follow the method set out by Fiedler et al.[164]

Equation 2.20 gives the ratio by which the detected intensity in CEAS is reduced compared with an equivalent single pass measurement. Therefore, the SNR ratios in the CEAS and single pass techniques are related by:

$$S/N_{\mathrm{CEAS}}(I) = \sqrt{\frac{(1-R)^2\mathrm{e}^{-\alpha l}}{1-R^2\mathrm{e}^{-2\alpha l}}}\; S/N_{\mathrm{single}}(I). \tag{2.28}$$

However, in the small loss regime, CEAS benefits from an increase in the effective pathlength by a factor equal to the CEF, $(1-R)^{-1}$, and so the maximum enhancement of the CEAS technique is given by:

$$S/N_{\mathrm{CEAS}}(\alpha) = \sqrt{\frac{(1-R)^2\mathrm{e}^{-\alpha l}}{\left[1-R^2\mathrm{e}^{-2\alpha l}\right](1-R)^2}}\; S/N_{\mathrm{single}}(\alpha). \tag{2.29}$$

In the case of small losses ($\alpha \to 0$) and high reflectivities ($R \to 1$), this simplifies to:

$$S/N_{\mathrm{CEAS}}(\alpha) = \sqrt{\frac{1}{2(1-R)}} S/N_{\mathrm{single}}(\alpha), \tag{2.30}$$

and a maximum enhancement factor, Q, can be defined:

$$Q = \sqrt{\frac{1}{2(1-R)}}. \tag{2.31}$$

The condensed phase adds further complication, as there may be additional loss processes due to scattering of the sample, and absorption and scattering of any intracavity elements used to constrain the sample such as a cell. These additional background losses, L_{b}, contribute to the total loss, L, given by:[165]

$$(1-L) = (1-L_{\mathrm{b}})\mathrm{e}^{-\alpha l}. \tag{2.32}$$

Assuming that the losses due to the absorption of the sample (αl) are dominated by the background losses, and therefore $L \approx L_b$, it has been shown that:[165]

$$Q = \frac{(1-R)[1+(1-L)^2R^2]}{\sqrt{[1-(1-L)^2R^2]^3}} \approx \frac{1}{\sqrt{2(1-R)}}, \tag{2.33}$$

where the approximation is valid for low losses ($L \to 0$) and high reflectivity mirrors ($1+R \to 2$), leading to the recovery of Equation 2.31.

In Figure 2.9, the exact version of Equation 2.33 is used to simulate the dependence of Q on a) mirror reflectivity, and b) background losses, which are assumed to be dominant.

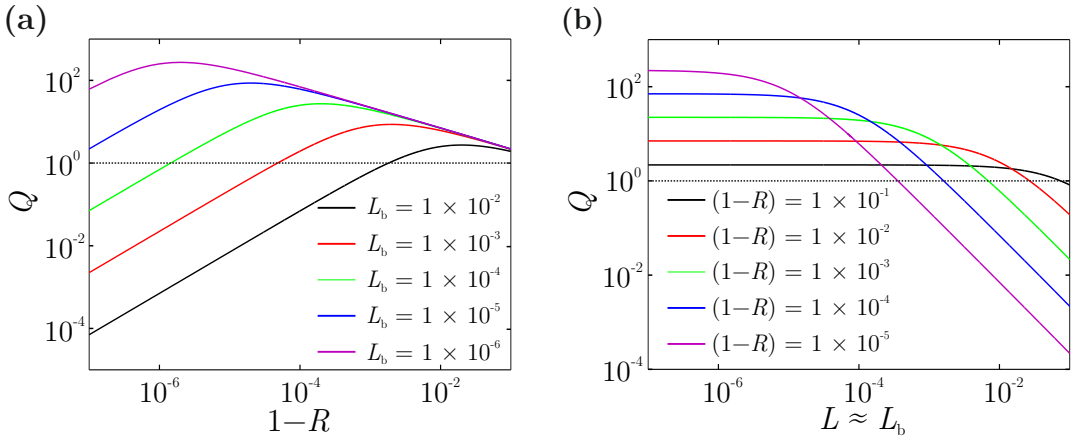


Figure 2.9: Numerical simulations of the SNR enhancement of CEAS over an equivalent single-pass technique, Q, using Equation 2.33, following the method of Fiedler et al.[164] a) as a function of mirror reflectivity for a range of background losses, and b) as a function of background losses for a range of mirror reflectivities. For a given background loss there is an optimum mirror reflectivity, and cavity mirrors should be chosen as close to this value as possible.

The dotted black line in each case shows a $Q = 1$, which corresponds to no enhancement over the single pass detection. What is clear from both plots is that there is an optimal mirror reflectivity corresponding to the size of the background losses. For a given magnitude of background losses, increasing mirror reflectivity above this value does not improve the detection limit of CEAS, and in fact decreases it back towards the single-pass

value due to the low cavity transmission.

Enhancements of 100 or more are only available to cavities with low inherent background losses ($L_b \leq 10^{-5}$), demonstrating the importance of good cavity alignment, low solvent absorption and scatter, and maintaining clean optical surfaces.

In our experiments the background losses can be approximated as 10^{-3} using $R_{eff} = R_{pure}(1 - L_b)$, and the values for R_{pure} and R_{eff} measured in the next chapter. This corresponds to an optimum mirror reflectivity of 0.999 in Figure 2.9, very close to the value used in our studies (Chapter 3). However, all of the above conclusions are based on the assumption that shot noise dominates, which may not be the case in our set-up as discussed in the next section.

2.5.3 Origin of sensitivity

This section summarises a detailed treatment of the origin of the enhancement (or more accurately noise suppression) offered by optical cavities, published by Ouyang and Jones.[166] Although it is appealing to think of optical cavity gains in terms of increased optical pathlength, the number of photons interacting with the sample is never more than in an equivalent single pass experiment due to the need to couple light into the cavity via the back of a highly reflective mirror.

By following their method, differential equations are set up for the light intensity circulating in a continuously pumped optical cavity in CEAS. For an empty cavity with no absorber present (indicated by the 0 subscript in Equation 2.34), there is only one loss process, given by the product of the circulating light intensity ($I_{0,cav}$) with the mirror transmission ($T = 1-R$, assuming ideal mirrors). The gain process is given by the incident light intensity from the source with the mirror transmission and a coupling constant, γ, here assumed to be unity. For an empty cavity of length d, the resulting circulating light

intensity is given by:

$$\frac{\mathrm{d}I_{0,\mathrm{cav}}}{\mathrm{d}t} = \frac{c}{d}\left[-I_{0,\mathrm{cav}}(1-R) + \gamma I_{\mathrm{in}}(1-R)\right]. \tag{2.34}$$

In the presence of an absorbing species there is an additional loss process due to interaction of the intracavity light intensity with a sample of pathlength l:

$$\frac{\mathrm{d}I_{\mathrm{cav}}}{\mathrm{d}t} = \frac{c}{d}\left[-I_{\mathrm{cav}}(1-R) - I_{\mathrm{cav}}\alpha l + \gamma I_{\mathrm{in}}(1-R)\right]. \tag{2.35}$$

The time-dependent solution of these equations for an ideal cavity (with $d = 1\,\mathrm{m}$) is shown in Figure 2.10a), where the intracavity light intensity is plotted as a fraction of the incident pumping intensity. The initial rise occurs within a few ring-down times, and for this idealised system with no background losses, the steady-state intensity reached is equal to the incident light intensity.

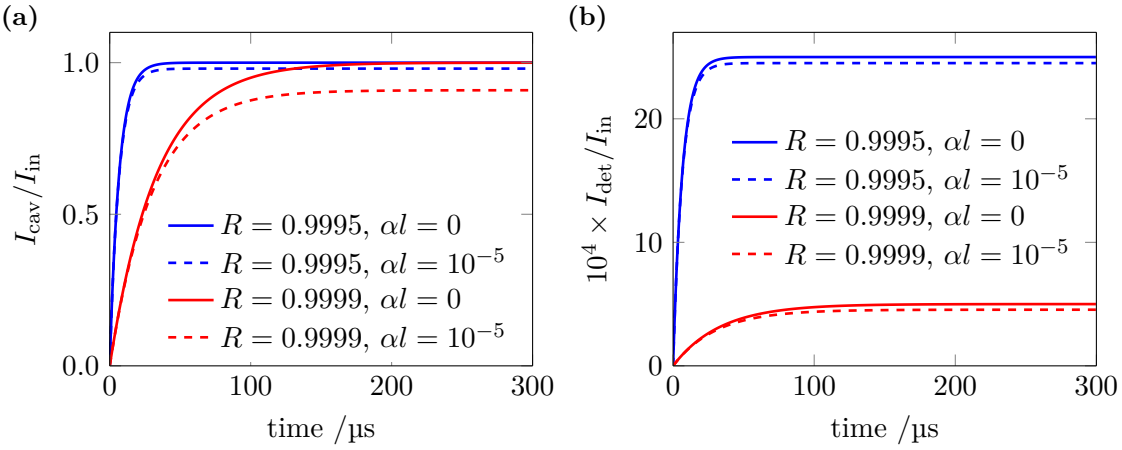


Figure 2.10: a) The time dependence of the intracavity light intensity, I_{cav}, in a continually pumped CEAS cavity, shown for $R = 99.95\%$ (blue) and $R = 99.99\%$ (red). The effect of introducing a weak per-pass absorbance into the cavity is also shown (dashed lines). b) The time dependence of the light intensity detected behind the rear cavity mirror, I_{det} under the same conditions. In both cases the cavity length, d, is 1 m. Simulations were performed following the method reported by Ouyang and Jones.[166]

Therefore, even in the ideal case, there are never more photons interacting with the

sample than in the equivalent single pass experiment. Two mirror reflectivities (R = 99.95%, 99.99%) are shown, and it is evident that the only difference is the longer time required to establish the same steady-state circulating light intensity in the case of higher reflectivity. The effect of including an absorbance loss in the cavity is indicated by the dashed lines. Although it appears that there is a greater drop in the higher R case, this is of little relevance as I_{cav} itself is not directly measured and a detector must be placed outside the cavity.

The detected intensity, I_{det}, leaking from the cavity is shown in Figure 2.10b). Due to the need to couple light into the cavity via the rear of one of the mirrors, it can only be monitored from one end of the cavity. A scaling factor must therefore be used, which in the case of sufficiently high mirrors ($R_1 = R_2 > 0.9$) is equal to $1/2$. The time-dependence of the intensity throughput of the cavities with different R are shown in terms of the incident intensity. It should be noted that these are only a small fraction of I_{in}, corresponding to the product of I_{cav} with the mirror transmission and the scaling factor of $1/2$.

The measured signal in CEAS is the difference in light intensities with and without an absorber present:

$$\Delta I_{\text{det}} = I_0 - I = (I_{0,\text{cav}} - I_{\text{cav}}) \times \frac{T}{2}. \tag{2.36}$$

When αl is much smaller than $(1 - R)$, which is normally the conditions under which CEAS operates, the decrease in transmitted intensity (the signal) is very similar between high R cavities, as evident from Figure 2.10b). This can be understood as follows: I_{cav} has been shown to be identical in the two cases, and so the number of photons interacting with the sample should be the same. However, in the higher R case, the absolute light intensity transmitted through the mirror to the detector is much smaller and this same signal is therefore recorded against a much reduced, and hence less noisy, background.

The authors identified three types of noise present in a CEAS experiment: environmental (type 1, $\propto I$), shot-to-shot quantum noise (type 2, considered by Fiedler et al.,[164,165] $\propto \sqrt{I}$), and thermal noise on the detector (type 3, no dependence on I). Assuming low

absorbance and high reflectivity, under the different noise regimes the SNR enhancement ratio, Q, takes the values $(1-R)^{-1}$, $\sqrt{2(1-R)}^{-1}$, and $1/2$, respectively.

The effect of the cavity is to suppress both environmental and shot-to-shot noise. At high enough light intensities, the SNR enhancement is given by the CEF, as implied by Equation 2.27. In this regime, increasing R does therefore lead to an enhancement in sensitivity. On increasing the mirror reflectivity, the transmitted intensity will decrease and at some point the (type 2) shot-to-shot noise will begin to dominate (which drops less sharply due to its $\sqrt{I}$ dependence). Once this type 2 noise begins to dominate, the effect of the background losses on Q becomes an important consideration, and plots such as Figure 2.9 should be consulted. Care should be taken not to increase R to the point where detector noise begins to dominate, as optical cavities offer no improvement in sensitivity and should not be employed under these conditions.

Depending on the relative values of I_{in} and R, a combination of these noises will be present and the overall SNR enhancement due to the cavity will lie somewhere between the two extremes. For the studies performed in this project, $R_{\text{eff}} \approx 0.998$ and the limiting values of Q are 500 or 15.8, depending on whether type 1 or 2 noise dominates, respectively. Due to the high spectral irradiance of the light source used it is likely to lie nearer the upper end of these values, which is supported by comparison of minimum detectable absorbances obtained in this study with single pass variants (1×10^{-5} vs 1×10^{-3}).

2.6 Light Sources

2.6.1 Pulsed vs continuous wave (CW) light sources

The suitability and implementation of different light sources for use in CRDS and CEAS are discussed in detail elsewhere,[152,167] and while much is applicable to condensed phase variants, the most pertinent points are emphasised briefly here.

The CRDS technique introduced previously was initially developed in the gas phase

using pulsed lasers, including dye lasers and OPOs. The high pulse energies permit the transmitted ring-down signals to be directly monitored with very good SNR. However, the repetition rate of these lasers, typically $10 - 20\,\text{Hz}$, precludes the measurement of fast kinetic processes, and while the tunability of these sources permits the acquisition of spectral information, the scanning rate is often slow. This is particularly problematic for condensed phase systems, whose broad spectra span several tens to hundreds of nanometres.

Additionally, pulsed lasers often have an associated broad bandwidth (GHz), larger than the free spectral range of a typical cavity, which therefore excites multiple cavity modes simultaneously. If the laser linewidth is broader than or comparable to the gas-phase absorption feature of interest, these modes coincide with different absorbance losses and the ring-down decay is multi-exponential and can be complex to fit.[158,168] This problem is avoided in the case of broad absorption bands characteristic of the condensed phase.

The implementation of continuous wave (CW) light sources into cavity-based spectroscopic instruments has become much more commonplace in recent years as their cost has fallen. Diode lasers in particular are popular due to their low cost, compact size, ease of use and their availability over a wide wavelength range, from the UV to the mid-IR.

Highly monochromatic (narrow bandwidth of *ca.* 1 MHz) diode lasers can efficiently couple into a single mode of the optical cavity, leading to the maximum value of circulating light intensity and therefore the highest SNR on a detector. As well as being beneficial for CEAS studies, CW lasers can also be implemented in CRDS, where the intracavity light level is allowed to build up to a certain threshold. The incident radiation must then be rapidly extinguished, using an acousto-optic modulator (AOM)[169,170] for example, and the resulting ring-down signal monitored. Narrowband CW lasers are popular in the gas phase as they are narrower than the spectral features of interest, and avoid the need for complex fitting regimes of multi-exponential decays.

The complexity of coupling light into the cavity is increased when using narrow

linewidth lasers due to the need to mode match. The coupling condition is very sensitive to instabilities in laser frequency or cavity length. Even very small variations can cause a loss of resonance between the injected light and cavity mode. To avoid the large amount of noise that results from complete rejection of light from the cavity, the laser frequency or cavity length can be continually scanned across the FSR,[169,170] or locked to a single cavity mode.[171] Other methods employed include optical feedback CRDS (OF-CRDS),[172] and noise-immune cavity-enhanced optical heterodyne molecular spectroscopy (NICE-OHMS),[173] detailed descriptions of which are provided by Mazurenka et al.[152] and in an excellent recent book by Gagliardi and Loock.[160]

Broadband CW diode lasers are also available, which simultaneously excite many thousands of cavity modes, removing the need to mode lock the laser and hence significantly reducing experimental complexity. They may be modulated using simple signal generators,[174–177] allowing ring down events to be measured after the steady state light intensity has been reached, or extinguished using AOMs like their narrow-band analogues.[178]

2.6.2 Broadband light sources

The light sources considered in the previous section are less suitable for study of the condensed phase due to their relatively narrow linewidths in comparison with the absorption features of interest. To obtain a full absorption spectrum the laser wavelength must be scanned in a stepwise manner, increasing the acquisition time. Broadband variants of CRDS and CEAS have been developed, which take advantage of light sources with wide bandwidths to simultaneously acquire entire absorption spectra in a single shot. They also permit different species with overlapping absorbance features to be distinguished, or the production and removal of products and reactants in a chemical reaction to be monitored simultaneously. Typically, the light sources used have outputs much wider than the absorption features being studied, although the previous considerations of cavity modes still apply (Section 2.3.1) and so only certain wavelengths can be successfully coupled into

the cavity.[179] Two types of broadband light source have been used: incoherent sources such as lamps or light emitting diodes (LEDs), and coherent sources such as lasers.

The first broadband CRDS (BBCRDS) technique was demonstrated by Ball et al.,[180] using a broadband (20 nm coverage) dye laser along with a clocked charge coupled device (CCD) camera to record ring-down times at two different wavelengths simultaneously. This initial example has since been developed into a range of existing techniques, all optimised for their particular application. However, few are truly broadband, with the requirements of simultaneous time and wavelength resolution proving challenging.[158–160,181]

An incoherent Xe-arc lamp was used in the first example of a broadband CEAS (BBCEAS) instrument, reported by Fiedler et al.,[163] who dispersed its continuous output (spanning UV to IR) onto a CCD detector. LEDs have also found successful application in BBCEAS field instruments for trace detection of atmospherically important species[182] due to their low cost, compact size and robust nature. Both LEDs and lamps have also been used as light sources for BBCEAS studies of solutions and interfaces.[164,183–187]

Despite their popularity, there are issues inherent to the use of incoherent light sources. Due to the uncollimated nature of the beams, efficient coupling into the cavity is challenging. The resulting large intracavity beam spot leads to an increase of the minimum sample volume probed and limits their suitability for some condensed phase applications. Their low brightness requires integration of the signal at the detector for sufficient SNR, which also limits the time resolution of techniques employing such light sources. These problems can be solved by the use of intense, highly directional light sources, notably broadband supercontinuum radiation (SCR) sources.[188]

The combination of bright spectral irradiance, highly collimated output (sub mm spot size) and very wide spectral coverage (> 1000 nm) make SCR sources a powerful tool in spectroscopy, particularly those techniques that involve optical cavities. The high spatial coherence permits efficient coupling into cavities, with high beam collimation maintaining the small beam spot required for low sample volume studies. The high output power leads

to high throughput intensity striking the detector, reducing the integration time required for precise measurements and improving the time resolution of the technique.

Supercontinuum generation encompasses a wide variety of non-linear processes that occur when short pulses (nanosecond or picosecond) are fired through a non-linear medium (typically photonic crystal fibre), resulting in significant spectral broadening. Due to their inherently pulsed nature they suffer from significant shot-to-shot fluctuations and long-term drift in intensity. The desirable combination of high irradiance, wide spectral coverage and highly directional output comes at a price, and although the cost has decreased in recent years, it still represents a significant investment compared to LED or lamp sources. A number of recent BBCEAS studies in the condensed phase (including work reported in this thesis)[142,187,189–192] and a BBCRDS study,[193] have employed SCR sources as the probe beam. The 80 MHz SCR source used in this project is characterised in Chapter 3 and the results of studies where it was employed as the probe beam are reported in Chapters 5 and 6.

2.7 Cavity Enhancement in the Condensed Phase

The desire to increase the sensitivity of direct absorption measurements in the condensed phase has led to the implementation of CRDS and CEAS techniques in an effort to reproduce the impressive effective optical pathlengths characteristic of gas phase measurements. However, a number of additional challenges must be overcome in the condensed phase, which act to lower the sensitivity gains optical cavities can offer.

Due to the higher molecular density inherent to the condensed phase, the sample of interest and its solvent contribute much greater absorption, scattering and diffraction losses than in a comparable gas phase experiment. Additionally, some method of sample constraint is required, usually in the form of a sample cell or cuvette, and the introduction of such an intracavity element increases background losses due to absorption and scattering of its surfaces. The effect of these increased background losses have been discussed in

detail in Section 2.5.2. It is clear that the high sensitivity of gas-phase CEAS and CRDS measurements cannot simply be recovered by further increasing the mirror reflectivity to extend the optical pathlength,[164] and other more subtle approaches must be found. The following is a brief summary of previous applications of CRDS and CEAS to the condensed phase, and is based on previous work in the group which included the important experimental parameters in a comprehensive table.[43]

2.7.1 CRDS in the condensed phase

The condensed phase variant of CRDS that shares most similarity to the gas phase is the so-called 'wet-mirror' variant, in which the cavity is filled with the liquid analyte in contact with the mirrors.[194–196] In these studies it is crucial to carefully select a solvent with low scattering losses and low absorption in the wavelength region of interest. Hallock et al.[194] managed to obtain ring-down times of hundreds of nanoseconds in a 21 cm cavity using such an approach, which was followed by the study of the kinetics of methylene blue[195] with no degradation effects on the reflectivity of the cavity mirrors. The consequence of such an approach is the need for large sample volumes, rendering it unsuitable for many liquid phase applications.

In an effort to reduce the demands on sample volume, as well as the per-pass loss due to sample scatter, much reduced cavity lengths have been employed (miniresonators, $d = 2\,\text{mm}$) by Bahnev et al.[197] and van der Sneppen et al.[198,199] This was achieved by clamping a rubber spacer leak-tight between the mirrors, resulting in a constrained volume of just 12 µL. However, the very small mirror separation leads to very short ring-down times (tens of nanoseconds), which require short laser pulses, fast electronics and high digital resolution for accurate measurement. These all increase the complexity and therefore expense of the set-up.

A simpler alternative is the use of an intracavity sample cell, the size of which can be matched to the available sample volume while maintaining the long ring-down times asso-

ciated with large mirror separation. However, as discussed in Section 2.5.2, the associated increase in background losses must be carefully considered in order to maintain the enhanced sensitivity of cavity detection, implying that the cell faces must be of good optical quality (smooth) and as close to mutually parallel as possible. The first implementation of this approach was by Xu et al.,[200] where the cuvette was aligned in a Brewster's angle arrangement in an effort to minimise reflection losses from the cell surfaces. For broadband studies, however, a single Brewster's condition cannot be defined and in that case it is preferable to align the cell at normal incidence to the cavity axis, constraining back reflections within the cavity. Although this leads to more challenging optical alignment of the system[164] compared with the forgiving Brewster's arrangement, it avoids the use of custom-made (and therefore costly) sample cells.

A more experimentally complex approach is to circumvent the need for a sample cell completely, as demonstrated by Alexander[201] with the introduction of a fast flowing liquid-sheet jet into the cavity. This removes the additional scattering losses introduced by a sample cell while providing a very short (*ca.* 23 µm) pathlength, although the high flow velocity requires very large sample volumes, meaning the advantages over a long wet-mirror cavity are not as dramatic. To address this shortcoming, a soap film requiring much less rapid flow was introduced by Vogelsang et al.[202] This approach successfully combines a very small probe volume (*ca.* 28 nL) with an impressive minimum detectable absorbance (4×10^{-6}).

A BBCRDS variant using a SCR source was reported by Kiwanuka et al.,[193] encompassing a custom-made optical cell with windows that can be independently aligned to ensure both are as close to normal incidence as possible. The detection was performed by a custom-built array of photodiodes, permitting ring-down traces from 64 spectral channels to be measured simultaneously. The resulting sensitivity of the technique was comparable to the BBCEAS variants described in the next section.

Other manifestations have involved fibre-based cavities, whereby light is trapped within

lengths of optical fibre, either by adding reflective coatings or fibre Bragg gratings (FBGs) to the ends,[203] or constructing fibre loops by splicing the ends of the fibre together.[204,205] In both variants, the sample cell is constructed from a small gap in the fibre, typically on the order of tens of microns, permitting the study of sample volumes as small as nanolitres or picolitres. Early efforts were largely hampered by poor sensitivity due to the large losses associated with coupling light into and out of the cavity, although recent advances in the field appear to be promising.[160,206,207]

The work reported in this thesis makes use of an intracavity cuvette to constrain low (sub-mL) volumes of protein sample. CRDS is used to enhance the sensitivity of a pump-probe technique used to study the kinetics and MFEs of radical pair reactions in solution. The results are reported in Chapter 4, with absorbance sensitivities on the order of 10^{-6}.

2.7.2 CEAS and BBCEAS in the condensed phase

Despite not being limited by the short ring-down times characteristic of condensed phase CRDS studies, applications of CEAS detection to the liquid phase are not as common. The measurement of time-integrated intensities renders CEAS more susceptible to fluctuations in transmitted light, either due to the light source or the sample (for instance due to refractive index variations). Accurate absorbance values are therefore challenging to extract. Most CEAS studies that do exist aim to take advantage of the multiplexing abilities of BBCEAS variants to measure entire absorption spectra in a single acquisition.

The first example of BBCEAS being applied to the condensed phase was performed by Fiedler et al.,[163] where a conventional UV-Vis spectrometer was modified by retrofitting with highly reflective optical mirrors into the beam path. The readily available reference beam was also monitored to remove intensity fluctuations due to the light source, and the resulting sensitivity of the instrument exhibited approximately an order of magnitude improvement over the original single pass spectrometer ($\alpha_{\text{min}} = 2 \times 10^{-5}\text{cm}^{-1}$).

LEDs are amongst the most widely used light sources in existing BBCEAS studies, due

to their low cost and very low intensity fluctuations, which are often the dominant form of noise. However, their low power output and relatively narrow bandwidth (in comparison to lamps or SCR sources) limits their applications in some areas. Their successful use has been reported with 2 mm cuvettes,[184] HPLC cells,[185] and a wet-mirror liquid-filled 20 cm cavity.[186] Seetohul et al.[185] demonstrated the powerful capability of spectrally distinguishing multiple species with overlapping absorption bands, by coupling a white LED with CCD detection.

Kiwanuka et al.[190] have demonstrated the suitability of SCR sources as probe beams for condensed phase CEAS studies. In contrast to the above techniques, in which calibration must be performed with an analyte of well-characterised single-pass absorbance, the CEF of this set-up could be calibrated by CRDS as a function of wavelength without any change in optical alignment being required. The visible output (480–700 nm) was coupled into an optical cavity before being dispersed onto a CCD detector by a grating spectrograph, and used to detect full absorption spectra of trace concentrations of dyes. The bright spectral irradiance enabled the use of fast acquisition times (10–50 ms), which in turn permitted the oscillatory behaviour of the Belousov-Zhabotinsky reaction to be monitored in real time. More recently BBCEAS variants have been used for sensitive detection in microfluidics,[191,208,209] and as part of a fibre-coupled integrated sensor for low volume liquid samples.[210]

The work reported here uses a broadband SCR source as the probe beam in a BBCEAS variant to permit the elucidation of tiny magnetic field effects across the entire visible absorption spectrum of small volume (*ca.* 200 µL) biological protein samples. These results are reported in Chapter 5. The limit of detection in equivalent chemical model system studies approaches 1×10^{-7}. A completely new cavity-based instrument, optical cavity-enhanced transient absorption spectroscopy (OCTAS), has also been developed. It is the result of modifications to the existing BBCEAS technique, sacrificing nanometre wavelength resolution to permit microsecond timescale kinetics to be studied. This potentially

powerful new instrument is the subject of Chapter 6.

Chapter 3

Experimental Characterisation

3.1 Introduction

This chapter gives an overview of the experimental aspects of this work, including the apparatus common to the various cavity-based instruments introduced in later chapters, and the chemical and biological systems they are harnessed to study. The structure, absorption spectra and photochemistry of flavin-based chemical model systems and proteins are introduced and discussed. The light sources used for detection and photoinitiation of radical reactions are described, along with the characteristics of the highly reflective cavity mirrors common to all instruments. The procedure for cavity-enhancement factor (CEF) calibration is described in detail as it is crucial to the extraction of absolute absorbance values from both the BBCEAS and OCTAS techniques presented in Chapters 5 and 6, respectively. Finally, the stability of the supercontinuum source used as the light source in these techniques, and its impact on the instrument detection limit, is assessed.

3.2 Materials: Preparation and Characterisation

Flavin mononucleotide (FMN), flavin adenine dinucleotide (FAD), hen egg-white lysozyme (HEWL), and tryptophan (W) were used as supplied from Sigma-Aldrich, without further

purification.

FMN/HEWL solution was made up with ultra-pure water (Milli-Q, resistivity 18.2 MΩ cm, pH 6.3) to final concentrations of 10 µM FMN and 500 µM HEWL.

FAD solution was made up with citrate buffer solution ($Na_2HPO_4 \cdot 10\,H_2O$: citric acid monohydrate, 4 mM : 98 mM, pH 2.1) to a final concentration of 10 µM. The low pH prevents ring-stacking in the ground state.[211] The FAD/W solution was made up with the same buffer solution to final concentrations of 10 µM FAD and 500 µM tryptophan.

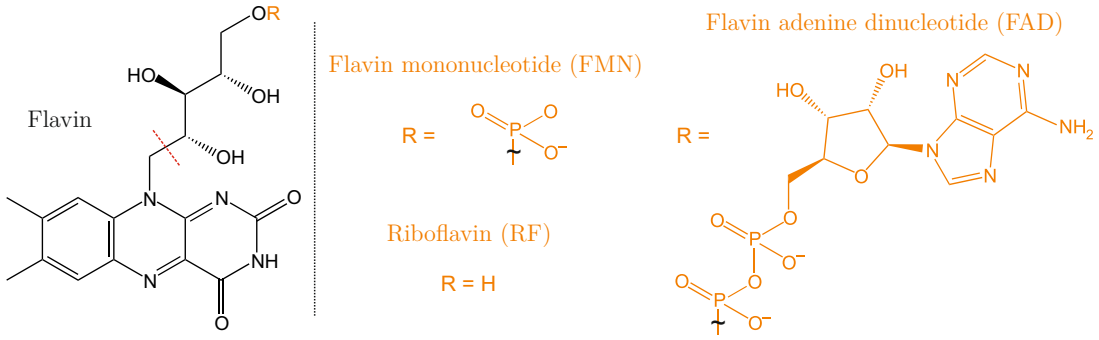


Figure 3.1: The structures of the flavin chromophores used in this project. The black structure on the left is the isoalloxine ring system and ribityl chain common to all. The orange '-R' groups attached to the end of the chain differentiate FMN, FAD and RF.

The structures of FMN and FAD are shown in Figure 3.1. Both structures share a common isoalloxine ring and ribityl chain (black), with different end groups attached. In FAD, electron transfer from the additional adenine group to the flavin results in the formation of an intramolecular radical pair (see Section 3.3.2). Cleavage at the dashed red line shows one possible route of photodegradation, forming lumiflavin (lumichrome if the resulting methyl group is replaced with a hydrogen). Flowing the FMN- and FAD-containing samples minimises the build-up of these photoproducts. Lumichrome and lumiflavin have no absorption above 450 nm and so their production adds to the complexity of interpreting spectra lacking information at shorter wavelengths.

All the model systems were available in sufficient quantities (mL) that they could be flowed through the sample cell using a syringe pump (Chemyx, Fusion 200) during

the course of a measurement. A rate of 0.25 mL min^{-1} was chosen based on the Allan deviation studies performed in Section 3.8.2. This slow rate replenishes the entire 180 µL cell volume in less than one minute, ensuring the availability of fresh sample to be probed, while avoiding any turbulence that is likely in the temperature-controlled Hellma flow cell (Section 3.6), due to the sample entrance and exit ports both being located on its top side. Samples were flowed through a syringe filter (0.2 µm, Pall Corp., Acrodisc) as this was found to reduce the fluctuations in the transmitted light intensity, presumably by removing scattering particulates (see Section 3.8.3).

The UV-Vis spectra of FMN and FAD are shown in Figure 3.2a), demonstrating the close similarities between the two molecules. The FAD has a slightly reduced molar extinction coefficient, ϵ, (see figure caption for values) and neither chromophore has substantial absorbance above 500 nm. The two peaks at 450 nm and 373 nm are assigned to the $S_0 \rightarrow S_1$ ($\pi \rightarrow \pi^*$) and $S_0 \rightarrow S_2$ ($n \rightarrow \pi^*$) transitions, respectively.

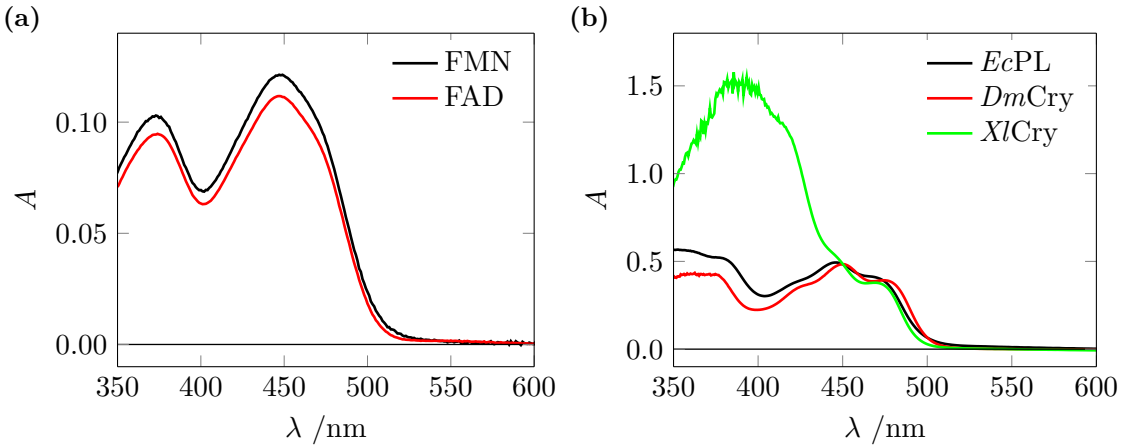
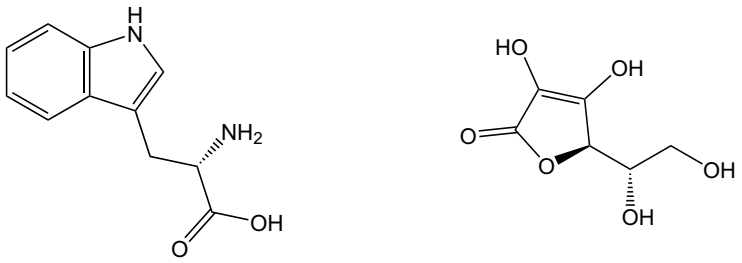


Figure 3.2: a) the UV-Vis spectra of FMN (black) and FAD (red), both *ca.* 10 µM (FMN: $\epsilon_{446} = 12\,200\,\text{M}^{-1}\,\text{cm}^{-1}$, FAD: $\epsilon_{443} = 11\,200\,\text{M}^{-1}\,\text{cm}^{-1}$).[212] b) the UV-Vis spectra of the proteins *Ec*PL (black), *Dm*Cry (red), and *Xl*Cry (green), scaled to the same 450 nm value.

The absorption spectra of the biological protein samples studied in this project are shown in Figure 3.2b). DNA Photolyase from the *Escherichia coli* bacterium (*Ec*PL) and cryptochrome from the *Drosophila melanogaster* fruit fly (*Dm*Cry) were both provided by

our collaborators Stefan Weber, Erik Schleicher and co-workers (University of Freiburg, Germany). The expression and purification of the proteins are described elsewhere.[128,213] Samples of *Ec*PL were provided in 50 mM Hepes buffer solution (pH 7.0) with 100 mM KCl present, which were then diluted using a 50/50 (vol/vol) glycerol/water mixture to give an *Ec*PL concentration of approximately 60 µM. The sample of *Dm*Cry, which does not bind the methenyltetrahydrofolate (MTHF) cofactor,[113] was provided in the same buffer solution (Hepes, pH 7.0, 100 mM KCl) and diluted with 20/80 (vol/vol) glycerol/water mixture to a final concentration of approximately 60 µM.



Tryptophan Ascorbic acid

Figure 3.3: The structures of the electron donor molecules used in this project. Tryptophan is used in its pure form as well as being the relevant residue in the HEWL protein. Ascorbic acid is chosen for its low hyperfine couplings and high solubility.

The *Xl*Cry sample – cryptochrome-DASH (*Drosophila*, *Arabidopsis*, *Synechocystis* and Human)[214] from the African clawed frog (*Xenopus laevis*) – was supplied by Kenichi Hitomi (Scripps Research Institute, USA). The expression and purification procedures are described elsewhere.[119] The sample was supplied in 50 mM Tris/HCl buffer (pH 8.0) containing 250 mM NaCl, with 5% glycerol. Prior to experiment, the sample was diluted with a 50/50 (vol/vol) glycerol/water mixture to give a final *Xl*Cry concentration of approximately 60 µM. In contrast to the other proteins used, *Xl*Cry does bind MTHF, and this is the origin of the strong absorbance below 450 nm. This does not interfere with our measurements, which all focus on wavelengths longer than 500 nm.

Cryptochrome and photolyase samples were centrifuged for 90 min before each exper-

iment to remove any precipitates or aggregates. To ensure that the FAD cofactor was in its fully oxidized redox form, the *Dm*Cry protein sample was pre-treated with potassium ferricyanide before use. Excess ferricyanide was then removed by three consecutive ultrafiltration steps using 30-kDa membranes.[128] The 50% glycerol concentrations used in the other protein samples slow the rate of diffusion to such an extent that the effect of an oxidant is limited, and the use of ferricyanide was avoided.

The most commonly used electron donor molecule in this project is the amino acid tryptophan, due to its presence in cryptochromes as the crucial "tryptophan-triad" molecular wire. It is either added to the flavin solutions in its pure state or as the active residue of the HEWL protein. Ascorbic acid is used in some studies due its high solubility permitting concentration dependence studies, and small hyperfine interactions, which help to boost the size of the low-field effect in any radical pairs it forms (see Section 1.6.3). Neither tryptophan nor ascorbic acid absorbs in the visible region, and their structures are shown in Figure 3.3.

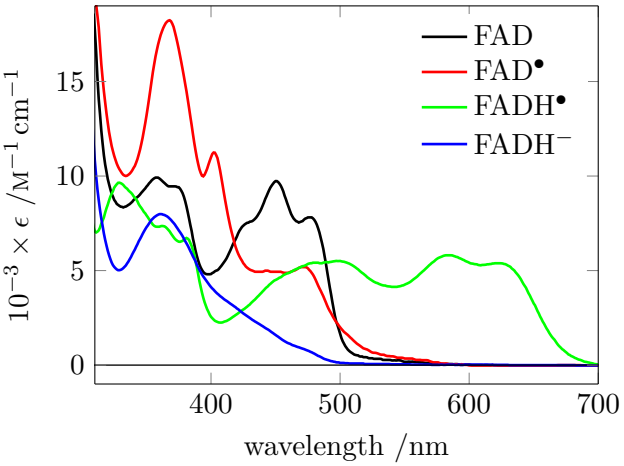


Figure 3.4: The absorption spectra of the various redox states of FAD present in solution. Figure reproduced from data published for a plant cryptochrome by Liu et al.[215]

Finally, to demonstrate the necessity for the broadband light sources used in this project (Section 3.4), the absorption spectra of the various flavin redox states present in solution are shown in Figure 3.4. The presence of multiple overlapping absorbance bands

due to interconverting species makes the results of a single-wavelength study difficult to interpret.

3.3 Photochemical Schemes

3.3.1 FMN/HEWL

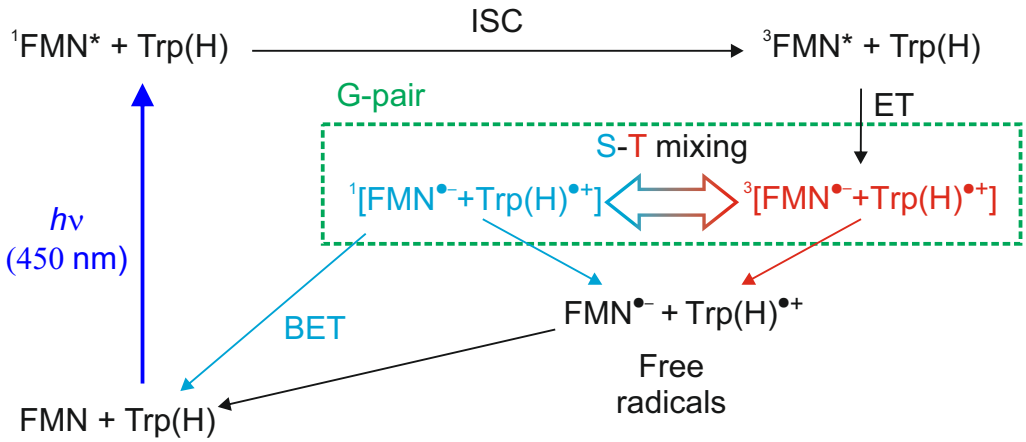


Figure 3.5: A schematic representation of the FMN/HEWL photochemical reaction scheme, where Trp(H) represents the tryptophan residue in lysozyme. ISC = intersystem crossing; ET = electron transfer; S-T mixing = singlet-triplet mixing; BET = back electron transfer.

The photocycle for the FMN/HEWL system[136] is shown in Figure 3.5. This system is used extensively throughout this thesis due to its relatively large MFE, cheap cost of components, good characterisation in existing literature and wide experience of working with it in the group.[142,216]

Blue-light photoexcitation at 450 nm, i.e. close to the $S_0 \rightarrow S_1$ absorption maximum of FMN (see Figure 3.2a), generates the electronically excited singlet-state flavin ^{1}FMN*, which subsequently undergoes fast intersystem crossing (on the timescale of a few nanoseconds) to yield the excited triplet state, ^{3}FMN*. Subsequent electron transfer (ET) from a

tryptophan (Trp) residue in lysozyme (most likely Trp123 or Trp62 or both),[217,218] with conservation of total spin angular momentum, generates the triplet-born radical pair, ^{3}[FMN$^{\bullet-}$ Trp(H)$^{\bullet+}$]. Immediately after formation, the RP is initially trapped in a solvent cage and is referred to as a 'geminate pair' (G-pair), shown in the green box in the figure.

The triplet-born radical pair interconverts with singlet state RPs via a variety of mechanisms outlined in Section 1.6, collectively known as 'singlet-triplet mixing'. Crucially for these studies, the efficiency of these mixing processes is affected by the application of an external magnetic field via the Zeeman interaction. At the relatively low field strengths used to produce the results published in this thesis, only the LFE and hyperfine-dominated 'normal' MFE need to be considered (see Section 1.6).

For the triplet-born SCRP considered, the normal MFE results in a decrease in S-T mixing efficiency with increasing field strength, as the T_+ and T_- levels get progressively energetically isolated due to the Zeeman interaction (see Section 1.4, Figure 1.3a). Upon re-encounter, only the singlet SCRPs have a spin-allowed recombination pathway to the ground state precursor(s), as recombination from the triplet state is spin-forbidden. Any RPs that avoid recombination in the solvent cage can escape into bulk solution, becoming free radicals, which themselves may eventually re-enounter one another and recombine to form the molecular precursor. The recombination route via free radicals is much slower (hundreds of microseconds to milliseconds vs nanoseconds for G-pair route), and so the radical absorbance measured is dominated by the free radicals, which have identical absorption spectra to the G-pairs. The MFE, which only arises in G-pairs, is transferred to the free radicals upon escape from the solvent cage and can therefore be measured by monitoring the change in free radical concentration upon application of a magnetic field.

3.3.2 FAD

The photochemical scheme for FAD (shown in Figure 3.6)[19] shares close similarities with that of the FMN/HEWL system, the main difference being that electron transfer

is now intramolecular between the covalently bound flavin (acceptor) and adenine (donor) components. The radical pair $^{3}[FH^{\bullet}–AH^{\bullet+}]$ is formed via ET accompanying a proton transfer from adenine to the excited triplet state of the flavin. In this case, free radical species can be formed by bimolecular reaction of the excited triplet state, but due to its short lifetime the steady-state free radical concentrations are much lower compared to FMN/HEWL. The radical lifetime in FAD (1–10 µs) is also significantly shorter than in FMN/HEWL.[133,136,219]

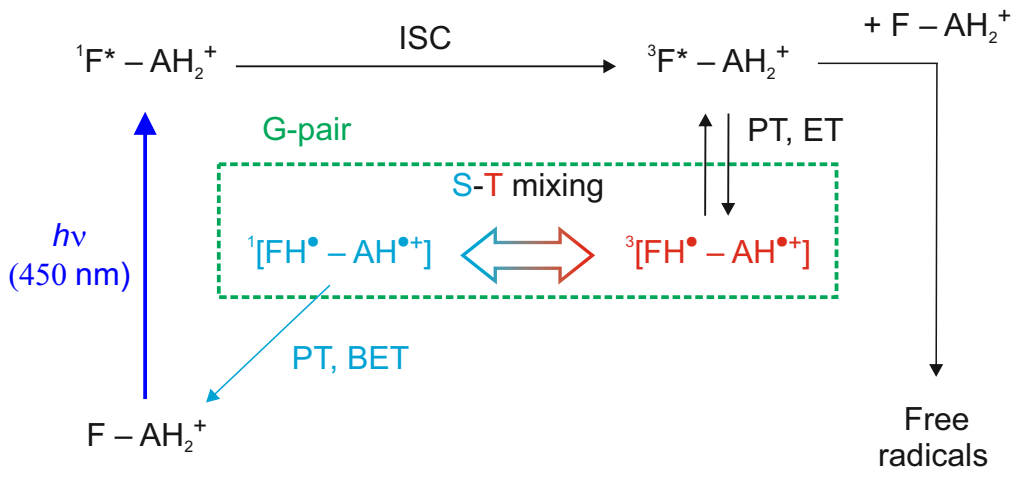


Figure 3.6: A schematic representation of the FAD photochemical reaction scheme. ISC = intersystem crossing; PT = proton transfer; ET = electron transfer; S-T mixing = singlet-triplet mixing; BET = back electron transfer.

3.3.3 FAD/W

As shown in Figure 3.7, addition of tryptophan to the FAD solution leads to the formation of intermolecular radical pairs between the flavin and tryptophan, in addition to the intramolecular $^{1,3}[FH^{\bullet}–AH^{\bullet+}]$ RPs present in pure FAD.[220]

These $[FH^{\bullet}–AH_2^{+}\ Trp^{\bullet}]$ radical pairs can either return to the ground state via reverse electron transfer, or diffuse to become free radicals. Following the same argument laid

out in the FMN/HEWL case, the MFE of the intramolecular RP is transferred to the diffusing free radicals, which have a much longer second order decay process and hence a typical lifetime much longer than that of the intramolecular RP. As a result, the lifetime of the MFE in the FAD/W system is enhanced compared with that of pure FAD.

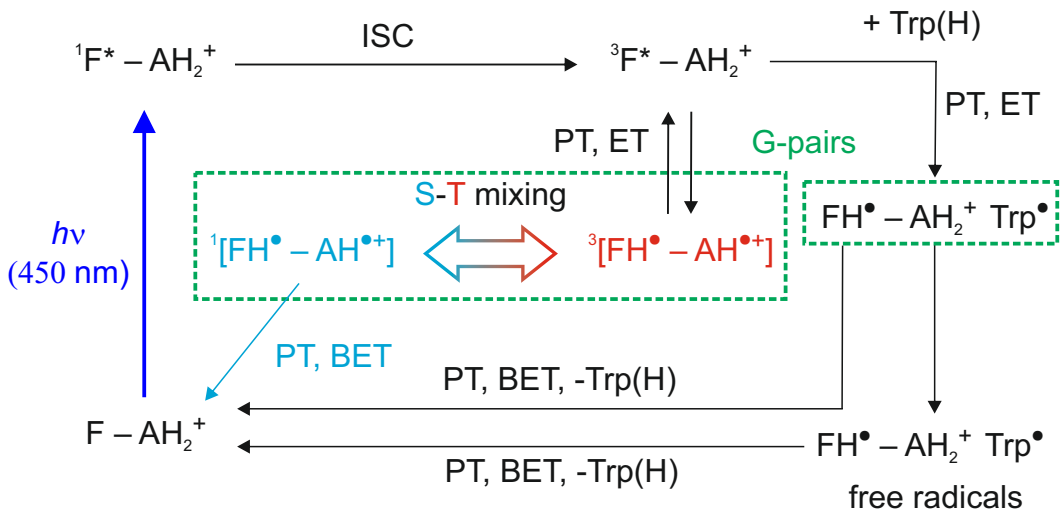


Figure 3.7: A schematic representation of the FAD Tryptophan system photochemical reaction scheme. ISC = intersystem crossing; PT = proton transfer; ET = electron transfer; S-T mixing = singlet-triplet mixing; BET = back electron transfer.

3.3.4 Cryptochromes and photolyase

Cryptochrome and photolyase proteins share a high degree of sequence homology (Section 1.7.2), and their previously published photochemical scheme is shown in Figure 3.8.[96,128] Photoexcitation of the fully oxidized redox state of the FAD cofactor in photolyase or cryptochrome forms the excited singlet state, ^{1}FAD*. Subsequently, a rapid (*ca.* 30 ps)[114] electron transfer occurs via a cascade mechanism along a trio (or as very recently suggested, a tetrad)[116,221,222] of conserved tryptophan residues nearby in the protein scaffold – the "Tryptophan triad"[112,114,223] – outcompeting ISC and forming a singlet-born SCRP, $^1[FAD^{\bullet-}\ TrpH^{\bullet+}]$, due to conservation of spin angular momentum.

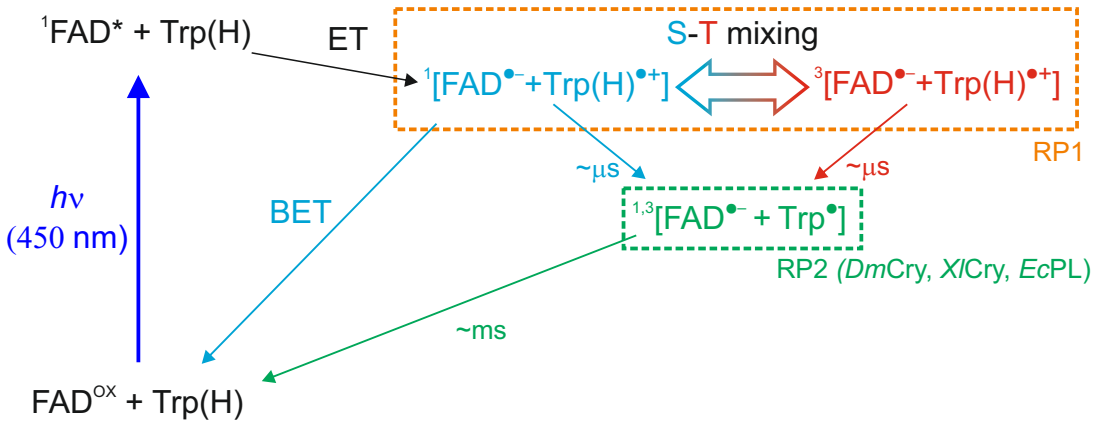


Figure 3.8: A schematic representation of the proposed cryptochrome photochemical reaction scheme. FAD^{OX} indicates the fully oxidized redox state. RP1 and RP2 differ in the protonation state of the tryptophan, as discussed in the text.

This initially formed radical pair, from now on referred to as RP1, can either recombine spin-selectively to form its ground state precursor (from the singlet state only) or undergo coherent singlet-triplet mixing, the extent of which can be influenced by the application of an external magnetic field as in the model system G-pairs. A further alternative is that one of the components of RP1 undergo a non spin selective change in protonation state to give the long-lived RP2 – ^{1,3}[FAD$^{\bullet-}$ Trp$^{\bullet}$] in *Ec*PL, *Dm*Cry and *Xl*Cry – occurring at equal rates for both singlet and triplet RPs. This long-lived RP2 can eventually recombine to the ground state on a millisecond time scale.[96] As the application of a magnetic field alters the S-T mixing efficiency, and therefore the time-dependent probability that RP1 is in the singlet or triplet state, it affects the ratio of RPs proceeding along the competing pathways – recombination to ground state (available to singlet only) and deprotonation (both singlet and triplet). If these rates are approximately similar, this leads to a magnetic field dependence of the concentration of RP2 molecules. Energetically isolating the T_+ and T_- levels via the Zeeman interaction leads to an increase in ^{1}RP1 population, and therefore

a relative increase in the number of molecules able to recombine to the ground state, subsequently reducing the population trapped in the long-lived RP2 state. A magnetic field effect in a cryptochrome or photolyase protein should therefore manifest itself as a reduction in this long-lived radical absorbance in the presence of a magnetic field.

3.4 Light Sources

This section is split into two parts, the first describing the cavity light sources (i.e. probe beams) used in this project, and the second the photoexcitation sources (i.e. pump beams) used with each instrument.

The BBCEAS instrument uses a high-repetition rate (pseudo-CW) supercontinuum radiation (SCR) source as its probe beam, permitting acquisition of the entire visible region simultaneously, while the CRDS instrument utilises a tunable OPO laser which requires scanning in order to obtain a spectrum.

The steady-state BBCEAS technique utilises a CW diode laser to provide the blue-light photoexcitation for the production of radical species, while CRDS takes advantage of its faster time resolution by using a pulsed Nd:YAG-pumped dye laser to provide a fast initiation event in a pump-probe variant.

The newly developed OCTAS instrument should be considered as a hybrid of the BBCEAS and CRDS techniques, in terms of both capabilities and apparatus. It combines the broadband coverage provided by the SCR source used as its probe beam with the short, high energy pulses provided by the dye laser for photoexcitation, resulting in simultaneous temporal and spectral resolution.

3.4.1 Probe light sources

The specific light sources used in each experiment are listed in Table 3.1. As indicated previously, the BBCEAS and OCTAS instruments share the SCR source. Supercontinuum radiation is generated by pumping a non-linear medium, most commonly photonic crystal

fibre (PCF),[224–226] with short (picosecond) laser pulses, which undergo extreme spectral and temporal broadening to produce an intense white light output.

	BBCEAS & OCTAS	**CRDS**
Make	NKT Photonics	Opotek
Model	Koheras SuperK Power Blue	Opolette
Wavelength	478–2100 nm (478–830 nm after SpectraK split)	410–2200 nm
Maximum output power	Full spectrum: 3 W Visible region: 300 mW	4 mJ per pulse
Beam diameter	< 1 mm	3 mm
Repetition rate	80 MHz (pseudo-CW)	1–20 Hz
Pulse length	*ca.* 5 ps fundamental *ca.* 50–450 ps output	5 ns
Linewidth	N/A	*ca.* 5–7 cm^{-1}

Table 3.1: The cavity light sources used as the probe beam for the experiments reported in this thesis. The supercontinuum source is common to both the BBCEAS and OCTAS instruments, and the tunable OPO laser is used in CRDS.

The source used in these studies is the NKT Koheras SuperK Power Blue, which produces broadband radiation from $450 - 2100$ nm. The output is filtered prior to the cavity using a passive spectral filter (SuperK Split), which separates the visible (450–900 nm) from the IR component (900–2100 nm) which is then safely dumped.

The light source is a solid-state Nd:YAG laser operating at 80 MHz. Due to the slow nature of the integrating CCD camera used as the detector in the BBCEAS experiments (minimum integration time = 3.66 ms), the individual pulses are not resolved and the source is treated as pseudo-CW. The non-linear processes involved in SCR production mean that although the pumping lasers are very stable, the output from supercontinuum

sources suffers from large intensity fluctuations. These are characterised in detail for this set-up in Section 3.8.

The CRDS instrument uses a tunable pulsed OPO laser (Opotek, Opolette) as its probe beam, which can be scanned across the entire visible region with 1 nm resolution.

3.4.2 Photoexcitation light sources

	BBCEAS	**OCTAS & CRDS**
Make	Power Technology	Pump laser: Continuum Dye laser: Sirah
Model	APMT35 (450-50) G2/9907	Pump laser: Surelite I Dye laser: Cobra
Wavelength	450 nm	450 nm
Maximum output power	35 mW	7 mJ per pulse
Beam diameter	2 mm	3 mm
Repetition rate	CW or TTL-modulated	OCTAS: 20 Hz CRDS: 10 Hz
Pulse length	N/A	5 ns
Linewidth	~ 1 nm	$\sim 5\,\mathrm{cm}^{-1}$

Table 3.2: The photoexcitation sources used in this project. The CW diode laser is used to produce a steady-state concentration of radicals in the BBCEAS experiments, while a Nd:YAG pumped dye laser is used to produce high, transient concentrations of radicals in the CRDS and OCTAS studies.

The lasers used to produce radical species in the model systems and proteins are listed in Table 3.2. BBCEAS uses a 450 nm diode with a maximum output power of 35 mW. The model system studies are typically performed at 10 mW, while the delicate cryptochrome and photolyase systems are only subjected to 0.5 mW. The vast majority of experiments

are performed with the laser operating in CW mode, apart from the modulated BBCEAS variant introduced in Section 5.9, where it is modulated using the TTL output from a pulse generator (with 100% modulation depth). The stability of the diode laser has previously been characterised,[227] and the noise induced by intensity fluctuations in its output is found to be dominated by other sources of noise, e.g. from the supercontinuum source output intensity fluctuations.

The CRDS and OCTAS instruments both employ a Nd:YAG pumped dye laser, in which the 1064 nm fundamental is frequency tripled to 355 nm and used to excite Coumarin 2 laser dye (Coumarin 450) to produce short, intense pulses of 450 nm radiation. The dye laser typically suffers from shot-to-shot intensity fluctuations of around 4%.

3.5 Photodetectors

Photomultiplier tubes (PMTs) are highly sensitive photo-detectors, with a fast time response. They are used in this project for measuring the ring-down time of the CRDS instrument in Chapter 4 with sub-microsecond time resolution (in conjunction with an 8-bit LeCroy Wavesurfer oscilloscope). A custom-built array containing eight such detectors is used as the detection method in the OCTAS instrument (Chapter 6), with an optical fibre arrangement that renders each PMT sensitive to a different wavelength of visible light. In this case the digitiser employed is a 12-bit, 8-channel oscilloscope (LeCroy, HDO8058), which provides very high resolution in both intensity and time allowing small magnetic field effects to be resolved. The PMT model chosen for these applications (Hamamatsu R928) has wide spectral coverage across the UV, visible and near-IR regions of the spectrum (185–900 nm).

PMT detectors individually provide no spectral information. Where high resolution broadband information is required, such as in the BBCEAS studies, a CCD camera is combined with a grating spectrograph (Andor Newton and Andor SR-303i, respectively). The cavity light is delivered to the spectrograph via an optical fibre and dispersed onto

the pixel array of the camera (1024 x 256 pixels). For a typical input slit width of 100 µm the resolution is approximately 0.6 nm per pixel. The minimum integration time for the CCD camera is 3.66 ms, putting a lower limit on the kinetics of processes which can be studied. This may be circumvented by using gated CCD cameras or streak cameras, which were not available for these studies, or the much cheaper array of PMTs constructed for the OCTAS experiment.

3.6 Sample Cell

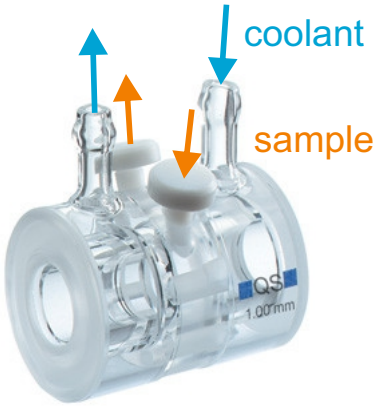


Figure 3.9: The Hellma 165-QS temperature controlled sample cell used in all the studies performed in this thesis. Image provided by the manufacturer.

The same design of intracavity cell was used in all studies to constrain the sample of interest (Hellma 165-QS), shown in Figure 3.9. The optical pathlength through the sample is 1 mm and sample flow is permitted through the two apertures located on its top side. The cell design is a cylindrical barrel shape, with the inner sample reservoir surrounded by an outer jacket through which coolant can be flowed. This permits the temperature control of samples, and is important for protein studies where high temperatures lead to protein aggregation and deposition. It also helps in the detection of MFEs by slowing down the photochemical kinetics and prolonging the lifetime of the geminate radical pair, required for the development of measurable field effects.

To reduce the impact of background losses introduced in Section 2.5, the optical surfaces of the cell windows should be smooth (surface flatness $< 1\,\mu m$) and highly parallel to minimise scattering and diffraction losses.

3.7 Cavity Mirrors

The same set of custom-coated (Layertec) broadband mirrors were used to form the optical cavities in all instruments, the specifications of which are listed in Table 3.3. Broadband coverage is achieved by interference effects between multiple thin dielectric layers deposited on a transparent substrate. However, the resulting reflectivity often shows highly wavelength dependent structure, which must be characterised to prevent false structure appearing in absorbance spectra. This is done via the cavity enhancement factor (CEF), introduced in Section 3.7.1. As it is a crucial step in extracting absolute absorbance values from both the BBCEAS and OCTAS measurements performed in Chapters 5 and 6, respectively, it is discussed in detail in the following section.

λ /nm	D /mm	Flatness	R	r_c /mm
400–800	25.4	$\lambda/4$	99.85–99.98%	500

Table 3.3: The specifications of the Layertec broadband mirrors used in this project. The rear side has an anti-reflection coating ($R < 1\%$).

As discussed in Section 2.5.2, the choice of mirror reflectivity is important in the condensed phase where the SNR of a cavity technique can be severely limited by background losses inherent to e.g. the sample cell. As for any cavity technique, the radii of curvature and mirror separation should be carefully chosen to fulfil the stability criterion given by Equation 2.7.

3.7.1 CEF calibration

The data presented in this section was recorded with the supercontinuum producing spectral output down to 450 nm. Due to a component failure, the majority of the remainder of the thesis uses a repaired light source, where the spectral output was limited to wavelengths longer than 478 nm, precluding much interesting and useful study of the flavin ground state absorption region.

After each new cavity alignment the CEF must be measured in order to provide an accurate calibration curve for the calculation of absolute absorbance values. Calibration is not necessary for the determination of MFE values, but it i) is experimentally simple and adds no more than 5 minutes to the preparation of the instrument, ii) gives an accurate early indication of whether the cavity is well-aligned and the intracavity surfaces sufficiently free of dirt to make the acquisition of data worthwhile, and iii) makes negligible contribution to the final uncertainty in the measured values (see Section 5.3.3). However, every effort has been made to record the CEF as precisely as possible, including an optimisation of the previously reported calibration method.[227]

The CEF is given by a straightforward rearrangement of Equation 2.24:

$$\mathrm{CEF}(\lambda) = \frac{\left(\frac{I_0(\lambda)}{I_{\mathrm{dye}}(\lambda)} - 1\right)}{\ln(10)A(\lambda)} \frac{l_{\mathrm{UV}}}{l_{\mathrm{BBCEAS}}}, \tag{3.1}$$

where I_0 and I_{dye} are the light intensities with water and calibrant dye in the sample cell, respectively, A is the single-pass absorbance measured by UV-Vis, and l_{UV} and l_{BBCEAS} account for the difference in pathlengths between the UV-Vis cuvette (1 cm) and BBCEAS sample cell (1 mm).

Calibration is performed with a mixture of laser dyes, Acid Red 27 (Amaranth) and Acid Green 25, chosen to provide a broad absorbance spanning the entire spectrum of the BBCEAS instrument. Previous work has used a 1 µM : 1 µM ratio,[227] but here a higher concentration was employed (3 µM : 6 µM) to avoid unnecessarily high levels of

noise from the less sensitive UV-Vis instrument. The relative concentration of the Acid Green component was doubled to increase the absorbance of the dye mix in the red region, and hence the accuracy of the calibration in this region of the spectrum. The concentration should not be so high as to lead to a breakdown in Equation 3.1 (see Section 2.5) or a significant reduction in the light intensity reaching the CCD detector (see Section 2.5.2).

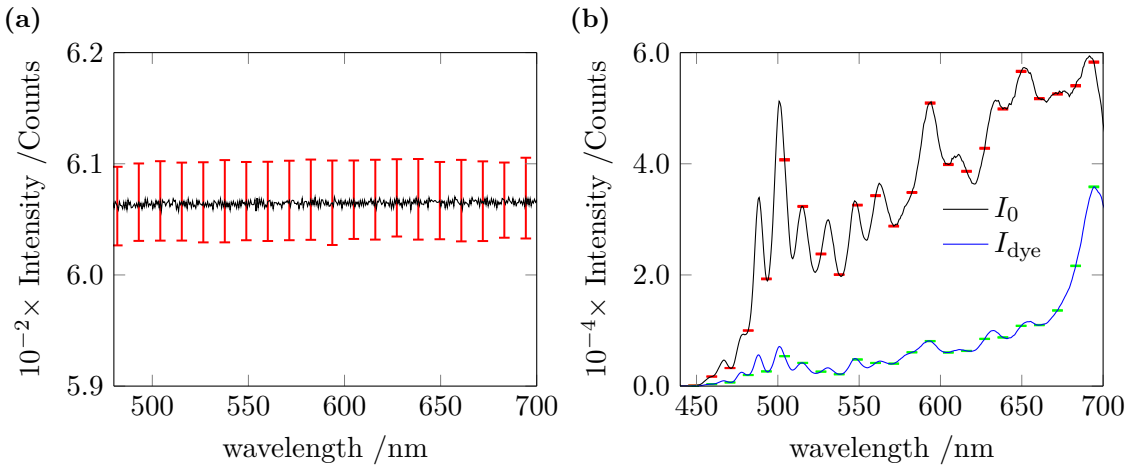


Figure 3.10: a) The dark counts signal on the CCD used for BBCEAS studies, and associated standard deviation (red), due to background thermal noise. These are subtracted from all measured signals to give accurate intensities. b) The raw cavity transmission spectrum with water (black) and calibrant dye solution (blue) in the sample cell. The CCD saturates at 60,000 counts and so a neutral density filter is used to attenuate the probe beam light after it exits the cavity. The dark counts have been subtracted from the data to provide I_0 and I_{dye} values. The error bars represent the standard deviation of 500 acquisitions.

The CEF calibration procedure is outlined below. For all BBCEAS spectra recorded the first step is to correct for the dark counts on the CCD detector due to random thermal fluctuations, shown in Figure 3.10a). Figure 3.10b) shows the raw $I_0(\lambda)$ and $I_{\mathrm{dye}}(\lambda)$ spectra, with water and calibrant mix in the sample cell, respectively. These are the values used in Equation 3.1 to determine the CEF.

The single-pass absorbance spectrum of the calibrant mix is also required and is recorded using a UV-Vis spectrometer (Agilent, Cary 60). Figure 3.11a) shows the UV-Vis measured absorbance (blue, right axis), overlaid with the calculated BBCEAS observable

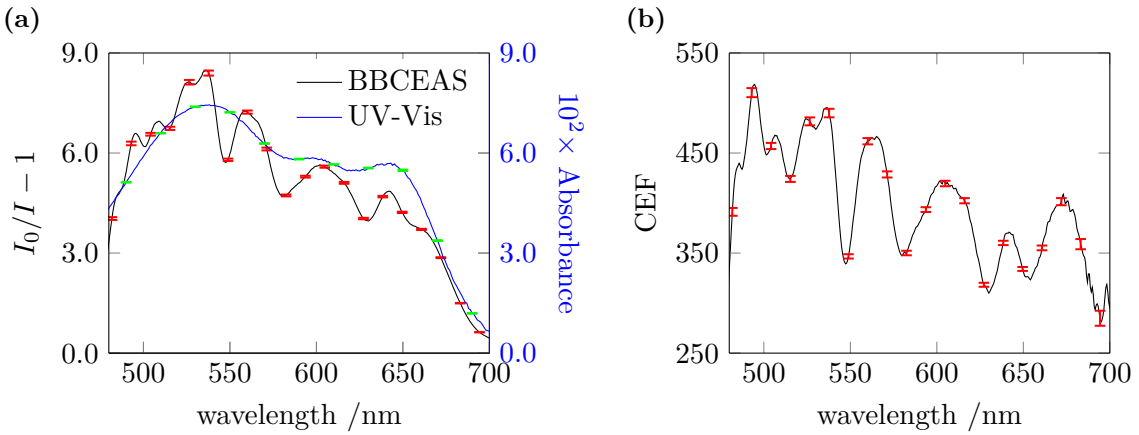


Figure 3.11: a) The BBCEAS observable $(I_0(\lambda)/I_{\text{dye}}(\lambda) - 1)$ for the calibrant dye mix. The $I_0(\lambda)$ and $I_{\text{dye}}(\lambda)$ are those shown in Figure 3.10b). The single-pass absorbance spectrum of the same calibrant dye recorded by UV-Vis is shown in blue. Error bars represent one standard deviation of the mean of 500 measurements (BBCEAS) and 10 measurements (UV-Vis). b) The CEF(λ) profile calculated from the data shown in a) using Equation 3.1. Error bars represent one standard deviation, following Gaussian error propagation of the uncertainties shown in a).

obtained from the spectra in Figure 3.10b). The general spectral shape is similar, with the false structure in the BBCEAS data due to the broadband cavity mirrors. The difference in magnitude of the signals gives an indication of the enhancement offered by the cavity.

Finally, the ratio of these signals is taken, adjusting for the difference in pathlength between the BBCEAS sample cell (1 mm) and the UV-Vis cuvette (1 cm), and a factor of ln(10) to account for the switch from decadic to natural absorbance values. The resulting CEF is shown in Figure 3.11b), representing the number of passes made by light of each wavelength through the sample. The value of the CEF is lower than would be expected from the direct measurement of the mirror reflectivity (1000–1700, see Section 3.7.2). This is due to the extra absorbance and scattering losses caused by the mirrors and sample cell not taken into account, which reduce the pure mirror reflectivity to an effective R_{eff}. This effective reflectivity can, therefore, be calculated as ranging from 0.997–0.9985 based on the calibrated CEF. The per-pass background losses, L_{b}, can also be calculated as *ca.* 1.2×10^{-3} using Equation 2.25.

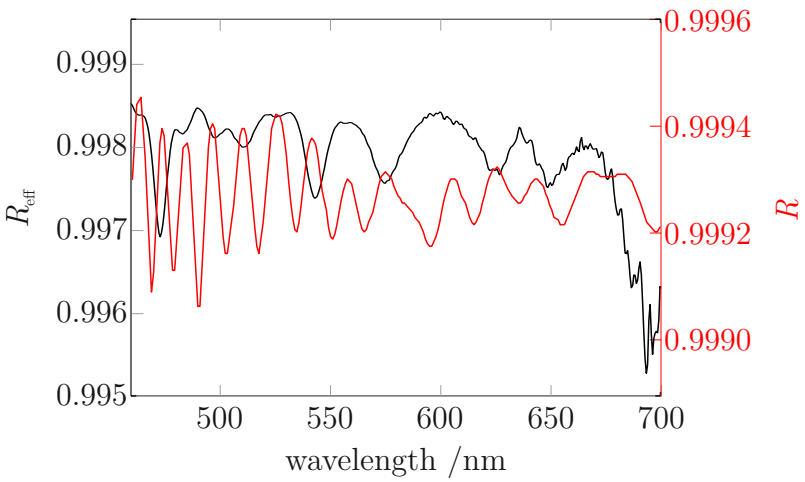


Figure 3.12: Comparison of the effective mirror reflectivity, R_{eff} (black), calculated as $(1 - {}^{1}/_{\text{CEF}})$ using the CEF profile shown in Figure 3.11b), and the simulated mirror reflectivity provided by the manufacturer (red).

The wavelength dependent structure in the CEF (and therefore R_{eff}) has long been a cause for concern, particularly the large dips at 473 nm, 543 nm and 575 nm in Figure 3.11b). These do not agree with the simulated spectral profile supplied by the manufacturer, but curiously seem to coincide perfectly with peaks in the reflectivity spectrum where there should be dips, as shown in Figure 3.12. In an effort to assign these features, the mirror reflectivities were measured directly using the BBCEAS instrument.

3.7.2 Mirror reflectivity profile

Accurately measuring the reflectivity of high quality mirrors is challenging due to the small amount of transmitted light. However, the high intensity of the SCR source and good sensitivity of the CCD camera meant it could be attempted here. The biggest issue was saturation of the CCD camera in the absence of the cavity mirror. To counter this problem the integration time was set to a minimum (4 ms) and the ND filter shut far enough that the CCD did not saturate with both cavity mirrors removed from the beam path.

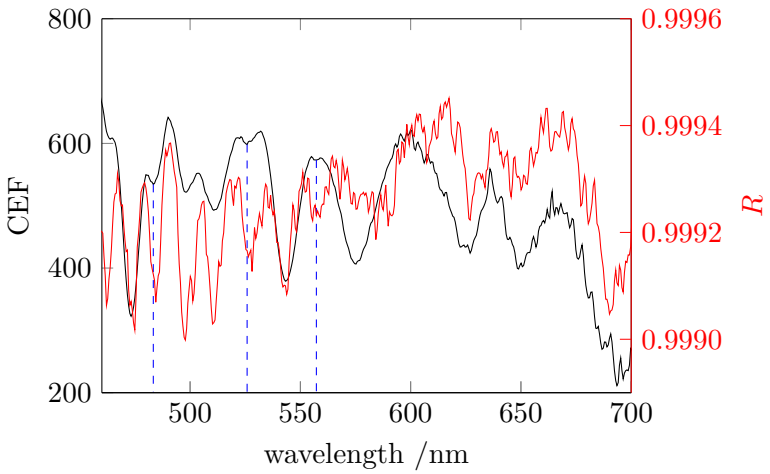


Figure 3.13: Spectrally resolved profiles of the cavity enhancement factor (black) and the broadband coated mirror reflectivity (red), both measured using the BBCEAS instrument. All of the previously unassigned structure in the CEF(λ) profile is accounted for by the mirror reflectivity. Blue dashed lines indicate the major discrepancies between the size of the features in the CEF and mirror reflectivity.

Subsequently, 500 acquisitions of the unadulterated SCR output, I_{in}, were recorded. A cavity mirror was then replaced in the mount at normal incidence (aligned via a back reflection through a pinhole) and the light intensity transmitted through the mirror was recorded, I_{tr}. However, due to the low transmission through a highly reflective mirror, the intensity on the CCD was barely above dark counts and so the integration time was increased to 2 s. Before the calculation of transmittance, $T = \frac{I_{\text{tr}}}{I_{\text{in}}}$, the I_{in} reading was scaled up by a factor of 500 ($\frac{2\,\text{s}}{4\,\text{ms}}$) to account for the difference in exposure time. The assumption that the mirror was ideal (i.e. zero absorbance) was made and the reflectivity determined from $T = (1 - R)$.

Figure 3.13 shows the measured spectrum of the mirror reflectivity overlaid with the CEF profile determined previously. The spectral agreement is striking, with a good match between high reflectivity and high CEF. Structure in the CEF is undeniably a result of the underlying mirror spectrum structure. The inherent causes of the structure are not investigated any further here, it is sufficient to know their origin in the CEF profile. They are likely a result of the same interference effects that endow the mirrors with their high

reflectivity in the first place. What remains unclear is the relative depth of the features – some large dips in the reflectivity are hardly seen in the CEF (at 483 nm, 525 nm and 557 nm for instance, as indicated on the plot).

What remains unresolved is the reason for the inversion of the simulated data provided by the manufacturers. The measured reflectivity matches the structure in the CEF, and hence the R_{eff}, and so must disagree with the manufacturer's (simulated) specifications.

3.8 Instrument Stability

3.8.1 Supercontinuum stability

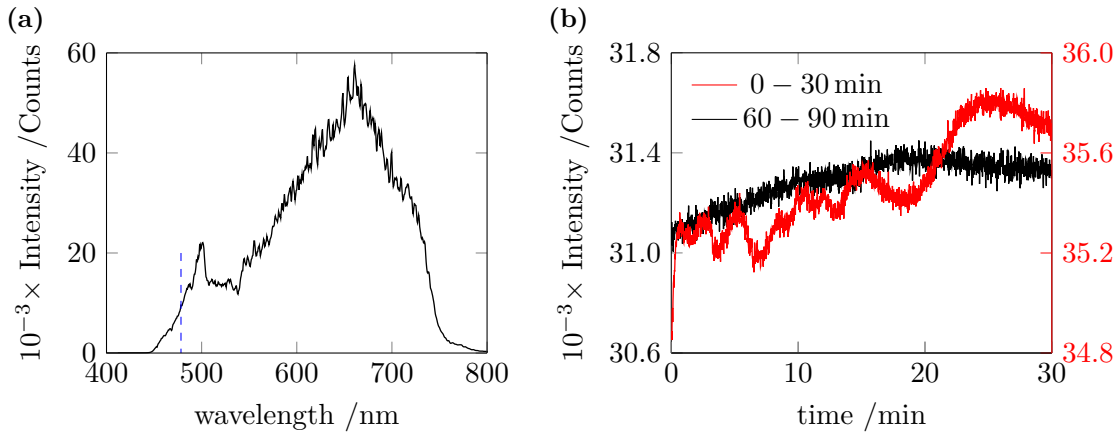


Figure 3.14: a) SC source output spectrum after filtering through the passive SpectraK Split filter (average of 500 acquisitions). Blue dashed line indicates the new cut off wavelength after SC source refurbishment. b) The temporal behaviour of the intensity output (averaged 500–600 nm). A 50 ms acquisition recorded every second for 30 min (1800 in total). Shown for first 30 min after source turned on (red, std. dev. = 1987 counts) and after the source has been warming up for an hour (black, std. dev. = 891 counts). No data should be recorded within the first 30 mins to allow the source to stabilise.

As indicated in Section 3.4 the SCR source is used as the probe beam in two of the cavity-based instruments used in this project, namely BBCEAS and OCTAS. Due to the highly non-linear optical processes involved in supercontinuum generation, such light sources suffer from inherent instabilities. Therefore, it is important to assess the stability

of this light source using the BBCEAS instrument.

The raw output spectrum of the NKT SCR source (after filtering by a hot mirror to remove the IR components > 800 nm) is shown in Figure 3.14a). The comparatively weak output to the blue is apparent, which is a characteristic shortcoming of this generation of SCR sources. This issue has been compounded since refurbishment, where the new cut-off wavelength has been increased to 478 nm, further reducing the amount of information obtainable in the flavin ground state absorption region (< 500 nm).

The inherent pulsed nature of these sources is evident in their long-term instability, but the measurement noise introduced by these effects can be reduced by allowing a warm-up time. This is demonstrated in Figure 3.14b), where the output spectrum (averaged 500–600 nm) is monitored for the typical length of a BBCEAS MARY experiment (30 min) immediately after (red), and an hour after (black), the source being turned on. The standard deviation in the latter case is reduced by a factor of two (see figure caption), and the higher frequency components have disappeared. It is, therefore, crucial that no data should be recorded within the first half an hour of the source being switched on. This is particularly important in the case of the CEF calibration procedure, which is typically recorded at the beginning of the day, and whose accuracy will be severely impacted by any large variations in probe beam intensity between the measurement of I_0 and I.

3.8.2 Allan deviation

The standard deviation, σ_x, of a series of N measurements is one way of assessing the quality of the measured data:

$$\sigma_x = \sqrt{\frac{1}{N-1}\sum_{i=1}^{N}(x_i - \bar{x})^2}, \tag{3.2}$$

Repeating a measurement an increasing number of times would be expected to give a better and better representation of the true value. This effect is represented by the

standard error of the mean (SEM), $\sigma_{\bar{x}}$, which is defined as:

$$\sigma_{\bar{x}} = \frac{\sigma_x}{\sqrt{N}} \tag{3.3}$$

where, σ_x is the standard deviation of the series of measurements, indicating the spread of the data from the mean value, $\bar{x}$, and N is the total number of measurements.

Equation 3.3 suggests that taking an infinite number of measurements reduces the uncertainty in the measured quantity to zero (albeit the effect is less dramatic as N increases). This results in an infinitely precise value for the quantity equal to the mean of the infinite number of measurements, which becomes equivalent to the true value.

While this is true for an ideal instrument affected only by pure shot-to-shot quantum noise, it is not sufficient for real experiments, in which some form of systematic error (e.g. long-term drift) is always present affecting the reliability of the measurements. In this case, the Allan deviation should be calculated, which demonstrates the characteristic balance of random noise and systematic noise in a series of measurements performed by a real instrument.[228]

The N measurements can be split into M subgroups, each containing k individual measurements ($M = {}^{N}/_{k}$). In these measurements, N was chosen to be 18480 due to its high number of integer factors. For instance, when $k = 2$, two adjacent spectra are averaged together to form a series of $M = 9240$ spectra, and so on for all integer values of ${}^{\mathrm{N}}/_{\mathrm{k}}$. The standard deviation, σ_s, and Allan deviation, σ_A, are calculated for each value of k using the following equations:

$$\sigma_{\mathrm{s}}(k) = \sqrt{\frac{1}{M-1}\sum_{i=1}^{M}(x_i - \bar{x})^2}, \tag{3.4}$$

$$\sigma_{\mathrm{A}}(k) = \sqrt{\frac{1}{2(M-1)}\sum_{i=1}^{M-1}(x_{i+1} - x_i)^2}. \tag{3.5}$$

By calculating the Allan deviation, an optimum number of averages, k_{opt}, can be determined from the minimum in a plot of k vs σ_{A}. The Allan deviation for a 20 cm optical cavity formed between the high reflectivity broadband mirrors characterised in Section 3.7 containing a water-filled cell (no flow) is shown in Figure 3.15a). The CCD camera was set to its shortest integration time of 3.66 ms per acquisition.

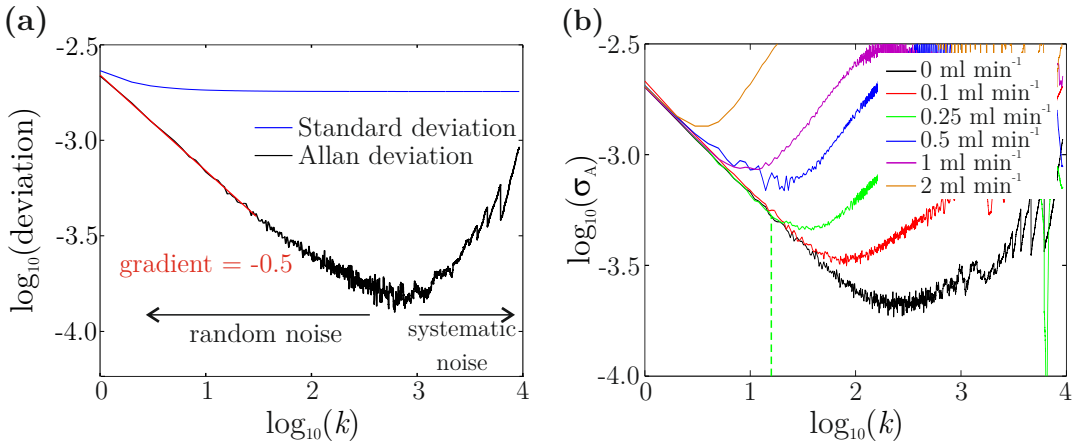


Figure 3.15: a) Allan deviation (black) and standard deviation (blue) of the BBCEAS observable $\left(\frac{I_0}{I} - 1\right)$ calculated for various acquisition numbers (k, see text). I_0 is the mean of 100 acquisitions recorded immediately prior to the sequence of measurements. b) Effect of flow rate through the sample cell on instrument stability. The optimum integration time for the rate chosen for this work (0.25 mL min^{-1}) is marked with a dashed line and corresponds to *ca.* 58 ms ($10^{1.2} \times 3.66$ ms).

The standard deviation as a function of group size calculated from Equation 3.4 is also plotted (blue). There is an initial slight drop as the dataset increases in size, but it then plateaus as the spread in any particular measurement (i.e. the probability of the next measurement lying within 68% of the mean of all previous measurements), should not be expected to be dependent on the number of measurements. Even at low numbers of acquisitions, the gradient of the line never corresponds to a white noise dominated regime (gradient $= -0.5$ on a log-log plot), indicating the long-term drift dominates very rapidly and cannot be resolved by the instrument i.e. it occurs in less than 3.66 ms. The Allan deviation, on the other hand, does show such an improvement at early times as the white

noise regime dominates. There is a minimum in the plot around 1000 acquisitions (10^3), after which the long-term drift in the instrument begins to dominate and the deviation begins to increase. After this point, averaging further offers no increase in precision and is no longer beneficial.

The effect of flow rate through the sample cell was also investigated using this approach, and the results are shown in Figure 3.15b). On flowing water at different rates through the cell using a syringe pump, the same analysis can be applied and the effect of the noise introduced by turbulent flow examined. As the flow rate increases so do the accompanying noise levels, and consequently the optimum integration time drops. A flow rate of $0.25\,\mathrm{mL\,min^{-1}}$ is chosen for this work for comparability with existing results and the fluorescence technique studies performed concurrently within the group.[134] Lower flow rates would permit the use of smaller sample volumes for a given number of acquisitions, but could lead to the build up of unwanted photoproducts in the sample cell. The rate chosen here ensures the replenishment of the entire cell volume (180 µL) in under a minute.

From these measurements an optimum integration time can be chosen, which balances the reduction in white noise with the long-term effects of systematic noise. For the chosen flow rate, the corresponding optimum number of acquisitions is around 50. However, another important consideration is the overall length of the experiment, which is in part determined by the length of each acquisition. This is particularly crucial for low temperature protein studies, where maintaining good cavity alignment and reducing sample exposure to photoexcitation are important considerations. In an effort to get the best signal-to-noise from the shortest experiment, the acquisition time is set to 50 ms in the majority of these studies.

3.8.3 Additional sources of uncertainty

Where sample volumes are large enough to permit it, the sample should be flowed during measurements to prevent the build-up of photoproducts that can stick to the inside of the

cell windows, ruining the cavity finesse through excessive scatter. It is important to filter any samples before flowing as the movement of large (> 10 µm) particulates through the probe beam can lead to dramatic fluctuations in the detected intensity. This is exhibited very clearly in Figure 3.16a), which shows a drastic increase in short-term baseline stability on implementing a syringe filter into the flow set-up.

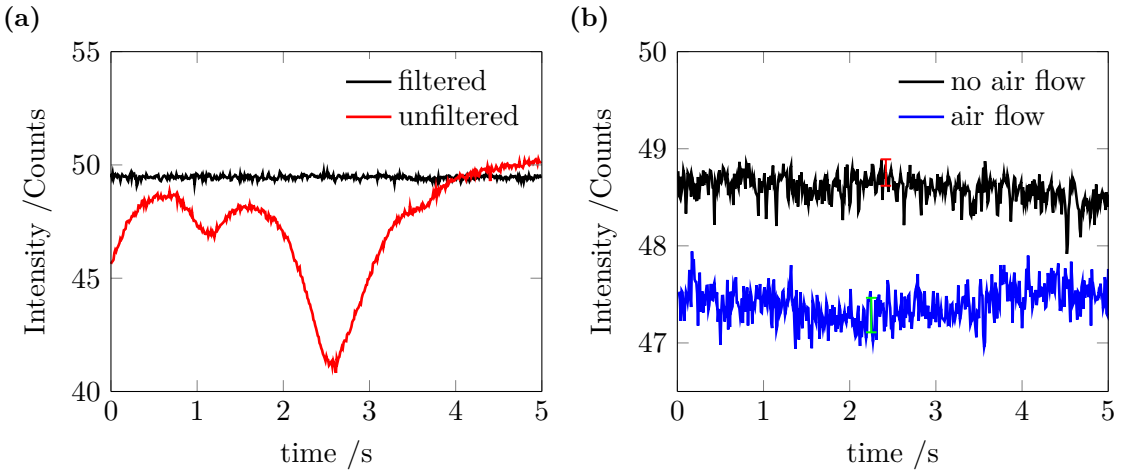


Figure 3.16: a) The effect of including a 0.2 µm syringe filter when flowing model system solutions. With the filter present (black), 500 acquisitions (10 ms each, recorded back-to-back to give a 5 s exposure) have a standard deviation of 86 counts. The absence of a filter (red) causes the standard deviation to increase to 2298 counts. b) The effect of blowing dry air at the faces of the cell windows. The lower absolute light intensity is not caused by air flow and is indicative of long timescale fluctuations inherent to SCR sources. The standard deviation of the measurement series increases by *ca.* 30% when the air is blowing.

The improvement in standard deviation is over an order of magnitude (0.17% with a filter, reduced from 4.6% without one present). Although the effect on the quality of the collected data is significant, this is an overestimate of the actual improvement due to the fast field modulation (*ca.* 17 Hz) used in BBCEAS experiments (see Section 5.2.2). It will, however, improve the accuracy of the extracted absorbance values, as the I_0 reference reading must be recorded once prior to the experiment. A more stable I value will lead to much more representative average absorbances, with the noise dominated by the long-term drift in the probe beam which can be characterised accurately and successfully minimised

by the approach laid out in the previous section.

When studying biological samples, it is necessary to cool the cell to stabilise the protein structure and prevent aggregation and denaturing. This leads to formation of a layer of scattering condensation on the cell windows, dramatically increasing the background losses, L_b, and therefore reducing the cavity finesse and hence the sensitivity of the technique. In extreme examples, this can lead to a reduction in SNR below that of an equivalent single-pass experiment (as discussed in Section 2.5.2), and so every effort should be made to keep the cell faces clear of condensation. This is currently done by blowing dry compressed air gently at the cell windows. The effect of this on the measured light intensity is to increase the uncertainty due to mechanical vibrations of the cell windows. This is demonstrated in Figure 3.16b), where the standard deviation when the air flow is on (178 counts, shown as a representative error bar in green) is increased by *ca.* 30% compared to when no air is flowed (136 counts, red error bar). The decrease in light intensity is not attributed to the presence of the air flow and is indicative of the long-term intensity fluctuations in the SCR source.

To permit comparison of the effect of air flow, this demonstration was performed at room temperature, and it is assumed that the effects are similar in the 0–5 °C temperature range used for the protein studies in this work. It would probably be more accurately treated as a lower limit, as the cell windows may lose flexibility as the temperature is lowered, enhancing the effects of any mechanical vibrations.

3.9 Conclusions

This chapter has introduced and characterised the experimental apparatus used in the CRDS, BBCEAS and OCTAS studies presented in subsequent chapters. The light sources, cavity mirrors, sample cell, and photodetectors have been described, along with the photochemistry of the flavin-based model systems and proteins investigated. Particular attention has been focused on the BBCEAS and OCTAS instruments which share the SCR

source as their probe beam, including a detailed discussion of the CEF calibration used to determine the effective mirror reflectivity of the optical cavity, and the stability of the cavity light source. The long-term drift has been characterised and found to agree with previous work, and optimum experimental parameters such as acquisition time and sample flow rate have been established.

All of this work has informed the experimental procedure to monitor MFEs in chemical and biological systems performed using these three cavity-based instruments. The results of these studies, and their discussion and interpretation, is the subject of the remainder of this thesis.

Chapter 4

BBCRDS Studies of MFEs in Biologically Relevant Systems

4.1 Introduction

Cavity ring-down spectroscopy (CRDS) has long been used in the gas phase to enhance the sensitivity of optical measurements. In CRDS, the rate of decay of the intensity of a laser radiation pulse making a large number of round trips between two highly reflective mirrors is used to extract accurate absorbance measurements with high signal-to-noise. In solution, the gains are typically less striking due to scattering and absorptive losses caused by intracavity elements used to constrain the sample, as well as the sample itself, but still offer substantial improvements over traditional single-pass optical measurements.[192,195,229] This chapter introduces the first of the optical cavity-based techniques developed by our group, based on CRDS, to measure the tiny changes in absorbance of flavin-based solutions caused by magnetic fields.

Traditionally, CRDS has been performed at a single probe wavelength due to the ease of fitting individual ring-down decays. This can be effective in monitoring small changes in absorbance but provides little insight into photochemical mechanisms, as the spectral

signature of absorbing species cannot be resolved. This chapter reports on the successful application of a newly developed broadband-CRDS (BBCRDS) instrument to the measurement of MFEs in solutions of both chemical model systems and real biological protein samples. Work presented here is based upon (and an extension of) the monochromatic proof-of-principle studies carried out previously in the group.[19] The use of a pulsed tunable OPO laser as the probe beam provides the means to add spectral resolution (albeit in a stepwise manner) to an already powerful technique, by scanning the frequency of radiation used for interrogating the sample. Alternative approaches involve the use of a white light source to measure data across the entire visible spectrum in a single shot. However, expensive instrumentation (e.g. streak cameras) is required to measure and resolve the simultaneous overlapping ring-down decays at different wavelengths, and complex fitting procedures employed to extract the required information. By stepping the probe wavelength, a simple low-cost PMT detector can be used for all data measurement at the expense of experimental duration.

Our technique is based on the same principle as transient absorption spectroscopy, using varying pump-probe delay times to build up a temporal profile of the absorbing species of interest. It is particularly useful for studying relatively short-lived intermediates such as the triplet states involved in flavin photochemistry, which typically survive for a matter of microseconds. Decay traces are measured in the presence and absence of an applied magnetic field and examined for a difference in ring-down times, and therefore by implication absorbance and kinetics. At heart, it is essentially a transient absorption experiment with CRD detection for enhanced sensitivity. This permits the use of much reduced sample volumes (i.e. microlitre probe volumes) and photoexcitation energies (i.e. hundreds of microjoules per pulse) while still offering the high-sensitivity (i.e. baseline noise of 10^{-6} A.U.) required for the successful measurement of MFEs under such gentle conditions.

This rare combination of instrument characteristics is emphasised by its successful

application to the first unambiguous ring-down based measurement of a MFE exhibited by an animal cryptochrome protein, *Xl*Cry, from the African clawed-toad *Xenopus laevis* (paper currently in preparation). This provides a key piece of evidence in support of the cryptochrome hypothesis for animal magnetoreception.

4.2 Experimental

4.2.1 BBCRDS experimental set-up

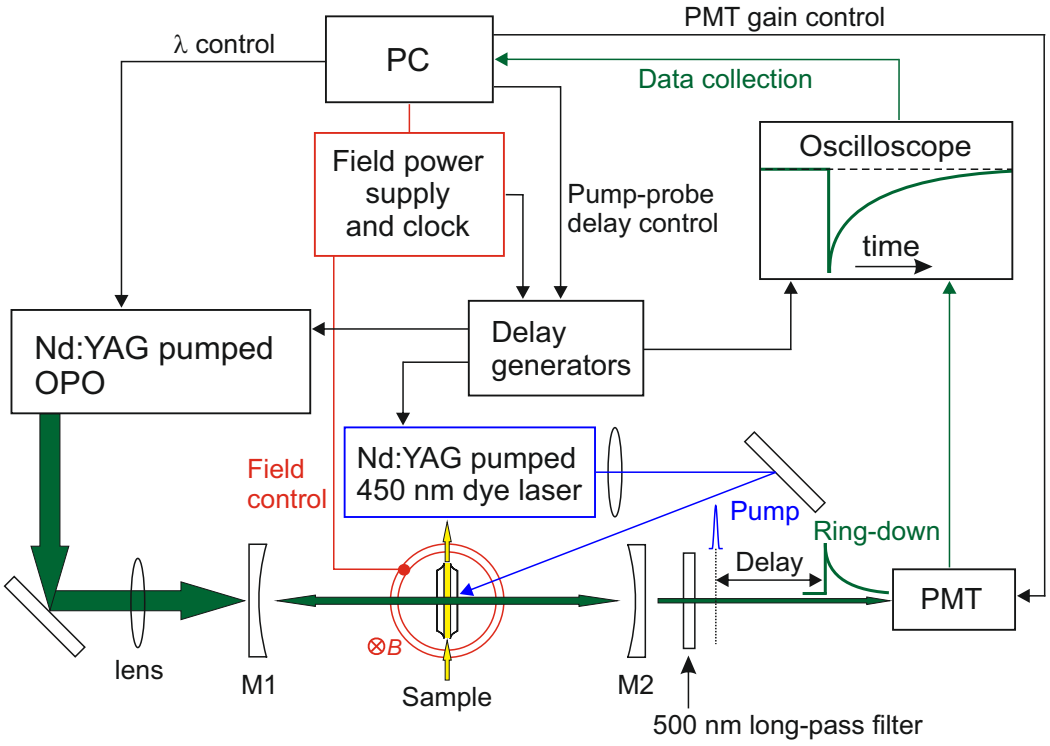


Figure 4.1: A schematic representation of the BBCRDS experimental set-up.

The BBCRDS experimental set-up is shown schematically in Figure 4.1. The optical cavity is formed by a pair of high-reflectivity mirrors (Layertec, 400–800 nm, $R = 99.85$–99.98%, $r_c = 0.5$ m, see Section 3.7), mounted in a linear configuration with a cavity length of 60 cm. A Nd:YAG pumped OPO (Opotek, pulse width 5 ns, 1–20 Hz, tunable between 410 and 2200 nm, Section 3.4.1) is used as the probe beam and directed into the

cavity via turning mirrors through the back of the input mirror, M1. A lens is used to focus the probe beam on to the sample cell, which sits in the centre of the cavity. Light escaping the cavity through the back mirror (M2) is detected by a PMT (Hamamatsu, R928, see Section 3.5) connected to a digital oscilloscope (LeCroy Wavesurfer 42Xs, 8-bit, 2.5 GS s^{-1}, 400 MHz) via a BNC cable terminated with 50 Ω resistance. The data is then transferred to a PC and the ring-down time, τ, determined by a linear least-squares curve-fitting routine in Igor Pro© (Wavemetrix).

The sample cell (Hellma 165-QS, UV Quartz, pathlength = 1 mm, see Section 3.6) is oriented at normal incidence to the cavity axis using a goniometer stage, previously shown to be a preferable geometry to Brewster's angle arrangement, provided the cell windows are of good optical quality.[18] The cell is surrounded by a glass jacket contacting the sample, through which coolant can be flowed to permit temperature control.

During measurements, samples were either flowed through the cell using a syringe pump (Chemyx, Fusion 200, 0.25 mL min^{-1}) for model systems available in large sample volumes (mL), or held static in the case of the precious *Xenopus* cryptochrome protein sample. During measurements on the protein below room temperature, dry nitrogen gas is gently blown at the cell windows in an effort to minimise the build up of a condensation film, which otherwise scatters light and greatly reduces the cavity finesse. The cell is positioned in between a pair of Helmholtz coils to provide a homogeneous magnetic field at the sample, the strength of which can be varied by controlling the current.

The photoexcitation (pump) pulse is provided by a dye laser (Sirah, Cobra) working at 450 nm, pumped by a Nd:YAG (Continuum, Surelite, 355 nm, pulse width 5 ns, 10 Hz, see Section 3.4.2). Alignment of the pump beam, maximising overlap with the probe, is achieved by minimising the ring-down time of a model system sample at a probe wavelength where the radical species absorbs. A PC-controlled delay generator (SRS, DG645) is used to vary the pump-probe delay time (t_d) in a random order between chosen limits, controlled by the PC software. Similarly, the strength of the applied field can be conve-

niently (and randomly) varied by adjusting the current supplied to the coils by a power supply also controlled by the PC. All measurements reported here were recorded at 3.33 Hz to avoid overheating of the air-cooled field coils. In the case of the model systems, there is scope to increase the repetition rate to reduce experimental time as they are less prone to photodegradation and can be flowed to replenish the probe volume. In the case of protein samples, however, a lower photoexcitation rate is preferable as it allows slow recombination to the ground state and reoxidation of the flavin cofactor by dissolved dioxygen. *Xl*Cry is comparatively robust, and the repetition rate need be reduced no further, but transient absorption (TA) studies on related proteins such as *Dm*Cry are regularly performed at 1/120 Hz to maintain sample quality in the face of the much harsher (i.e. 7 mJ) photoexcitation required for large enough signals.

4.2.2 Measuring MFEs

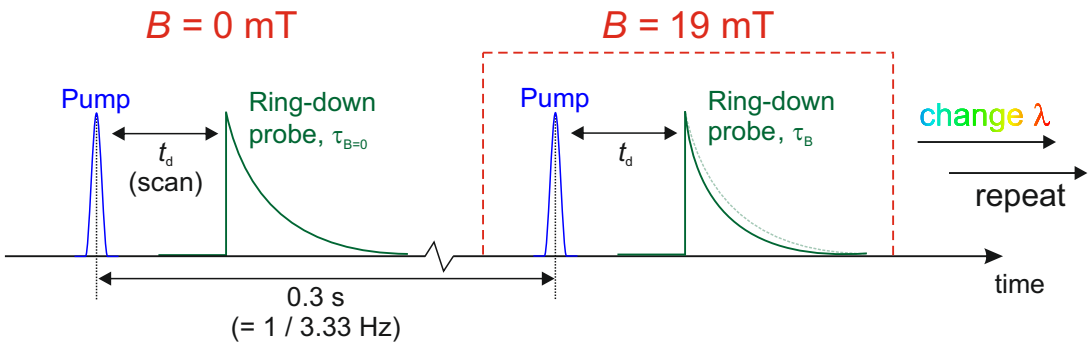


Figure 4.2: A schematic representation of the BBCRDS pulse scheme. The pump pulse is shown in blue and the ring-down probe in green, separated by the variable pump-probe delay time (t_d). Ring-down times are recorded with (τ_B) and without ($\tau_{B=0}$) a magnetic field applied, shown here for a system in which application of a field leads to an increase in absorbance.

A schematic of the laser and field pulse sequence used in CRDS is shown in Figure 4.2. By varying the pump-probe delay time, t_d, and scanning the OPO probe wavelength (as explained in Section 4.2.1), a temporally resolved spectral change can be constructed of

the change in per-pass absorbance, $\Delta A(\lambda, t)$, calculated from the ring-down times recorded with, $\tau_{B=0}$, and without, τ_0, photoexcitation, using Equation 4.1:

$$\Delta A_{B=0}(\lambda, t) = \frac{d}{\ln(10)c}\left(\frac{1}{\tau_{B=0}(\lambda, t)} - \frac{1}{\tau_0(\lambda, t)}\right), \tag{4.1}$$

where L is the cavity length, and c is the speed of light. A similar expression is used for the absorbance change in the presence of both photoexcitation and applied field:

$$\Delta A_B(\lambda, t) = \frac{d}{\ln(10)c}\left(\frac{1}{\tau_B(\lambda, t)} - \frac{1}{\tau_0(\lambda, t)}\right), \tag{4.2}$$

where τ_B is the ring-down time in the presence of a non-zero external field, and therefore the change in differential absorbance due to the application of an external magnetic field can be calculated as:

$$\begin{aligned}\Delta\Delta A(\lambda, t) &= \Delta A_B(\lambda, t) - \Delta A_{B=0}(\lambda, t) \\ &= \frac{d}{\ln(10)c}\left(\frac{1}{\tau_B(\lambda, t)} - \frac{1}{\tau_{B=0}(\lambda, t)}\right).\end{aligned} \tag{4.3}$$

This demonstrates why no calibration or water reference reading is required in CRDS – differences in signal due to sample absorbance, photoexcitation or applied fields are simply reflected in the difference between two ring-down times, and so any references cancel out. This contrasts with CEAS-based measurements where the absorbance is extracted from ratios of intensities (Section 2.5), and so both water references and calibration curves need to be recorded and applied at all stages of the data analysis.

We can define the percentage MFE as:

$$\text{MFE}(\lambda, t) = \frac{\Delta\Delta A(\lambda, t)}{\Delta A_{B=0}(\lambda, t)} \times 100, \tag{4.4}$$

calculated by dividing the change in absorbance due to the field at a particular pump probe delay and wavelength by the zero-field radical signal under the same conditions.

This allows comparability between different methods in which sample concentrations and photoexcitation powers may lead to different absolute changes in absorbance values. For pulsed techniques, the fractional MFE is expected to show no dependence on experimental parameters and be characteristic only of the particular photochemical species. It is worth noting, however, that under steady-state illumination conditions the MFE is very sensitive to any change in the position of photochemical equilibrium, as shown in Chapter 5.

In principle, the temporal resolution of this approach is only limited by the electronics used to provide the delay timings and the pulse duration of the light sources. However, this assumes that the absorbance remains constant over the duration of the ring-down time of the cavity.[230] In all studies presented in this chapter, the ring-down times collected have been determined under this assumption via fitting to single exponential functions. In model systems studies, the ring-down time takes values between 600–800 ns, while for *Xl*Cry, due to excessive scattering losses from the protein and condensation on the cell windows, this drops to 100–200 ns. While this drop has a negative effect on SNR, it improves the effective temporal dynamic range of the technique.

For the free radical species of interest here, with lifetimes of hundreds of microseconds (if not milliseconds) the assumption of constant absorbance is good. However, in spectral regions where the technique is applied to the measurement of rapidly decaying species, such as excited triplet states, the ring-down times can be expected to be distorted so they are no longer a single exponential. Accurate kinetic information can still be obtained, but for accurate absorbance values these effects need to be deconvoluted by fitting to more complex decay profiles. An application of one such method will be shown briefly at the end of this chapter (Section 4.3.4), but as this thesis is more concerned with the detection of MFEs it will not be dealt with in detail. Current work being performed in the group on artificial "maquette" models of cryptochrome proteins involves very rapid electron transfers. In such cases it is crucial to apply these deconvolution methods rigorously to perform a full kinetic analysis of the data.

If the lack of early time resolution becomes a limiting factor in the usefulness of the instrument in the future, CRDS offers the option of reducing the length of the cavity without sacrificing the number of passes made through the sample. As long as the digitiser is sensitive enough to measure changes in the resulting shorter ring-down times this should not adversely affect the SNR of the data. Furthermore, in order for radical pairs to exhibit any sensitivity to the relatively weak magnetic fields of interest to the magnetoreception community (millitesla and below) they must exist for at least several hundred nanoseconds.[39] Reducing the time resolution further is not necessary while the detection of MFEs in SCRPs is the principal application of the instrument.

4.3 Results and Discussion

4.3.1 BBCRDS MFE study of FMN/HEWL

Figure 4.3a) shows the transient CRDS signal, $\Delta A(t)$, recorded for FMN/HEWL at 540 nm, near the peak of the free radical absorption. Photoexcitation with a 450 nm laser pulse at $t = 0$ leads to RP generation within a few nanoseconds,[231] which is temporally unresolved. An initial fast decay component due to geminate RP decay and the overlapping absorption band of the short-lived triplet FMN species is seen, in addition to a very long-lived component due to diffusing free radical species. The blue line is a double exponential fit to the data with fast time constant 1.7 ± 0.7 µs and slow component $\tau > 100$ µs. As explained in Section 3.3.1, these radical pairs inherit the magnetic sensitivity from the short-lived geminate pair precursors. Upon the application of a 19 mT magnetic field, a marked increase in free radical concentration is detectable, shown as an increase in absorbance in Figure 4.3a) (red).

The transient action spectrum, $\Delta\Delta A(t)$, i.e. the effect of the magnetic field on sample absorbance, is shown in Figure 4.3b) and is obtained simply by taking the difference of the two traces in Figure 4.3a). It is seen to grow in and reach a maximum value around

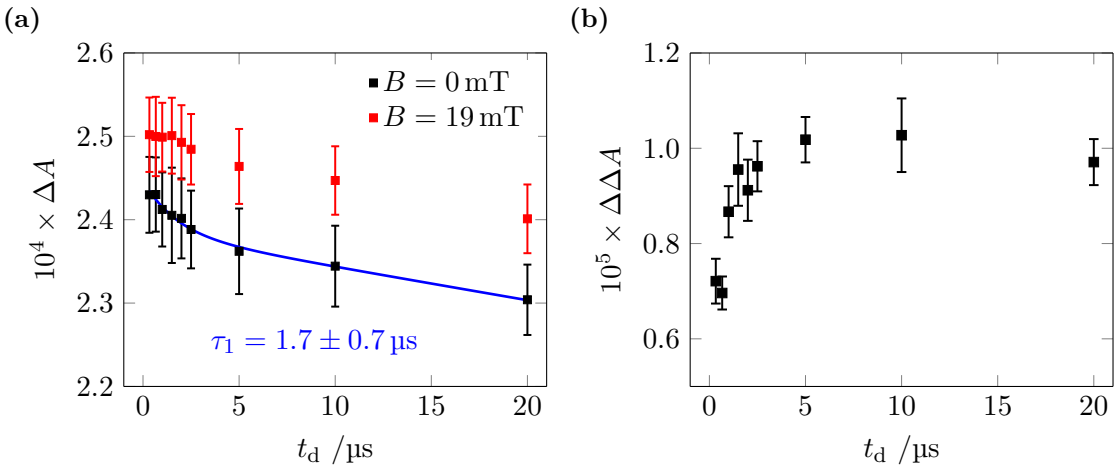


Figure 4.3: a) $\Delta A(t)$ and b) $\Delta\Delta A(t)$ for 10 µM FMN 500 µM HEWL, following photoexcitation with a 200 µJ 450 nm dye laser pulse. a) shows the decay of the ΔA signal at 540 nm with (red) and without (black) a 19 mT magnetic field applied. The blue line is a double exponential fit to the data, with a fast decay constant of 1.7 ± 0.7 µs. Each point is the average of 500 measurements, error bars represent one standard deviation. b) shows the action spectrum, obtained as the difference of the two plots in a), as a function of time. An increase in radical absorbance is clearly observed, as expected for a triplet-born SCRP. Error bars represent the standard error of the mean of 500 measurements. Experiment duration *ca.* 1 h at a repetition rate of 3.33 Hz. Experiment performed at room temperature (293 K), sample flowed at 0.25 mL min^{-1}.

5 µs after photoexcitation.

The same experiment is repeated at a variety of probe wavelengths by scanning the output from the OPO laser. In this case a resolution of 20 nm was chosen, sufficient to map the broad absorption features of interest in solutions of these samples while keeping experimental time reasonable (*ca.* 1 h), and thus minimise sample degradation.

The result is a 2-D surface plot of the time-resolved absorbance spectrum of photoexcited FMN/HEWL, $\Delta A(\lambda, t)$, shown in Figure 4.4a). Clearly visible is the long-lived radical absorption (500–600 nm), assigned to the neutral FMNH$^\bullet$ radical generated by proton transfer from a water solvent molecule following electron transfer from a tryptophan residue in HEWL.[216,227,232] The short-lived triplet state ($\lambda > 620$ nm), which decays almost entirely within 5 µs has an absorption band that extends down to 500 nm, adding an additional fast decay component to a region of the spectrum that initially appears to

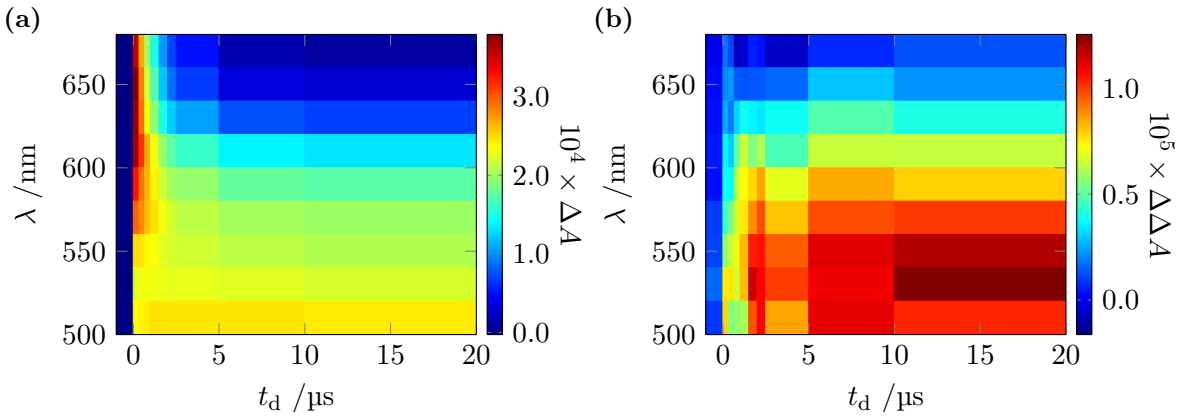


Figure 4.4: surface plots showing a) $\Delta A(\lambda, t)$ and b) $\Delta\Delta A(\lambda, t)$ for 10 µM FMN 500 µM HEWL obtained by varying both the OPO probe wavelength and pump-probe delay time. Comparison of the two figures shows that the application of a 19 mT magnetic field leads to a clear increase in the population of the long-lived free radical species ($500 < \lambda < 580$ nm). Data is the average of 50 field on-off measurements at each time and wavelength, b) smoothed with a 3 point (60 nm) moving boxcar average. Experiment duration *ca.* 1 h, with the same sample and photoexcitation conditions as Figure 4.3.

be purely due to the free radical species.

Figure 4.4b) shows the action spectrum, $\Delta\Delta A(\lambda, t)$, demonstrating the response of the FMN/HEWL system to a 19 mT field as a function of wavelength and delay time. Upon exposure to the field, the spectral region which exhibits an enhanced absorption (orange/red) mirrors that of the long-lived free radical absorption in Figure 4.4a), confirming that it is only the free radical yield that exhibits field sensitivity. The triplet state, which exhibits a peak at 670 nm,[233] does not exhibit an MFE as there is no reverse electron transfer from the magnetically sensitive geminate pair.

To enhance this point, Figure 4.5 shows cuts through the $\Delta A(\lambda, t)$ surface plot a) spectrally, at a variety of fixed pump probe delay times and b) temporally, at fixed wavelengths, spanning regions of purely triplet absorbance (680 nm, red) to principally free radical absorbance (540 nm, blue). Under the low photoexcitation conditions and sample concentrations used in these experiments, any bimolecular decay processes of the triplet (e.g. triplet-triplet annihilation or self-quenching with flavin ground state) are avoided

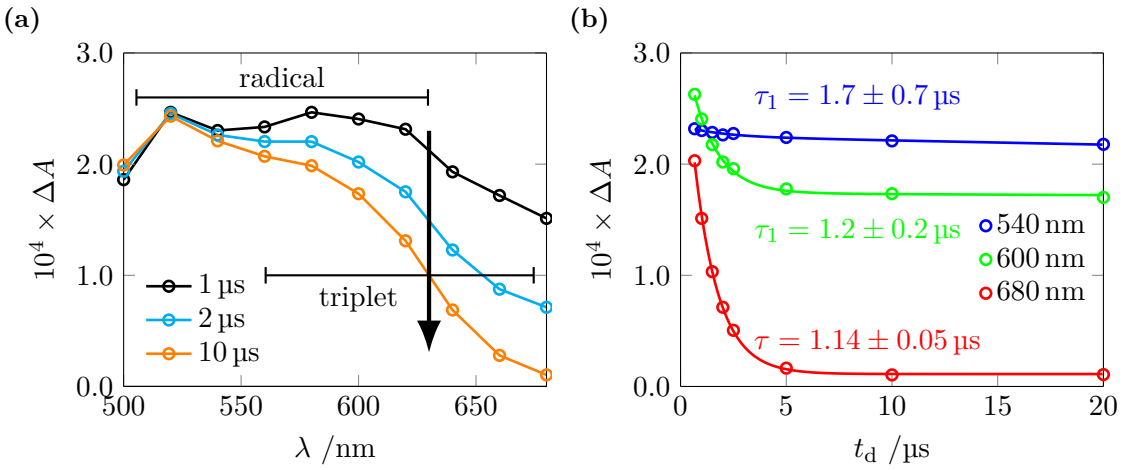


Figure 4.5: a) $\Delta A(\lambda)$ for 10 µM FMN 500 µM HEWL, which can be thought of as cuts through the surface plot in Figure 4.4a) at the fixed pump-probe delay times shown in the legend. The long-lived free radical signal ($500 < \lambda_{max} < 580$ nm) hardly decays within the first 10 µs, while the triplet signal decays rapidly (> 600 nm). b) $\Delta A(t)$ for the FMN HEWL system, which can be thought of as cuts through the surface plot in Figure 4.4a) at the wavelengths shown in the legend. The dominant faster decay of the triplet species at longer wavelengths is apparent. Solid lines show a single exponential fit (red) and biexponential fits (blue, green). Data is the average of 50 on-off measurements at each time and wavelength point, although only the field off data is shown here. Same sample and experimental conditions as Figure 4.3.

and the triplet decay can be treated as a first order process, fit by a single exponential. The decay constant of the FMN triplet ($\tau = 1.14 \pm 0.05$ µs) is matched within 95% confidence intervals by the fast decay components of biexponential fits to a predominantly radical absorbance (540 nm, $\tau_1 = 1.7 \pm 0.7$ µs) and an intermediate wavelength (600 nm, $\tau_1 = 1.2 \pm 0.2$ µs). In both cases the slow component decayed with a time constant of greater than 100 µs. More precise agreement could be obtained by sitting at these three wavelengths and increasing the number of averages taken, but as the focus of this chapter is on the capability to measure MFEs it was not attempted here. They also agree within uncertainty with previous work conducted in the group, where the early time behaviour was studied in more detail but fit with single exponential functions.[227]

The long-lived, virtually static nature of the free radical signal is clear from both plots, while the triplet state largely disappears in under 5 µs. The long time delay spectral

shape shown in orange in Figure 4.5a) is characteristic of the free radical spectrum, with little absorbance above 650 nm, and will become familiar in Chapter 5, where steady-state BBCEAS experiments, integrating over millisecond time windows, show no sensitivity to the short-lived triplet species.

A further application of the high sensitivity of the BBCRDS instrument is to the study of Magnetically Altered Reaction Yield (MARY) curves, in which the response of the system to varying strengths of magnetic field is recorded at a fixed time and wavelength. Despite their lack of temporal or spectral information, these plots are useful in the identification of radical pair partners from the width of its magnetic response profile. A characteristic value, $B_{1/2}$, the field at which the response reaches half of its maximum saturated magnitude, can be extracted from a Lorentzian fit to the data. This value can also be predicted theoretically via the Weller formula (Section 1.8.1), although in the majority of experimental studies presented here the agreement is poor due to the high degree of relaxation present in real systems but neglected in the Weller treatment. The theoretical value should be seen more as a general rule of thumb. In all cases, the value predicted by the Weller formula provides a lower bound to the $B_{1/2}$ value, as relaxation acts to broaden the response. Furthermore, the %MFE plot establishes if a given system exhibits a significant LFE.[132]

Figure 4.6 shows the fractional MFE MARY curve, the response as a function of applied field strength for the FMN/HEWL system. The gradual increase in absorbance as a field of increasing strength is applied is clearly detectable and is as expected for the triplet-born [$FMN^{\bullet -}$ $Trp(H)^{\bullet +}$] radical pair by the RPM. The T_+ and T_- levels become progressively energetically isolated, reducing the extent of S-T mixing and leading to an increase in the free radical yield (due to increased probability of escape from the solvent cage). The relatively large MFE ($\approx 4.5\%$) is in good agreement with work previously performed in the group.[43] The FMN carries a negative charge in solution at pH 6.3 ($pK_{a_1} = 0.7$), and there is a Coulombic attraction with the positively charged HEWL (isoelectric point 11.4) which

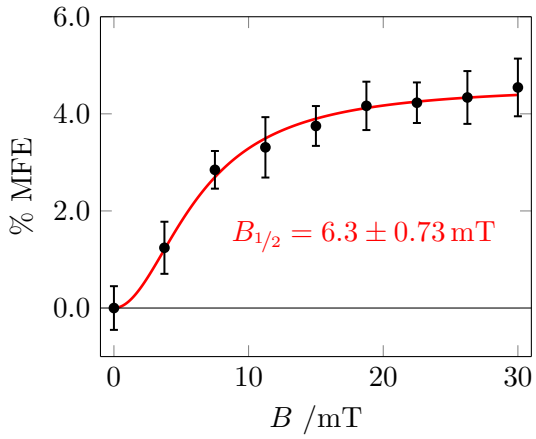


Figure 4.6: The MARY curve for 10 µM FMN 500 µM HEWL, showing the percentage MFE (see Equation 4.4) as a function of applied magnetic field strength. Data recorded at 540 nm and 5 µs after photoexcitation (long enough for field effect to reach a maximum value in Figure 4.3b), and is the average of 1000 on-off shots at each field. $B_{1/2} = 6.3 \pm 0.7$ mT, extracted from the Lorentzian fit to the data shown in red. Error bars represent the standard error of the mean. Experiment duration *ca.* 45 min. Sample and photoexcitation conditions are the same as in Figure 4.3.

prolongs the geminate radical pair lifetime and leads to an increased MFE. The Lorentzian fit to the data (shown in red) gives a $B_{1/2}$ value of 6.3 ± 0.7 mT, in good agreement with those obtained from measurements using the BBCEAS and OCTAS techniques developed in this thesis (see Section 5.3.5 and Section 6.3.3, respectively). As expected, it is much larger than the theoretically predicted value (3 mT)[138] due to the slow spin dynamics of the system, with the MFE attributed to a combination of the hyperfine and spin relaxation mechanisms (Section 1.6).

4.3.2 Comparative BBCRDS MFE study of FAD and FAD/W

FAD is of great interest in the magnetoreception community as it acts as the blue-light chromophore in the cryptochrome proteins suggested to play a crucial role in any biological compass. It is also an interesting molecule to study as its photochemistry is intramolecular, forming radical pairs between regions of the same molecule. This speeds up electron transfer rates resulting in absorbance changes on a fast timescale, providing a good test

of the temporal capabilities of any instrument used to measure MFEs. The addition of tryptophan to a solution of FAD provides an external electron donor, which leads to the formation of intermolecular radical pairs, [$FH^{\bullet}$–AH_2^{+} $Trp^{\bullet}$], similar to those formed in FMN/HEWL as discussed in Section 3.3.3. This system is of interest as the species forming the radical pairs are the same as in the cryptochrome proteins.

In this section, comparisons are made between the photochemical behaviour of the biologically relevant FAD and FAD/W systems using BBCRDS measurements. FAD data is shown in panel a) of the following figures (note the shorter timebase where appropriate), and FAD/W in panel b).

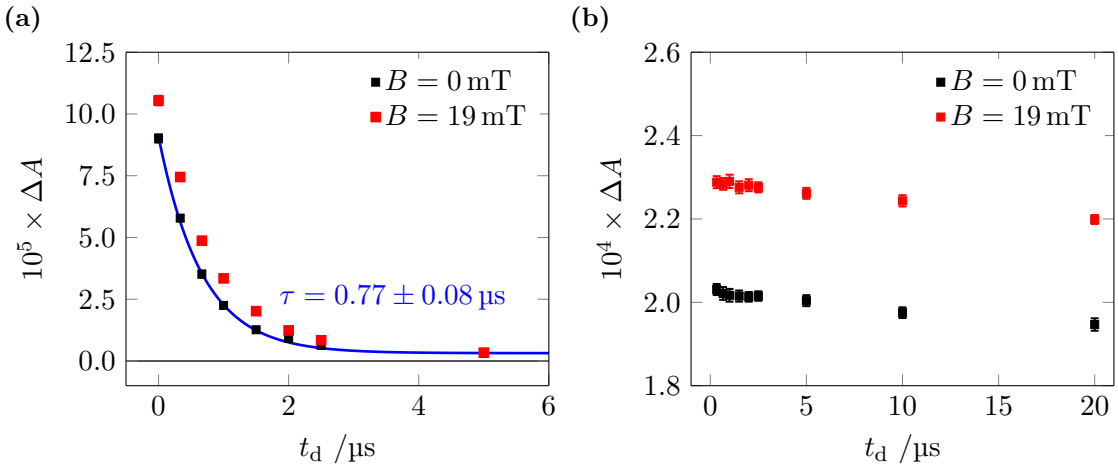


Figure 4.7: $\Delta A(t)$ at 540 nm with (red) and without (black) a 19 mT magnetic field applied for a) pure 10 µM FAD (pH 2.2), and b) with added 500 µM tryptophan, following photoexcitation with a 200 µJ 450 nm dye laser pulse. The blue curve in a) is the result of a single exponential fit to the FAD data, with time constant 0.77 ± 0.08 µs. Each point is the average of 500 measurements, error bars representing one standard deviation are within the size of the marker. Experiment duration *ca.* 1 h at a repetition rate of 3.33 Hz. Experiment performed at room temperature (293 K), sample flowed at 0.25 mL min^{-1}.

Figure 4.7a) shows the decay of photoexcited FAD at 540 nm, chosen as the probe wavelength for comparability with other model systems that exhibit long-lived magnetically sensitive free radical absorbance at this wavelength. As discussed in Section 3.3.2, free radicals can be formed by pure FAD, but via the short-lived triplet state leading to a much reduced radical yield. The very slight offset at 5 µs is likely due to a very low background

of diffusing free radicals (although it is not conclusive within SNR). Comparison with the FAD/W data in Figure 4.7b) is striking as here the absorbance at 540 nm shows little to no temporal decay, indicating the formation of long-lived free radical species formed by diffusion. A similar contrast is seen with the intermolecular FMN/HEWL system shown in Figure 4.3a).

In FAD, the fast decay absorbance can be attributed to a combination of the radical and triplet species. As these are in equilibrium they can be treated as decaying at the same rate. Consequently, a single exponential decay is a good fit at all wavelengths (with a constant offset term to allow for the very long-lived background of free radical product). The blue line in Figure 4.7a) shows the result of such a fit with time constant 0.77 ± 0.08 µs. The absorbance change in the presence of a 19 mT magnetic field is shown (red); a clear increase is evident at early times, which decays away within 5 µs. In the case of FAD/W, however, the magnetic response survives for more than 100 µs mirroring the long-lived nature of the free radicals.

The transient $\Delta\Delta A(t)$ is shown for both systems in Figure 4.8, calculated as the difference in data with (red) and without (black) a magnetic field applied from the respective plots in Figure 4.7. Application of a magnetic field leads to an increase in the free radical yield, detected as an increase in the absorbance, demonstrating that the radical pairs are formed from the excited triplet state. This indicates that the intramolecular electron transfer in FAD is still not fast enough to outcompete ISC. The rapid (sub 5 µs) decay of the FAD field effect in a) is due to the short lifetime of the species involved, in contrast to the long-lived MFE exhibited by the intermolecular FAD/W system in b) as well as the FMN/HEWL system in Section 4.3.1. The prolonged effect seen for FAD/W (>100 µs) is due to the diffusion of free radical species $FH^{\bullet}$–AH_2^+ and $Trp^{\bullet}$.

Figure 4.9a) shows the $\Delta A(\lambda, t)$ surface plot for FAD, demonstrating that the absorbance at all wavelengths has decayed within 5 µs, with no long-lived components. Neutral flavin radical absorption ($FH^{\bullet}$, $\lambda_{max} = 502, 580$ nm)[232] could not be distinguished

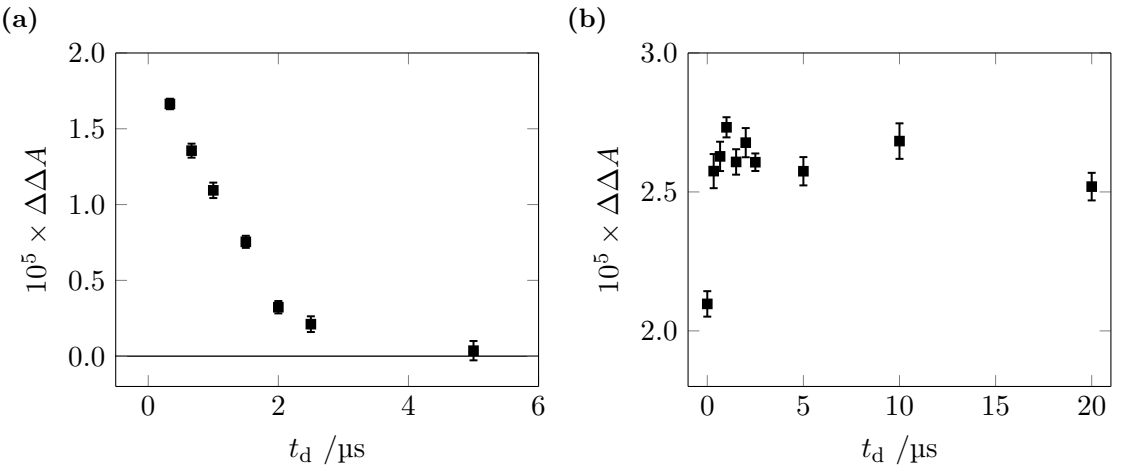


Figure 4.8: $\Delta\Delta A(t)$ at 540 nm for a) pure 10 µM FAD and b) with added 500 µM tryptophan, following photoexcitation with a 200 µJ 450 nm dye laser pulse. Calculated as the difference in on (red) and off (black) $\Delta A(t)$ data from the respective plots in Figure 4.7. An increase in radical absorbance is observed in both systems, indicating a triplet-born SCRP. Error bars represent the standard error of the mean of 500 measurements. Experiment duration *ca.* 1 h at a repetition rate of 3.33 Hz. Experiment performed at room temperature (293 K), sample flowed at 0.25 mL min^{-1}.

against the intense broad absorption band of the triplet ($500 < \lambda < 700$ nm).[136,219] The broad peak centred around 650 nm is assigned to the T-T absorption of the cationic form of the flavin ($^3FH^+$).[234] This is in stark contrast to the $\Delta A(\lambda, t)$ surface for FAD/W shown in Figure 4.9b), in which a long-lived absorbance assigned to the free radicals formed by diffusion is clear ($500 < \lambda < 600$ nm). At longer wavelengths there is the hint of a very short-lived FAD triplet state, decaying away within a couple of microseconds. The intensity of this band is much reduced in comparison with that for the FAD only solution, as the fast ET from the tryptophan acts to quench it and rapidly form intermolecular RPs.

Figure 4.10a) shows the effect of a 19 mT field on pure FAD, which confirms a positive field response across the entire triplet absorbance band. The spectral intensity mirrors that of the $\Delta A(\lambda, t)$ surface, indicating that the fractional effect is approximately constant across the absorption band as a result of the equilibrium between the geminate radical pair and triplet states. The effect is still growing in the first 0.33 µs (the earliest time point recorded here) and then decays away within 5 µs. The FAD/W action surface in

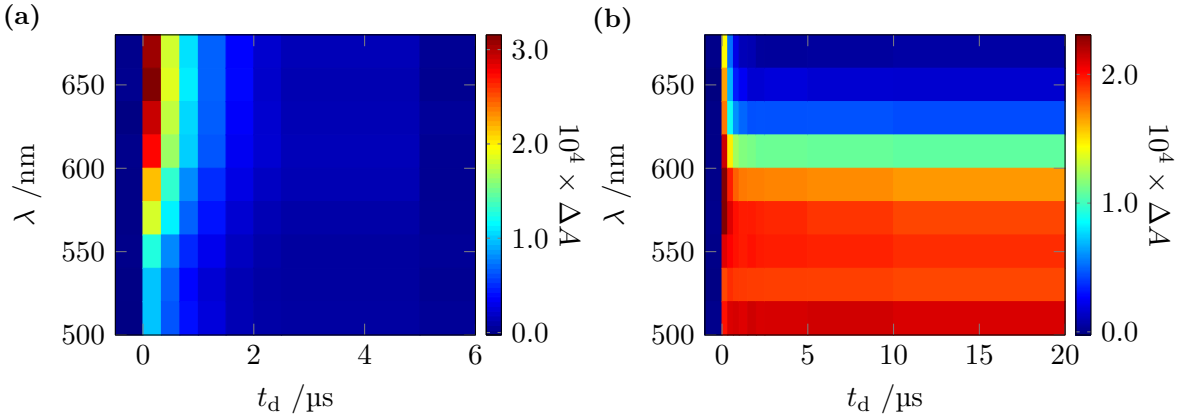


Figure 4.9: $\Delta A(\lambda, t)$ surface plots for a) FAD and b) FAD/W, obtained by varying both the OPO probe wavelength and pump-probe delay time, t_d. In a) the purely intramolecular photochemistry of FAD is complete in under 2 µs. The addition of tryptophan as an external electron donor in b) leads to intermolecular RPs, and hence a long-lived signal characteristic of free radical species ($500 < \lambda < 600$ nm). Data is the average of 50 on-off measurements at each time and wavelength. Experiment duration *ca.* 1 h, with the same sample and photoexcitation conditions as Figure 4.7.

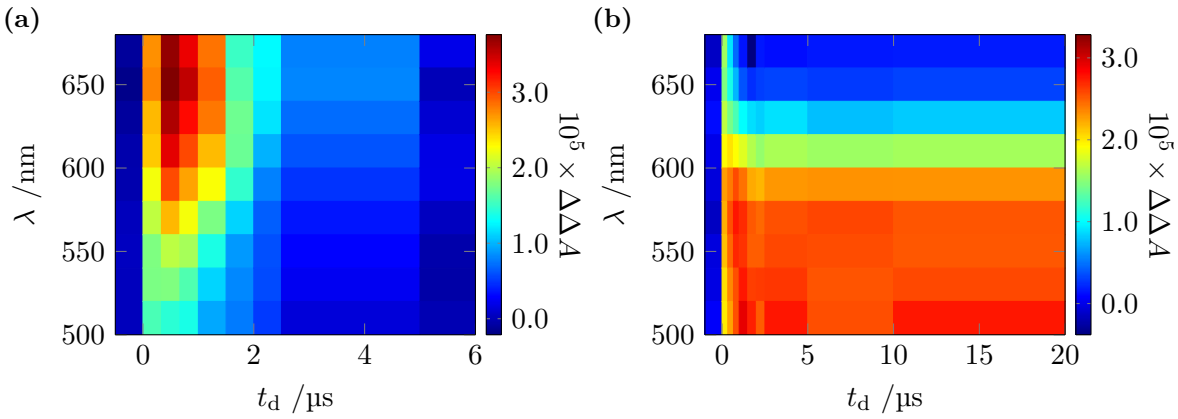


Figure 4.10: $\Delta\Delta A(\lambda, t)$ surface plots for a) FAD and b) FAD/W on application of a 19 mT magnetic field. Due to the equilibrium between the triplet and intramolecular radicals, a short-lived field effect is seen across the entirety of the triplet absorption region in both systems. In b) the free radicals formed with the external electron donor tryptophan leads to a long-lived magnetic response ($500 < \lambda < 600$ nm, compare with corresponding $\Delta A(\lambda, t)$ plot in Figure 4.9). Data is the average of 50 field on-off measurements at each time and wavelength, smoothed with a 3 point (60 nm) moving boxcar average. Experiment duration *ca.* 1 h, with the same sample and photoexcitation conditions as Figure 4.7.

Figure 4.10b) matches the spectral shape of the transient absorbance shown in Figure 4.9b) almost exactly. The free radical species carry the long-lived MFE, while the small triplet yield is magnetically sensitive within its short lifetime due to the equilibrium established with the intramolecular FAD RP.

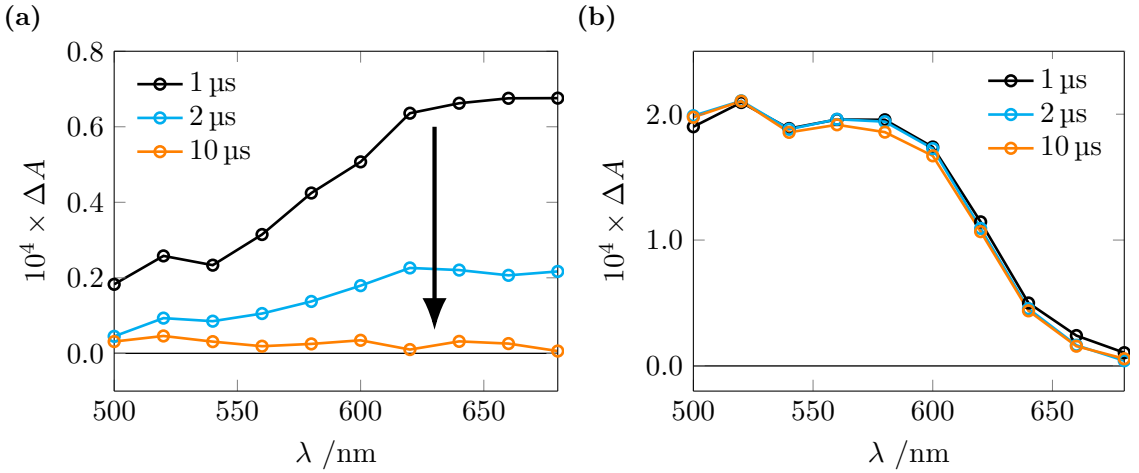


Figure 4.11: $\Delta A(\lambda)$ for a) pure FAD and b) FAD/W, which can be thought of as cuts through the surface plots in Figure 4.9 at the fixed pump-probe delay times shown in the legend. In a) the broad triplet signal ($500 < \lambda < 680$ nm) decays rapidly within the first 2 µs, and is entirely gone by 10 µs after which only a slight hint of long-lived intramolecular radical signal can be detected. In b) the long-lived FAD/W free radical signal ($500 < \lambda < 600$ nm) hardly decays within the first 10 µs, while the triplet signal (> 600 nm) has already been almost entirely quenched within 1 µs. Data is the average of 50 on-off measurements at each time and wavelength point, although only the field off data is shown here. Same sample and experimental conditions as Figure 4.7.

Cuts through the $\Delta A(\lambda, t)$ surface plots in Figure 4.9 at fixed delay times are shown in Figure 4.11. The broad, featureless triplet band characteristic of pure FAD in a) contrasts with the FAD/W spectrum in b), which is dominated by free radical absorbance. The spectral shape is broadly similar to that of the FMN/HEWL system (see Figure 4.5a), with the exception of the much reduced triplet signal due to its rapid quenching by electron transfer.

Figure 4.12 shows temporal profiles for both a) FAD and b) FAD/W at a selection of wavelengths spanning the monitored absorption spectrum. The solid lines in a) are single

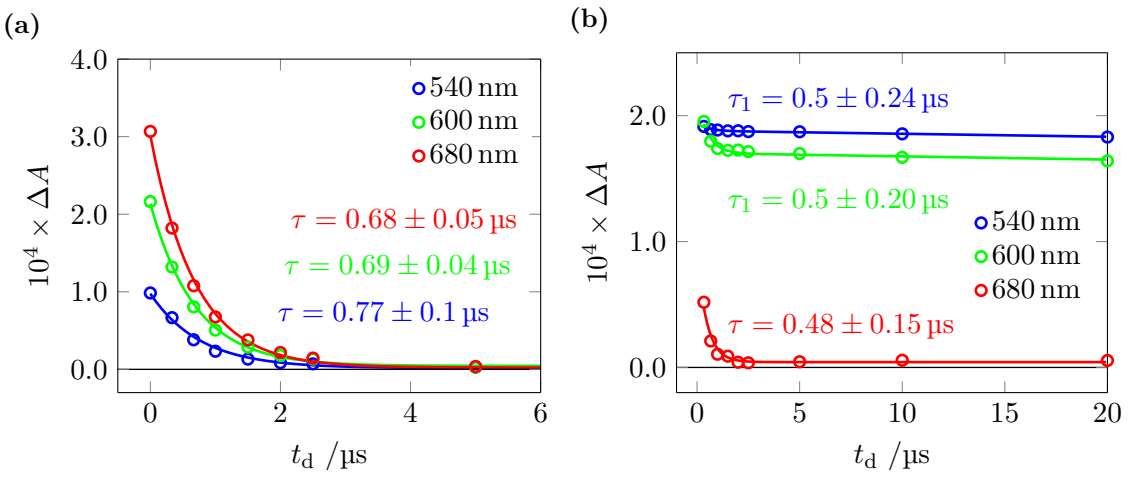


Figure 4.12: $\Delta A(t)$ for a) FAD and b) FAD/W, which can be thought of as cuts through the surface plot in Figure 4.9a) at the wavelengths shown in the legend. Fits to the data are shown as solid lines with accompanying time constants: a) monoexponential decays and b) biexponential decays (540 nm, 600 nm) and a monoexponential decay (680 nm). The faster decay constants in b) indicate the extra quenching pathway due to external electron donation by the tryptophan. The uncertainty on the time constant represents a 95% confidence interval. Data is the average of 50 on-off measurements at each time and wavelength point. Same sample and experimental conditions as Figure 4.7.

exponential fits to the FAD data and confirm (within 95% confidence intervals) that the decay constants are equal across the absorbance spectrum due to the equilibrium between the triplet and intramolecular radicals; 540 nm: $\tau = 0.77 \pm 0.1$ µs, in good agreement with Figure 4.7a); 600 nm: $\tau = 0.69 \pm 0.04$ µs; 680 nm: $\tau = 0.68 \pm 0.05$ µs. As the FAD system exhibits absorbance decaying at a rate faster than the ring-down time (800 ns) across the wavelength range, this data is a prime candidate for the temporal deconvolution performed in Section 4.3.4. It is concluded that despite underestimating the absolute absorbance at early timescales, the kinetics are still accurate.

In the case of FAD/W shown in 4.12b), the decay at 680 nm is treated as representative of the pure triplet state, and can be fitted by a single exponential. The faster decay constant reflects the additional triplet loss process due to quenching by electron transfer from the tryptophan. The 540 nm and 600 nm data, spectral regions treated as probing overlapping absorbances of both the triplet and free radical species, can be described by

biexponential fits, with fast decay constant $\tau_1 = 0.5\,\mu s$ for the FAD triplet decay, and long component over 100 µs.

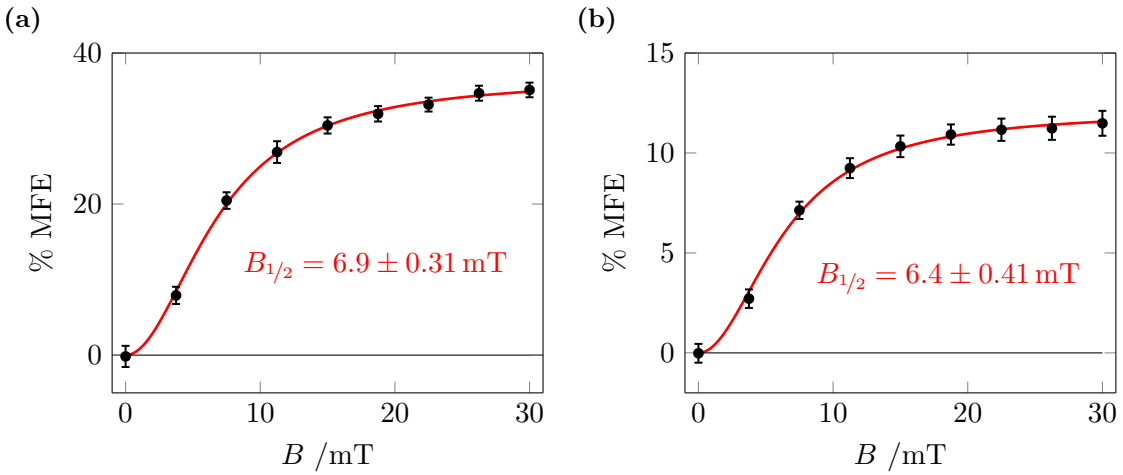


Figure 4.13: The MARY curve for a) pure FAD and b) FAD/W, showing the percentage MFE as a function of applied magnetic field strength. In both cases the data was recorded at 540 nm but in a) at $t_d = 1\,\mu s$ (before the field effect has decayed away in Figure 4.8a), and b) $t_d = 5\,\mu s$. The $B_{1/2}$ values are shown on the respective plots, extracted from the Lorentzian fits to the data shown in red. Error bars represent the standard error of the mean of 1000 measurements at each field strength. Experiment duration *ca.* 45 min. Sample and photoexcitation conditions the same as in Figure 4.7.

The fractional response as a function of applied field strength is shown in the MARY curves in Figure 4.13, measured at 540 nm. While the FAD/W experiment could be performed at the same pump-probe delay as the FMN/HEWL data in Figure 4.6 ($t_d = 5\,\mu s$) to allow time for the MFE to fully develop, the FAD measurement was performed at $t_d = 1\,\mu s$. This is simply a necessity in the FAD system as the magnetic response has already disappeared within 5 µs. It is also chosen because it lies outside of the ring-down time and so will not be affected by any distortion of a decaying absorbance signal. In both cases the increase in radical yield (and therefore absorbance) with increasing strength of the applied magnetic field is clear, indicating a triplet-born SCRP, and is rationalised in the same way as the FMN/HEWL system in Section 4.3.1. The resulting MFE of FAD is shown to be very large, saturating at over 30%, suggesting effective competition between the different recombination pathways available to the radical species. The red

curves are Lorentzian fits to the data, from which $B_{1/2}$ values are extracted (see figures for values), later shown to be in good agreement with that measured by BBCEAS and OCTAS (Section 5.6 and Section 6.4, respectively).

4.3.3 BBCRDS cryptochrome MFE studies

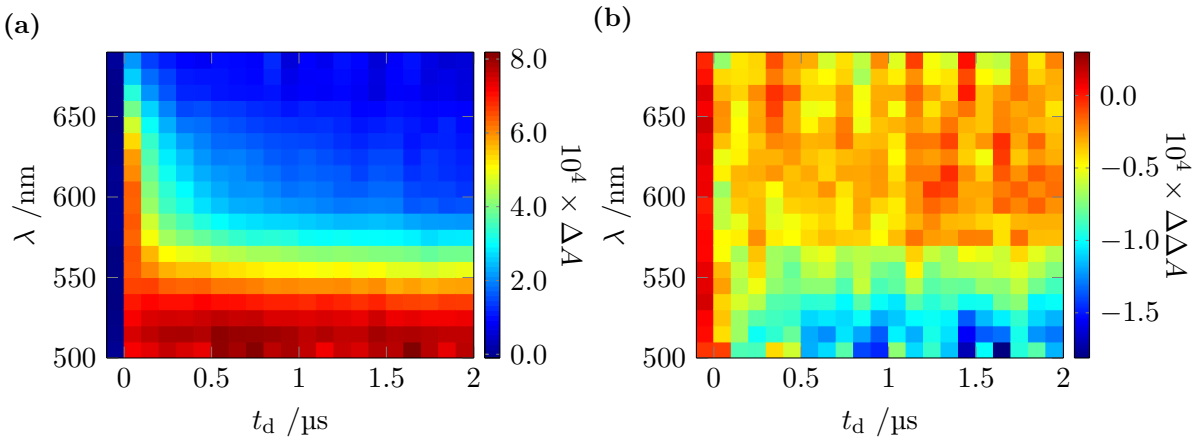


Figure 4.14: Surface plots showing a) $\Delta A(\lambda, t)$ and b) $\Delta\Delta A(\lambda, t)$ for the *Xl*Cry protein following 150 µJ 450 nm photoexcitation. a) The long-lived RP2 state is clearly seen as an increase in absorbance (red) after photoexcitation ($500 < \lambda < 550$ nm) and the short-lived $TrpH^{\bullet+}$ radical (> 570 nm) deprotonates within around 200 ns. b) The $\Delta\Delta A(\lambda, t)$ action surface on application of a 19.5 mT magnetic field, exhibits a decrease in radical absorbance (negative MFE) in a spectral region corresponding to the long-lived RP2 absorbance seen in a). Data is the average of 20 measurements at each wavelength and pump probe delay, smoothed with 5 point (50 nm) moving boxcar average. Experiment duration *ca.* 2 h at 3.33 Hz. Sample is held static (no flow) at 273 K.

Following optimisation of the BBCRDS instrument for MFE studies using the flavin model systems reported in previous sections, the technique was applied to the detection of a magnetic field effect in the animal cryptochrome protein, *Xl*Cry.

Figure 4.14a) shows the $\Delta A(\lambda, t)$ surface for *Xl*Cry, recorded at 278 K, with 3.33 Hz 150 µJ photoexcitation at 450 nm. The gentle photoexcitation conditions are used in an effort to reduce the chance of photodegrading the precious cryptochrome sample. Cooling the sample below room temperature necessitates the blowing of dry compressed nitrogen at the cell windows to avoid the build up of condensation, although this can introduce

some mechanical vibration which reduces the SNR.

The spectrum shows an initial increase in absorbance between $500 < \lambda < 650\,\text{nm}$ due to the rapid formation of singlet born RP1 via cascade ET (Section 3.3.4). The rapid ($< 200\,\text{ns}$) decay of the signal at wavelengths longer than 570 nm is assigned to the deprotonation of the $\text{TrpH}^{\bullet+}$ radical in the formation of RP2. The strong absorbance below 550 nm is contributed by the flavin component of the RP, the concentration of which remains virtually constant on this timescale. In order to map out the response of a previously unstudied system in greater detail, the time and wavelength resolution of the instrument was increased by recording data every 100 ns and every 10 nm respectively. This has the undesirable consequence of increasing the experimental time, in this case approximately doubling it in comparison to the lower resolution proof-of-principle studies of the flavin-based model systems shown in the previous sections.

The magnetic sensitivity is passed to RP2, as confirmed by spectral comparison of the MFE action spectrum, $\Delta\Delta A(\lambda, t)$, in Figure 4.14b) with the $\Delta A(\lambda, t)$ surface. Now the application of an external field acts to reduce the proportion of molecules that undergo deprotonation to form the long-lived RP2 species, by trapping them in the singlet RP state from which spin-allowed electron-hole recombination to the ground place takes place. As a result, the absorbance due to long-lived RP2 decreases, shown as the blue region in the figure ($500 < \lambda < 550\,\text{nm}$).

Figure 4.15 shows corresponding temporal cuts through the surface plots in Figure 4.14, averaged over the RP2 absorption band ($500 < \lambda < 550\,\text{nm}$) to enhance SNR. The radical absorbance shown in black in Figure 4.15a) shows a very slow decay, due to the recombination of RP2 to the molecular precursors,[96,112] remaining virtually constant on the timescale of the experiment. The application of a 19.5 mT magnetic field leads to a substantial decrease in radical absorbance (red), reflecting the higher probability of singlet recombination to the ground state. The action spectrum measured as a function of time, $\Delta\Delta A(t)$, plotted in Figure 4.15b) shows the magnetic field response is fully developed

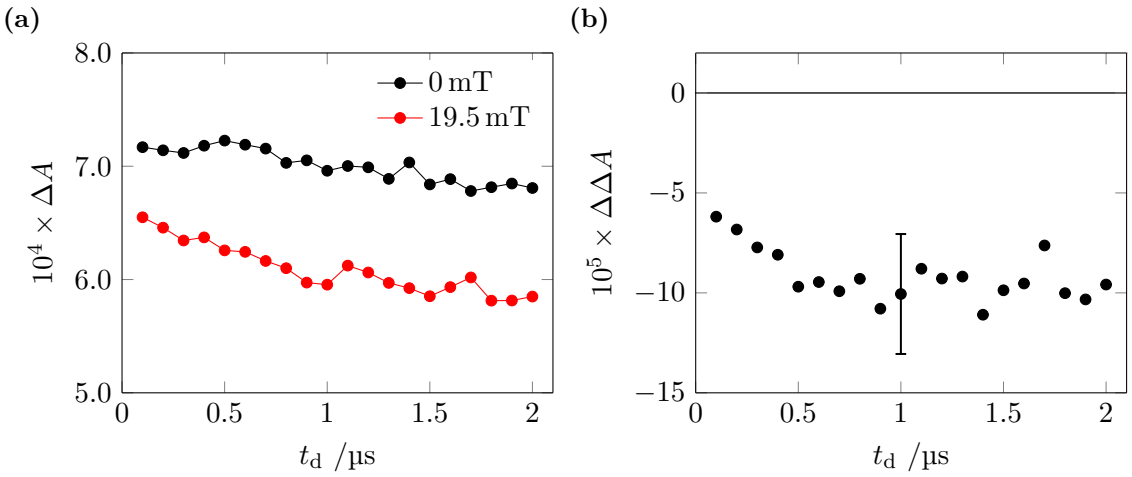


Figure 4.15: a) $\Delta A(t)$ and b) $\Delta\Delta A(t)$ for *Xl*Cry, following photoexcitation with a 150 µJ 450 nm dye laser pulse. a) shows the decay of the ΔA signal averaged 500–550 nm with (red) and without (black) a 19.5 mT magnetic field applied. b) shows the action spectrum, obtained as the difference of the two plots in a), as a function of time. A decrease in radical absorbance is clearly measurable, as expected for a singlet-born SCRP. An error bar representative of the standard error of the mean is shown. Same sample and experimental conditions as Figure 4.14.

within 0.5 µs and then remains approximately constant (within SNR) on the timescale recorded here.

The larger uncertainty, shown as a representative error bar in Figure 4.15b), can be attributed to the shorter cavity ring-down time resulting from the increased scatter due to the large protein molecules in solution, as well as the formation of any condensation on the cell windows. Based on the size of the uncertainty, any change in absorbance smaller than 1×10^{-5} would be very challenging to measure. This is in agreement with protein CRDS MFE studies performed previously in the group,[227] where investigations of *Dm*Cry and *Ec*PL proteins, which exhibit less pronounced magnetic field sensitivity, showed that any field effects on this order were within noise levels.

Despite the challenging experimental conditions, here an unambiguous spectrally resolved magnetic field effect on an animal cryptochrome protein has been clearly demonstrated, measured using BBCRDS.

Figure 4.16 shows the CRDS measured MARY curve for *Xl*Cry, the fractional response

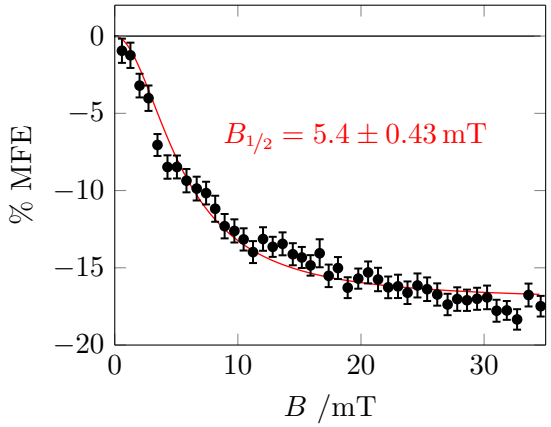


Figure 4.16: The MARY curve for *Xl*Cry, showing the fractional change in absorbance as a function of applied magnetic field. The error bars show one standard error of the mean of 400 measurements. Same photoexcitation and sample conditions as Figure 4.14, but with a 10 s delay between field sweeps to allow for sample recovery. Experiment duration *ca.* 2.5 h.

of the system as a function of applied field strength. A Lorentzian fit to the data provides a $B_{1/2}$ value of 5.4 ± 0.4 mT. The negative field response is detectable at all field strengths, and thus far there is no hint of the elusive but much sought after biological low field effect. The magnitude of the MFE, which looks to be approaching a saturated value of $\approx 16\%$, is the largest recorded in any protein and makes this system a good candidate for biological LFE investigations in the future. The response of an animal cryptochrome protein to an external field (albeit *in vitro* under non-physiological conditions) is a key result in the mounting body of evidence for cryptochrome-mediated magnetoreception.

4.3.4 Deconvolution of the ring-down time and spectral decay

As suggested in Section 4.2.2, when the ring-down time of a cavity is comparable to the timescale of the kinetics of the chemical process being investigated, the two effects should be deconvoluted in order to obtain accurate results. For the long-lived RP species exhibiting MFEs studied in this chapter, these effects can be neglected as the tens of microseconds lifetimes are far in excess of the typical ring-down times achieved in a well-aligned optical cavity containing a sample cell (500–800 ns).

However, in certain cases these effects become important. The shortest lived species accessible to study here are the sub-microsecond decays of excited triplet states. In the FMN/HEWL model system (Section 4.3.1) this species was shown to be magnetically insensitive due to its short lifetime and the lack of any reverse electron transfer process. The FAD system, on the other hand, shows magnetically sensitive photochemistry, dominated by the intense, short-lived triplet absorption band, making it a prime candidate to demonstrate one approach for extracting accurate data. The ring-down deconvolution procedure has acquired increased importance in recent times as the artificial 'maquette' flavoprotein models of cryptochromes, which are currently being studied using CRDS, exhibit decays on the order of 100 ns that require deconvolution. The approach used here follows the method laid out by Brown et al.,[235] and has previously been applied successfully to our single wavelength studies.[43] This work was performed in collaboration with Tilo Zollitsch.

From Equation 2.13 (Section 2.4), the time dependent intensity of light circulating within the cavity, $I(t)$, is given by:

$$I(t) = I(0) \exp\left(-\frac{ct}{d}\left(1 - R + \alpha l\right)\right), \tag{4.5}$$

where $I(0)$ is the initial intensity, c is the speed of light, t is time, d is the length of the cavity, R is the mirror reflectivity, and αl is the per-pass absorbance by the sample constrained in a cell of pathlength l. By making the substitution for the ring-down time of an empty cavity, τ_0, given by Equation 2.15, this can be expressed as:

$$I(t) = I(0) \exp\left(-\left(\frac{\alpha c l}{d} + \frac{1}{\tau_0}\right) t\right), \tag{4.6}$$

where the factor enclosed in the brackets is the inverse of the ring-down time in the presence of an absorbing species. This formulation clarifies that the ring-down time has two components: that of an empty cavity ($\frac{1}{\tau_0}$) and an additional contribution from a background absorber (in this case of constant concentration). Clearly, if no absorber is

present (i.e. $\alpha = 0$) then the intensity reduces to that for an empty cavity, I_0:

$$I_0(t) = I(0)e^{-\frac{t}{\tau_0}}. \tag{4.7}$$

In our data, this applies at negative pump-probe delay times, where excited species are yet to be produced by photoexcitation. By taking a ratio of the ring-down decays with and without absorbance the decay profile of an empty cavity can be factored out, leaving a function solely characteristic of any absorbing species:

$$R_\tau(t) = \frac{I(t)}{I_0(t)} = \frac{I(t)}{I(0)e^{-\frac{t}{\tau_0}}}. \tag{4.8}$$

For the trivial case of no absorbing species being present, $I(t)$ is given by Equation 4.7 and so the ratio is unity. Figure 4.17a) shows such a case: this example is taken from the FAD data at a delay time sufficiently long that the excited species have already returned to the ground state ($t_\mathrm{d} = 5\,\mu\mathrm{s}$). The lack of any absorbance at this wavelength (680 nm) means the ring-down times are approximately equal within SNR – the noise increases as the ring-down profiles both approach zero after 2 µs – and so the ratio is flat and constant around one.

In the case of an absorbing species being present, but at constant concentration on the ring-down timescale, $I(t)$ is given by Equation 4.6 and so the ratio is given by:

$$R_\tau(t) = \frac{I(t)}{I(0)e^{-\frac{t}{\tau_0}}} = \exp\left(-\frac{\alpha c l}{d}t\right). \tag{4.9}$$

This applies in the case of long-lived free radical species in the FMN/HEWL study in Section 4.3.1. Figure 4.17b) shows the ratio of ring-down times at 540 nm and 5 µs pump-probe delay taken from the FMN/HEWL traces used to calculate the $\Delta A(t)$ profile shown in Figure 4.3a). In this case, the presence of the absorber leads to a difference in the ring-down times (the ratio is no longer one), but the free radical absorbing species

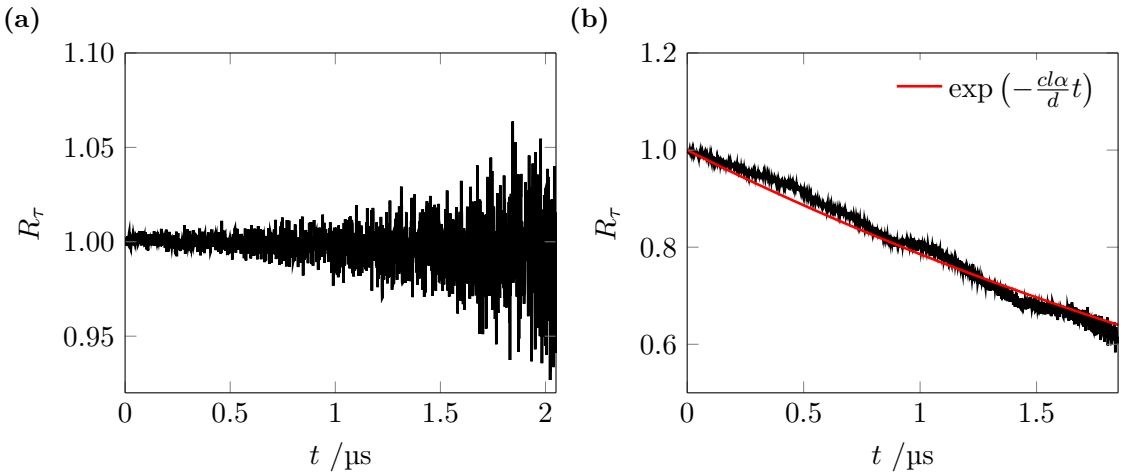


Figure 4.17: a) R_τ (defined in text) for the FAD system at a pump probe delay of 5 µs. As all of the transient species have decayed away in this time, the ring-down time is equal to that of an empty cavity (within noise). b) R_τ for a long-lived species, in this case the intermolecular radicals formed in the FMN/HEWL system, probed at 540 nm and $t_\mathrm{d} = 5$ µs. Due to their long lifetime, the ratio of ring-down times can be approximated well by a single exponential fit.

are sufficiently long-lived that the absorbance can be treated as a constant. The ratio can thus be well described by the single exponential function given in Equation 4.9, which is only dependent on the ring-down decay itself.

If, however, the absorbance can no longer be treated as a constant, due to the concentration of the absorbing species changing (i.e. decaying) on the ring-down timescale, the substitution $\alpha = \alpha(t)$ is made:

$$I(t) = I(0) \exp\left(-\frac{cl}{d}\int_0^t \alpha(t)dt - \frac{t}{\tau_0}\right). \tag{4.10}$$

In the case of FAD, the decay of the triplet is treated as a pseudo-first order process for reasons outlined in Section 4.3.2, $\alpha(t) = \alpha_0 e^{-kt}$, and so:

$$I(t) = I(0) \exp\left(\frac{c}{d}\frac{\alpha_0 l}{k}\left(e^{-kt} - 1\right) - \frac{t}{\tau_0}\right). \tag{4.11}$$

As above, the ring-down time of an empty cavity (in the absence of photoexcitation

leading to the production of decaying species) can be conveniently and simply removed by taking the ratio, R_τ, leaving only the time-dependent behaviour characteristic of the decaying species:

$$R_\tau(t) = \frac{I(t)}{I(0)e^{-\frac{t}{\tau_0}}} = \exp\left(\frac{c}{d}\frac{\alpha_0 l}{k}\left(e^{-kt}-1\right)\right). \tag{4.12}$$

This ratio can then be fit by the function in Equation 4.12 with k and α_0 allowed to vary. An initial value of k taken from the single exponential fit of the triplet absorbance decay (assuming constant absorbance) is used as a sensible starting point.

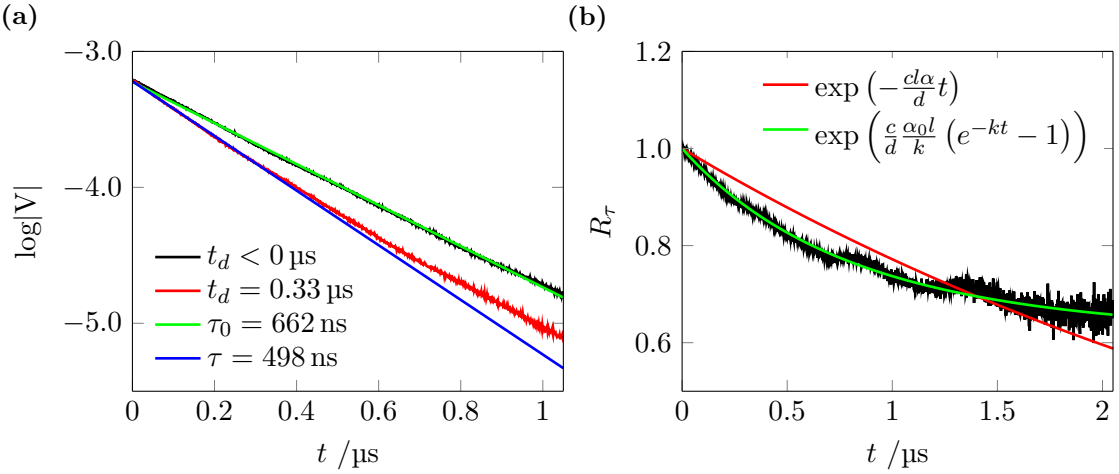


Figure 4.18: a) the ring-down decays measured for FAD at 680 nm in the presence (red, $t_\mathrm{d} = 0.33\,\mu s$) and absence (black, $t_\mathrm{d} < 0\,\mu s$) of photoexcitation ($\tau = 498\,\mu s$ and $662\,\mu s$, respectively). V is the voltage recorded on the oscilloscope. The deviation from single exponential behaviour in the presence of photoexcitation is clear. b) the ratio of the two plots in a), fit assuming constant absorbance (red) and first order decay (green).

The ring-down times recorded for FAD at 680 nm and used to calculate the red $\Delta A(t)$ decay in Figure 4.12a) are shown in Figure 4.18a) as a log plot. The single exponential behaviour of the 'empty' cavity (shown in black) is clear from the good fit to a straight line (green, $\tau_0 = 662\,ns$). This is data recorded at negative pump-probe delay times, and there is no absorbance due to photoexcited species. The red line shows the ring-down decay for $t_\mathrm{d} = 0.33\,\mu s$, and the additional decay component from the short-lived triplet species can be seen as the deviation of the plot from a straight line fit shown in blue ($\tau = 498\,\mu s$), i.e.

biexponential behaviour.

The ratio of the two ring-down decays plotted in Figure 4.18a) is shown in Figure 4.18b). The red line is the best fit assuming a constant absorbance on this timescale (Equation 4.9), while the green line is a fit to the function given by Equation 4.12, where the absorber shows first order decay. Clearly, the latter more accurately describes the data, and from this fit a value for the decay parameter, k, and its initial absorbance, α_0, can be extracted.

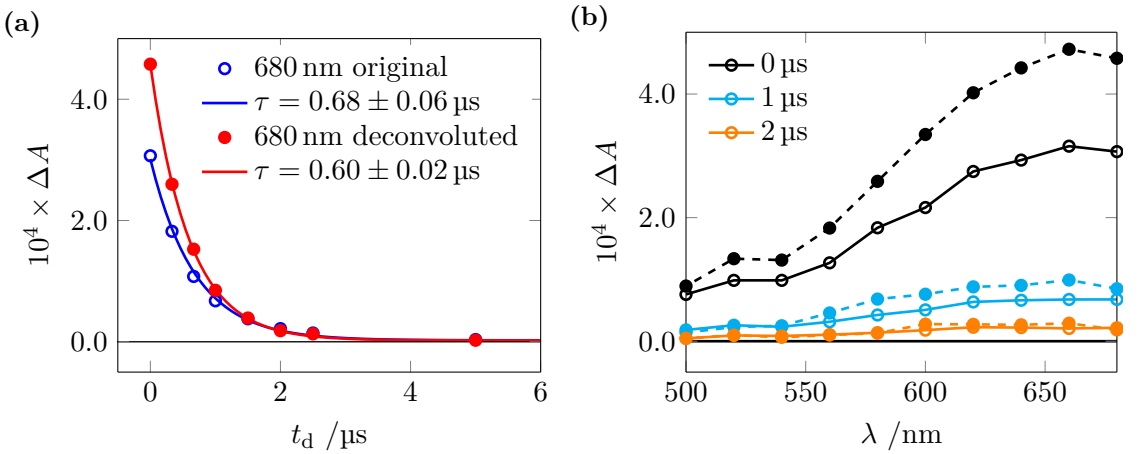


Figure 4.19: a) the effect of deconvolution on $\Delta A(t)$ at each pump probe delay for FAD at 680 nm, showing original data (blue, open) and deconvoluted data (red, filled). b) the effect of deconvolution (dashed, filled) on the $\Delta A(\lambda)$ spectrum of FAD at a variety of pump probe delay times. The difference is most pronounced at early timescales.

This fitting procedure is repeated for each wavelength and pump-probe delay time, deconvoluting the effects of a fast first-order absorbance decay from the inherent ring-down time response of the cavity. Shown in Figure 4.19a) is the original decay (blue, open) and the deconvoluted data (red, filled). The most striking difference is that the absorbance is underestimated without taking the effects of convolution into account, although this effect is only significant at early times (the difference is negligible by 2 µs). The kinetics extracted from a fit to the adjusted data, however, are relatively unchanged (deconvoluted $\tau = 0.62 \pm 0.03$ µs vs $\tau = 0.68 \pm 0.06$ µs originally) and are equal within 95% confidence limits.

Figure 4.19b) shows the same procedure carried out spectrally, at a number of pump-probe delay times. In agreement with Figure 4.19a), the difference is only substantial at early timescales during which the ring-down time and decay rate are comparable – no difference is apparent in the 2 µs spectrum. The discrepancy is also most noticeable to longer wavelengths, where the rapidly decaying triplet absorbance is most intense.

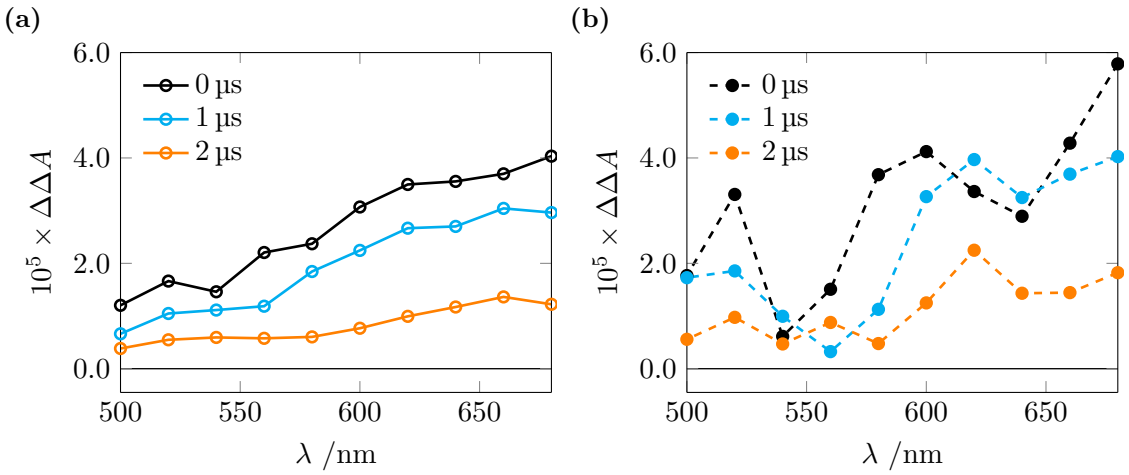


Figure 4.20: The $\Delta\Delta A(\lambda)$ spectrum of FAD, a) prior to, and b) following deconvolution of the ring-down time. The large uncertainties introduced reduces the effectiveness of the instrument in characterising MFEs.

Figure 4.20 shows the effect of deconvolution on the $\Delta\Delta A(\lambda)$ spectrum. While this procedure may be important for the extraction of absolute absorbances and precise decay constants, it should be avoided where possible in MFE studies, as the level of uncertainty introduced renders the temporal behaviour of field effects virtually unresolvable. That is to say the field effects themselves are real, but their absolute magnitude and kinetics are likely to be inaccurate.

The application of the ring-down time deconvolution procedure outlined by Brown et al. presented in this section demonstrates that it is only important for the extraction of precise absorbance values at early times (within the ring-down time of the cavity), for samples whose concentrations vary on these timescales. For long-lived species, the procedure is unnecessary as the only decaying signal comes from the ring-down itself, and

extracted absorbance values at all times are accurate. Even for species decaying rapidly, the extracted kinetics are in good agreement whether or not a detailed deconvolution procedure is applied in the data analysis. The significant uncertainty introduced into the data by such an approach means that only MFEs recorded with the highest SNR can be accurately characterised by CRDS in terms of their absolute magnitude and kinetics.

4.4 Conclusions and Future Directions

This chapter has reported on developments in the application of broadband CRDS (BBCRDS) to the study of magnetic field effects in biologically relevant systems, building on previously reported single wavelength work performed by the group.[19] Clear MFEs have been resolved in all systems studied with good SNR, with the instrument demonstrating the capability of measuring changes in absorbances on the order of 10^{-6}. The main improvement has been the introduction of a tunable OPO laser as the probe beam, introducing spectral resolution into an already powerful technique. The monochromatic variant had previously been shown to offer significant sensitivity gains over its single-pass TA analogue on small volumes of dilute samples, while using much reduced photoexcitation powers. A procedure deconvoluting combined decay signals due to the probe ring-down and rapidly decaying concentrations of absorbing species has also been demonstrated, and while it is effective in improving the accuracy of extracted absorbances at early times, it appears to have little effect on the measurement of kinetic parameters (in this example).

Recent, and ongoing, work in the group has harnessed these impressive instrument capabilities for the MFE studies of synthetic 'maquette' model systems of cryptochrome protein photochemistry. Here the timescales can be much shorter than one microsecond and the deconvolution procedure outlined here will need to be fine-tuned to provide the greatest possible insight into the new data.

Although this technique has been presented as 'broadband', and the final result is a spectrum spanning hundreds of nanometres, it can only be achieved in a time-consuming

step-wise manner by scanning the frequency of the probe laser. For the characterisation of previously unstudied systems it can be tedious to achieve sufficiently high resolution to permit worthwhile global analysis, with experiments running to multiple hours in length. As well as leading to prohibitively long experimental time for high resolution studies, this can be particularly inconvenient for systems which are highly sensitive to photodegradation (such as the cryptochromes or maquette samples of current interest). Different wavelengths will be probed with different quantities of intact protein surviving, leading to artefactual effects in the data further complicating the analysis. Furthermore, high cavity finesse only has a finite lifetime at low-temperature as the cell alignment can change and, despite best efforts, a film of condensation inevitably forms on the cell windows. The faster an experiment can be performed the better, both for the quality of the data and the longevity of photosensitive samples. For each additional wavelength that is probed per photoexcitation pulse, the fewer high energy photons the sample will be subjected to during an experiment without sacrificing spectral resolution. A more powerful instrument would be one in which all wavelengths were collected simultaneously.

While this is challenging for a CRDS-based instrument due to the need to extract and distinguish multiple ring-down times at each wavelength simultaneously, it is much more achievable without the need for prohibitively expensive equipment by using a CW cavity-based variant, cavity enhanced absorption spectroscopy (CEAS). However, the much improved spectral resolution that can be achieved by combining a continuous, spectrally broad probe laser with CEAS detection comes at the expense of microsecond time resolution. Broadband CEAS (BBCEAS) using a white-light supercontinuum radiation source as the probe beam to provide simultaneous spectral coverage over hundreds of nanometres, without sacrificing the high sensitivity offered by an optical cavity necessary for successful MFE studies, is the subject of the next chapter.

Chapter 5

BBCEAS Studies of MFEs in Biologically Relevant Systems

5.1 Introduction

This chapter introduces the first of the cavity-enhanced absorption spectroscopy (CEAS)-based variants developed by our group for the study of magnetic field effects exhibited by radical recombination reactions. As introduced in Chapter 2, CEAS was initially developed in the gas phase, and, in contrast to CRDS, measures the integrated intensity of light escaping from a continually pumped optical cavity in order to measure low absorbances with high sensitivity. More recently, it has been successfully applied in solution,[164,184,190,236] where the introduction of scattering losses associated with a condensed-phase sample and the cell used to constrain it reduces the sensitivity of the instrument in comparison to that achievable in the gas phase. Typically, CEAS is performed with a narrow bandwidth, monochromatic laser source to achieve efficient coupling into the cavity mode structure. In the liquid phase, where absorption profiles are homogeneously broadened and can span hundreds of nanometres, a light source with wider spectral coverage is required and careful matching is not as important.

The work reported in this chapter uses a high intensity white light supercontinuum radiation (SCR) source as the probe beam in a broadband CEAS (BBCEAS) variant. The result is an instrument capable of detecting very small changes in absorbance across the entire visible spectrum simultaneously with the enhanced sensitivity (and high SNR) afforded by an optical cavity. The new instrument is applied to the study of MFEs in both chemical model systems and real biological protein samples, including an animal cryptochrome protein. In the former case, changes in absorbance as low as 1×10^{-7} can be detected if coupled with magnetic field modulation. In the latter case, although the experiments are more challenging, a MFE has been successfully detected in an animal cryptochrome protein from the *Drosophila melanogaster* fruit fly. This was the first such demonstration of an animal protein exhibiting a response to an external magnetic field, and the large improvement in sensitivity meant that BBCEAS succeeded where traditional single-pass absorption techniques had previously failed. These cryptochromes are hypothesised to play a key role in animal magnetoreception, and this is a key piece of evidence in the search for the underlying physical mechanisms that govern this fascinating phenomenon (see Chapter 1).

In the previous chapter a BBCRDS instrument, using a tunable pulsed OPO laser as the probe beam, was successfully used to measure spectrally and temporally resolved MFEs in a range of relevant systems. The major shortcoming of this technique was identified as the need to scan the frequency of the probe beam to build up the spectral information, rather than it being available in a single shot. The principal disadvantage of an instrument acting in such a stepwise manner is increased experimental duration; the associated challenges of maintaining good cavity alignment and finesse have already been discussed, particularly during low temperature protein studies. More crucially the sample is subjected to a greater number of high energy photons from the pump laser providing photoexcitation. As one of the main motivations behind introducing cavity enhanced detection is the ability to use much gentler photoexcitation conditions on the

photosensitive cryptochrome samples of interest, this is an obvious limitation.

BBCEAS provides the means to acquire the entire spectrum in a single shot (or more accurately a single integrated CCD exposure), lasting on the order of milliseconds. Subsequently, the only determinant of experimental duration is the amount of averaging required to resolve the effect of interest within the desired signal-to-noise. The increased spectral coverage, reduced experimental time and reduced photoexposure of the sample comes at the expense of temporal resolution. The BBCEAS instrument is essentially a CW technique, and the millisecond time windows required for signal integration preclude it from following radical pair kinetics occurring on the order of microseconds, routinely accessible by both CRDS and single-pass TA.

The work presented here is further development of previous studies performed in the group, particularly those performed at single wavelengths reported elsewhere.[18] Some of the proof-of-principle work in this chapter has previously been reported.[142] The results of the *Drosophila melanogaster* cryptochrome protein study shown in Section 5.8.2 is the subject of a new communication (in preparation). All of the data in this thesis were recorded by the author, with the exception of the TA data on the *Dm*Cry sample in Section 5.8.2 (recorded by Dr Kevin Henbest and Dr Erik Schleicher) included for comparison.

5.2 Experimental

5.2.1 BBCEAS experimental set-up

The BBCEAS instrument is shown in schematic form in Figure 5.1. The light source used as the probe beam is a broadband supercontinuum radiation (SCR) source, producing a brilliant white output initially from 455–2000 nm (NKT, Koheras, SuperK Power Blue). It is spectrally filtered using a passive acousto optic tunable filter (AOTF) and a hot mirror to remove the IR components, leaving a spectral output covering the entire visible region ($455 < \lambda < 800$ nm). Following a component failure and subsequent repair, the output

was limited to $\lambda > 478\,\text{nm}$ only. The AOTF can be used to limit the output to a single wavelength for the safe alignment of the optical cavity. The fibre output is then swapped back to the full spectral output while maintaining optimal alignment of the instrument.

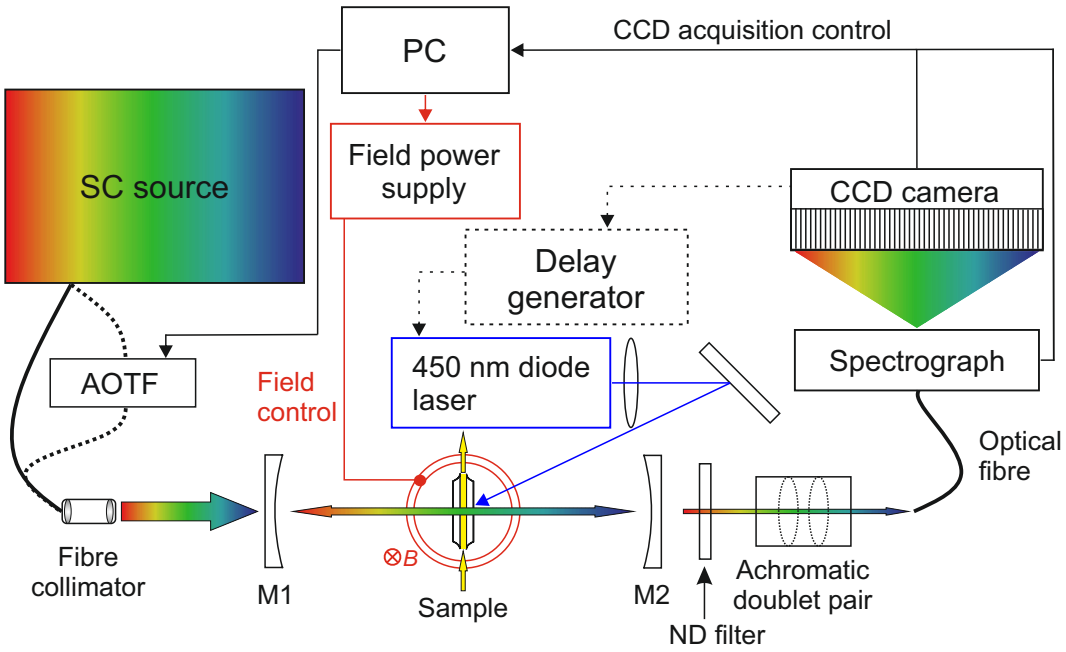


Figure 5.1: A schematic representation of the BBCEAS instrument used in this work. The probe beam is provided by a white-light SCR source and sample photoexcitation is provided by a CW 450 nm diode laser. The optical cavity is formed between two highly reflective mirrors (M1, M2) separated by 20 cm. A pair of Helmholtz coils (red concentric circles) are used to apply a homogeneous magnetic field to the sample. The dashed lines indicate a delay generator, which is used for the photoexcitation modulation studies in Section 5.9. All other instrument control and timings are provided by the PC.

The probe beam is delivered via optical fibre through the back of the cavity input mirror (M1). The sample cell (Hellma, 165-QS, UV-quartz, 1 mm pathlength, see Section 3.6) is mounted at the centre of the optical cavity on a goniometer-rotation stage arrangement, which allows alignment of the cell optical surfaces at normal incidence to the cavity axis. As such, all reflections are constrained within the stable optical cavity (see Section 2.3.1). The Hellma cell is constructed with a jacket around the sample, which permits temperature control via the flow of coolant. This is used to perform the low temperature

protein studies presented in Section 5.8. All model system samples, which are available in large quantities, are flowed through the cell during an experiment to replenish the probed volume and guard against the build up of undesirable photoproducts. The slow rate of $0.25\,\mathrm{ml\,min^{-1}}$ is chosen to minimise the noise introduced by flow based on the Allan deviation studies performed in Section 3.8.2. The optical cavity itself is formed between two highly reflective broadband coated mirrors (Layertec, $R = 99.85$–99.98%, $r_\mathrm{c} = 0.5\,\mathrm{m}$).

The sample cell is surrounded by a pair of home-built magnetic field coils (diameter $= 20\,\mathrm{cm}$)[A] in a Helmholtz arrangement, in order to apply homogeneous magnetic fields at the position of the sample. The intensity of the field is varied by applying different currents through the coils using a custom-made power supply,[A] whose output is controlled via a PC running custom-written C++ software.[B] This program is also responsible for synchronising the CCD acquisition with the field and collecting the data.

Continuous photoexcitation is provided by a blue 450 nm diode laser with a narrow emission band (*ca.* 1 nm, max. power = 35 mW, see Section 3.4.2), which is focused through a 1 m focal-length lens and directed into the sample cell at a shallow angle by a turning mirror. In the experiments presented in Section 5.9 the output is modulated by a TTL output from a delay generator (SRS, DG645) taking an external trigger signal from the 'Fire' port of the CCD camera for synchronisation.

Light escaping through the rear cavity mirror (M2) is collected by an achromatic doublet pair (Thorlabs) and focused onto an optical fibre (Thorlabs, 400 µm core, NA 0.39), through which it is transmitted to the spectrograph (Andor Technology, SR-303i) and dispersed into its constituent wavelengths onto a CCD camera (Andor Technology, Newton). The entrance port of the spectrograph has a variable slit width, which can be set to compromise between high wavelength resolution (narrow slit) and high light intensity throughput (wide slit). For the studies presented in this chapter, there is plenty of light available for the sensitive CCD camera while high wavelength resolution is not

[A] Neville Baker, PTCL workshops
[B] Jonathan Storey, Timmel Group

required due to the broadened nature of the absorbance bands in solution. A value of 100 µm is typically used as a compromise, although this could be increased in future with little reduction in wavelength resolution if it is desired to reduce the amount of probe light incident on the sample from the probe beam using a neutral density filter. The spectrograph grating (150 lines /mm) disperses the white light horizontally onto the CCD camera (1024 x 256 pixels). At these settings, each pixel represents a spectral resolution of approximately 0.6 nm. All acquisitions are performed using full vertical (spatial) binning of the charge on the CCD array before readout. A neutral density filter is positioned after the cavity to prevent saturation of the CCD camera.

5.2.2 Measuring MFEs

To perform MFE studies, the light intensity on the CCD is recorded while the sample simultaneously undergoes continuous photoexcitation and magnetic fields of varying strengths are applied. The PC synchronises the CCD acquisition with the application of the magnetic field, enabling data acquisition with magnetic field alternately on and off at a high repetition rate. This field modulation offers a pseudo lock-in detection method, and mitigates against the effects of long-term drift exhibited by the relatively unstable SCR source probe beam intensity, exhibited in Figure 3.14b). The pulse sequence is shown schematically in Figure 5.2. There are two parameters which must be set in order to accurately detect field effects: the exposure time and the field delay.

The length of time the CCD camera is sensitive to light for (and integrates the signal over) is the exposure time, which is set in accordance with the Allan variance calculations outlined in Section 3.8.2. This is also affected by the flow rate as discussed above. Therefore, in the interest of reducing the experimental time and thereby the amount of photoexcitation the sample is subjected to, the exposure time is set to 10 ms for all studies presented here. Although this may not be ideal in terms of the Allan deviation measurements (performed with water in the sample cell, Chapter 3), the resulting signal-to-noise

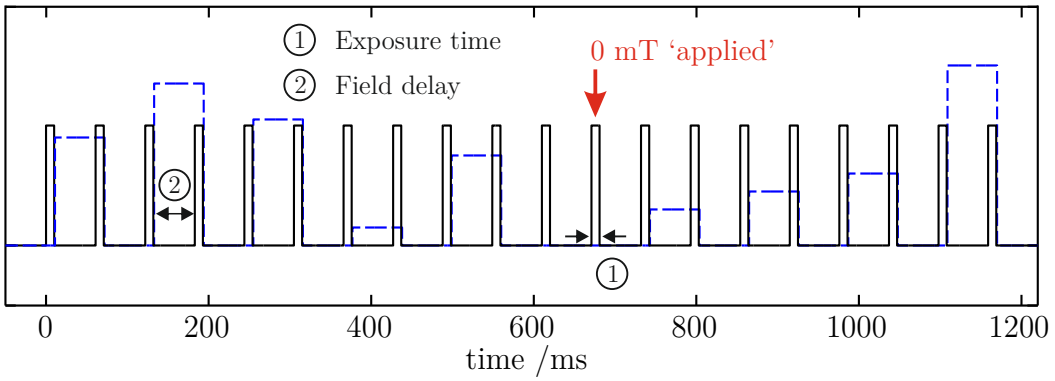


Figure 5.2: A schematic representation of the pulse sequence used to perform MFE studies using the BBCEAS instrument. The two key timings for the accurate measurement of a MFE are the exposure time and field delay, both set on the acquisition software (see text for discussion).

is sufficiently high in the model system studies.

For the protein studies there are more pressing considerations, mostly inherent to the samples themselves. The lack of sufficient sample volume for flow means the build up of photodegradation products adds an additional complication to the determination of an optimum integration time. The high amount of optical scatter present in the protein samples, particularly those which require glycerol for stabilisation, is not conducive to maintaining a high finesses as it is difficult to constrain the light entirely within the cavity. The requirement for proteins to be studied at low temperatures approaching the freezing point of water can also lead to the formation of a highly scattering layer of condensation on the cell windows. In an effort to prevent this, dry air is blown at the cell windows, although this introduces mechanical noise in the form of vibrations (Figure 3.16b).

The field delay is added to provide time for the field to ramp up to the desired value (which has been measured to take less than 10 ms), and allow the sample to respond to establish a new equilibrium. In the majority of the following studies the delay is set to 50 ms. The field is switched immediately after the exposure time has elapsed. The repetition rate of the experiment therefore is equal to the inverse of the sum of the exposure time and field delay. For the typical values used in this work (10 ms and 50 ms

respectively), that leads to an acquisition rate of *ca.* 17 Hz.

The alternating field-off, field-on acquisition sequence is apparent from Figure 5.2. The change in signal upon field application is calculated from the two surrounding field-off acquisitions in an effort to mitigate the effects of long-term drift in the signal. As any individual field-off reading can be used as both the before and after references for its surrounding field-on readings only $2n + 1$ acquisitions are required to produce a MARY curve consisting of n field steps, rather than the $3n$ that might be assumed necessary for such averaging. It is advantageous to reduce both the exposure time and the field delay as far as possible while still allowing time for sample response and data transfer.

In the simulated pulse scheme shown in Figure 5.2, the field can be thought of as being varied from 0 to 9 mT. Although many zero field readings are taken as a result of the field modulation, there is also a 0 mT field 'applied' on each MARY sweep (labelled in red), which can lead to an offset from zero when all the data is averaged together depending on the presence of long-term drift in the system.

As shown in Section 2.5, the absorbance of a sample can be measured by BBCEAS and is calculated as:

$$\begin{aligned} A(\lambda) &= \frac{1}{\ln(10)} \left(\frac{I_0(\lambda)}{I(\lambda)} - 1 \right) \left(1 - R_{\text{eff}}(\lambda) \right) \\ &= \frac{1}{\ln(10)} \left(\frac{I_0(\lambda)}{I(\lambda)} - 1 \right) \frac{1}{\text{CEF}(\lambda)}, \end{aligned} \tag{5.1}$$

where A is the single-pass absorbance value at each wavelength (λ), I_0 is the light intensity transmitted by an empty cavity (i.e. one containing water in the sample cell), I is the intensity transmitted by a cavity containing the absorbing species of interest, and R_{eff} is the effective mirror reflectivity taking account of all the background losses inherent to the cavity.

Therefore, the absorbance of the ground state of the protein solution studied can be

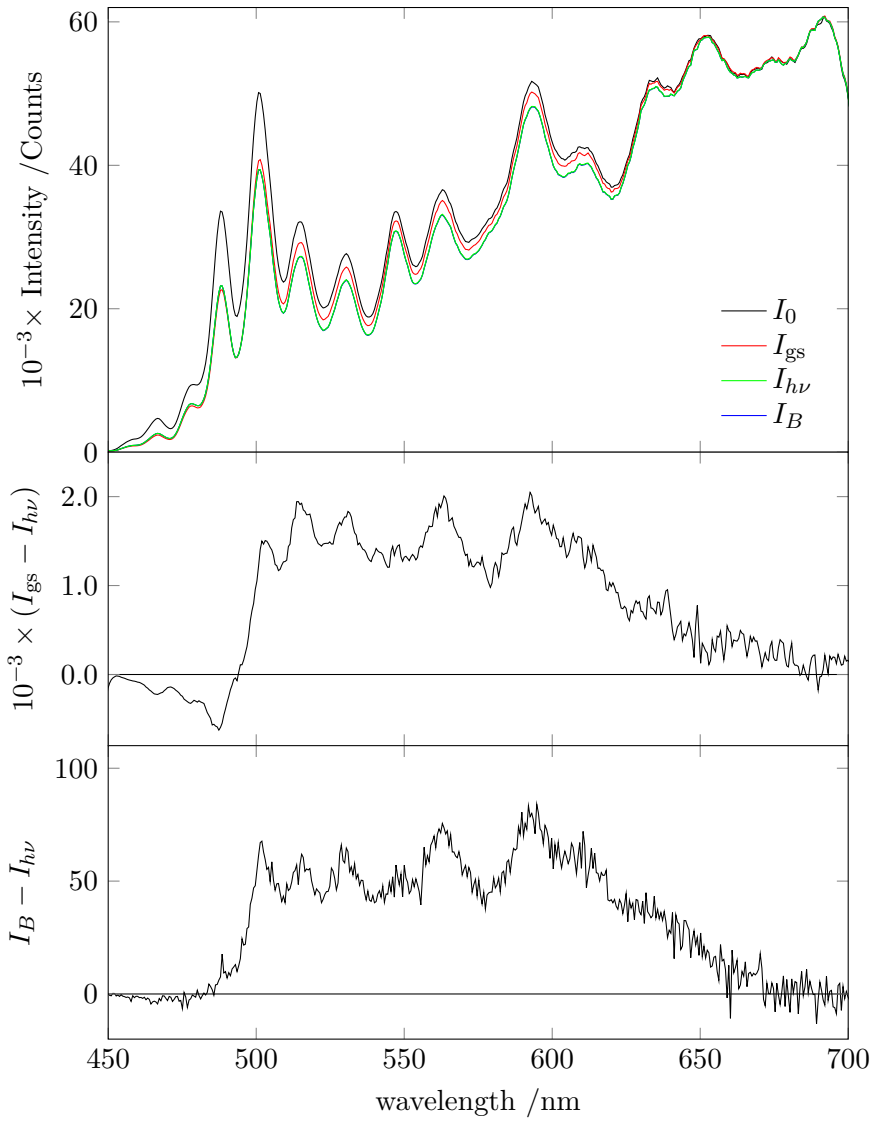


Figure 5.3: Example raw CCD spectra (minus the dark counts) for calculating MFEs from BBCEAS. The I_0 (water) spectrum is needed (along with the CEF, not shown) to convert intensities into absorbances. Introduction of the sample leads to a reduction in transmitted light intensity (I_{gs}, red) which drops further upon photoexcitation ($I_{h\nu}$, green) (*ca.* 2000 counts $500 < \lambda < 650\,\mathrm{nm}$, shown in the middle panel), due to the production of radicals. There is a slight increase in transmitted intensity below 500 nm due to the accompanying ground state bleaching. For a triplet-born SCRP, application of a field leads to a further small reduction in transmitted intensity (*ca.* 50 counts, shown in the bottom panel), which needs multiple averaging to be detected, even with the high SNR of a cavity-based instrument. On this scale $I_B(\lambda)$ completely overlays the $I_{h\nu}$ spectrum.

expressed as:

$$A_{\mathrm{gs}}(\lambda) = \frac{1}{\ln(10)\mathrm{CEF}(\lambda)}\left(\frac{I_0(\lambda)}{I_{\mathrm{gs}}(\lambda)} - 1\right), \tag{5.2}$$

and that of the protein solution in the presence of blue-light photoexcitation as:

$$A_{h\nu}(\lambda) = \frac{1}{\ln(10)\mathrm{CEF}(\lambda)}\left(\frac{I_0(\lambda)}{I_{h\nu}(\lambda)} - 1\right), \tag{5.3}$$

where I_{gs} and $I_{h\nu}$ are the intensities transmitted by the protein sample in the absence and presence of photoexcitation, respectively. These raw intensity spectra are shown in Figure 5.3, along with I_0.

The differential absorbance spectrum, $\Delta A(\lambda)$, is defined as the difference in absorbance signals with and without photoexcitation and is given by:

$$\begin{aligned}\Delta A(\lambda) = A_{h\nu}(\lambda) - A_{\mathrm{gs}}(\lambda) &= \frac{1}{\ln(10)\mathrm{CEF}(\lambda)}\left[\left(\frac{I_0(\lambda)}{I_{h\nu}(\lambda)} - 1\right) - \left(\frac{I_0(\lambda)}{I_{\mathrm{gs}}(\lambda)} - 1\right)\right] \\ &= \frac{I_0}{\ln(10)\mathrm{CEF}(\lambda)}\left(\frac{I_{\mathrm{gs}}(\lambda) - I_{h\nu}(\lambda)}{I_{h\nu}(\lambda)I_{\mathrm{gs}}(\lambda)}\right).\end{aligned} \tag{5.4}$$

Similarly, the absorbance in the presence of both photoexcitation and an applied magnetic field can be defined as:

$$A_B(\lambda) = \frac{1}{\ln(10)\mathrm{CEF}(\lambda)}\left(\frac{I_0(\lambda)}{I_B(\lambda)} - 1\right), \tag{5.5}$$

where I_B is the light intensity transmitted by the photoexcited sample in the presence of a magnetic field, and hence the differential absorbance in an applied field given by:

$$\begin{aligned}\Delta A_B(\lambda) = A_B(\lambda) - A_{\mathrm{gs}}(\lambda) &= \frac{1}{\ln(10)\mathrm{CEF}(\lambda)}\left[\left(\frac{I_0(\lambda)}{I_{B(\lambda)}} - 1\right) - \left(\frac{I_0(\lambda)}{I_{\mathrm{gs}}(\lambda)} - 1\right)\right] \\ &= \frac{I_0}{\ln(10)\mathrm{CEF}(\lambda)}\left(\frac{I_{\mathrm{gs}}(\lambda) - I_B(\lambda)}{I_B(\lambda)I_{\mathrm{gs}}(\lambda)}\right).\end{aligned} \tag{5.6}$$

The wavelength resolved action spectrum, $\Delta\Delta A(\lambda)$, is the change in absorbance signal

induced by the external field and can be defined as:

$$\begin{aligned}\Delta\Delta A(\lambda) &= \Delta A_B(\lambda) - \Delta A(\lambda) \\ &= \frac{1}{\ln(10)\mathrm{CEF}(\lambda)}\left[\left(\frac{I_0(\lambda)}{I_{B(\lambda)}} - \frac{I_0(\lambda)}{I_{gs(\lambda)}}\right) - \left(\frac{I_0(\lambda)}{I_{h\nu(\lambda)}} - \frac{I_0(\lambda)}{I_{gs(\lambda)}}\right)\right] \\ &= \frac{I_0(\lambda)}{\ln(10)\mathrm{CEF}(\lambda)}\left(\frac{I_{h\nu}(\lambda) - I_B(\lambda)}{I_B(\lambda)I_{h\nu}(\lambda)}\right).\end{aligned} \tag{5.7}$$

The MFE can be defined as the percentage change induced by the field on the change induced by the photoexcitation (e.g. the percentage change in the radical population):

$$\begin{aligned}\mathrm{MFE}(\lambda) &= \frac{\Delta\Delta A(\lambda)}{\Delta A(\lambda)} \times 100 \\ &= \frac{I_{\mathrm{gs}}(\lambda)}{I_B(\lambda)}\left(\frac{I_{h\nu}(\lambda) - I_B(\lambda)}{I_{\mathrm{gs}}(\lambda) - I_{h\nu}(\lambda)}\right) \times 100.\end{aligned} \tag{5.8}$$

Writing the MFE in this way elucidates some interesting points. It should be noted that it is independent of CEF and therefore day-to-day alignment – this will affect the quality of the data (via SNR) but not the magnitude of the measured field effect. It also means that determination of an accurate MFE value can be achieved without the calibration procedure outlined in Section 3.7.1, albeit this is a straightforward process and circumventing it does little to reduce experimental complexity.

Interestingly, and perhaps more unexpectedly, it is also independent of the empty cavity intensity, I_0. This means that if dynamic range is a problem (for instance if the sample leads to significant light scattering and I_{gs} is strongly reduced compared with I_0), the CCD signal can be increased by opening the ND filter to increase light transmission to the detector and SNR can thus be improved. Following this approach would of course preclude the calculation of any intermediate values (i.e. A, ΔA or $\Delta\Delta A$) but should be considered in extreme circumstances when dealing with the most challenging protein samples (*Dm*Cry for instance). It is important to note that, in such cases, the CEF calibration is no longer applicable due to the large degree of scattering introduced by the

protein sample, and so these intermediate values would be of limited applicability anyway.

Throughout the remainder of this chapter, some data will be plotted as ΔA_{r} and $\Delta\Delta A_{\mathrm{r}}$. The 'r' subscript indicates that these are the 'raw' BBCEAS observables, proportional to absorbance but not yet calibrated by the ln(10)CEF factor.

5.3 BBCEAS Study of the FMN/HEWL Model System

5.3.1 Absorbances

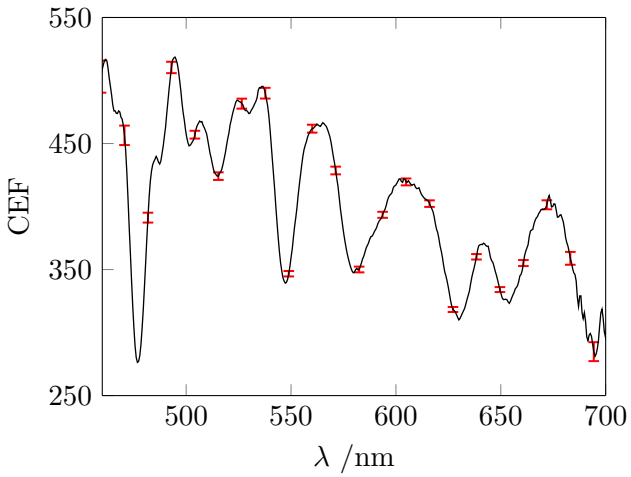


Figure 5.4: The Cavity Enhancement Factor (CEF) used to calibrate all of the data in this section to absolute absorbances, following the procedure outlined in Section 3.7.1. Error bars show one standard deviation.

Figure 5.4 shows the cavity enhancement factor (CEF) profile used to calibrate the data presented in this section, following the method described in Section 3.7.1. The CEF indicates a measure of the sensitivity gain provided by the cavity over a single-pass measurement, and can be interpreted as the effective number of passes a photon makes through the sample. However, for reasons described in Section 2.5.2, this increased interaction does not mean that the SNR increase between the single-pass and cavity variant of a similar experiment is equal to the CEF. Indeed, due to the lower absolute transmission of light to the detector as a result of using highly reflective cavity mirrors, the SNR increase

can be relatively modest (*ca.* 22 if $R = 0.999$ and shot-to-shot noise is dominant). The dips in the CEF profile correspond to regions where the light transmission is highest and the reflectivity of the cavity mirrors is lowest. The raw BBCEAS spectra shows false structure due to these features, which are shown to be successfully removed upon calibration to absolute absorbance values.

Figure 5.5a) shows the spectrum of a 1 µM FMN 500 µM HEWL model system sample measured by BBCEAS. The spectrum is shown in the absence (black) and presence (blue) of 10 mW 450 nm photoexcitation. The increased absorbance above 500 nm is due to the production of $FMN^{\bullet-}$ and $TrpH^{\bullet+}$ radical species, which between them comprise the magnetically sensitive SCRP of interest. The drop in absorbance below 500 nm reflects the corresponding ground state bleaching.

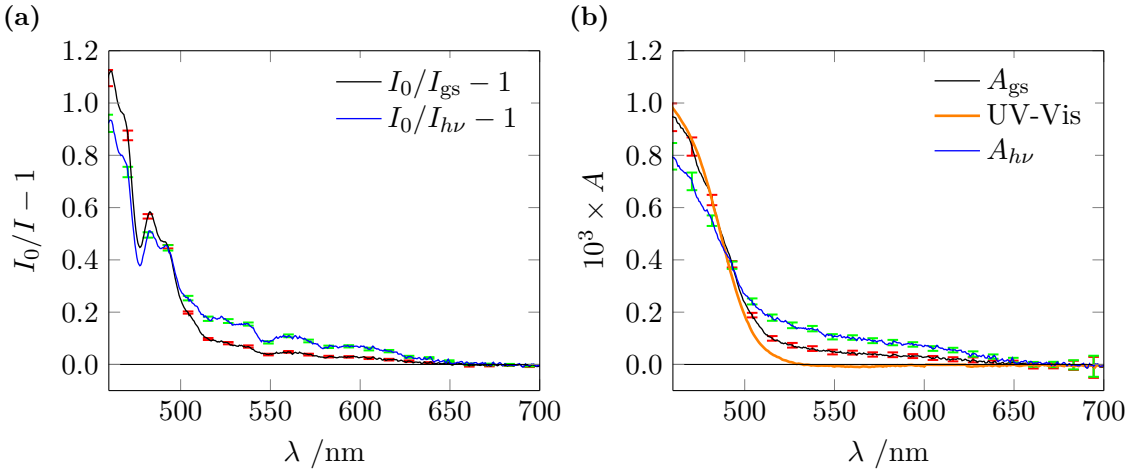


Figure 5.5: Effect of 10 mW 450 nm photoexcitation on a) the uncalibrated BBCEAS observable and b) the absorbance of a 1 µM FMN 500 µM HEWL sample. Note that calibration using the CEF in Figure 5.4 removes the false structure around 480 nm and 550 nm from the uncalibrated spectrum. The UV-Vis spectrum is for 10 µM FMN, scaled to account for the pathlength and concentration differences. 1 µM FMN is approaching the detection limit of the instrument and its recorded spectrum is very noisy. Error bars show one standard deviation, propagated through from 500 (10 ms) acquisitions of I_0, I_{gs} and $I_{h\nu}$, recorded at 100 Hz.

The error bars show one standard deviation of 500 acquisitions of the individual intensities (I_0, I_{gs} and $I_{h\nu}$), combined and propagated through the calculation of the BBCEAS

observable. The increase in uncertainty towards the blue indicates the lower flux of light incident on the CCD detector. This is due to the combined effect of lower SC source intensity output in this region (Figure 5.3) and high flavin ground state absorbance reducing the cavity throughput still further. The error bars increase in size on calibration to absorbance as the uncertainty in the CEF value is propagated through.

The success of the calibration procedure is demonstrated by the excellent agreement of the ground state absorbances shown in Figure 5.5b) measured by BBCEAS (black) and UV-Vis (orange), appropriately scaled to account for the difference in pathlength.

The discrepancy above 500 nm is expected and can be rationalised by considering that low levels of blue light ($\lambda < 500$ nm) circulate in the cavity from the broadband SC source probe beam. This provides weak on-axis sample photoexcitation to produce a low steady-state background concentration of radical species, even without the photoexcitation from the diode laser.

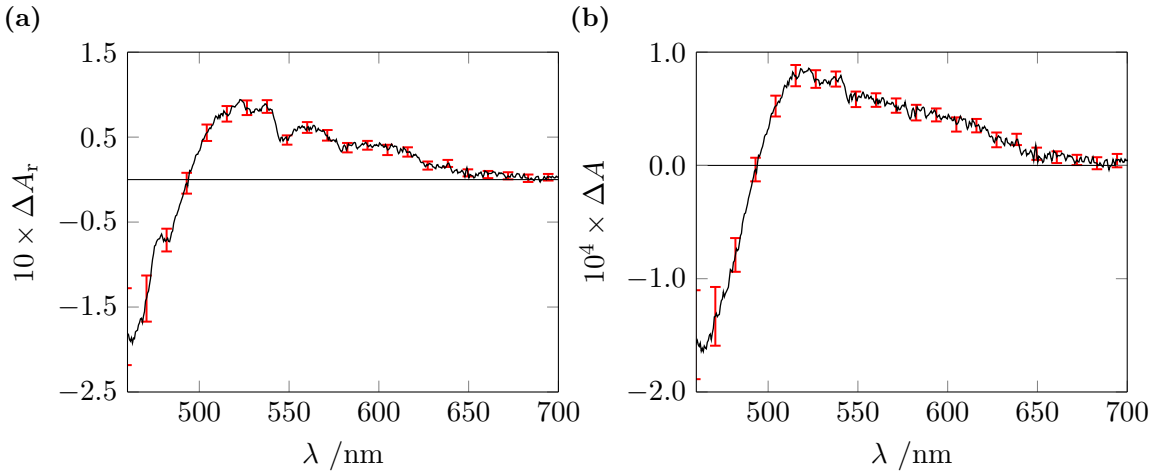


Figure 5.6: Difference spectra of 1 µM FMN 500 µM HEWL measured by BBCEAS upon 10 mW 450 nm photoexcitation, simultaneously demonstrating ground state bleaching (< 500 nm) and radical production (> 500 nm). a) uncalibrated, in terms of ΔA_r (see text for definition), and b) calibrated to absorbance. Error bars represent one standard deviation of the mean of 500 acquisitions.

Figure 5.6a) shows the $\Delta A_r(\lambda)$ spectrum obtained from taking the difference in spectra recorded with and without photoexcitation. The increase above 500 nm can be assigned

to the production of the radical species, while the ground state bleach is evident at shorter wavelengths. Figure 5.6b) shows the effect of calibrating this raw difference spectrum to an absolute absorbance value. The features around 480 nm and 550 nm disappear as the artefacts from the mirror reflectivity profile are removed, and the larger error bars result from propagation of the CEF uncertainty.

5.3.2 MFE action spectrum

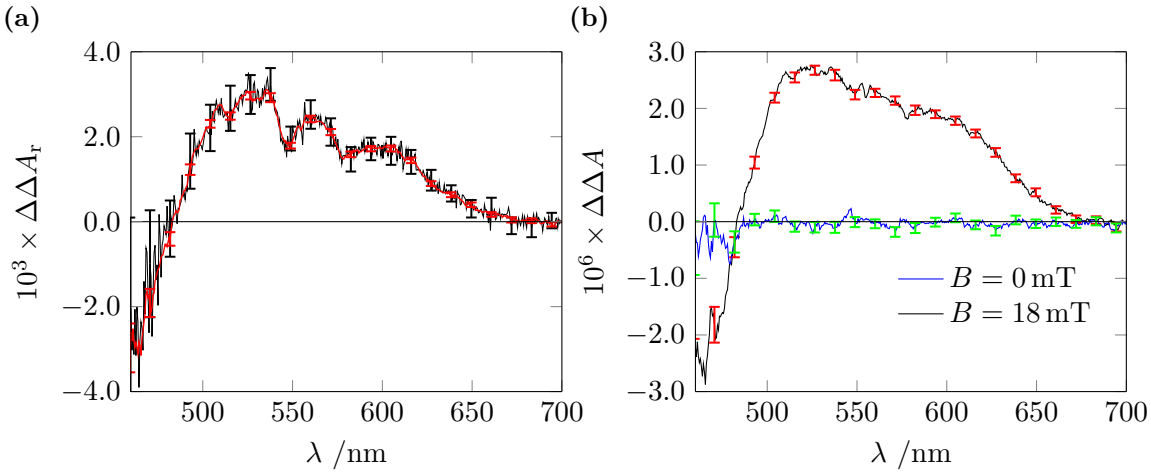


Figure 5.7: MFE action spectrum of 1 µM FMN 500 µM HEWL measured by BBCEAS, a) uncalibrated and b) calibrated, upon application of an 18 mT external field. a) Obtained from the average of 500 $B = 0\,\mathrm{mT}$ spectra from the experimental dataset. The red curve shows the result of a 5 pixel ($\approx 3\,\mathrm{nm}$) boxcar smoothing in the wavelength direction along with the resulting reduction in the standard error of the mean. b) Obtained by applying the CEF calibration to the smoothed data from a). Error bars represent one standard error of the mean of 500 measurements.

Figure 5.7a) shows the $\Delta\Delta A_r$ spectrum (see Equation 5.7 for definition) for the FMN/HEWL system. BBCEAS permits the simultaneous observation of the increase in radical population and decrease in ground state population expected for a triplet-born SCRP (see Section 3.3.1 for explanation). The change in the uncalibrated BBCEAS observable upon the application of an 18 mT magnetic field is plotted, with its characteristic false structure. Both unsmoothed (black) and smoothed (red, details in legend) data is

shown, along with the accompanying decrease in uncertainty.

Figure 5.7b) shows the calibration of the smoothed data, which will be used for the rest of the analysis, to an absolute absorbance difference on application of an external field. Clearly visible are the opposing responses of the ground state and radical absorbance regions, as more molecules are removed from the ground state population and trapped as free radicals. The increased noise in the ground state bleaching region is a result of low light transmission in this region, but also the fact that the radical absorbance band does not stop at 500 nm but extends to the blue. The 'ground state' region ($\lambda < 500\,\text{nm}$) therefore monitors two competing effects simultaneously.

The application of BBCEAS to these studies permits the monitoring and clear resolution of magnetic field induced changes in absorbances on the order of 1×10^{-6}, with uncertainties dipping below 1×10^{-7}. The change on 'applying' a 0 mT field is also shown (blue) to act as a negative control and also indicate the minimum detectable change in absorbance due to a field (2×10^{-7} for $\lambda > 500\,\text{nm}$, and 1×10^{-6} for $\lambda < 500\,\text{nm}$). The $\Delta\Delta A(\lambda)$ spectrum is a useful way of identifying the spectral contribution of a magnetically sensitive species to composite absorbance bands. For instance, the $FMN^{\bullet -}$ and $TrpH^{\bullet +}$ radicals can be seen to only absorb as far as 650 nm after which the action spectrum returns to zero. If other magnetically insensitive species were present in the $\Delta A(\lambda)$ spectrum with absorbance spectra extending above 650 nm, this would provide a powerful route to deconvolution of the relative contributions.

5.3.3 Percentage MFE spectrum

Figure 5.8a) shows the percentage MFE as a function of wavelength, calculated using Equation 5.8. In the radical region this is simply the percentage change in absorbance on application of a field. In the ground state region it is not quite so straightforward due to the overlapping radical and ground state absorbance bands. The flat region from $500 - 650\,\text{nm}$ indicates that there is only one magnetically sensitive species absorbing in

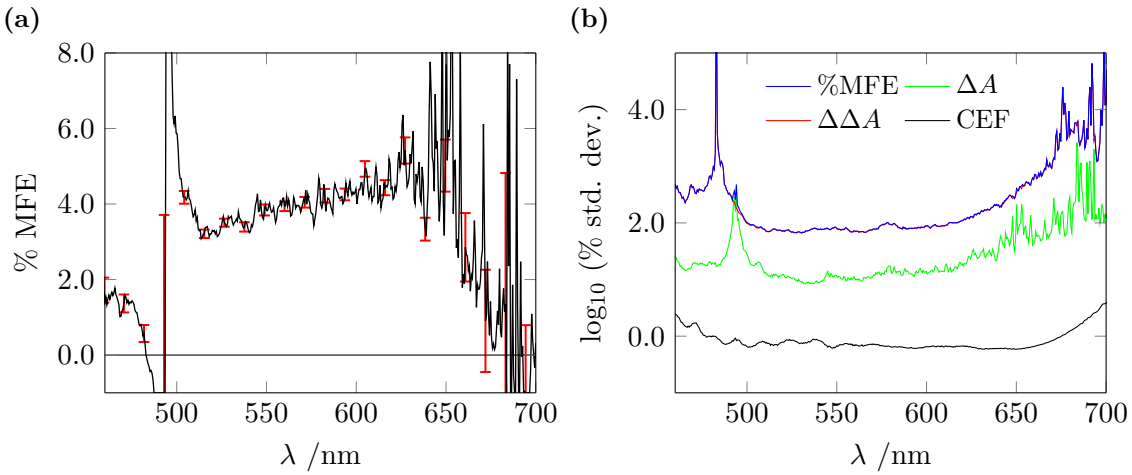


Figure 5.8: a) The percentage MFE spectrum of the 1 µM FMN 500 µM HEWL system at 18 mT, calculated from the smoothed data shown in Figures 5.6 and 5.7. Error bars represent one standard error of the mean of 500 measurements. b) The percentage standard deviations in the data used to calculate MFEs measured by BBCEAS. The final uncertainty in the MFE (blue) is dominated by the noise on the $\Delta\Delta A$ spectrum (red), with only a small additional increase from the ΔA contribution (green). Calibration using the CEF has a negligible effect as its associated uncertainty is smaller by at least an order of magnitude (black).

this region. The large discontinuity around 500 nm is a result of the $\Delta\Delta A(\lambda)$ and $\Delta A(\lambda)$ spectra passing through zero. The high amount of noise above 650 nm is due to the division of two vanishingly small signals.

Figure 5.8b) shows that the dominant uncertainty is in the $\Delta\Delta A$ data, due to taking the difference of two very small values. This dominates the final uncertainty in the percentage MFE value as addition in quadrature used in Gaussian error propagation lends a much greater weight to the largest uncertainty. When plotted on a log scale the uncertainties in percentage MFE and $\Delta\Delta A$ virtually overlay (blue and red, respectively), with only a very slight increase in the former due to the smaller uncertainty associated with the ΔA spectrum (green). The effect of introducing the small uncertainty associated with the CEF (black) upon absorbance calibration is negligible.

Introducing greater error into the final calculated MFE value can no longer be used as an excuse not to work up the data rigorously and calibrate to absolute absorbances. As

this practically only requires the acquisition of one extra spectrum (I_{dye}, see Section 3.7.1) it is no great demand of the experimental operator. The UV-Vis spectrum of the calibrant mix must be recorded regularly to ensure any degradation of the stored dye solution is taken into account.

5.3.4 Spectrally-resolved MFE surface plots

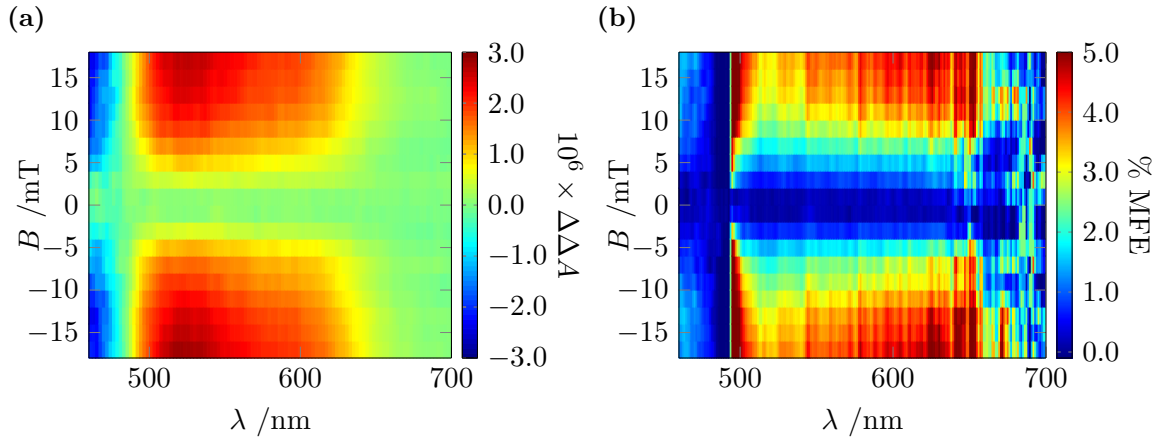


Figure 5.9: a) A 2-D surface plot of $\Delta\Delta A(\lambda, B)$, showing the effect of sweeping the strength of the external magnetic field on the absorbance signal measured by BBCEAS. Increasing the field leads to an increase in the concentration of radicals detected (500–650 nm), and a concomitant decrease in the flavin ground state absorbance (< 490 nm). b) 2-D surface plot of MFE(λ, B) obtained by dividing the $\Delta\Delta A(\lambda, B)$ surface in a) by the $\Delta A(\lambda)$ plot in Figure 5.6b). In both the ground state region (< 490 nm) and the radical region (500–650 nm) the surface is approximately flat, demonstrating the existence of a single magnetically sensitive species absorbing over these regions. Data is the average of 500 measurements at each field strength.

Figure 5.9a) shows a 2D-surface plot of the spectral response of the FMN/HEWL system to a range of external field strengths. Red indicates an increase in absorbance relative to the zero field case (here shown as pale green) and blue indicates a reduction. This is a powerful way to display the broadband capabilities of the BBCEAS instrument as the magnetic responses of both radical and ground state species can be monitored simultaneously. The red region clearly indicates the pure radical absorbance, increasing in proportion to the strength of the applied external field (see MARY schematic in Figure

1.6). The ground state field effect is visible as the dark blue regions below 480 nm, and is only resolvable at low flavin concentrations where the cavity throughput is high enough in this region for sufficient SNR. The symmetry of the field response around 0 mT confirms that in solution the direction of applied field makes no difference to the measured response (and that the field calibration is accurate).

Figure 5.9b) is a percentage MFE surface plot, obtained by dividing the $\Delta\Delta A(\lambda, B)$ surface in Figure 5.9a) by the $\Delta A(\lambda)$ plot in Figure 5.6b). The sharp discontinuity around 500 nm is where both the $\Delta A(\lambda)$ and $\Delta\Delta A(\lambda)$ plots pass through zero. The increased noise above 650 nm is due to the lack of field sensitive absorbance in this region (i.e. $\Delta A \to 0$). The ground state exhibits a 'positive' MFE (*ca.* 1%, pale blue), i.e. a negative response to a ground state bleach ($\Delta A(\lambda)$ and $\Delta\Delta A(\lambda)$ are both less than zero in this region). For the FMN/HEWL system at this pump power the MFE approaches a saturated value of 4%. The power dependence of these values are investigated and discussed in detail in Section 5.4.

5.3.5 MARY plots

Figure 5.10 shows the MFE of the FMN/HEWL system at a variety of field strengths (MARY plots, see Section 1.8.1 for details), averaged over a) primarily the ground state absorption region (460–475 nm) and b) the pure radical absorbance band (530–630 nm). The multiplexing advantages of BBCEAS are clear from the low uncertainties at each field point due to the Fellgett advantage (*ca.* $\pm 0.1\%$ on ΔA signals of less than 1×10^{-4}). The larger uncertainties in the ground state region have been discussed previously in terms of the lower SCR output intensity, high flavin ground state absorbance, and overlapping and opposing radical and ground state responses to a field. In this case they are also due to limited averaging over a relatively narrow wavelength window (15 nm *cf.* 100 nm for the radical region) due to the lack of spectral coverage from the supercontinuum source.

In equivalent experiments performed on solutions of pure FMN and HEWL (not shown)

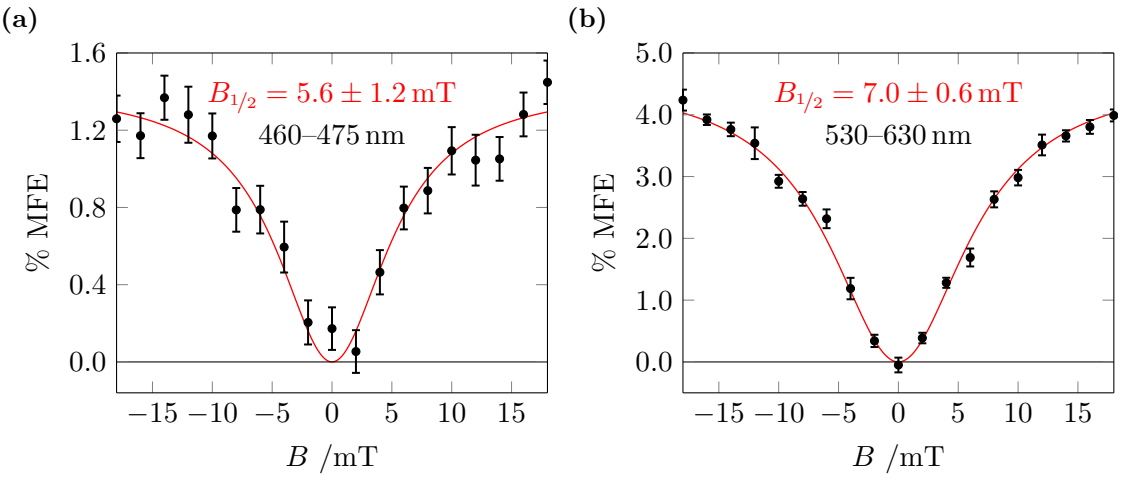


Figure 5.10: a) The MARY curve for the FMN/HEWL ground state absorbance region as a function of applied field strength, obtained by averaging Figure 5.9b) over 460–475 nm. Magnetic field response in this spectral region is challenging to measure, and only possible at flavin concentrations of less than *ca.* 10 µM. b) The MARY curve of the FMN/HEWL radical absorbance region as a function of applied field strength, obtained by averaging Figure 5.9b) over 530–630 nm. In both figures, the red line is the result of a Lorentzian fit to the data from which a $B_{1/2}$ value can be extracted (5.6 ± 1.2 mT for the ground state and 7.0 ± 0.6 mT for the radical). Uncertainties reflect the noise in the fitted data, and agree within error as expected for two probes of the same photocycle. Error bars show one standard error of the mean of 500 measurements.

no MFE is observed, confirming the requirement for a spin-correlated radical pair to be formed.

A Lorentzian curve is fitted to the data, and from this the characteristic $B_{1/2}$ value can be extracted. This is the field strength at which the MFE reaches half its maximum saturated value and is characteristic of the magnetically sensitive species which make up the radical pair. Using known hyperfine interactions, $B_{1/2}$ values can be predicted from the Weller equation.[138] In most cases the measured value is larger than predicted due to spin relaxation that is not taken into account by this theoretical model (S-T dephasing). The agreement (within mutual uncertainties) between the extracted $B_{1/2}$ values from the ground state region and radical region is expected as they are both probes of the same flavin/tryptophan photocycle (see Figure 3.5). They are also satisfyingly close to those measured by other cavity techniques used in this thesis, as well as a sensitive prompt-

fluorescence instrument also developed in the group.[133]

5.4 Power Dependence of the MFE in FMN/HEWL

5.4.1 Experimental results

For a flavin-based SCRP model system, continuous photoexcitation can lead to interesting effects on the magnitude of the measured magnetic field effect, which is no longer solely a characteristic of the identity of the radical pair partners. Changes in the position of equilibrium, due to the myriad of competing photochemical processes lead to variations in the size of the effect induced by an external field. In this section, the effects of steadily increasing the 450 nm photoexcitation power is investigated, and a detailed photochemical scheme simulated in order to gain insight into the hidden complexity of these reactions.

Figure 5.11a) shows the $\Delta A(\lambda)$ spectra for the FMN/HEWL system for a variety of photoexcitation powers (colours shown in legend). Here a 10 µM FMN concentration is selected so that a larger range of laser powers can be used while maintaining good SNR. The increase in the proportion of the molecules transferred from the ground state to the free radicals is clear from the increasing size of the radical absorbance signal and ground state bleach. The power dependence is shown more clearly in Figure 5.11b) for a fixed wavelength ($\lambda = 550$ nm) near the peak of the radical absorbance. At low powers there is a sharp increase in absorbance with pump power, but this appears to approach saturation at around 15 mW.

The change in the absorbance spectrum on magnetic field application (18 mT) is shown in Figure 5.11c) for the same photoexcitation powers. A general increase at low powers is seen, as would be expected from the increasing ΔA signal in Figure 5.11a) if the percentage MFE remained constant. The $\Delta\Delta A$ is plotted as a function of pump power (at 550 nm) in Figure 5.11d), which shows this effect has also saturated around 15–20 mW.

The most interesting plot, however, is Figure 5.12 showing the magnitude of the MFE

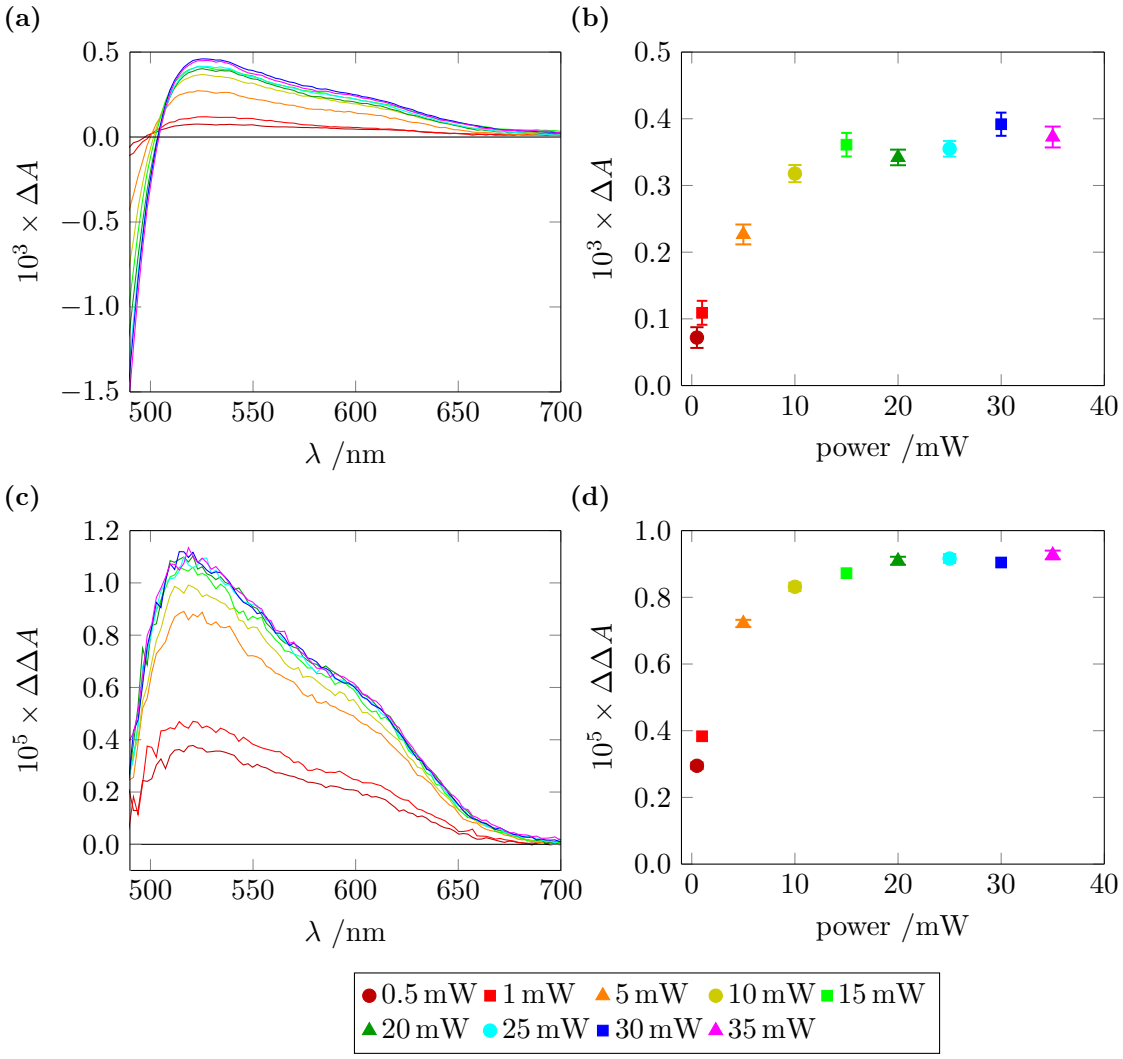


Figure 5.11: a) power dependence of $\Delta A(\lambda)$ spectra for 10 µM FMN 500 µM HEWL, showing an increased radical concentration ($>$ 510 nm) and ground state bleach ($<$ 510 nm) with increasing photoexcitation intensity. b) ΔA at 550 nm as a function of pump power. The error bars show the standard deviation of 500 measurements. c) power dependence of $\Delta\Delta A(\lambda)$ spectra for 10 µM FMN 500 µM HEWL, showing an increased absorbance change on application of a static 18 mT magnetic field with increasing pump power. Data smoothed using a 5-pixel ($\approx$ 3 nm) moving boxcar average in the wavelength dimension. d) $\Delta\Delta A$ at 550 nm as a function of pump power. The error bars representing one standard error of the mean of 500 measurements at each concentration ($\approx \pm 2\times10^{-7}$) are within the size of the markers.

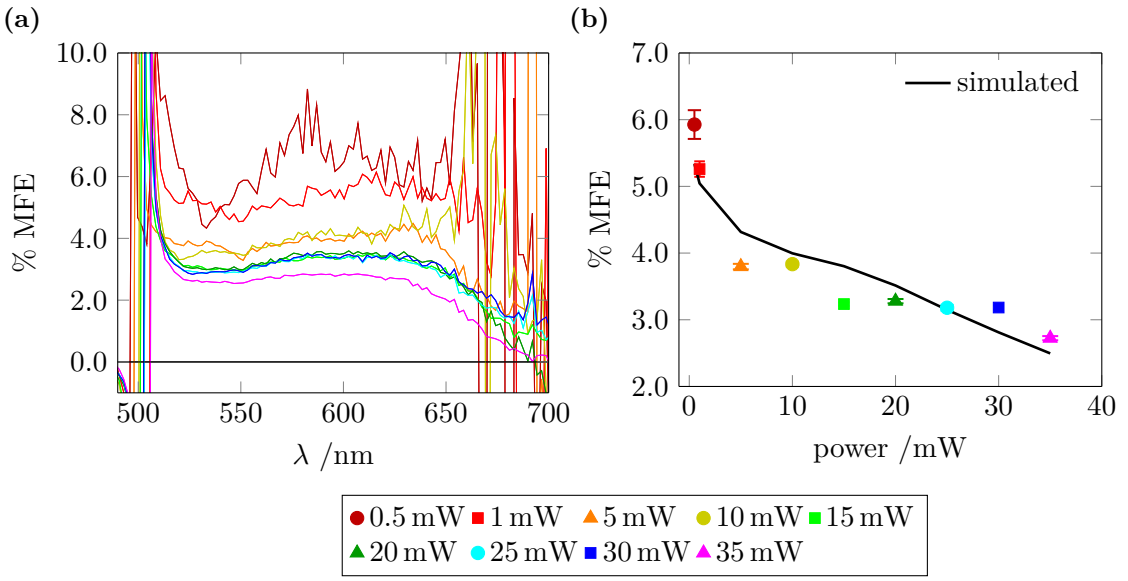


Figure 5.12: a) power dependence of MFE(λ) spectrum (B = 18 mT) for 10 µM FMN 500 µM HEWL, showing a decrease in the percentage effect with increasing photoexcitation intensity. Data smoothed using a 5-pixel ($\approx$ 3 nm) moving boxcar average in the wavelength dimension. b) MFE as a function of pump power averaged over 530–630 nm, chosen as the flattest region in Figure 5.12a) for each pump power. Error bars representing one standard error of the mean of 500 measurements at each pump power ($\approx \pm 0.02\%$) are within the size of the markers apart from the 1 µM dataset ($\pm 0.1\%$).

at 18 mT as a function of photoexcitation power. Counterintuitively, the magnitude shows a strong power dependence, particularly at low laser powers, where the magnitude drops from 6% to less than 4% on increasing the power from 0.5 mW to 5 mW. A less dramatic, approximately linear decrease in MFE is evident as the pump power is further increased up to a maximum of 35 mW. These MFE plots are displayed as a function of wavelength in Figure 5.12a) to check that there are no other species present. In addition to the change in magnitude, the only other difference apparent on increasing photoexcitation intensity is the decrease in signal noise because the effect is measured on a larger radical population. The flat nature of the spectrum above 520 nm indicates that no other magnetically sensitive species are formed (e.g. by photodegradation) and the effect is purely due to the equilibrium position of the photochemical cycle for the intermolecular RP system.

A simulation procedure has been attempted, detailed in the next section, and the

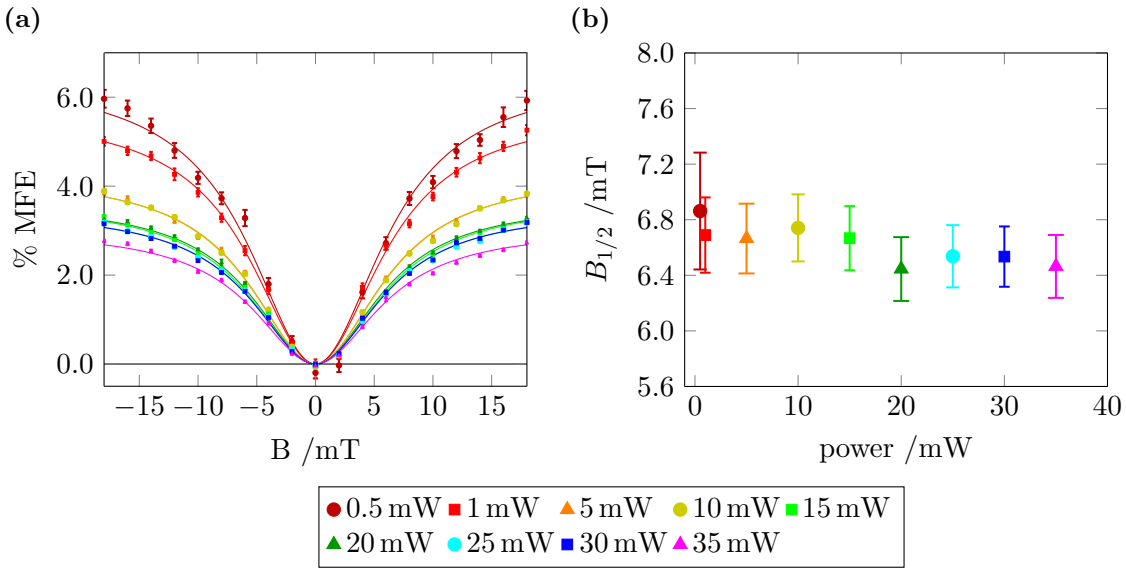


Figure 5.13: a) MARY curves for 10 µM FMN 500 µM HEWL, as a function of 450 nm photoexcitation power (averaged 530–630 nm, data smoothed by a 5-pixel (≈ 3 nm) running boxcar average in the wavelength dimension). Error bars show one standard error of the mean of 500 measurements at each field strength (≈ ±0.02%), and are generally within the size of the marker. The solid lines are Lorentzian fits to the data. b) Extracted $B_{1/2}$ values from the Lorentzian fits in a), demonstrating it is a characteristic of the identity of the radical pair and independent of the position of photochemical equilibrium (within error, 95% confidence bound of fit shown).

results of this fit to the data is shown as the solid black line in Figure 5.12b). The good agreement suggests that the proposed, more complex photochemical scheme shown in Section 5.4.2 is a reasonable attempt at describing the complex photochemistry involved.

Figure 5.13a) shows the full MARY spectrum recorded under each pump power condition. The trend of decreasing magnitude as the power is increased is clear. The high sensitivity of BBCEAS allows these sub 1% changes in MFE to be measured with high precision – most of the error bars are within the size of the markers. To further confirm the lack of any additional contributions to the MFE, Lorentzian fits are performed on each MARY curve and the resulting $B_{1/2}$ value extracted. These are plotted as a function of pump power in Figure 5.13b). Within uncertainty, the widths of the curves show no dependence on the photoexcitation power as the $B_{1/2}$ values all lie within 0.5 mT of one

another. To check for a potential weak negative correlation, the data has been fitted to a straight line whose gradient has confidence intervals that include zero. This is strong confirmation of the lack of any other magnetically sensitive radical pair species being formed at high (or low) laser powers that might contribute to the MFE.

5.4.2 Photochemical simulation

In an attempt to explain the observed trend in the MFE power dependence a more rigorous photocycle was developed, providing a more complete description of the photochemical reactions available to a photoexcited flavin/donor system. The method presented here is adapted from an approach previously used in the group.[237] The work reported here was performed in collaboration with Emrys Evans.

The improved photochemical scheme used to simulate the power dependence data in the previous section is shown in Figure 5.14. It is an extension of the simplified scheme shown in Figure 3.5 with additional reaction pathways introduced. These include the S-T mixing processes occurring in the geminate pair, as well as pathways to return singlet and triplet excited states to the ground state. Bimolecular processes, including triplet-triplet annihilation and a disproportionation pathway for the flavin radicals, are also accounted for. It is assumed that there are no other possibilities for the radical species to return to the ground state other than re-encounter to form a new geminate pair, in which the RP spin states are created in a statistical manner ($^1/_4$ of the population in each of S, T_0, T_+ and T_-). All of the associated rate constants are defined in Table 5.1.

The field effect is accounted for by setting the spin relaxation rate constant, k_r, equal to the rate of hyperfine induced interconversion, k_{hfc}, at zero-field, representing the fact that all of the RP spin-states are degenerate and can freely interconvert with one another. Following the steady state approximation for all species leads to the construction of differential equations that describe the concentration of each species as a function of time. For numerical simulation these differential equations are re-written in matrix form. All of

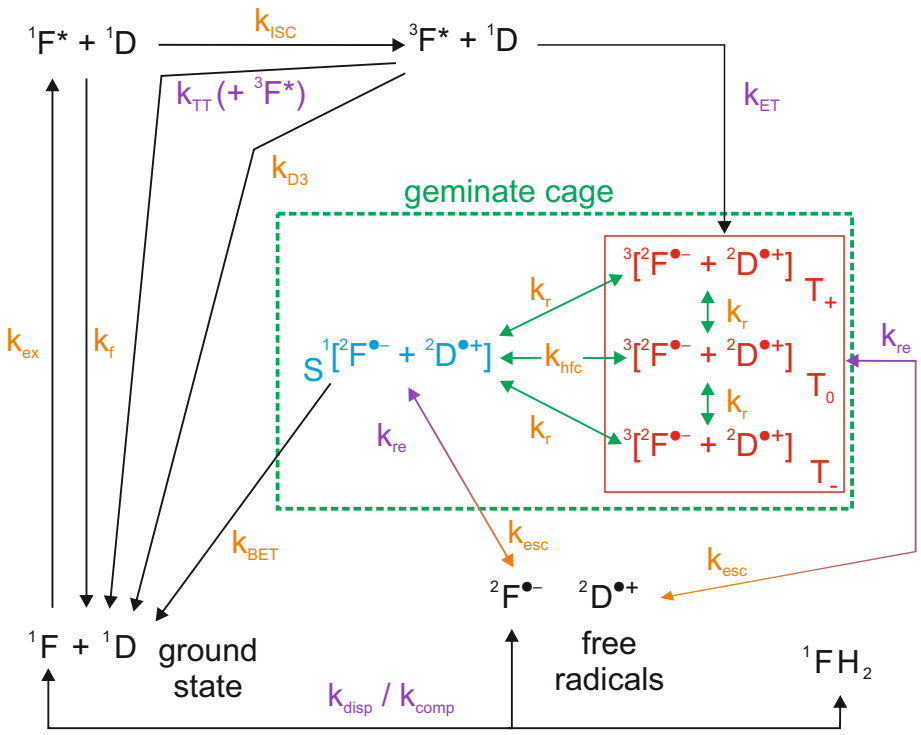


Figure 5.14: Detailed photochemical scheme, showing all the processes involved in the simulation performed for the MFE power dependence data in Section 5.4.1. In this case F = FMN and D = Trp(H). The overall spin states of the SCRPs are indicated as S (blue), and T_0, T_+ and T_- (red). Individual radical species are labelled with their doublet spin multiplicity. The rate constants are defined in Table 5.1, along with literature references, where appropriate. First-order processes are labelled in orange and second-order processes in purple. The values for k_{esc} and k_{BET} were determined by least squares fitting to the experimental data, as described in the text.

the first order processes (orange rate constants in Figure 5.14) are combined into a single matrix, K_i. Additional matrices are constructed (K_{j-n}) one for each of the second order processes modelled (shown as purple rate constants): i) re-encounter of the free-radicals to the geminate pair; ii) triplet-triplet annihilation; iii) disproportionation and iv) comproportionation of the radical species; v) electron transfer from the donor molecule to quench the excited flavin triplet state. These are multiplied by the respective indices of a matrix representing the concentration of all the species present, C.

Using the matrices shown on page 156, the overall expression used to simulate the

concentrations of the photochemical species is:

$$\begin{aligned}\frac{\mathrm{d}C}{\mathrm{d}t} = CK_i + C(7)C(8)K_j + C(3)^2K_k + C(7)^2K_l \\ + C(1)C(9)K_m + C(3)([\mathrm{D}]_0 - C(8))K_n,\end{aligned} \tag{5.9}$$

where $[\mathrm{D}]_0$ is the initial concentration of the donor species (in this case lysozyme).

The differential equations were solved numerically using the MATLAB 15s ordinary differential equation solver by substituting the values reported in Table 5.1. The change in the population of free radical species on the application of an external field could be calculated, and a percentage MFE determined using the zero-field population. This was fit to the power dependence data, using a least-squares method to determine the rate constants for which no literature values were available, namely the escape rate of the radical pairs from the solvent cage (k_{esc}) and the spin-allowed singlet state recombination from the geminate pair (k_{BET}).

The extracted values of $k_{\mathrm{esc}} = 2.31 \times 10^8$ s^{-1} and $k_{\mathrm{BET}} = 1.38 \times 10^8$ s^{-1} are consistent with the radical pair mechanism, where geminate pair lifetimes of more than a nanosecond are required for sensitivity to an external magnetic field to develop. The close agreement also indicates a good competition between the two decay pathways, which is crucial for a substantial field effect to be observed such as that seen in Figure 5.12b).

$$
C = \begin{pmatrix}
{}^1\mathrm{F} \\
{}^1\mathrm{F}^* \\
{}^3\mathrm{F}^* \\
\mathrm{T}_\pm \\
\mathrm{T}_0 \\
\mathrm{S} \\
{}^2\mathrm{F}^{\bullet-} \\
{}^2\mathrm{D}^{\bullet+} \\
{}^1\mathrm{FH}_2
\end{pmatrix}
$$

$$
K_i = \begin{array}{c}
\langle {}^1\mathrm{F}| \\
\langle {}^1\mathrm{F}^*| \\
\langle {}^3\mathrm{F}^*| \\
\langle \mathrm{T}_\pm| \\
\langle \mathrm{T}_0| \\
\langle \mathrm{S}| \\
\langle {}^2\mathrm{F}^{\bullet-}| \\
\langle {}^2\mathrm{D}^{\bullet+}| \\
\langle {}^1\mathrm{FH}_2|
\end{array}
\begin{pmatrix}
-k_{\mathrm{ex}} & k_{\mathrm{f}} & k_{\mathrm{D3}} & 0 & 0 & k_{\mathrm{BET}} & 0\,0\,0 \\
k_{\mathrm{ex}} & -(k_{\mathrm{f}}+k_{\mathrm{ISC}}) & 0 & 0 & 0 & 0 & 0\,0\,0 \\
0 & k_{\mathrm{ISC}} & -k_{\mathrm{D3}} & 0 & 0 & 0 & 0\,0\,0 \\
0 & 0 & 0 & -(k_{\mathrm{esc}}+2k_{\mathrm{r}}) & 2k_{\mathrm{r}} & 2k_{\mathrm{r}} & 0\,0\,0 \\
0 & 0 & 0 & k_{\mathrm{r}} & -(k_{\mathrm{esc}}+k_{\mathrm{hfc}} & k_{\mathrm{hfc}} & 0\,0\,0 \\
 & & & & +2k_{\mathrm{r}}) & & \\
0 & 0 & 0 & k_{\mathrm{r}} & k_{\mathrm{hfc}} & -(k_{\mathrm{BET}}+k_{\mathrm{esc}} & 0\,0\,0 \\
 & & & & & +2k_{\mathrm{r}}+k_{\mathrm{hfc}}) & \\
0 & 0 & 0 & k_{\mathrm{esc}} & k_{\mathrm{esc}} & k_{\mathrm{esc}} & 0\,0\,0 \\
0 & 0 & 0 & k_{\mathrm{esc}} & k_{\mathrm{esc}} & k_{\mathrm{esc}} & 0\,0\,0 \\
0 & 0 & 0 & 0 & 0 & 0 & 0\,0\,0
\end{pmatrix}
$$

$$
K_j = \begin{pmatrix}
0 \\ 0 \\ 0 \\ \frac{1}{2}k_{\mathrm{re}} \\ \frac{1}{4}k_{\mathrm{re}} \\ \frac{1}{4}k_{\mathrm{re}} \\ -k_{\mathrm{re}} \\ -k_{\mathrm{re}} \\ 0
\end{pmatrix}
$$

$$
K_k = \begin{pmatrix}
k_{\mathrm{TT}} \\ k_{\mathrm{TT}} \\ -2k_{\mathrm{TT}} \\ 0 \\ 0 \\ 0 \\ 0 \\ 0 \\ 0
\end{pmatrix}
$$

$$
K_l = \begin{pmatrix}
k_{\mathrm{disp}} \\ 0 \\ 0 \\ 0 \\ 0 \\ -2k_{\mathrm{disp}} \\ 0 \\ k_{\mathrm{disp}} \\ 0
\end{pmatrix}
$$

$$
K_m = \begin{pmatrix}
-k_{\mathrm{comp}} \\ 0 \\ 0 \\ 0 \\ 0 \\ 2k_{\mathrm{comp}} \\ 0 \\ -k_{\mathrm{comp}} \\ 0
\end{pmatrix}
$$

$$
K_n = \begin{pmatrix}
0 \\ 0 \\ -k_{\mathrm{ET}} \\ \frac{2}{3}k_{\mathrm{ET}} \\ \frac{1}{3}k_{\mathrm{ET}} \\ 0 \\ 0 \\ 0 \\ 0
\end{pmatrix}
$$

1^{st} order rate constant	Description of process	Value /ns^{-1}	Reference
k_{ex}	$^1F \rightarrow {}^1F^*$ excitation	power dependent	calculated
k_f	$^1F^* \rightarrow {}^1F$ fluorescence	0.109	Holzer et al. (2002)[238]
k_{ISC}	intersystem crossing $^1F^* \rightarrow {}^3F^*$	0.109	Losi et al. (2002)[239]
k_{D3}	decay of $^3F^*$ by processes other than T-T annihilation or quenching by the electron donor	3.83×10^{-4}	E. Evans (2012)[240]
k_{ET}*	$^1D \rightarrow {}^3F^*$ electron transfer	0.60	E. Evans (2012)[240]
k_r	relaxation $T_\pm \leftrightarrow S$, T_0	1×10^{-3}	Murakami et al. (2005)[136]
k_{hfc}	hyperfine induced $S \leftrightarrow T_0$ interconversion	0.182	Murakami et al. (2005)[136]
k_{esc}	formation of free radicals via escape from solvent cage	0.231	least squares fit to data
k_{BET}	spin-allowed geminate-pair recombination via back electron transfer	0.138	least squares fit to data
2^{nd} order rate constants	Description of process	Value /$M^{-1}ns^{-1}$	Reference
k_{TT}	triplet-triplet annihilation	0.89	Tsentalovich et al. (2002)[241]
k_{re}	re-encounter of radicals to form geminate-pair	9.33	calculated
k_{disp}	disproportionation: $2\ {}^2FH^\bullet \rightarrow {}^1F + {}^1FH_2$	0.5	Massey et al. (1994)[242]
k_{comp}	comproportionation: $^1F + {}^1FH_2 \rightarrow 2\ {}^2FH^\bullet$	1×10^{-3}	Massey et al. (1994)[242]

Table 5.1: Definitions of rate constants involved in the photochemical scheme shown in Figure 5.14. Values used for simulations to fit power dependence data are given, along with literature references where applicable. *pseudo-first order, value quoted for initial donor concentration of 500 µM.

5.5 Coulombic and Diffusive Effects

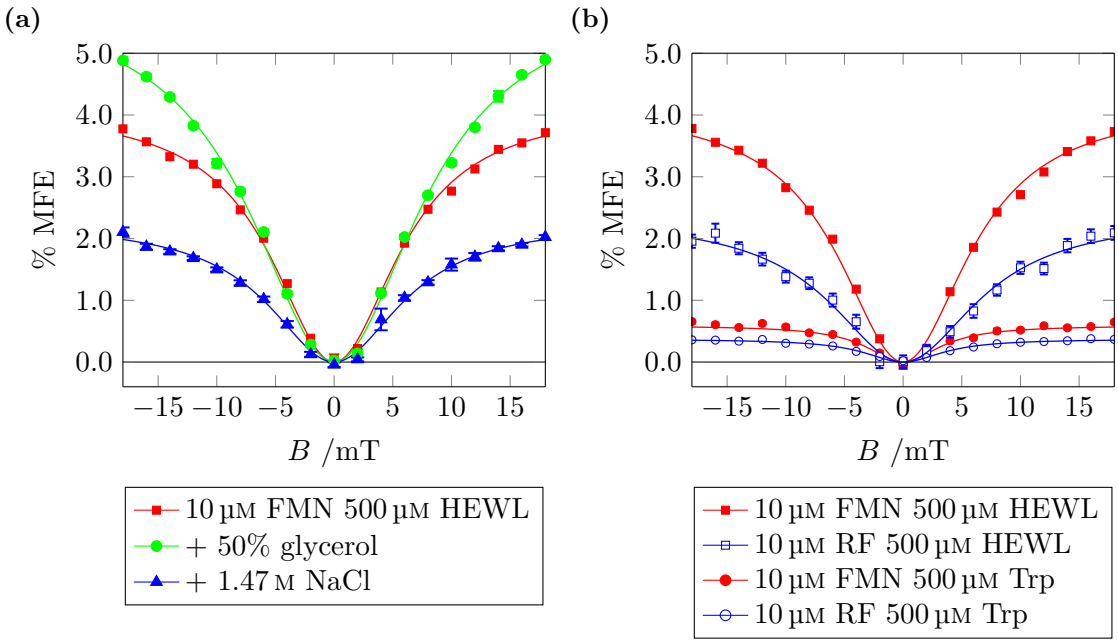


Figure 5.15: a) MARY curves for 10 µM FMN 500 µM HEWL (red squares), with added 50% glycerol (green circles) or 1.47 M NaCl (blue triangles). The solid lines are Lorentzian fits to the data, see Table 5.2 for extracted $B_{1/2}$ values. b) The effect of changing the identity of the flavin or donor on the observed MARY curve. All possible combinations of FMN (red, filled) or RF (blue, open) with HEWL (squares) or Trp (circles) are shown. All experiments performed under 10 mW, 450 nm photoexcitation and the data averaged over 530–630 nm. Error bars show one standard error of the mean of 500 measurements at each field strength and are generally within the size of the marker.

The aim of this section is to examine the effects of solution viscosity and radical partners on the magnitude and width of the MARY curves measured by BBCEAS. The results are in close agreement with those obtained using a fluorescence-based detection technique developed concurrently in the group and published previously.[134]

Figure 5.15a) shows the effect of adding glycerol (green circles) and NaCl (blue triangles) to a 10 µM FMN 500 µM HEWL sample. The higher concentration of flavin was used for the same reason as in the power dependence study, to provide a large radical signal on which to perform accurate MFE studies. It is also the same concentration as used in the equivalent fluorescence studies, although there the (405 nm) photoexcitation was at a

much higher power than the 10 mW used in these studies (i.e. 350 mW) to provide a large fluorescence signal. The unadulterated FMN/HEWL curve (red) is the data collected during the power dependence studies shown in Figure 5.12 (yellow).

The addition of glycerol leads to an increase in the measured MFE due to a prolonged geminate RP lifetime caused by slower diffusion in the more viscous solution. The increased viscosity also results in a slower tumbling rate and hence increased S-T dephasing, broadening the MARY curve ($B_{1/2} = 8.7 \pm 0.47$ mT vs 7.0 ± 0.6 mT, see Table 5.2). Miura et al.[216] have previously shown that the addition of salt screens the Coulombic attraction between the oppositely charged $FMN^{\bullet -}$ and HEWL species, resulting in a reduced geminate lifetime and an accompanying decrease in both the MFE and $B_{1/2}$. This is confirmed by a BBCEAS measurement of a sample of FMN/HEWL in sodium chloride solution of a concentration that matches the dielectric constant of the sample containing 50% glycerol (blue triangles). The reduction in MFE is clear, while the extracted $B_{1/2}$ value shows no effect within uncertainty.

The effects of Coulombic attraction and tumbling-induced S-T dephasing are also exemplified by the data shown in Figure 5.15b). Replacing FMN with riboflavin (RF), which lacks the charged phosphate group (see Figure 3.1), reduces the Coulombic attraction with the charged HEWL protein, leading to a reduction in MFE (blue, open squares). There is an excellent match with the MARY curve for FMN/HEWL in NaCl solution in Figure 5.15a) (blue triangles), indicating it is the reduced electrostatic attraction in both systems that results in smaller MFEs. If pure tryptophan is used instead of the full lysozyme protein, the attraction is further reduced as the neutral form of the tryptophan radical, $Trp^{\bullet}$, is present at pH 7.7 ($pK_a(TrpH^{\bullet +}) = 4.5$).[134] The much reduced size of the Trp species compared to the bulky HEWL protein leads to faster relative diffusion between the RP components. This results in the shortening of the geminate RP lifetime, which is the main contribution to the large reduction in observed MFE. The FMN/W curve is also much narrower than that for FMN/HEWL due to the Coulombic attraction being

RP partners	$B_{1/2}$ **/mT**		**Saturated MFE**
	BBCEAS	Fluorescence[134]	BBCEAS
FMN/HEWL	6.7 ± 0.24	6.5 ± 0.1	4.1%
FMN/W	3.8 ± 0.34	3.5 ± 0.1	0.8%
FMN/HEWL + glycerol (50%)	8.7 ± 0.47	–	6.0%
FMN/HEWL + NaCl (1.47 M)	6.8 ± 0.53	–	2.3%

Table 5.2: Experimental $B_{1/2}$ and saturated MFE values extracted from MARY curves measured by BBCEAS (this work) or fluorescence (Evans et al. 2015), for a variety of flavin-based radical pair systems. The magnitude of the saturated MFE measured by fluorescence is not expected to be comparable, so is not included. See text for discussion.

absent. Dephasing processes therefore have a reduced time in which to destroy the spin coherence, narrowing the MARY profile.[134,231,243]

A further effect of the smaller size of the tryptophan molecule is a change in the rotational correlation time (τ_c). The larger RP partner will tumble at the slowest rate. For FMN/W, the flavin radical is the larger and $\tau_c = 155\,\text{ps}$,[244] while for FMN/HEWL the bulky lysozyme protein tumbles much less rapidly, with a rotational correlation time of 7.2 ns.[245] Slower rotational motion is accompanied by more pronounced spin-dephasing and therefore a greater deviation from that predicted by the Weller formula (3 mT for the FMN/W radical pair in the absence of spin relaxation).[96,138] Comparison of the experimental $B_{1/2}$ values extracted from the FMN/W and FMN/HEWL curves demonstrates this dramatic increase (see Table 5.2).

5.6 BBCEAS MFE Studies of FAD and FAD/W

The contrast between the intramolecular and intermolecular nature of the photochemistry of FAD and FAD/W, respectively, were the subject of investigation by CRDS in Section 4.3.2. The fast time resolution of that technique permitted study of the early timescale kinetics and associated MFEs of the RP reactions involved. It is shown here that MFEs in FAD are still detectable by BBCEAS under CW photoexcitation conditions, demonstrat-

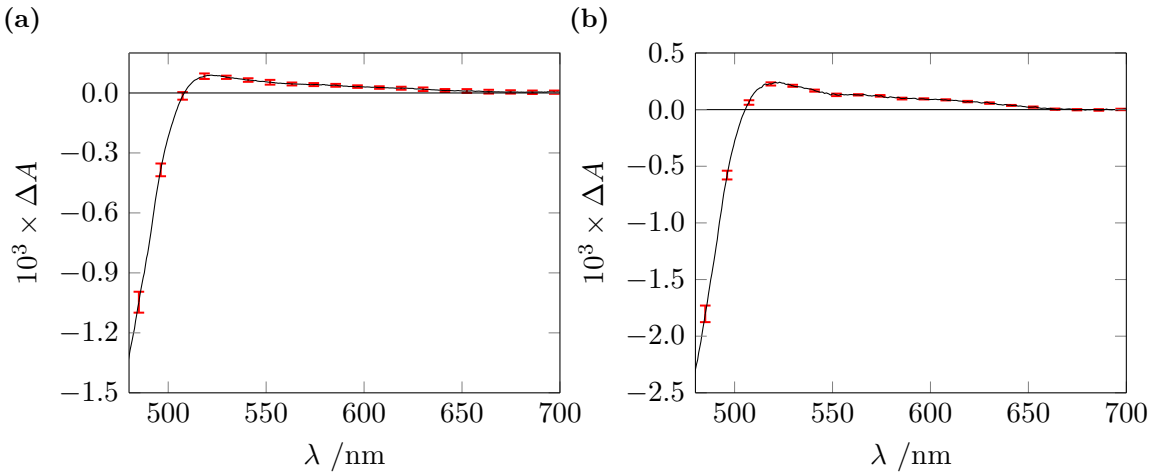


Figure 5.16: $\Delta A(\lambda)$ differential absorbance spectra of a) 10 µM FAD (pH = 2.2), and b) 10 µM FAD 500 µM W upon 10 mW 450 nm photoexcitation. Simultaneously demonstrates ground state bleaching (< 500 nm) and radical production (> 500 nm). Error bars represent one standard deviation of the average of 500 $B = 0$ mT spectra from the experimental dataset.

ing that the radical state survives in high enough yield to exhibit a change in absorbance. It remains unclear whether this is as a result of intermolecular free radical species formed via bimolecular reaction of the triplet state with a different molecule in its electronic ground state, or an equilibrium concentration of the SCRP and triplet species.

In either case, radicals are produced with a lower yield than in the purely intermolecular photochemistry of FMN/HEWL, as evident from Figure 5.16a). The $\Delta A(\lambda)$ spectrum of 10 µM FAD peaks at 1×10^{-4} ($\lambda_{max} = 521$ nm), the same value as FMN/HEWL containing only 1 µM of FMN chromophore (Figure 5.6b). The success of the CEF calibration procedure allows such comparisons between absorbance values to be made on data recorded under different experimental conditions.

The FAD/W radical pair is of particular interest to the magnetoreception community due to its proposed involvement as the carrier of the magnetic sensitivity of cryptochrome proteins. Adding tryptophan to a solution of FAD does not reproduce the singlet-born RP characteristic of cryptochrome proteins due to the lack of a rapid electron transfer pathway, provided in nature by the tryptophan triad.[114,115,118] Instead, an intermolecular triplet-

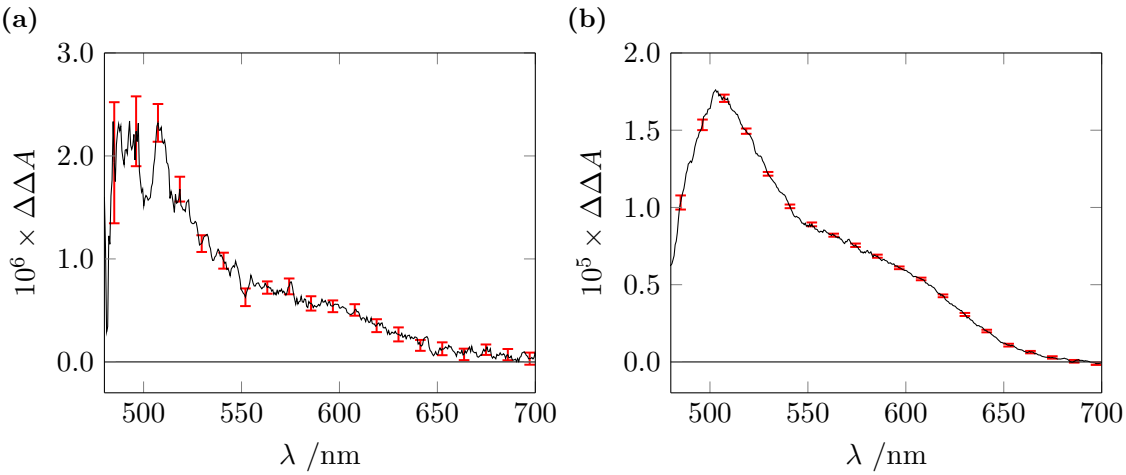


Figure 5.17: $\Delta\Delta A(\lambda)$ action spectrum of a) FAD and b) FAD/W, at ($B = 13.5\,\mathrm{mT}$) applied field. The data have been smoothed using a 5 pixel ($\approx 3\,\mathrm{nm}$) boxcar average in the wavelength dimension. Error bars represent one standard error of the mean of 500 measurements.

born radical pair is formed between freely diffusing species in solution, in an analogous fashion to those detected in the FMN/HEWL system. The $\Delta A(\lambda)$ spectrum for the FAD/W system is shown in Figure 5.16b). The now familiar radical signal is present above 500 nm along with the accompanying decrease in ground state absorbance ($\lambda < 500\,\mathrm{nm}$).

Figure 5.17a) shows the $\Delta\Delta A(\lambda)$ action spectrum of FAD. Upon application of a 13.5 mT magnetic field the free radical population increases, demonstrated by the positive absorbance change. This indicates that the radical pair is triplet-born (in agreement with the CRDS data) and therefore confirming that ISC outcompetes electron transfer, despite it occurring within the same molecule. The additional feature below 550 nm is yet to be assigned, however interestingly is also clearly visible in the intermolecular FAD/W system shown in Figure 5.17b). Previously, a similar feature has been observed in the $\Delta A(\lambda)$ spectrum of a pure FMN sample. In that case it was assigned to the anion and/or cation radical of the flavin semiquinone.[43,246] This feature renders any competing field effect on the ground state bleach impossible to detect without spectral coverage to lower wavelengths.

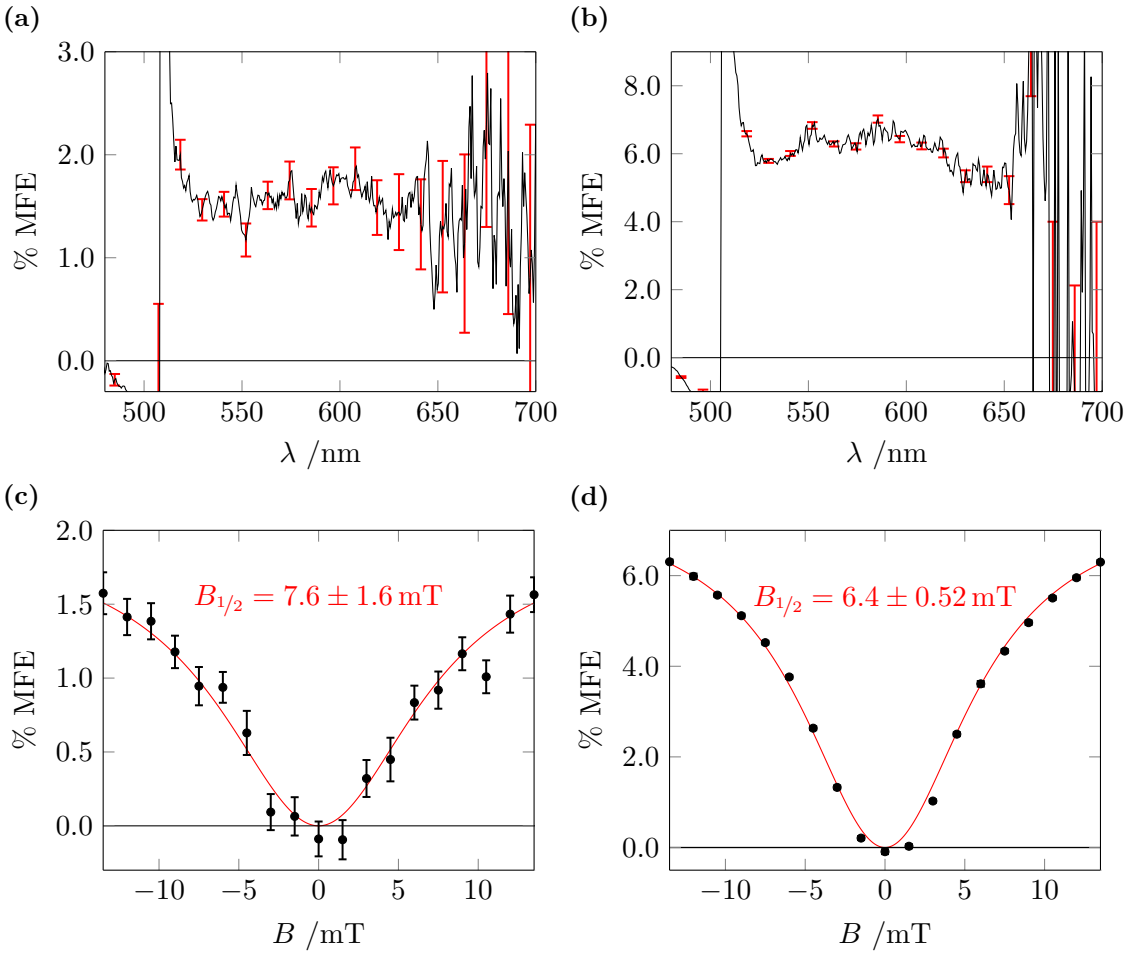


Figure 5.18: The percentage MFE(λ) spectrum at $B = 13.5\,\mathrm{mT}$ of a) FAD (10 µM, pH 2.2) and b) FAD/W, calculated from the data shown in Figure 5.16. The origins of both the approximately flat region and discontinuity around 500 nm are familiar. Data is smoothed by a 5-pixel ($\approx 3\,\mathrm{nm}$) boxcar average in the wavelength dimension. Error bars represent one standard error of the mean of 500 measurements. The MARY curve for c) the FAD and d) the FAD/W radical absorbance region (averaged over 530–630 nm). The red lines are the result of Lorentzian fits to the data from which $B_{1/2}$ values can be extracted, shown in plots. Error bars show one standard error of the mean of 500 measurements.

The $\Delta\Delta A$ signal for FAD/W shown in Figure 5.17b) is much larger than that seen for the pure FAD sample as the magnetic sensitivity is transferred to the freely diffusing radical species, prolonging its lifetime. This leads to a large difference between the pathways available to singlet and triplet SCRP states, providing the necessary conditions to observe a large MFE. The additional feature below 550 nm is much clearer here, owing to the reduced noise, and should be considered as real rather than an artefact due to poor CEF calibration due to its presence in both this data and the pure FAD action spectrum (recorded on different days). Although it has not been observed in previous BBCEAS studies on FAD containing systems, it can be confidently stated that it is not an impurity as it i) shows up in the action spectrum as a magnetically sensitive entity, and ii) the flat profile of the percentage MFE spectra in Figure 5.18a) and Figure 5.18b) identifies it as belonging to the radical species. Due to the dominant absorbance at these wavelengths, a MFE on the ground state bleach signal could not be detected.

The percentage MFE spectrum of FAD is shown in Figure 5.18a), the relatively noisy spectrum being a result of a comparatively small field effect detected on a small ΔA signal. The magnitude is smaller than for the FMN/HEWL system under identical conditions (10 mW photoexcitation, 10 µM flavin concentration), which is likely due to the comparatively higher re-encounter probability of the intramolecular RP components in FAD. As the radical pairs in FAD are covalently bound, they are limited in the extent to which they can separate, shortening the geminate RP lifetime. The effect is to reduce the extent to which singlet and triplet fates are different, thereby diminishing the impact of any applied field. The equivalent data for the FAD/W system is plotted in Figure 5.18b). In both cases, the flat profile in the radical absorbance region is indicative that all absorbing species respond in the same way to the 13.5 mT magnetic field.

The MARY curve for the FAD system is shown in Figure 5.18c). The $B_{1/2}$ value is slightly larger than for FMN/HEWL system, although similar within (the somewhat large) uncertainty (7.6±1.6 mT). This agrees with the value detected more precisely by the

CRDS instrument in Section 4.3.2 (Figure 4.13a), which provided a value (6.9 ± 0.3 mT) similar to the FMN/HEWL system (Table 5.2).

The corresponding MARY response for FAD/W is shown in Figure 5.18d). Comparison of Figure 5.18c) with Figure 5.18d) demonstrates the increased MFE on addition of tryptophan as an external electron donor, and therefore intermolecular RP partner (6.2% vs 1.5% at $B = 13.5$ mT). Dodson et al.[247] have proposed a more complex photocycle, which is applicable to any system involving FAD with an external electron donor, including the formation of both intra- and intermolecular SCRPs in which S-T mixing can occur. These could act as something of a feedback mechanism, enhancing the effect of being in one radical pair spin state over the other. This might be a reason for the larger MFE than recorded in the FMN/HEWL system under identical conditions (3.3%), despite the absence of a strong Coulombic attraction between the RP partners in FAD/W.

5.7 Cavity-Enhanced Detection of Low-Field Effects

None of the model systems studied so far have exhibited a detectable low field effect, crucial to the hypothesis of radical pair magnetoreception at Earth strength magnetic fields (0.05 mT). That leaves two possibilities: the cavity enhanced techniques used so far are not sensitive enough to detect a small inversion of the effect at low fields, or these flavin/tryptophan radical pairs do not possess the required properties.[39] However, recent results have indicated the existence of LFEs in systems such as FMN/HEWL[C] and FAD,[248] with both techniques taking advantage of the increased sensitivity of lock-in detection.

Subsequently, a system with optimum magnetic interaction between the radical pair partners was investigated to ascertain the smallest LFE detectable by the BBCEAS instrument. Ascorbic acid was chosen as the donor molecule as it is i) biologically relevant, and ii) is expected to have a large low field effect due to the very small hyperfine interactions in

[C] modulated MARY experiments performed by Marcin Konowalczyk, Timmel Group

the ascorbyl radical.[37,249] If present, these interactions would remove the long-term spin correlation necessary for the development of a substantial LFE.

Figure 5.19) shows the MARY curve for a 10 µM FAD 500 µM ascorbic acid ($AscH_2$) system. A magnification of the LFE region of the curve is shown in Figure 5.19b). The data show levels of uncertainty consistent with those associated with 10 µM flavin concentrations in previous sections (±0.02%). A LFE does appear to be detectable, although at 0.06% it is approaching the detection limit of the instrument. The slight offset from 0% MFE makes the data less convincing, and is a result of the long-term drift inherent to the SCR source during the course of 1000 acquisitions. Another characteristic of the measured MARY curve which indicates the existence of a LFE in this system is the return to the zero-field value at 1.5 mT. A flat region in the MARY profile at low field strengths cannot be explained by any plausible mechanism other than a LFE present beneath the detection limit of the technique.

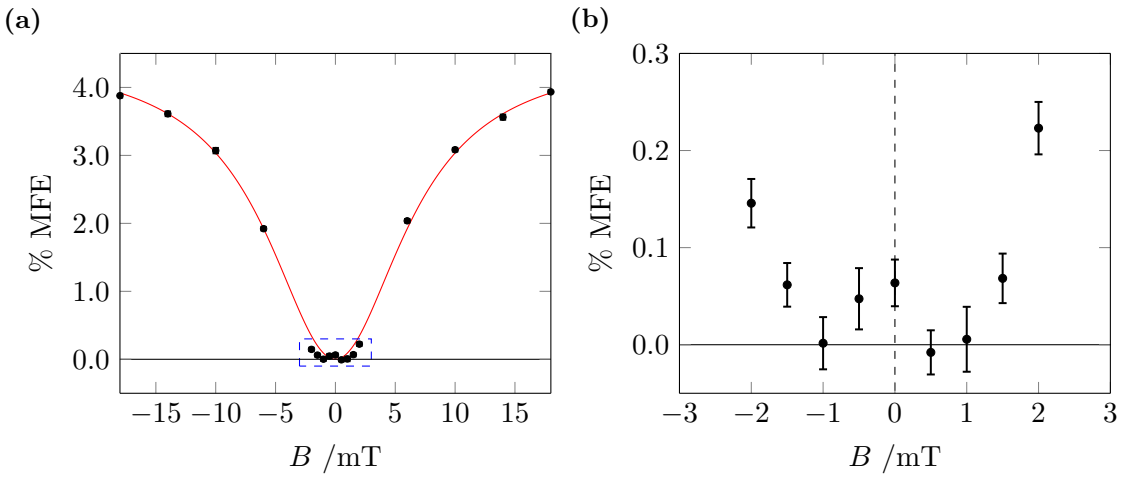


Figure 5.19: a) the MARY curve for 10 µM FAD 500 µM $AscH_2$ under 10 mW, 450 nm photoexcitation, with enhanced field resolution (0.5 mT) in the low field region (from −2 to 2 mT) in an effort to detect a low field effect, which are characterised by an inversion of the sign of the field effect compared with the high field MFE. b) An enhanced view of the LFE region, showing a clear inversion of the sign of the field effect. The data is the average of 1000 acquisitions at each field strength averaged over the radical absorbance band ($530 < \lambda < 630$ nm). Error bars represent the SEM.

The high water solubility of ascorbic acid makes it a good system on which to investigate the electron donor concentration dependence of MFEs. The electron transfer which quenches the excited state flavin is a bimolecular process, dependent on the availability of nearby donor molecules. Increasing the concentration of donor molecules, therefore, leads to a faster rate of electron transfer. If the concentration is sufficiently high, the ET can compete with the rate of intersystem crossing, forming a singlet born RP from the excited flavin singlet state (not shown in Figure 5.14). Adjusting the relative populations of RPs created in each spin state will affect the MFE as singlet- and triplet-born SCRPs exhibit opposite responses to the applied field (Section 1.5). Therefore, an increased rate of electron transfer, resulting from an increased concentration of donor molecules, should reduce the MFE as the singlet-born RPs act to cancel the response due to the triplet-born species. At high enough concentrations, the rate of ET should increase sufficiently to result in a predominantly singlet-born RP population and the MFE should change sign.

The results of systematically increasing the concentration of the ascorbic acid donor are shown in Figure 5.20a). The expected decrease in MFE is seen following the rationalisation above. Despite approaching zero, a full inversion of the MFE is not seen indicating predominantly singlet-born conditions are not reached. Upon increasing the $AscH_2$ concentration to 1 M (data not shown), the solution became highly scattering despite the solubility of ascorbic acid being 1.87 M in water, probably due to aggregation of the FAD. The cavity transmission was reduced to such an extent that data collection was impracticable.

Inversion has, however, been seen in a FMN/$AscH_2$ system using fluorescence detection by others in the group.[D] Figure 5.20b) shows the BBCEAS measurement of 10 µM FMN with the lowest ascorbic acid concentration investigated (i.e. 100 µM), which should correspond to the largest triplet-born MFE. The lack of the intramolecular RP pathway to boost sensitivity to the external magnetic field leads to a much smaller effect ($\approx 0.1\%$),

[D] Emrys Evans and Daniel Kattnig

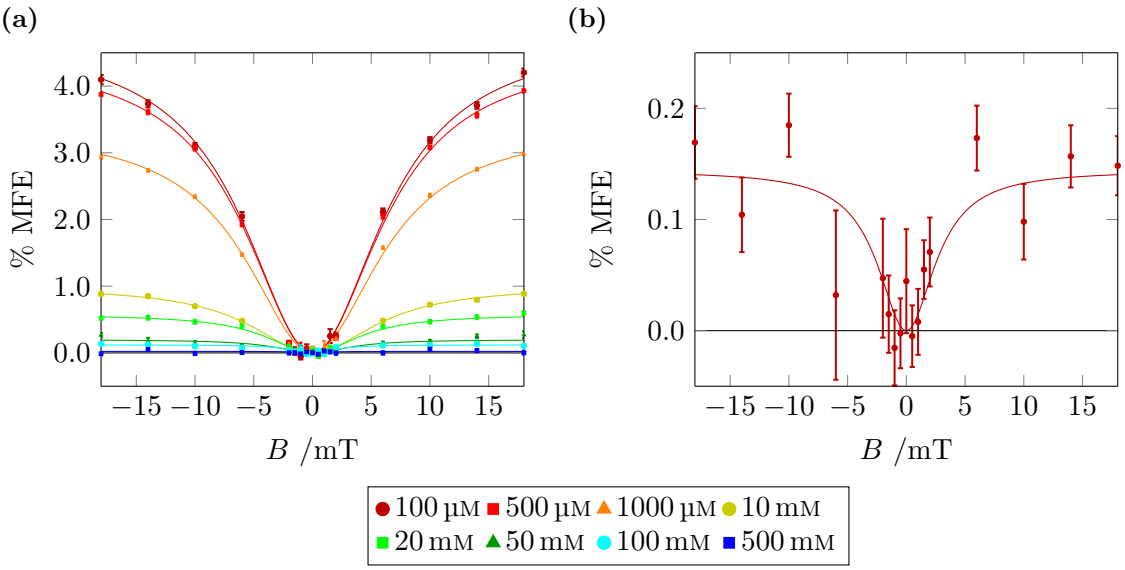


Figure 5.20: a) the MARY curve for [FAD] = 10 µM, [$AscH_2$] = x µM (see legend for individual concentrations of donor molecule), under 10 mW 450 nm photoexcitation. The data show that increasing the $AscH_2$ concentration leads to a reduction, and eventual cancelling, of the MFE as these two competing effects come into balance. b) the corresponding data for 10 µM FMN 100 µM $AscH_2$. The SNR is too poor to permit a concentration dependence study to be performed. Data averaged between 530–630 nm and the error bars represent one SEM of 1000 acquisitions at each field strength.

which is virtually undetectable by the BBCEAS instrument within noise. No LFE is detectable in contrast with the sensitive fluorescence method previously reported.[37] The solid line is a very poor Lorentzian fit to the noisy data, from which no useful information can be extracted.

5.8 BBCEAS MFE Studies of Cryptochrome and Photolyase

The overarching aim of this project is to develop instrumentation capable of recording MFEs in real biological protein samples. The previous sections in this chapter have demonstrated the suitability and optimisation of the technique for MFE detection through the investigation of chemical model systems, but its success will ultimately be judged on its applicability to cryptochrome MFE studies.

In this section, the suitability of BBCEAS for protein studies is demonstrated by the

detection of MFEs in two closely related biological systems relevant to magnetoreception. The magnetic response of the *Drosophila melanogaster* cryptochrome (*Dm*Cry) is compared to that of a closely related DNA photolyase protein from the *Escherichia coli* bacterium (*Ec*PL). The results of *Dm*Cry studies performed using single-pass TA apparatus are also included to highlight the quality of the cavity-enhanced data.

5.8.1 BBCEAS MFE study of *Ec*PL

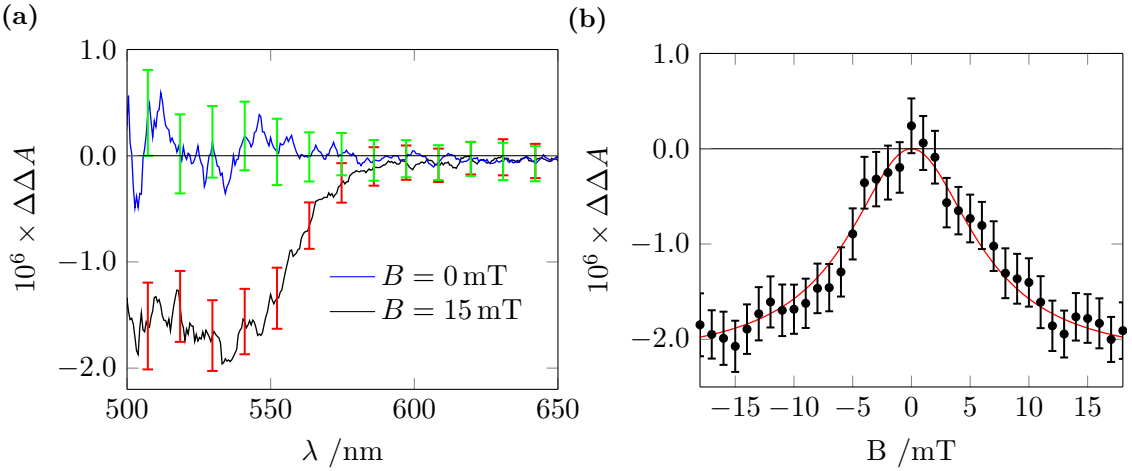


Figure 5.21: a) the BBCEAS action spectrum of a solution of *Ec*PL (≈ 60 µM) under 0.5 mW, 450 nm CW photoexcitation, in the presence (black) and absence (blue) of a 15 mT magnetic field. The negative response in the FAD/W radical pair absorbance region (500–580 nm) is indicative of a magnetically sensitive singlet-born RP. Data is smoothed with a 3 nm boxcar moving average, and the error bars represent one standard error of the mean of 500 measurements. b) MARY curve showing the change in *Ec*PL absorbance as a function of applied magnetic field strength (averaged over 500–550 nm). Smoothing of 2 mT in the field direction has also been applied. The error bars show one standard error of the mean of 500 measurements.

The response of the *Ec*PL sample to a magnetic field is shown in Figure 5.21. The decrease in absorbance between 500 and 560 nm is assigned to the FAD/W radical pair formed in the long-lived RP2 species (Figure 3.8), and is indicative of the singlet-born nature of the radical pair. The low temperatures required for protein studies (268 K) mean it is necessary to blow dry air over the sample cell windows to prevent the build up

of condensation. This is the dominant factor in the substantial increase in uncertainties compared with the model system experiments. The small volumes of protein available preclude sample flow and so photodegradation products build up. These can stick to the inside of the cell windows and provide an additional contribution to the scattering losses. The MARY profile shown in Figure 5.21b) shows a clear negative MFE at all field strengths. Despite the relatively good SNR for a protein MFE study, no LFE is discernible above the noise level.

The data is presented here as a change in absorbance, rather than a standardised percentage MFE value, as at the low cavity finesses and photoexcitation powers characteristic of protein studies a ΔA signal is virtually undetectable. The radical species are already produced in low concentrations by an on-axis blue light contribution from the blue light component of the SCR source,[43] and so the unshuttering of the pump beam leads to a negligible change in radical absorbance at these photoexcitation powers (0.5 mW). This is an indication of the effectiveness of modulating the field (see Figure 5.2), as reproducible changes in absorbance on the order of 10^{-6} can be detected where it is difficult to see a 10^{-4} change upon photoexcitation.

5.8.2 BBCEAS MFE study of *Dm*Cry

To demonstrate the improvement in sensitivity over the single-pass TA experiment traditionally used for MFE studies in proteins, the results from MFE studies on the *Drosophila melanogaster* cryptochrome performed by both BBCEAS and TA are compared here. Figure 5.22a) shows the *Dm*Cry action spectrum measured by BBCEAS at an applied field strength of 18 mT. The negative absorbance change is seen in the same spectral region as for the *Ec*PL protein, indicating that both systems share a common singlet-born FAD/Trp radical pair.[96] The data shares the same increase in uncertainty due to additional scattering losses introduced to the cavity by a low temperature protein study. In contrast with previous work,[227] which used a lower protein concentration (30 µM) to improve cavity

throughput below 500 nm, no ground state response was detectable here due to the large amount of absorbance and scattering loss caused by the sample in this region.

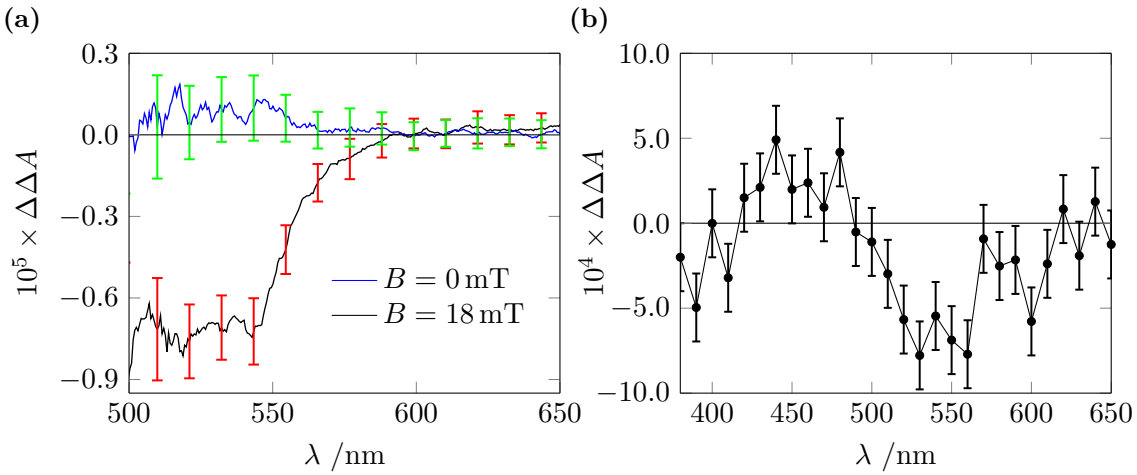


Figure 5.22: a) the BBCEAS action spectrum of a solution of *Dm*Cry (≈ 60 µM) under 0.5 mW, 450 nm CW photoexcitation, in the presence (black) and absence (blue) of a 18 mT magnetic field. The negative response of the absorbance in the FAD/W radical pair absorbance region (500–580 nm) is indicative of a magnetically sensitive singlet-born RP. Data is smoothed using a 6 nm boxcar moving average, and the error bars are one standard error of the mean of 500 measurements. b) the action spectrum measured by TA, showing the effect of applying a 22 mT magnetic field to a *Dm*Cry sample. Allowing for protein recovery between shots and repeated readings means this spectrum takes upwards of 10 hours to record. TA sample conditions: 50 mM Hepes buffer, 100 mM KCl, 50% glycerol, 267 K.

The equivalent action spectrum recorded by TA is shown in Figure 5.22b). The absolute size of the absorbance change is bigger due to the much larger ΔA signal produced by the intense photoexcitation pulse (7 mJ). The poorer SNR is clear, with a field effect only clear above the noise level at a few wavelength points. The advantage of the TA is shown in the increased spectral coverage, although like CRDS this must be collected in a stepwise manner. A xenon arc lamp can be used as the probe beam because a well-collimated output for effective coupling into an optical cavity is not a requirement. SCR sources with enhanced output in the blue wavelength region have only recently become commercially obtainable, and were not available for these studies due to prohibitively high cost.

Obtaining this action spectrum by TA takes up to 10 hours due to the need to run

the photoexcitation at a very low rate to allow time (120 s) between high intensity shots to permit recovery of the sample. Extra time is also required for refreshing the sample between certain wavelengths and changing between short and long pass filters depending on the wavelength being recorded.

In TA experiments, cryostats can be used to study MFEs at very low temperatures as a high cavity finesse does not have to be maintained throughout the acquisition. These low temperatures further stabilise the sample and prolong the radical pair kinetics. High glycerol concentrations are also required to maintain the solution phase under such conditions. Low temperature and high viscosity increase the geminate RP lifetime, significantly enhancing the size of any MFE. Although advantageous for MFE detection, these conditions are of very limited relevance to *in vivo* behaviour of proteins, and the enhanced sensitivity of BBCEAS permits the studies to be performed under more physiological conditions i.e. above the freezing point of water.

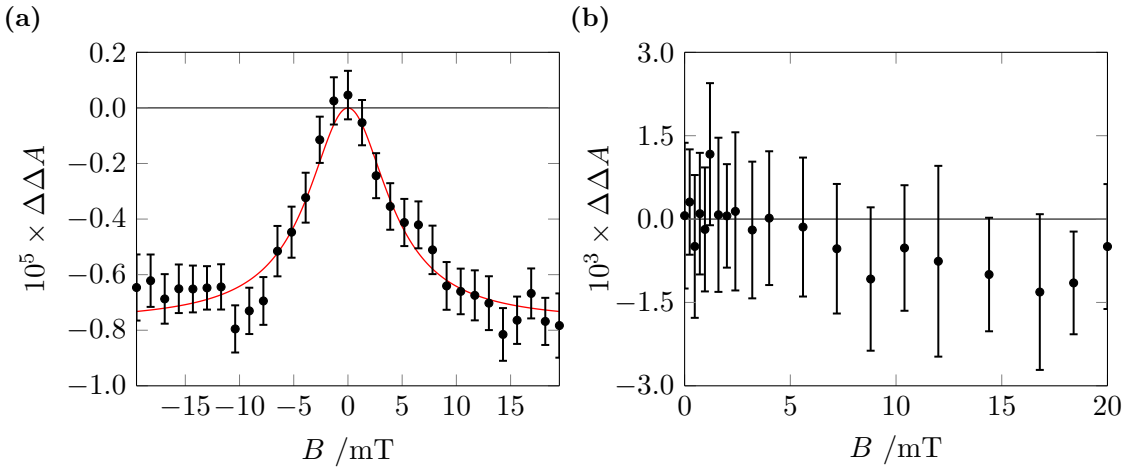


Figure 5.23: a) BBCEAS MARY curve, showing the change in *Dm*Cry absorbance as a function of applied magnetic field strength, averaged over 500–550 nm. The error bars show one standard error of the mean of 500 measurements. b) the MARY curve measured by TA showing the field response of *Dm*Cry at a range of magnetic field strengths. Recorded at 560 nm, averaged over the entire 80 µs decay trace. The error bars represent one standard error of the mean of 16 on-off measurements at each field point. Sample conditions for TA: 50 mM Tris/HCl buffer, 100 mM NaCl, 60% glycerol, 265 K.

The MARY curve for *Dm*Cry is shown in Figure 5.23a). The sample exhibits a negative

response at all field values with no sign of a low field effect. As in the *Ec*PL study, the lower cavity finesse due to the sample conditions means an accurate ΔA value could not be recorded, and therefore a percentage MFE could not be calculated. The corresponding MARY curve measured by TA is shown in Figure 5.23b). The improvement in SNR offered by cavity enhancement is demonstrated by comparison with the data obtained using the BBCEAS instrument.

5.8.3 Comparison of *Ec*PL and *Dm*Cry

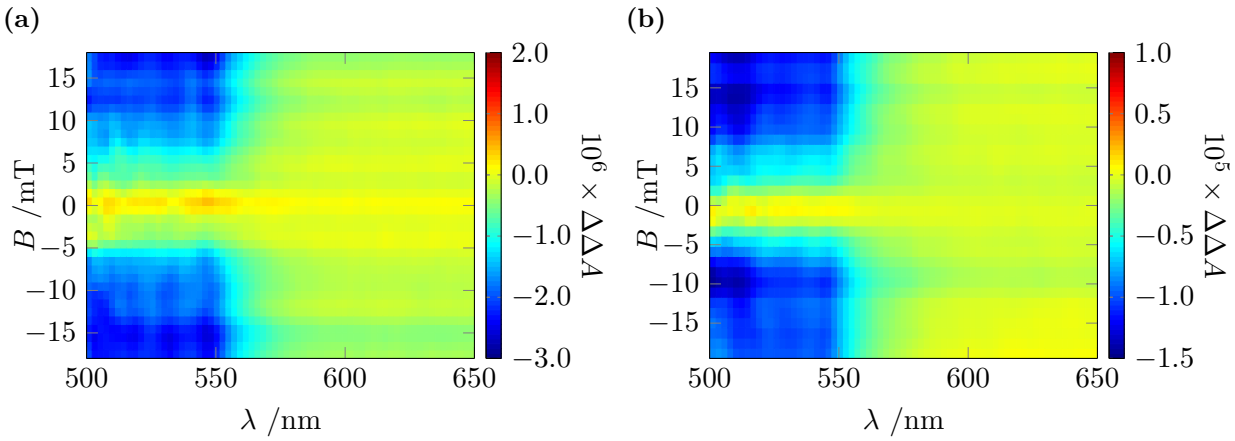


Figure 5.24: $\Delta\Delta A(\lambda, B)$ surface plots for a) *Ec*PL and b) *Dm*Cry, showing the spectral change in absorbance as a function of field strength. The similarities between the magnetic responses of these two proteins are striking and should be expected considering the close similarities in their early timescale photochemical behaviour monitored by TA. Data is the average of 500 measurements.

Figure 5.24 demonstrates the similarities between the magnetic responses of a) *Ec*PL and b) *Dm*Cry proteins, presenting the spectrally resolved absorbance change on application of varying field strengths. It is clear that in both cases the field sensitivity is exhibited by species absorbing over a relatively narrow range, which matches the known spectral shape of the ^{1,3}[FAD$^{\bullet-}$ Trp$^{\bullet}$] RP2 state.[128] The lack of an absorbance change above 550 nm is evidence that the tryptophan radical is deprotonated in both of these species, in contrast with the results published for the *Arabidopsis thaliana* plant cryptochrome.[96]

The detection of clear magnetic responses in protein systems is a big step towards the ultimate goal of resolving a biological LFE for the first time. However, the biggest challenge is inherent to the protein samples themselves and efforts should be focused on optimisation of the protein solutions for cavity-based studies. The high sensitivity of the BBCEAS instrument developed here indicates that a decrease in protein concentration to nearer 10 µM should still allow the detection of MFEs and is likely to increase the SNR, despite the reduction in absolute size of the radical signal, by reducing the prohibitively high levels of scatter.

5.9 Pump-Beam Modulated BBCEAS

The MFE studies employing BBCEAS presented in this chapter so far make use of slow field modulation (*ca.* 10 Hz) to reduce the effect of probe beam drift on the measurement of field induced absorbance changes, by minimising the time delay between recording the field-off and field-on spectra. This is approaching the limit at which the field can be switched due to the rise time of the coils, and the need to allow time for the system to respond. Modulating the field is key to increasing the SNR sufficiently to measure MFEs, but if the time between field-on and -off readings could be reduced further that would be even more beneficial. The diode laser providing the photoexcitation can be switched at a repetition rates up to 1 kHz, opening up the possibility of a further increase in SNR. It would also allow the measurement of the ground state spectrum throughout the course of the experiment, which is impossible under the continuous illumination conditions of the current methodology.

This section reports on early developments of a modulated BBCEAS variant, using the detection of a MFE in the FMN/HEWL system as a proof-of-principle. The differences in data collection and analysis from the normal CW experiment are explained in Section 5.9.2 and the results presented in Section 5.9.3. However, first the effect of pump beam modulation on the flavin photochemistry is investigated, to determine the speed at which

the system responds to changing photoexcitation conditions.

5.9.1 The establishment of photochemical equilibrium

This section presents some early findings on the transient behaviour of the FMN/HEWL system on the timescales accessible by this BBCEAS instrument, limited by the millisecond integration windows of the CCD camera. Behaviour on this timescale is due to the establishment of a new photochemical equilibrium under steady-state illumination conditions. The transient behaviour of the system to establish a new equilibrium in response to external stimuli (either photoexcitation or applied magnetic fields) can be followed using BBCEAS, provided the response is sufficiently slow.

Figure 5.25 demonstrates the behaviour of the FMN/HEWL model system under changing photoexcitation conditions for a) the radical absorbance ($500 < \lambda < 600\,\text{nm}$) and b) ground state absorbance ($478 < \lambda < 488\,\text{nm}$). The steady-state absorbances in each region are shown in the absence (black) and presence (red) of continuous 450 nm photoexcitation (10 mW), along with the transition between the two states when the diode laser is unshuttered at $t = 1\,\text{s}$ (orange). The response of the system to 5 Hz and 1 Hz diode laser modulation is also shown (50% duty cycles, blue and green, respectively).

The radical response to photoexcitation is rapid and the system equilibrates to a similar population of radical species in each case (Figure 5.25a). At the slower repetition rates a slight overshoot in radical absorbance is seen initially, which subsequently relaxes back to the equilibrium value within about 500 ms. However, the ground state behaviour plotted in Figure 5.25b) is quite different, requiring over 5 s to equilibrate to the population present under CW photoexcitation (orange to red). This is emphasised in the modulated signal, where the differences in the populations get progressively smaller as the rate is increased due to a lack of response time. At 5 Hz the change in ground state population is an order of magnitude smaller than its steady-state values (1.6% vs 16%). This difference will become important later, when examining the data obtained by a pump-modulated

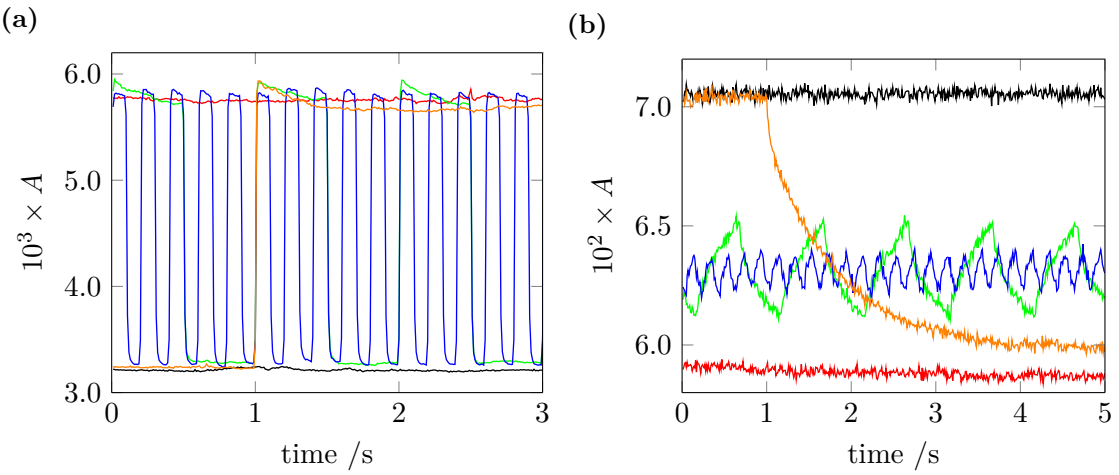


Figure 5.25: The response of a 10 µM FMN 500 µM HEWL system to modulated photoexcitation (10 mW, 450 nm), averaged over a) the radical absorbance region (500–600 nm) and b) the ground state bleaching region (478–488 nm). Shown are absorbances under no illumination (black), continuous illumination (red), continuous illumination switched on at $t = 1$ s (orange), and illumination modulated at 5 Hz (blue) and 1 Hz (green). The data is obtained by acquiring 500 (10 ms) CCD exposures continuously with no delay between successive shots. A delay generator is used to synchronise the start of the camera acquisition with the diode laser.

variant of BBCEAS (Section 5.9.3).

A similar effect is also seen if the magnetic field is switched on and off under constant photoexcitation. The system still receives a varying stimulus which affects its photochemical cycle, although the effect here is much smaller and challenging to detect. While no averaging is required for the data shown in Figure 5.25, the signals shown in Figure 5.26 are the average of 500 field switching cycles. In an attempt to give as much time as possible for an effect to develop in the ground state the field is switched at the slower rate of 0.5 Hz, chosen as a compromise between the required averaging and prohibitive experimental duration. However, long-term drift of the SCR probe beam becomes an issue in experiments spanning this kind of timescale.

In both the a) radical and b) ground state regions, an initial prompt response is exhibited by the system within the 10 ms CCD acquisition window. Subsequently, further evolution of the MFE occurs on a millisecond timescale, of similar form to that seen in

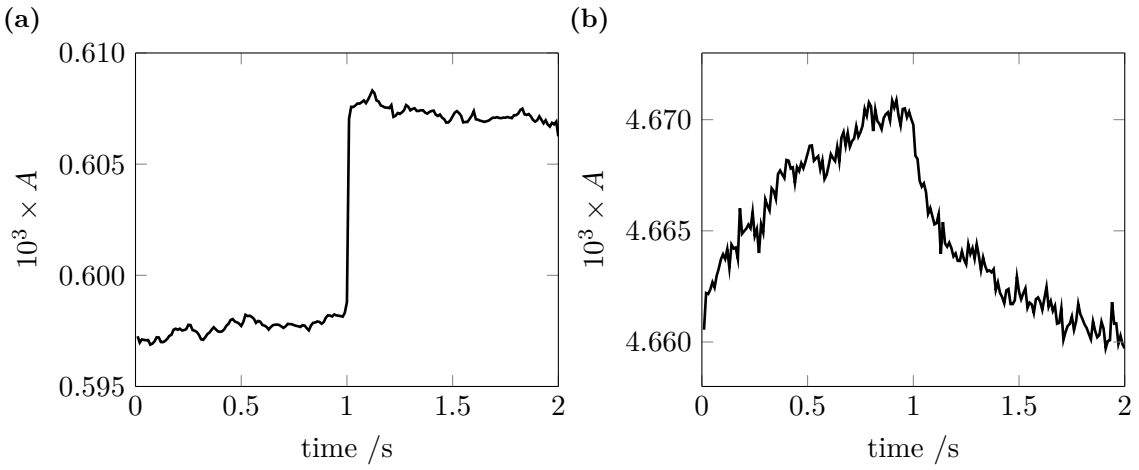


Figure 5.26: The response of a 10 µM FMN 500 µM HEWL system to a switching magnetic field, averaged over a) the radical absorbance region (500–600 nm) and b) the ground state bleaching region (478–488 nm). At 1 s, the field is switched from 0 mT to 13.5 mT. In both regions an initial prompt step is observed, followed by an evolution in the species' concentrations as discussed in more detail in the text. The data is the average of 50 on-off field cycles, each one consisting of 200 (10 ms) CCD exposures. The camera is run in continuous acquisition mode, with no delay between successive shots, and the experiment takes 1000 s.

the response to modulation of the photoexcitation intensity. These effects have been the subject of intense investigation in the group, using ultra-sensitive fluorescence detection.[37] Their proposed origin is differing rates of oxidation and reduction processes that return the flavin and donor free radical species directly to the ground state. This, by extension, would also explain the behaviour exhibited in response to a change in photoexcitation conditions, as fundamentally they are both a change in the relative rate constants involved in the photochemistry (see Figure 5.14). However, the effect of modulating photoexcitation, while straightforward to measure in absorbance with the high sensitivity of BBCEAS, would be impossible to monitor by fluorescence as switching off photoexcitation would extinguish the signal itself.

Initially, BBCEAS was used as proof-of-principle confirmation of the evolution of MFEs on a millisecond timescale, first observed using the fluorescence-based approach. These effects have become known as Enhanced Magnetic Field Effects (EMFEs), and could

have important implications for animal magnetoreception if nature has found a way to fine-tune the rate constants of the oxidation and reduction processes.[37] Furthermore, BBCEAS could find useful application in studying the same phenomena in cryptochromes, which seem to exhibit EMFEs but their low fluorescence yield makes them challenging to detect. Modulated photoexcitation of cryptochrome samples with BBCEAS measurements of absorbances could lead to powerful insights into the relative rates of the oxidative and reductive pathways, and therefore the mechanisms of magnetoreception, without any need for a magnetic field.

Of more importance to the modulated technique reported here, the radical population has been shown to respond rapidly (in under 10 ms) to pump laser modulation. The following sections introduce a pump-beam modulated variant of the BBCEAS instrument in an attempt to improve both its sensitivity and the accuracy of any extracted absorbance values.

5.9.2 Data collection and analysis

In pump-beam modulated BBCEAS experiments there is a compromise to be made between gaining an accurate measure of the ground state light intensity, allowing enough time for the system to respond to the light modulation, and keeping the experimental duration reasonably short. The choice of modulation rate must be tempered to allow sufficient time for the photocycle to respond. However, the ground state would require up to ten seconds to return to its steady-state equilibrium position (Figure 5.25b), so a compromise must be sought. The radical region should be the priority in these BBCEAS studies as the ground state region is already plagued by the problem of low light intensity, and the radical signal has been demonstrated to respond within 10 ms in Figure 5.25a). This implies that the pump laser could safely be modulated at 100 Hz. Such fast rates have not been attempted here but should be investigated further in the future to ensure the greatest benefit from the effects of modulation.

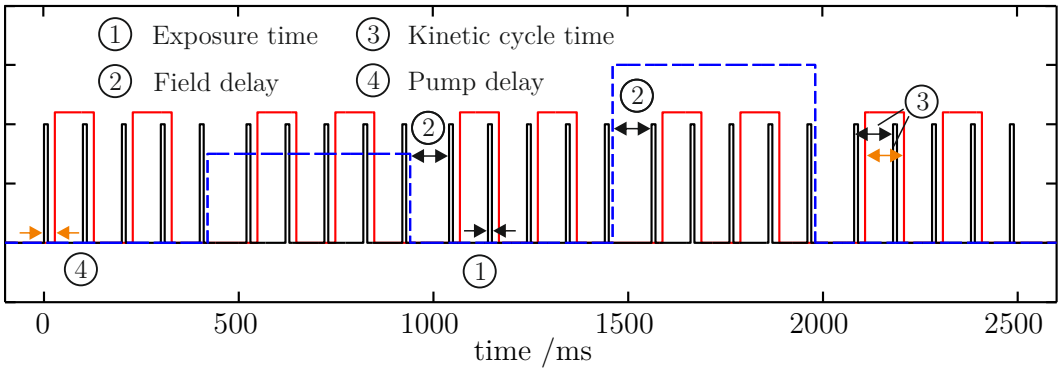


Figure 5.27: A schematic representation of the pulse sequence used to control the modulated BBCEAS instrument for MFE studies. The four key timings for the accurate measurement of a MFE are shown, see text for discussion. The orange arrows indicate those that are set on the delay generator and the black arrows those set in the acquisition software.

Figure 5.27 shows the pulse sequence for the modulated BBCEAS experiment. A number of CCD acquisitions is decided upon, which make up a 'kinetic series'. The chosen value should be a compromise of the improved SNR due to averaging and increased experimental duration. An odd number is always used (here set as 5) to ensure that a ground state is recorded before and after each photoexcited shot, in much the same way that zero-field readings are taken between each field-on reading (see Figure 5.2), to allow drift to be accounted for. The exposure time (1) in these experiments is set to 10 ms for comparability with the steady-state photoexcitation studies reported throughout the rest of this chapter. A field delay (2) is added to allow time for the field to reach the desired value. In this modulated variant, the sample response is not a consideration as in the absence of photoexcitation there is no radical population to respond. Both of these parameters are identical to those shown in Figure 5.2 for the standard CW BBCEAS experiment.

The kinetic cycle time (3) between CCD acquisitions is used to determine the acquisition rate, here set to 10 Hz. The output from the diode laser is modulated using a TTL output from a delay generator (SRS, DG645) triggered by the output from the CCD

camera. The on-off acquisition sequence is achieved by setting the pulse width of the diode laser output equal to the kinetic cycle time, which results in every second trigger signal being dropped. It also ensures a 50% duty cycle, and therefore that the system has equal time to respond to photoexcitation being switched either on or off before signal acquisition. An initial delay (4), longer than the exposure time, is added at the delay generator so that the first CCD acquisition corresponds to the absence of photoexcitation, and therefore measures the sample ground state. The shorter this delay, the more time the system has to respond to the change in photoexcitation before the next CCD exposure.

The result is a kinetic series of CCD exposures taken in alternating presence and absence of photoexcitation, from which a radical signal can be determined. The process is then repeated, this time in the presence of an external magnetic field, with the field delay time between the field being switched on and the first CCD acquisition of the kinetic series. The field remains on for the entirety of the kinetic series, before being switched off before the next kinetic series. As before, a kinetic cycle at zero-field is recorded before and after each field-on sequence, and so this experiment combines the benefits of field and photoexcitation modulation. This entire sequence is repeated for each field strength required in the MARY curve and the data is analysed in a slightly different way (outlined below). Unlike in the steady state variant, this permits the monitoring of I_{gs} throughout the course of the measurement rather than just as a one-off acquisition prior to the experiment. This means that the ratio $I_{\mathrm{gs}}/I_{h\nu}$ (without field) and I_{gs}/I_B (with field) is as accurate as possible and almost insensitive to probe beam intensity drift, as long as photoexcitation is modulated at a fast enough rate.

In Section 5.2.2, the differential absorbance spectrum, $\Delta A(\lambda)$, was defined as:

$$\Delta A(\lambda) = \frac{I_0(\lambda)}{\ln(10)\mathrm{CEF}(\lambda)} \left(\frac{I_{\mathrm{gs}}(\lambda) - I_{h\nu}(\lambda)}{I_{h\nu}(\lambda) I_{\mathrm{gs}}(\lambda)} \right). \tag{5.10}$$

In the modulated variant, however, to maximise the SNR gains by recording I_{gs} and $I_{h\nu}$

close to each other, it is calculated as:

$$\Delta A_{\mathrm{mod}}(\lambda) = \frac{1}{\ln(10)\mathrm{CEF}(\lambda)} \left(\frac{I_{\mathrm{gs}}(\lambda)}{I_{h\nu}(\lambda)} - 1 \right), \tag{5.11}$$

noting that this is very similar to the expression for the photoexcited absorbance given in Equation 5.3, with I_{gs} in place of the empty cavity intensity, I_0.

Following the same rationale, $\Delta A_{B,\mathrm{mod}}(\lambda)$ is calculated as:

$$\Delta A_{B,\mathrm{mod}}(\lambda) = \frac{1}{\ln(10)\mathrm{CEF}(\lambda)} \left(\frac{I_{\mathrm{gs}}(\lambda)}{I_B(\lambda)} - 1 \right), \tag{5.12}$$

and therefore the action spectrum, $\Delta\Delta A_{\mathrm{mod}}(\lambda)$, is given by:

$$\begin{aligned} \Delta\Delta A_{\mathrm{mod}}(\lambda) &= \Delta A_{B,\mathrm{mod}}(\lambda) - \Delta A_{\mathrm{mod}}(\lambda) \\ &= \frac{1}{\ln(10)\mathrm{CEF}(\lambda)} \left[\left(\frac{I_{\mathrm{gs}}(\lambda)}{I_B(\lambda)} - 1 \right) - \left(\frac{I_{\mathrm{gs}}(\lambda)}{I_{h\nu}(\lambda)} - 1 \right) \right] \\ &= \frac{I_{\mathrm{gs}}(\lambda)}{\ln(10)\mathrm{CEF}(\lambda)} \left(\frac{I_{h\nu}(\lambda) - I_B(\lambda)}{I_B(\lambda) I_{h\nu}(\lambda)} \right). \end{aligned} \tag{5.13}$$

Comparison of Equations 5.11–5.13 above with the corresponding steady state expressions (Equations 5.4–5.7) shows that while this approach provides no indication of real absorbances, the values of ΔA_{mod}, $\Delta A_{B,\mathrm{mod}}$ and $\Delta\Delta A_{\mathrm{mod}}$, can be straightforwardly converted to the more rigorous ΔA, ΔA_B and $\Delta\Delta A$, respectively, by applying a simple factor of $\dfrac{I_0(\lambda)}{I_{\mathrm{gs}}(\lambda)}$.

However, if the percentage MFE is all that is of interest,

$$\begin{aligned} \mathrm{MFE}(\lambda) &= \frac{\Delta\Delta A_{\mathrm{mod}}(\lambda)}{\Delta A_{\mathrm{mod}}(\lambda)} \times 100 \\ &= \frac{I_{\mathrm{gs}}(\lambda)}{I_B(\lambda)} \left(\frac{I_{h\nu}(\lambda) - I_B(\lambda)}{I_{\mathrm{gs}}(\lambda) - I_{h\nu}(\lambda)} \right) \times 100, \end{aligned} \tag{5.14}$$

which is exactly the same expression as that defined in Equation 5.8 for the steady state

case, in which true absorbance values were used throughout and intensities related back to I_0. This is the expected result, as the fractional change in signal should be independent of the exact mechanism of how that signal is measured and analysed. Similarly, CEF calibration and knowledge of I_0 are not necessary for calculation of the MFE, and the same implications for SNR and dynamic range still apply.

5.9.3 Modulated BBCEAS results

The following data shows the results of the modulated BBCEAS experiment described in the previous section. For this proof-of-principle study the FMN/HEWL model system was used, although in future this technique would be well-suited to the study of light sensitive protein systems as the modulation of the pump beam reduces the number of photons the sample is exposed to per experiment, while maintaining good SNR.

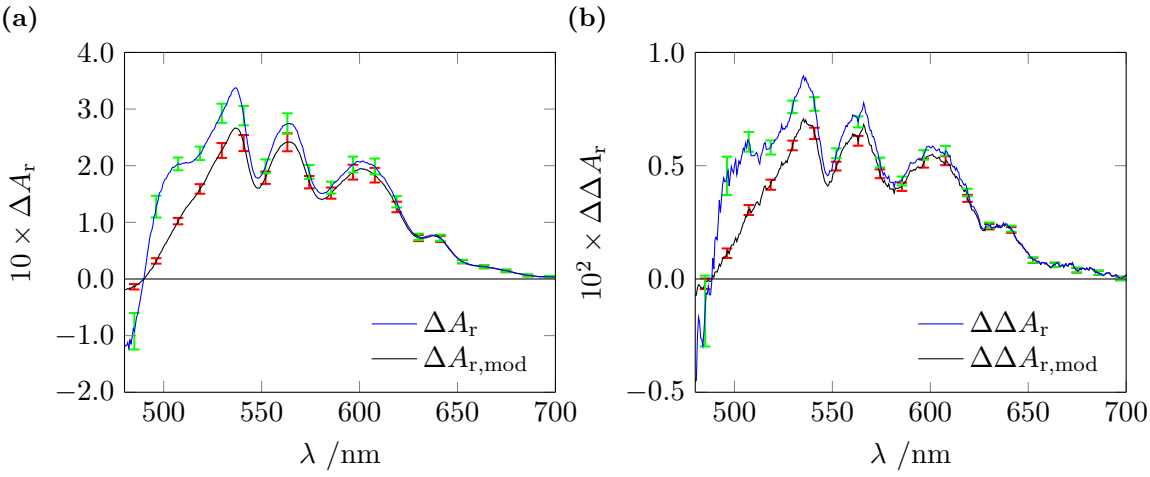


Figure 5.28: a) the modulated BBCEAS difference spectrum, $\Delta A_r(\lambda)$, of the 10 µM FMN 500 µM HEWL model system. b) the modulated BBCEAS action spectrum, $\Delta\Delta A_r(\lambda)$, of the FMN/HEWL model system. Also shown (in blue) is the application of the (I_0/I_{gs}) scaling factor to convert the data recorded in the modulated experiment (black) to observables, which match the steady state photoexcitation experiment (with accompanying increase in uncertainties). Error bars show the standard error of the mean of 100 acquisitions, each consisting of 5 kinetic steps. The 'r' subscripts indicate the data is not calibrated to absorbance values.

The uncalibrated difference spectrum is shown in Figure 5.28a), plotted as both

$\Delta A_{\mathrm{r,mod}}$ (black, Equation 5.11) and ΔA_{r} (blue, Equation 5.4). As with the CW data presented previously in the chapter, 'r' subscripts indicate data that is not calibrated to absorbances by the ln(10)CEF factor. The wavelength dependent mirror structure is highly apparent, which can successfully be removed by calibration using a measured CEF curve prior to the experiment (not shown).

The 450 nm photoexcitation power is 10 mW, but the 50% duty cycle results in an average power of only 5 mW over the course of the experiment. The relative size of the ground state bleach signal is much smaller in the modulated experiment compared with the CW photoexcitation (*cf.* Figure 5.6b). This can be explained by examining Figure 5.25b), in which it is evident that at a 10 Hz photoexcitation modulation rate (blue), the ground state does not have sufficient time to respond to the new conditions.

Figure 5.28b) shows the effect of applying a 13.5 mT magnetic field to the FMN/HEWL sample, with the data plotted as both $\Delta\Delta A_{\mathrm{r,mod}}$ (black) and $\Delta\Delta A_{\mathrm{r}}$ (blue), which are also related by a factor of I_0/I_{gs} (as shown in Section 5.9.2). The increase in absorbance due to the triplet-born $\mathrm{FMN}^{\bullet-}$ $\mathrm{TrpH}^{\bullet+}$ radical pair is clearly observable in agreement with the CW data in Figure 5.7b). The change extends to 650 nm, matching the absorption band of the radical species. A small negative effect is still visible in the ground state region, despite it being measured on a smaller ΔA bleaching signal, indicating the high sensitivity of the modulated variant.

The wavelength-dependent MFE (at 13.5 mT) is shown in Figure 5.29a), the flat region from $500 - 600$ nm confirming the exact spectral agreement between the $\Delta A(\lambda)$ and $\Delta\Delta A(\lambda)$ plots in Figure 5.28. The MFE is identical whether calculated from the modulated or true spectra as the I_0/I_{gs} factor cancels (compare Equations 5.14 and 5.8), as demonstrated by the complete overlay of the plots.

The MARY curve for the FMN/HEWL system is plotted in Figure 5.29b), obtained by performing the modulated BBCEAS experiment at a range of field values. The high SNR of this technique is evident, despite only being the average of 100 experimental runs (*cf.*

Figure 5.10b). Implementing the diode laser modulation increases the experimental time by a factor approximately equal to the number of kinetic series (in this case five), and so the number of MARY sweeps was reduced by the same factor to make the total length of the experiment comparable. This is the most important consideration when studying light-sensitive samples at low temperatures, as exposure to pump and probe beam should be reduced as much as possible, and the challenges of maintaining cavity quality are well documented.

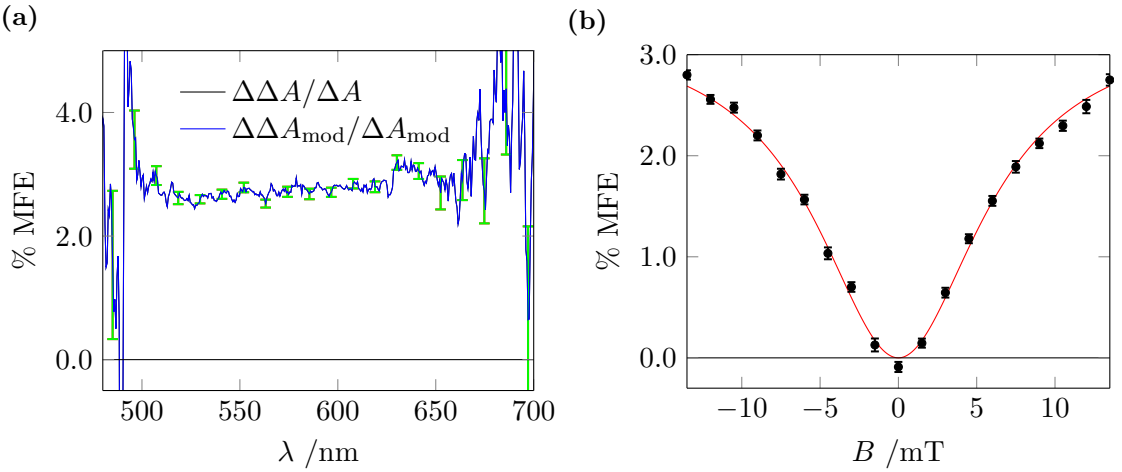


Figure 5.29: a) the fractional MFE of the FMN/HEWL model system as measured by modulated BBCEAS. The exact overlay of the two spectra is expected as the scaling factor (I_0/I_{gs}) simply cancels. The uncertainties are virtually identical in each case reflecting the dominance of the uncertainty in the $\Delta\Delta A$ spectrum relative to that of the scaling factor. b) the MARY curve for FMN/HEWL measured by modulated BBCEAS, averaged over the radical absorbance (530–630 nm).

Comparison of the extracted $B_{1/2}$ values from the steady state technique (6.7±0.24 mT, Table 5.2) and this modulated variant (6.4±0.4 mT) indicates that the modulation method provides a slightly less precise measurement of the field response. This is not very surprising as the field modulation in the CW variant (*ca.* 17 Hz) is faster than the 10 Hz diode laser modulation rate employed in this proof-of-principle study. Additionally, more averaging can be performed in the CW variant for the same experimental duration as repeated acquisition of the ground state absorbance is not performed.

While the widths of the MARY plots are in agreement, the magnitude of the MFE measured by the modulated technique is only 2.8% in contrast with 3.4% at 13.5 mT for the same sample under CW conditions (yellow data points in Figure 5.13a). This indicates different positions of the photochemical equilibrium, as predicted from Figure 5.25. A difference should also be expected given the more accurate knowledge of the ground state population provided by modulated BBCEAS.

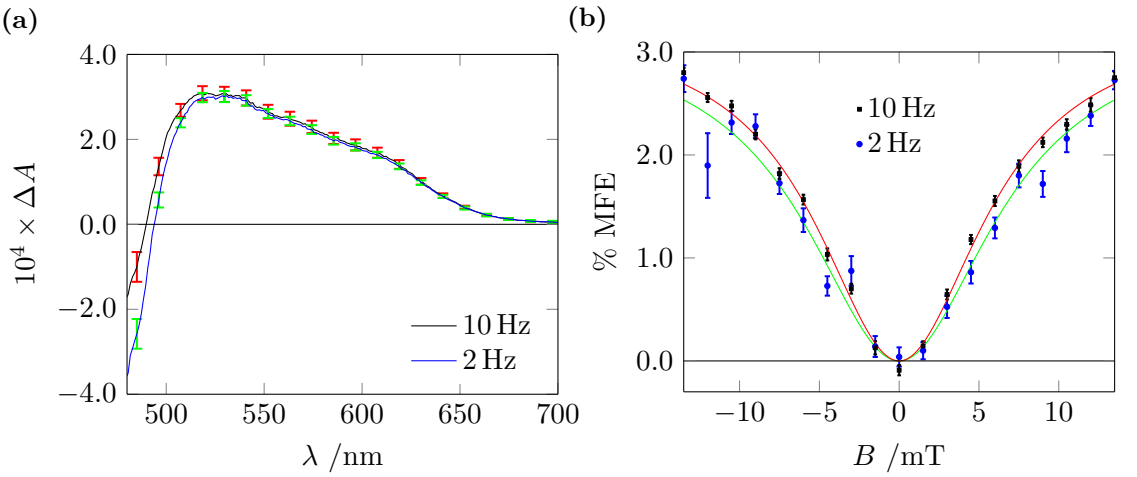


Figure 5.30: a) the effect of diode laser modulation frequency on the observed difference spectrum. The slower growing in of the ground state absorbance region, demonstrated in Figure 5.25b), results in a larger ground state bleach at a slower switching frequency. b) The MARY curves at the different repetition rates, which show a variation in percentage MFE due to a different equilibrium population of the radical species. The 2 Hz data (blue points, green fit) is the average of only 50 acquisitions at each field strength due to the prohibitively long nature of the experiment. Error bars represent a) the standard deviation and b) the standard error of the mean.

To confirm that the modulation rate affects the recorded spectra, the same experiment was run with the CCD acquisition rate cut to 2 Hz. The slower rate permits more time for the system to reach equilibrium before the acquisition and is predicted to favour ground state detection. This is confirmed by the larger ground state bleach signal seen in the $\Delta A(\lambda)$ spectrum plotted in Figure 5.30a). The radical signal is largely unaffected due to its own rapid re-equilibration.

The MARY curves for both experiments are overlaid in Figure 5.30b), indicating that

there is a small but measurable change in the MFE recorded at different modulation frequencies. The increased uncertainty in the 2 Hz dataset is not purely due to the fewer acquisitions recorded to reduce the experimental duration (50 vs 100, $\sqrt{2}$ decrease in SNR), but also reflects the long-term drift in the SCR source probe beam. This low frequency contribution becomes more dominant as the time between field-off and field-on readings is increased to *ca.* 2.5 s. Recording just 50 MARY sweeps still takes around 90 minutes, making these experimental parameters particularly unsuitable for the low temperature studies of protein samples.

In keeping with its original conception, the modulated variant only offers benefits at high acquisition rates. Fast modulation (50–100 Hz) should be the focus in future MFE studies of challenging biological molecules.

5.10 Conclusions and Future Directions

This chapter has demonstrated the successful application of a BBCEAS instrument to a myriad of MFE studies, involving both chemical and biological systems. The impressive combination of wide spectral coverage provided by a supercontinuum white light source probe, coupled with the high sensitivity afforded by optical cavity detection, has led to the detection of magnetic field induced absorbance changes orders of magnitude smaller than those accessible by analogous single-pass techniques. The simultaneous recording of entire absorbance bands using a CCD camera has considerably reduced experimental duration, which is a key consideration when studying light sensitive molecules with a CW technique.

The associated challenges of applying BBCEAS to the liquid phase have been successfully overcome by the use of fast field modulation, which has permitted magnetic field effects to be recorded on challenging protein samples, including a cryptochrome from an animal (the *Drosophila* fruit fly) which exhibits *in vivo* magnetosensitivity in behavioural assays. A low-field effect in a biologically relevant radical pair system has been observed

using an absorbance-based technique for the first time, a key piece of evidence in the elucidation of the mechanisms of magnetoreception in nature.

A further improvement to the technique has been developed, which involves the modulation of the photoexcitation experienced by the sample. As well as permitting more accurate values to be recorded throughout an experiment, the effective lock-in detection provided at sufficiently high repetition rates should provide a further increase in sensitivity, which is currently required to extract any low field effect present in the protein responses. The time integrated laser power striking the sample is also halved as a result of the modulation, providing even more suitable conditions for protein studies.

Despite being considered a CW technique, the millisecond time resolution of the BBCEAS instrument has been demonstrated by following the re-equilibration of a model system to changing light and magnetic stimuli. This provides a different route to the detection of enhanced magnetic field effects, previously studied by fluorescence. Along with power dependence studies, this information could be used to extract valuable and previously unreported values for crucial rate constants involved in the cryptochrome photocycle

The advantages of being able to collect the entire absorbance spectrum of a system in a single shot have been demonstrated in this work. However, the timescales accessible by this technique (millisecond and above) are still severely limited in comparison to the CRDS instrument described in the previous chapter (sub-microsecond), to the extent that all valuable kinetic information on the early radical pair behaviour is lost. What is required is an instrument that is able to record microsecond kinetics at a range of wavelengths simultaneously, while maintaining the high sensitivity of the cavity-based detection demonstrated thus far. The proposed solution, a brand new instrument developed for this project and known as Optical Cavity-enhanced Transient Absorption Spectroscopy (OCTAS), is the subject of the next chapter.

Chapter 6

Optical Cavity-Enhanced Transient Absorption Spectroscopy (OCTAS)

6.1 Introduction

The previous two chapters have demonstrated the suitability of existing cavity-enhanced detection methods for MFE studies by their successful application to chemical and biological systems. CRDS can monitor kinetic processes occurring on a sub-microsecond timescale, although temporal and spectral information must be collected in a step-wise manner by scanning both the frequency of the tunable OPO used as the probe beam and the time delay between it and the pump pulse. In contrast, utilising a white light SCR source as the probe beam coupled with a CCD detector gives BBCEAS the ability to monitor the entire visible absorbance spectrum in a single acquisition, although the CW nature of the photoexcitation restricts the time resolution.

Both techniques represent significant advances in sensitivity over existing methods in their application to measuring magnetic field effects. However, neither is perfectly suited

to the study of SCRPs in flavin-based systems. The plethora of species which coexist in solution evolve and interconvert on timescales of microseconds, leading to complex spectra composed of overlapping absorbance bands. In choosing which of the existing CRDS or BBCEAS instruments to use to investigate a new system, a compromise is made between acquiring temporal or spectral information at the expense of one another.

In an effort to address this, here a powerful new technique is introduced, Optical Cavity-enhanced Transient Absorption Spectroscopy (OCTAS), developed during this project. It offers the ability to simultaneously monitor microsecond timescale kinetics across wide spectral regions, while maintaining the crucial sensitivity gains of the existing cavity techniques already proved to be hugely beneficial in the study of magnetic field effects. That detailed spectral and temporal information are no longer mutually exclusive is an exciting advance in cavity-enhanced spectroscopy in general.

This chapter introduces the new OCTAS instrument, explaining how it can be used for MFE studies, and presents successful proof-of-principle results on the model systems prevalent in the earlier chapters of this thesis. Its suitability for biological MFE detection is demonstrated by the high quality of data obtained in a study of the animal cryptochrome, *Xl*Cry. Field effects are clearly resolved in all systems studied, with comparable signal-to-noise to the existing cavity-based techniques. Comparison of microsecond MFE evolution of each system is made with data obtained at a single wavelength by CRDS, which demonstrates satisfyingly good agreement despite the fundamentally different methodology used to acquire and analyse the data in each case.

6.2 Experimental

6.2.1 The OCTAS instrument

OCTAS is essentially a BBCEAS experiment at heart, using a white light SCR source to provide a continuous broadband probe. However, in order to follow radical pair kinetics

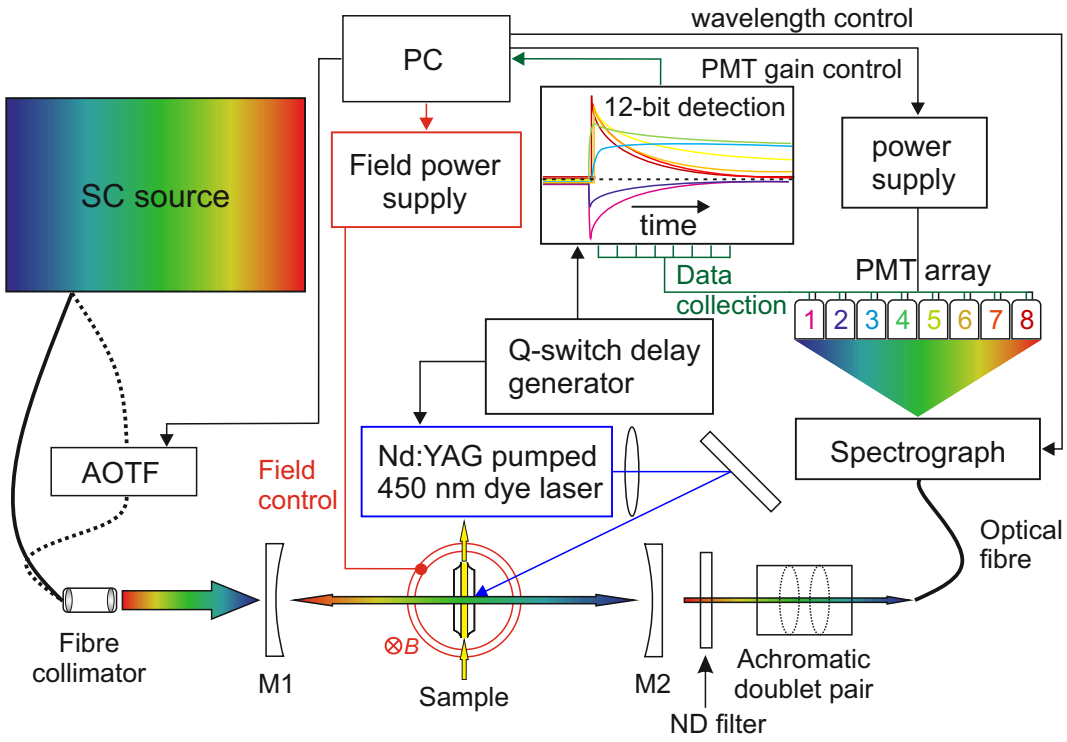


Figure 6.1: A schematic representation of the OCTAS experimental set-up. Similarities should be noted with the BBCEAS set-up, shown in Figure 5.1. The cavity, SCR source and spectrograph are common to both, while the detection and photoexcitation are different. Due to geometrical constraints, the transmission of dispersed light to the PMTs is not through space as indicated, but via an optical fibre array (not shown).

over microseconds the short photoinitiation pulse required is provided by a dye laser in place of the CW diode laser. Fast PMT detection is used to detect absorbance as a function of time and wavelength instead of an integrating CCD camera. A schematic of the experimental apparatus is shown in Figure 6.1. OCTAS can be thought of as a cavity-enhanced variant of the single-pass TA instrument currently used in the group, but one that is capable of simultaneous spectral acquisition via the use of an array of eight PMTs rather than a single detector. If the optics are arranged in such a way that each PMT is only sensitive to a certain wavelength region of light then low resolution spectral information can be recorded concurrently, in real time.

To achieve this, eight optical fibres are held in fixed relative positions (2 mm centre-

to-centre) by a custom made fibre mount,[A] placed at a second camera port of the Andor spectrograph (SR303i). The SCR source used as the probe beam (NKT photonics) and the high reflectivity broadband mirrors used to form the optical cavity (Layertec, $R = 99.85$–99.98%) are the same as used in the BBCEAS studies reported in the previous chapter. Once the light leaking out of the rear cavity mirror has been collected and transferred to the spectrograph, the white light beam is dispersed onto the fibre array and each collects light from a different region of the visible spectrum by virtue of its spatial position. As each fibre has a finite width (1 mm), a narrow range of wavelengths of light is collected and transmitted to the associated PMT detector. This PMT signal is recorded on an oscilloscope (LeCroy, HDO8058, 12-bit). The gain voltage is applied via a power supply controlled by PC software and is set to a value that provides a water reading (V_0) of approximately 100 mV at the impedance settings described below.

The data is collected for a fixed spectrograph grating position, providing data at over eight spectral regions simultaneously. The optical fibres are positioned so their centre-to-centre separation is *ca.* 1 mm, which corresponds to a peak-to-peak separation in the wavelength coverage of approximately 30 nm (see Section 6.2.2). Intermediate wavelength regions are accessed by stepping the angle of the spectrograph grating via PC control. This changes the wavelength range to which each PMT is sensitive, allowing a mapping of the full spectrum without gaps. In the following studies, the grating position is shifted to the red in two 10 nm steps to obtain an overall wavelength resolution of 10 nm.

To guard against any systematic error in the signal e.g. caused by a reduction in cavity finesse, the grating position was varied at regular intervals throughout the experiment, in a random order. The 1000 measurements at each wavelength and field point in the final data consists of 5 measurements per grating position (cycled in a random order), each composed of 20 acquisitions at the required magnetic field. Each acquisition comprises 10 averages on the scope to reduce the data transfer time as a proportion of the overall

[A] Charlie Evans, PTCL workshops

experiment duration.

A custom-written C++ program[B] synchronises the acquisition of data from the oscilloscope with the application of a magnetic field via the same Helmholtz coil arrangement used for BBCEAS studies. It also controls the random variation in the grating position. The oscilloscope and YAG laser pulse are synchronised by using a delay generator along with a variable pulse divider that allows the Q-switch to be fired at different rates. The YAG flashlamps fire at a continuous 20 Hz while the Q-switch repetition rate can be varied, effectively dropping pulses, to allow the sample and field time to recover. All model systems experiments reported in this chapter were performed at an acquisition rate of 5 Hz as the water-cooled coils can be run at a faster repetition rate than the air-cooled analogues on the CRDS experiment. For comparability with CRDS, and to protect the sample from photodegradation, the *Xl*Cry data was collected at 3.33 Hz.

Early data that was recorded without reference to a water reading showed an artefactual background increase at long timescales. This was discovered to be due to electronic noise from the YAG flashlamp. This can be eliminated by recording a water reference prior to the experiment as the artefact cancels on calculating a BBCEAS-style observable. The data analysis is explained in detail in the next section.

6.2.2 Detection wavelength characterisation

To map out the wavelength region each PMT is sensitive to, the spectral output from the SCR source is scanned in 1 nm steps using the AOTF. The cavity mirrors are removed to increase light transmission to the detectors and the voltage reading on the oscilloscope is recorded, shown in the lower half of Figure 6.2. The spectral separation between adjacent channels is around 30 nm and the FWHM of each profile is approximately 20 nm. Spectral resolution can be increased by adjusting the grating position via the Andor spectrograph software, shifting the central wavelengths of all channels.

[B] Jonathan Storey, Timmel Group

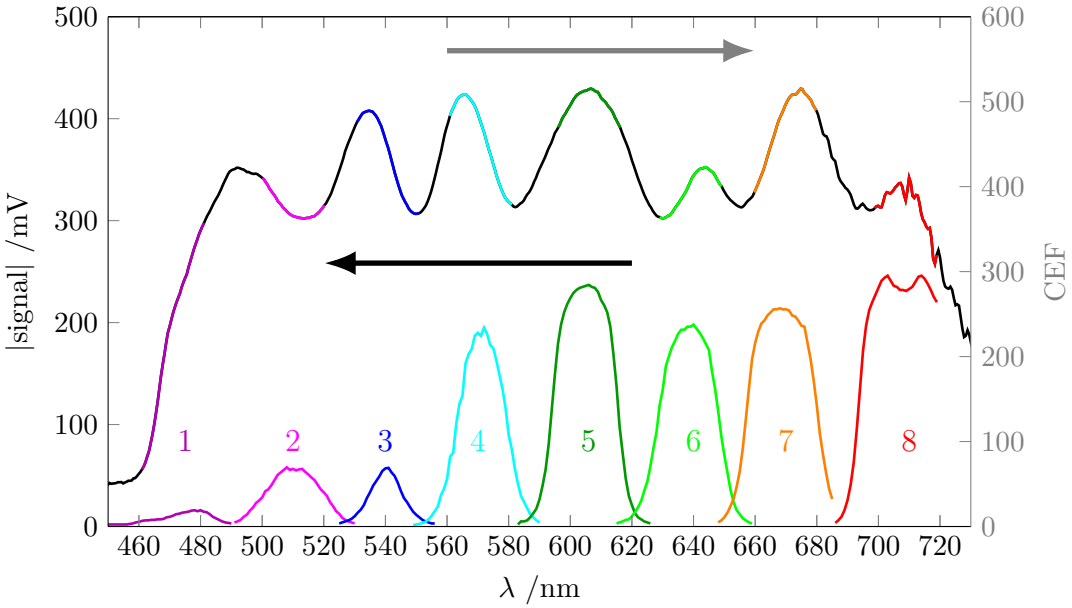


Figure 6.2: Lower: the absolute voltage signals recorded on the eight PMTs that comprise the OCTAS detection (colour-coded to represent wavelength region). The lower output intensity of the SCR source at short wavelengths is apparent. Upper: a typical Cavity Enhancement Factor (CEF) plot (black) recorded using the CCD camera by the method explained in Section 3.7.1, at a spectrograph input slit width of 1 mm.

As OCTAS uses CEAS detection (i.e. a continually pumped optical cavity) a CEF calibration must be performed to convert data to absorbances (see Section 3.7.1). A typical CEF profile is shown in the upper half of Figure 6.2, recorded on the CCD camera by BBCEAS. The colour-coded spectral regions are averaged over to calibrate data collected by the corresponding PMT, ±10 nm either side of the maximum peak intensity for that detector. It is purely coincidental that at this spectrograph grating position some of the peaks in the CEF match the fibre positions.

6.2.3 Impedance and time-response

To counteract the low light intensity, exacerbated by fibre insertion losses and monochromator transmission, the impedance is artificially increased. A higher value of 1 kΩ is applied at each end of the BNC cable (at both the PMT and oscilloscope input) using

custom made impedance loads.[C] The overall impedance of the system is therefore 500 Ω. The internal impedance of the oscilloscope is changed from the default 50 Ω setting to its higher 1 MΩ value. This has permitted the acquisition of the high quality data presented in this chapter.

Any effect on the time response of the instrument has been assessed via the comparison with the values extracted from CRDS studies performed in Chapter 4. The OCTAS instrument suffers from the same PMT blinding as the single-pass TA instrument used in the group, which is caused by a combination of pump pulse scatter and sample fluorescence. The accepted value for the TA instrument response is 0.7 µs. A further consideration in time-resolved cavity-enhanced studies is the effect of trapping the circulating light in the cavity. The ring-down time of the system provides an effective lower limit to the time resolution of a cavity-based technique (without deconvolution being required, see Section 4.3.4). The inferred ring-down time for the optical cavity system reported here varies between approximately 250–350 ns, based on:

$$\tau(\lambda) = \frac{L}{c(1 - R_{\text{eff}}(\lambda))}, \tag{6.1}$$

where L is the 0.2 m cavity length used in OCTAS, c is the speed of light, and $(1 - R_{\text{eff}}(\lambda))$ is calculated as $\text{CEF}(\lambda)^{-1}$ which varies between 400–500 depending on the wavelength (see upper plot in Figure 6.2). The time constant for the PMT model used in these studies has previously been determined as 50 ns for a 62.5 mV output at an impedance of 500 Ω.[220] For the extraction of kinetic parameters reported in this work, a conservative instrument response time of 1 µs is assumed, and no data earlier than this is included in fitting procedures.

[C] Neville Baker, PTCL workshops

6.2.4 Measuring MFEs

Due to the CW nature of the probe beam in common with CEAS methodologies, the analysis of OCTAS data bears close resemblance to that laid out for BBCEAS in Section 5.2.2. The major difference is that signals are measured in voltages on the oscilloscope, with V taking the place of intensity (I) output from the CCD software. The signal itself now also has a time dependence, $V(t)$.

In the following section, the data analysis procedure for a single PMT will be described. This is identical for all detectors and the final step combines all of the data, either for averaging time decays over wide wavelength bands (benefiting from the Fellgett advantage of multiplexing), or for displaying as a contour plot as a function of both wavelength and time. In BBCEAS, the absorbance of a sample is calculated as:

$$A(\lambda) = \frac{1}{\ln(10)\mathrm{CEF}(\lambda)} \left(\frac{I_0(\lambda)}{I(\lambda)} - 1 \right), \tag{6.2}$$

where A is the single-pass absorbance value at each wavelength, I_0 is the light intensity transmitted by an empty cavity (i.e. one containing water in the sample cell), I is the intensity transmitted by a cavity containing the absorbing species of interest, and CEF is the cavity enhancement factor.

Because CEAS absorbances are calculated from ratios of intensities, and the voltage signal of the PMT is directly proportional to the intensity of light it detects, raw voltages from the scope can be used in these expressions. For an individual PMT detector in OCTAS, there is no wavelength resolution, but the data represents a wavelength band *ca.* 20 nm in width (see Figure 6.2, lower plots). To take this into account, the CEF is recorded exactly as for a standard BBCEAS experiment, using the CCD camera, although with the wider slit width used for OCTAS to allow maximum light throughput. This has very little effect on the spectral structure of the measured CEF, but is done for completeness. The ND filter is set so that the I_0 reading in the CEF acquisition is maximised without

saturating, before being set to maximum transmission for the OCTAS experiment. The mean value of the CEF over the wavelength band detected by the PMT is taken and applied to the data (Figure 6.2, upper plot).

The PMT gains are set by choosing a value of 100 mV for the V_0 reading on the scope and applying voltage to the PMTs until this level is reached. A full OCTAS experiment is then run with water in the sample cell. This has several functions: i) the V_0 level is known precisely due to the large number of acquisitions taken, ii) reference back to the V_0 signal is necessary for absorbance values to be calculated from BBCEAS/OCTAS detection (continual cavity pumping), iii) any artefacts in the data common to the water and sample readings disappear on taking the ratio, iv) a negative control confirming that water does not show an artefactual MFE as detected by our experiment is performed automatically each day, providing confidence that any subsequent results are real. The PMT gains are then held fixed at this value for the remainder of the day's experiments, equivalent to the ND filter being maintained in the same position during the BBCEAS measurements in Chapter 5.

The disadvantages of running a water reference are a doubling of the experimental time (although this is not harmful to the sample in terms of photodegradation), and propagation of noise onto the measured absorbance and MFE values. For comparability with sample data 1000 acquisitions of the water signal were recorded at each wavelength, and an average taken for each time point. However, due to the long-term drift in the SCR source this is likely to introduce more uncertainty than strictly necessary into the results. A full Allan deviation study (such as that reported in Section 3.8.2) should be carried out to determine the optimum number of water readings to take, but this has not been performed here.

The water data for each PMT and grating position is collected and analysed, but it is not averaged over all time points to ensure removal of the time-dependent electronic artefact. Acquiring the water spectrum with the pump beam unshuttered also allows

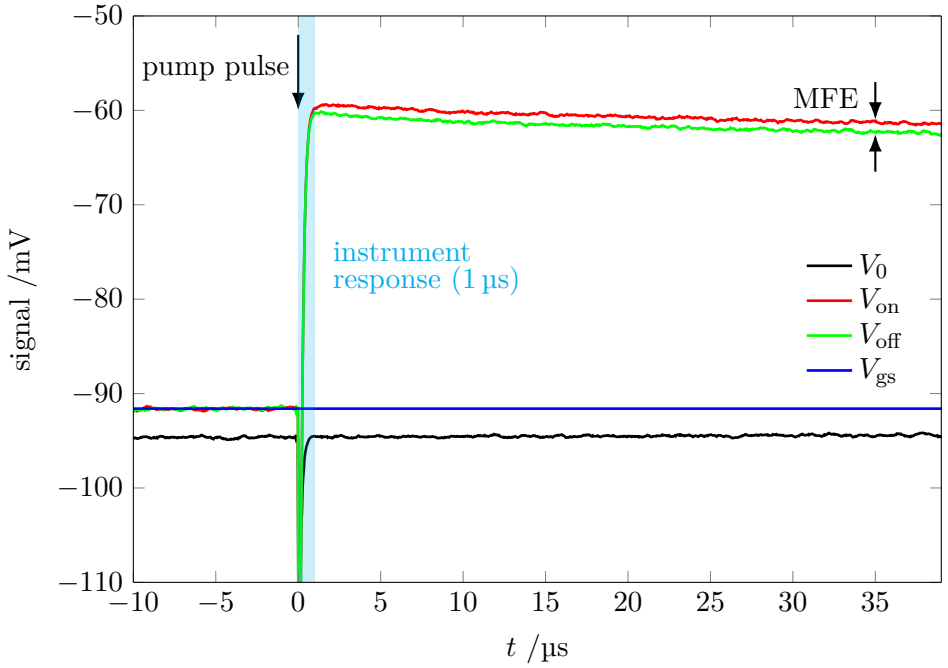


Figure 6.3: Raw signals as recorded on the oscilloscope during an OCTAS experiment (taken from the FMN/HEWL study in Section 6.3, $\lambda = 530\,\text{nm}$). The PMT gain is set so that the V_0 signal (water, black) is close to 100 mV and held constant throughout. V_{on} (red) and V_{off} (green) indicate the signal due to the sample in the presence and absence of an 18 mT magnetic field, respectively. A difference is only seen after photoexcitation produces radical species at $t = 0$. The data collected before the pulse ($t < 0$) is averaged and used as a measure of the sample ground state (V_{gs}, blue). The pale blue shading represents the time response of the instrument, before which data is unreliable, and will be added to all relevant figures in the remainder of this work.

the scatter to be removed from the sample data in the absorbance calculation, as it is expected to be constant. This leads to a much reduced peak due to scatter in the difference spectrum. Any remaining small negative peak can be assigned to the sample fluorescence.

The sample of interest is flowed through the sample cell at the standard rate of $0.25\,\text{ml}\,\text{min}^{-1}$. A separate ground state measurement is not required as the absorbance of the ground state of the protein solution can be calculated from the negative time points collected on the scope (i.e. before the photoexcitation laser pulse). This is shown clearly in Figure 6.3 (blue line). These points can only be used as a measure of the ground state when the sample fully recovers from the photoexcitation pulse within the repetition rate of

the experiment (5 Hz for model systems corresponding to a maximum permissible recovery time of 200 ms). This treatment is valid for all of the studies reported in this chapter.

Individual PMTs have no wavelength resolution but do provide a temporal response. For a given PMT detector, n, and grating position, m, which is sensitive to a wavelength range $\lambda_{m,n}$, the absorbance of a sample is defined as:

$$A_{\lambda_{m,n}}(t) = \frac{1}{\ln(10)\mathrm{CEF}(\lambda_{m,n})}\left(\frac{V_{0,\lambda_{m,n}}(t)}{V_{\lambda_{m,n}}(t)} - 1\right), \tag{6.3}$$

and the ground state absorbance of the same sample is taken as the average of all the negative time data i.e. before blue-light photoexcitation ($t < 0$):

$$A_{\mathrm{gs},\lambda_{m,n}} = \frac{1}{\ln(10)\mathrm{CEF}(\lambda_{m,n})}\left[\mathrm{mean}\left(\frac{V_{0,\lambda_{m,n}}(t<0)}{V_{\lambda_{m,n}}(t<0)}\right) - 1\right], \tag{6.4}$$

where V_0 and V are the raw voltages recorded by the oscilloscope with water and sample in the cell respectively. Note that this shows no time dependence as the mean value is used.

The differential absorbance at any time, $\Delta A(t)$, is defined as the difference in absorbance signals with and without photoexcitation, and is given by:

$$\begin{aligned}\Delta A_{\lambda_{m,n}}(t) &= A_{\lambda_{m,n}}(t) - A_{\mathrm{gs},\lambda_{m,n}} \\ &= \frac{1}{\ln(10)\mathrm{CEF}(\lambda_{m,n})}\left[\frac{V_{0,\lambda_{m,n}}(t)}{V_{\lambda_{m,n}}(t)} - \left(\mathrm{mean}\left(\frac{V_{0,\lambda_{m,n}}(t<0)}{V_{\lambda_{m,n}}(t<0)}\right)\right)\right].\end{aligned} \tag{6.5}$$

In the absence of photoexcitation ($t < 0$) this gives the expected result that the $\Delta A(t)$ signal is zero within uncertainty.

Similarly, the absorbance in the presence of an applied magnetic field can be defined as:

$$A_{B,\lambda_{m,n}}(t) = \frac{1}{\ln(10)\mathrm{CEF}(\lambda_{m,n})}\left(\frac{V_{0,\lambda_{m,n}}(t)}{V_{B,\lambda_{m,n}}(t)} - 1\right), \tag{6.6}$$

where V_B is the voltage signal in the presence of a magnetic field, and hence the differential

absorbance in an applied magnetic field is given by:

$$\begin{aligned}\Delta A_{B,\lambda_{m,n}}(t) &= A_{B,\lambda_{m,n}}(t) - A_{\mathrm{gs},\lambda_{m,n}} \\ &= \frac{1}{\ln(10)\mathrm{CEF}(\lambda_{m,n})}\left[\frac{V_{0,\lambda_{m,n}}(t)}{V_{B,\lambda_{m,n}}(t)} - \left(\mathrm{mean}\left(\frac{V_{0,\lambda_{m,n}}(t<0)}{V_{\lambda_{m,n}}(t<0)}\right)\right)\right].\end{aligned} \tag{6.7}$$

The time-resolved action spectrum, $\Delta\Delta A(t)$, is the change in absorbance signal induced by the external field and can be defined as:

$$\begin{aligned}\Delta\Delta A_{\lambda_{m,n}}(t) &= \Delta A_{B,\lambda_{m,n}}(t) - \Delta A_{\lambda_{m,n}}(t) \\ &= \frac{1}{\ln(10)\mathrm{CEF}(\lambda_{m,n})}\left(\frac{V_{0,\lambda_{m,n}}(t)}{V_{B,\lambda_{m,n}}(t)} - \frac{V_{0,\lambda_{m,n}}(t)}{V_{\lambda_{m,n}}(t)}\right) \\ &= \frac{V_{0,\lambda_{m,n}}(t)}{\ln(10)\mathrm{CEF}(\lambda_{m,n})}\left(\frac{V_{\lambda_{m,n}}(t) - V_{B,\lambda_{m,n}}(t)}{V_{B,\lambda_{m,n}}(t)V_{\lambda_{m,n}}(t)}\right).\end{aligned} \tag{6.8}$$

The time-dependent percentage MFE is defined as the percentage change in absorbance induced by the field on the absorbance change induced by the photoexcitation (i.e. the percentage effect on the radical population):

$$\mathrm{MFE}_{\lambda_{m,n}}(t) = \frac{\Delta\Delta A_{\lambda_{m,n}}(t)}{\Delta A_{\lambda_{m,n}}(t)} \times 100. \tag{6.9}$$

As for the BBCEAS experiment in the previous chapter, the MFE is independent of CEF calibration. The dynamic range considerations are of little importance in OCTAS as currently the light transmission is maximised as far as possible. Any increase in light throughput would be better used reducing the applied gains on the PMT to minimise any amplified electronic noise on the signal.

This analysis is performed for each combination of PMT detector and grating position to give a maximum of 24 wavelength points with highly resolved temporal information, determined only by the number of data points recorded in an oscilloscope trace. As evident from Figure 6.2, however, the light intensity reaching PMT 1 is very low to the

point where little signal is discernible above the baseline. This precludes any measurement of the ground state population of flavin-based systems until a SCR source with increased power to shorter wavelengths is available, or an alternative approach is found to boost the sensitivity in this region.

The following sections present the results of MFE studies performed on the well-characterised flavin-based model systems used to characterise the capabilities of the other cavity-enhanced techniques in this thesis. First the large field effect in the intermolecular FMN/HEWL system is used as a proof-of-principle demonstration, followed by a comparison of the (intramolecular) FAD and biologically relevant (intermolecular) FAD/W system is examined. Having characterised and optimised the new instrument with these successful proof-of-principle studies, a MFE study on the *Xl*Cry system is performed with results in excellent agreement with those obtained by the CRDS technique in Chapter 4.

6.3 OCTAS Studies of FMN/HEWL

6.3.1 OCTAS detection of MFEs

The difference spectrum of FMN/HEWL recorded by OCTAS is shown in Figure 6.4a). Due to the high sensitivity afforded by the optical cavity detection, a low pulse energy can be used for photoexcitation (200 µJ). The reported data is the average over two wavelength regions to further enhance the SNR. The red curve shows the pure FMN triplet absorbance ($700-730$ nm) with its characteristic fast decay, while the black curve represents primarily the free radical absorbance band (520–600 nm) showing a short-lived component due to overlapping triplet absorbance and the long-lived free radical population.

The effect of an 18 mT magnetic field is shown by the dashed lines (green and blue for radical and triplet, respectively). The increase in the free radical absorbance is more clearly shown by the $\Delta\Delta A(t)$ plot in Figure 6.4b), the value of which increases to a steady value within 3 µs. The increase in free radical absorbance confirms the results from the

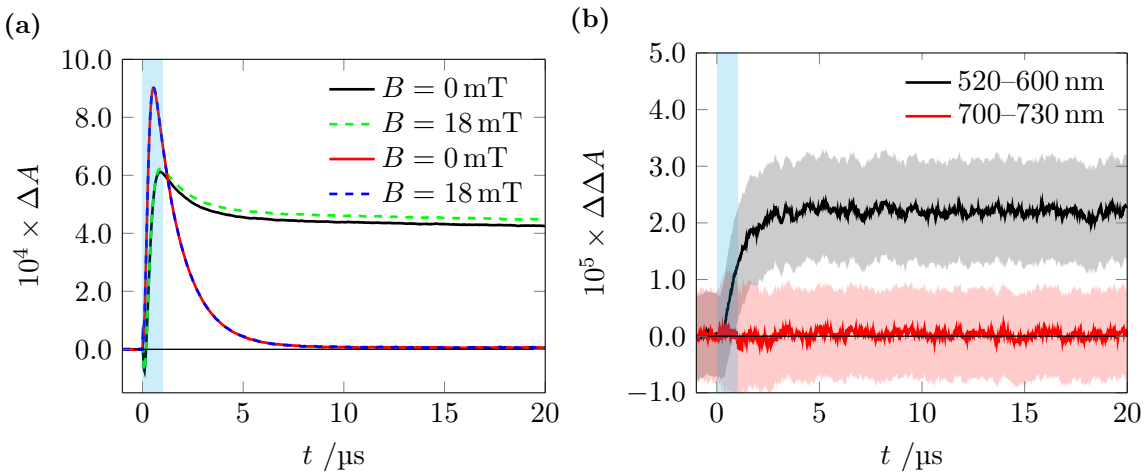


Figure 6.4: a) $\Delta A(t)$ decay profiles for 10 µM FMN 500 µM HEWL, with 200 µJ per pulse photoexcitation. Averaged over primarily the radical absorbance band (520–600 nm, black) and the pure triplet absorption band (700–730 nm, red). The dashed lines (green/blue respectively) show the response to an applied 18 mT magnetic field. b) $\Delta\Delta A(t)$ decay profiles for FMN/HEWL, averaged over the radical absorbance band (black) and the triplet absorption band (red). The shaded regions represent the SEM of 1000 measurements.

other techniques presented thus far, namely that the SCRP is triplet-born and so the Zeeman interaction favours the production of free radical species rather than spin-allowed recombination to the ground state. In contrast, the triplet region is too short-lived to show a response to the field in this system, and zero effect is seen in the $\Delta\Delta A(t)$ spectrum (red).

A more detailed view of the radical $\Delta A(t)$ decay trace is plotted in Figure 6.5a) where the fast component of the decay is clearer. Shaded regions in the plots correspond to the SEM. The orange dashed line is the result of a biexponential fit to the data, which gives a fast time constant of 0.74 µs and a slow time constant >100 µs which cannot be determined more accurately from this data. The fast time constant matches the single exponential decay constant of the triplet region, which is shown in Figure 6.5b).

Instead of averaging multiple decay profiles recorded at different wavelengths, they can be arranged to form a spectrum. Figure 6.6a) is the result of taking all of the traces recorded on each PMT at the different grating positions and sorting them in order of increasing wavelength. Different time bands can be averaged over (here 0.5 µs wide, colours

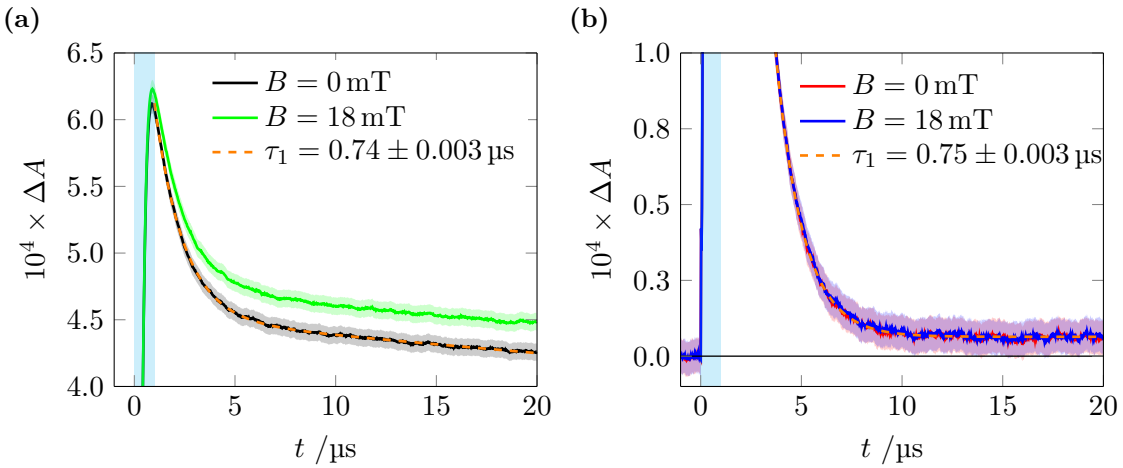


Figure 6.5: a) Expanded version of the $\Delta A(t)$ radical decay profile for FMN/HEWL (averaged 520–600 nm) in the presence (green) and absence (black) of an 18 mT magnetic field. b) Expanded version of the $\Delta A(t)$ triplet decay profiles for FMN/HEWL (averaged 700–730 nm) in the presence (blue) and absence (red) of an 18 mT magnetic field. The lack of a MFE on the short-lived species is clear. The shaded regions on all plots indicate the SEM of 1000 measurements.

are described in the legend) to map out the change of the spectral shape in time. The free radical concentration can be seen to remain virtually constant over the timescale shown here (1–8 µs), while the intense triplet band present at 1 µs has almost completely disappeared within 5 µs. At 8 µs, the spectrum strongly resembles the difference spectrum recorded under steady-state illumination measured by BBCEAS (Figure 5.6), which favours the detection of the long-lived free radical species over the fast decaying triplet. These time points were chosen to exemplify the most interesting kinetic timescales of this system, but the (variable) timebase on the oscilloscope is set to 4 ns resolution providing a huge range of possibilities for analysis.

Gaps at 590 nm and 700 nm are due to the separation between optical fibres in the mount not being exactly even (here between channels 4 and 5, and 7 and 8, respectively). This could be remedied by adding an extra grating position, although this would increase the experimental time by 33% for the sake of two extra points in regions that are sufficiently well described by the surrounding data. It should be remembered at this stage that

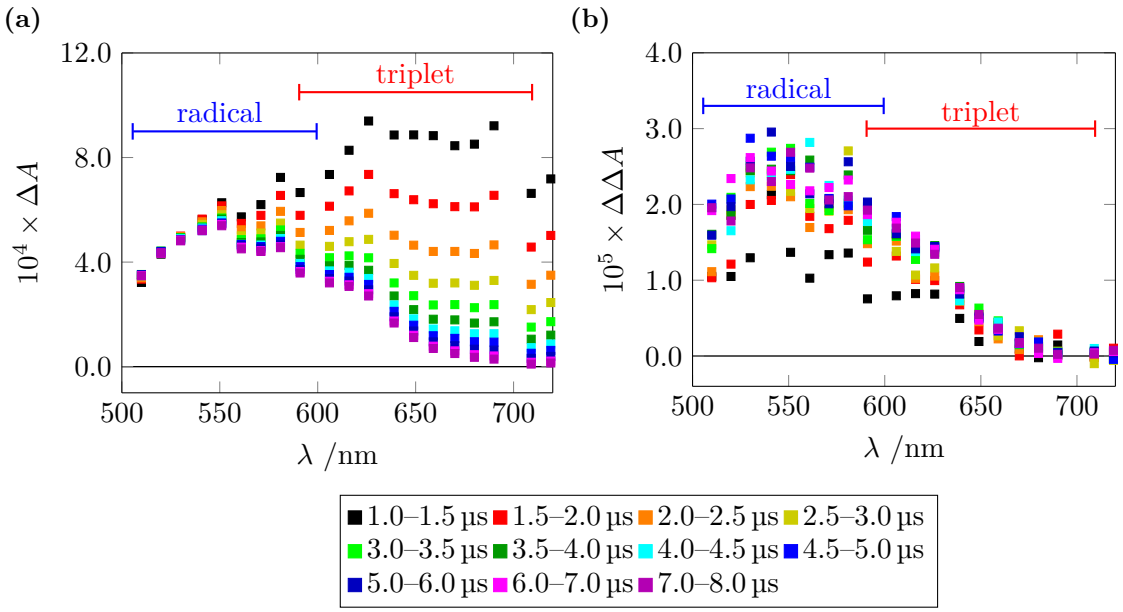


Figure 6.6: a) $\Delta A(\lambda)$ spectra for 10 µM FMN 500 µM HEWL, at a variety of delay times after 200 µJ 450 nm photoexcitation (see legend for details). The long-lived radical species (500–650 nm) and the fast-decaying triplet state (> 650 nm) are clear. b) $\Delta\Delta A(\lambda)$ spectra for FMN/HEWL at the same delay times. Comparison with a) demonstrates that only the long-lived radical species exhibits a response to the applied 18 mT magnetic field, and the fast-decaying triplet state shows no field sensitivity. In both plots each wavelength point should be considered as having an uncertainty of ±10 nm due to the finite width of the profiles shown in Figure 6.2 (not shown for clarity). All data is the average of 1000 measurements.

although represented here by single points, these wavelengths are only the peaks of a wide (≈ 20 nm) Gaussian profile collected by the optical fibre. Error bars are not shown here for clarity, but it is valid to perform significant spectral smoothing without the loss of any information.

Figure 6.6b) shows the effect of the application of an 18 mT magnetic field at each wavelength. After an initial growth period the effect is constant within noise levels, and only exhibited by the free radical absorbance spectrum. The spectral shape of the $\Delta\Delta A(\lambda)$ profile is in close agreement with the (purple) $\Delta A(\lambda)$ spectrum at 7.0–8.0 µs in Figure 6.6a). The triplet region shows a distinct lack of any kind of magnetic response on the timescales observable here.

The kinetic information in Figure 6.4 and the spectral information in Figure 6.6 can be combined into a 2-D surface plot, similar to those produced from the CRDS data in Chapter 4, but with much enhanced resolution, particularly in the time dimension.

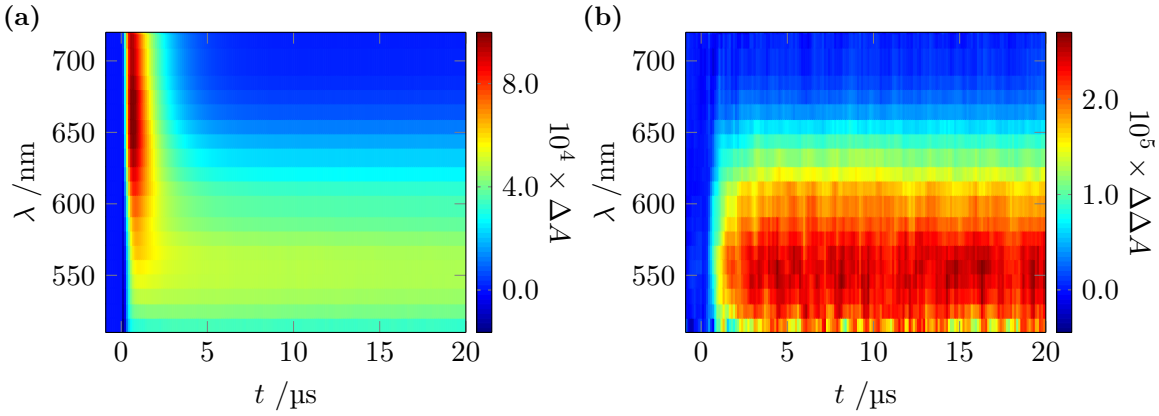


Figure 6.7: a) $\Delta A(\lambda, t)$ surface plot for 10 µM FMN 500 µM HEWL, obtained by combining the multiple decay traces recorded by individual PMT channels on the oscilloscope. The long-lived radical species (500–650 nm) and the fast-decaying triplet state (> 650 nm) are both discernible. b) $\Delta\Delta A(\lambda, t)$ surface plot for FMN/HEWL. Comparison with a) indicates that only the long-lived radical species exhibits a magnetic field response in this system. In both plots the data is the average of 1000 measurements and is smoothed by a 5-point moving average in the wavelength dimension (*ca.* 50 nm).

Figure 6.7a) shows the $\Delta A(\lambda, t)$ surface plot for the FMN/HEWL system. The broad wavelength profile on each detector means the data can be smoothed up to 50 nm in the wavelength direction with little loss of information. Clearly visible is the long-lived free radical absorbance (yellow/green, 510–620 nm) and the intense, fast decaying triplet band (red, 560–720 nm). The increase in absorbance on applying an 18 mT magnetic field is shown in Figure 6.7b) as a $\Delta\Delta A(\lambda, t)$ surface. The red region indicates an increase in absorbance and matches the spectral signature of the free radical species in a) exactly. The lack of a triplet response is clearly demonstrated.

For comparability between techniques, the percentage MFE can be calculated as a function of wavelength and time by dividing these surface plots (or more precisely the matrices from which they are constructed) by one another. The results are shown in

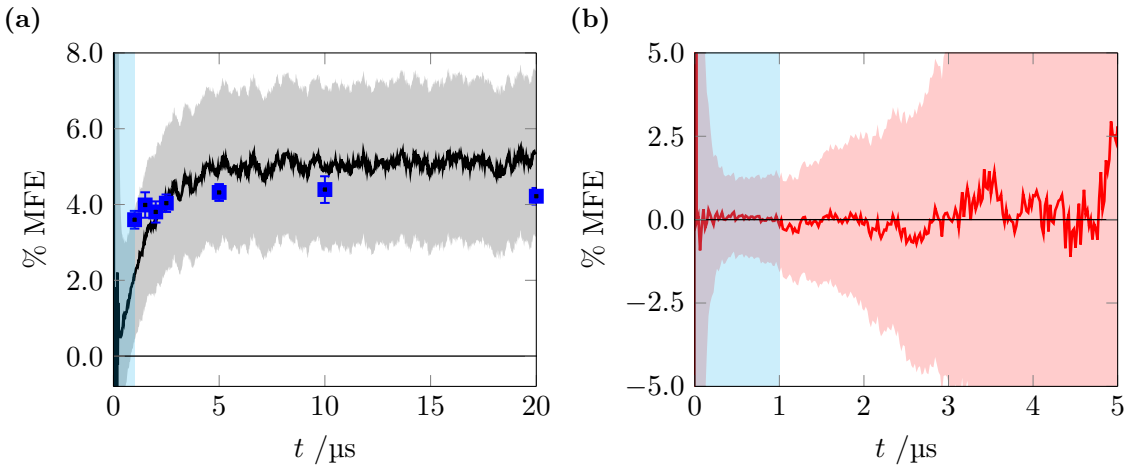


Figure 6.8: a) MFE of the FMN/HEWL system, averaged over the radical absorbance region (520–600 nm). The effect grows in and reaches its maximum value (*ca.* 5%) within 5 µs after which it remains approximately constant on the timescale of the experiment. Overlaid in blue is the MFE calculated from the CRDS data shown in Figure 4.3 at 540 nm and 19 mT. b) MFE of the FMN/HEWL averaged over the purely triplet absorbance region (700–730 nm). The shaded regions in both plots represents the SEM of 1000 measurements.

Figure 6.8, averaged over the same radical and triplet bands as the data in Figure 6.4. In the radical region, the effect is positive (as already discussed) and reaches its maximum value around 5 µs, after which it remains constant around 5%. The uncertainty in this value is considerable but not surprising when given the low light level and the need for calibration via the water reference. In BBCEAS, the I_0 reading (and its associated noise) could be neglected in the calculation of MFE to reduce the uncertainty. For OCTAS, however, this is not possible due to the time-dependent electronic artefact that it removes from the data.

Figure 6.8a) also shows data from the same experiment performed by CRDS overlaid in blue. The results are in close agreement from 2 µs onwards, although all data agree within uncertainties. The slight discrepancy in the 1 µs and 1.5 µs points could be due to the slow time response of the OCTAS instrument due to the 1 kΩ impedance, an inaccuracy in the CRDS data due to not deconvoluting the ring-down signal from the absorbance decays (Section 4.3.4), or a combination of the two. Despite this, the agreement between

two entirely unrelated techniques is satisfying.

Figure 6.8b) confirms the lack of magnetic response by the triplet species, which is measurably zero below 5 µs and then enters a noise dominated regime as the $\Delta A(t)$ decays towards zero.

6.3.2 Global analysis

The high quality of data obtained by the OCTAS instrument, good temporal and spectral resolution coupled with low noise, makes it well-suited for deconvolution using global analysis techniques. The FMN/HEWL data presented in this section is particularly suitable as it can be treated as two overlapping spectral profiles, assigned to the long-lived free radical species and short-lived triplet state, decaying at different rates.

A global analysis fitting procedure has been recently developed and applied within the group, initially on TA studies[D] and subsequently extended to CRDS data.[E] The huge increase in the number of time points available via the OCTAS methodology (10,000 vs 10 obtained by CRDS) suggests the success should transfer to OCTAS data, which has comparable spectral resolution.

The basic premise is to take a matrix consisting of time by wavelength data and deconvolute it into two new matrices: one containing the concentration profiles of the absorbing species at different measurement times, and the other containing the molar absorptivities of each species at the measured wavelengths.[250] A global analysis program has been written using MATLAB, with the recent addition of genetic fitting to improve the accuracy, using the inbuilt SimBio package.

To allow for instrument response, no data earlier than 1 µs is included in the analysis. As a starting point, the initial assumption is made that 100% of the population is in the triplet state. A sequence of random guesses of (constrained) rate constants are produced and the system optimised by minimising the residuals to the fit. This is repeated n times

[D] Emrys Evans, Timmel Group
[E] Marcin Konowalczyk, Timmel Group

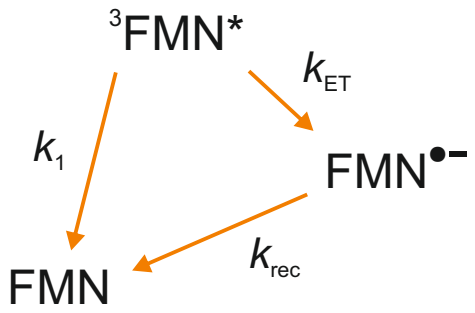


Figure 6.9: The simple model used for global analysis of the OCTAS data. The only species considered are the triplet, radical and ground states of the flavin. The three rate constants fitted are k_{ET} (electron transfer to form radical from triplet), k_{rec} (recombination of radical to form ground state), and k_1 (accounting for any processes that return triplet directly to ground state).

(here $n = 100$), and the residuals between the reconstructed spectra and the real data ordered by size. The combination of rate constants corresponding to the spectral fit with the lowest residual (assuming it is a physically sensible result) are extracted as the best description of the system. The deconvoluted spectra can be shown, as well as the time evolution of all the species involved in the fitted model.

In this early attempt a very simple photochemical scheme is used, consisting of the ground state, triplet and free radicals, as shown in Figure 6.9. The triplet can return to the ground state directly or via the radical, and the radical can only return to the ground state, providing three rate constants to be determined. The rate of ET to form the free radicals is expected to outcompete both other processes, to result in the long-lived, sizeable population in the free radical species that is detected experimentally.

The minimised residuals and the combination of rate constants corresponding to each solution are shown in Figure 6.10. As expected for the best fit to the experimental spectrum (index = 1) the rate of k_{ET} (i.e. triplet to radical) is much faster than either of the other two decay processes, resulting in a long-lived free radical population.

The deconvoluted species associated difference spectra (SADS) for the two components

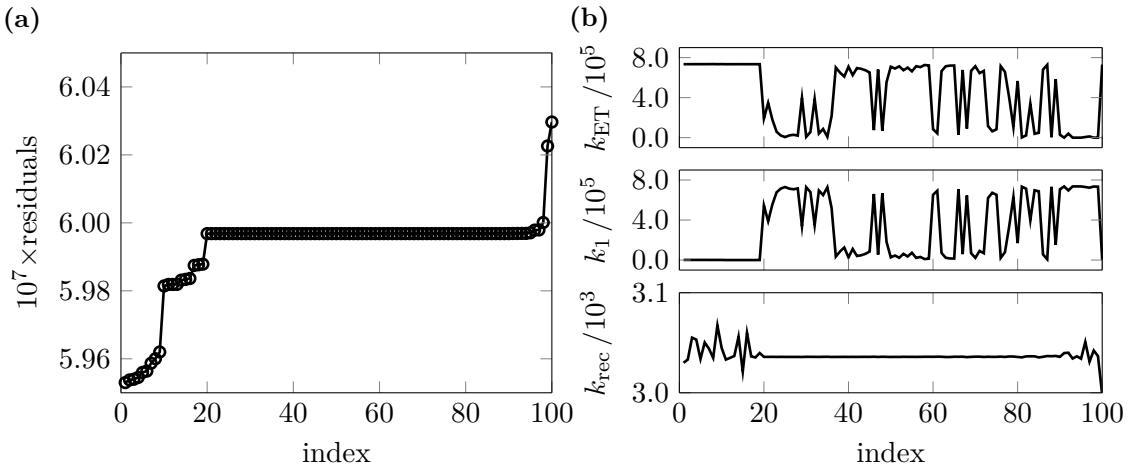


Figure 6.10: a) the residuals corresponding to the 100 global fits performed, ranked in order of best to worst fit. Several local minima are found, as can be seen by the stepped profile. b) the fitted rate constants corresponding to the residuals shown in a). The best fit is given by fast ET from triplet to radical (k_{ET}) and slow direct recombination of triplet to ground state (k_1).

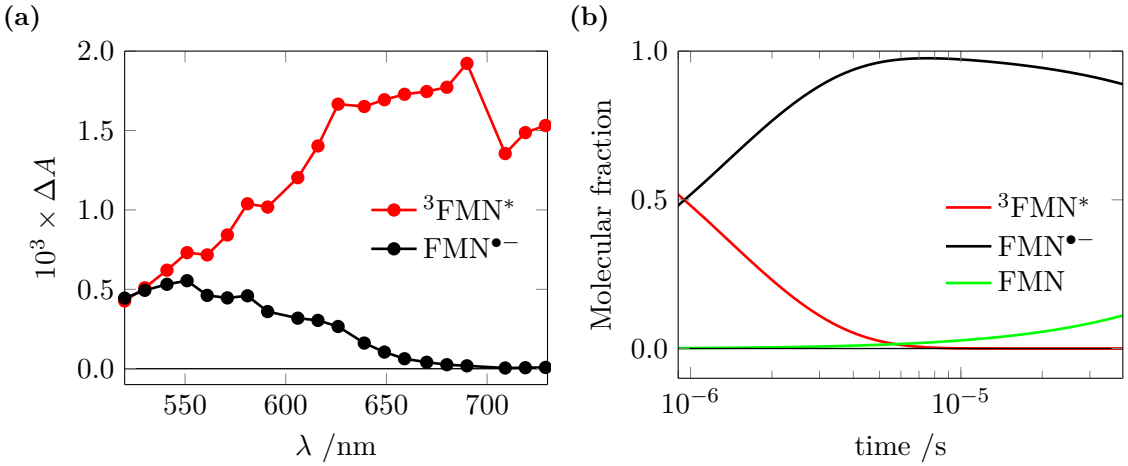


Figure 6.11: a) the species associated difference spectra (SADS) for the FMN radical (black) and triplet (red), deconvoluted using the rate constants associated with the lowest residuals in Figure 6.10 (index 1). b) the kinetic profiles of the populations of the FMN radical (black), triplet (red), and ground state (green) determined from the same optimised rate constants.

detectable in the spectral range of the OCTAS instrument, i.e. radical (black) and triplet (red), are shown in Figure 6.11a). The radical spectrum has the appearance of the 7.0–8.0 µs data plotted in Figure 6.6a), i.e. after complete decay of the triplet population. The triplet spectrum shows intense absorbance to the red, which matches well with the flavin triplet spectra recorded for FAD by CRDS (Figure 4.11) and OCTAS (Section 6.4).

The temporal populations of the three species simulated in the model are presented in Figure 6.11b) for these optimised rate constants. The fast decay of the triplet population and gradual recovery of the ground state are clear, while the radical passes through a maximum on being formed from the triplet, before recombining back to the ground state.

This is early work, and the procedure will be further refined in future. However, these are promising initial results and indicate the powerful capabilities of the OCTAS experiment when coupled with global analysis.

6.3.3 OCTAS MARY demonstration

Although it is principally designed for following kinetic processes, OCTAS can be applied to MARY plots in much the same way as CRDS. In the interest of experimental time, the grating position is only set at one wavelength, but in contrast to CRDS, this automatically provides MARY data over eight spectral regions simultaneously without any further work.

The number of field points is set as required, and as this is a substantial increase over the two field points (on and off), the number of acquisitions is reduced at each point. The net effect is a two-fold reduction in the number of acquisitions of the decay trace at each time point. For the field resolution chosen in this work (≤ 1 mT) the overall experimental time is approximately doubled in relation to the simple field on/off kinetic study. This resolution could be halved without many adverse effects in future to make the different acquisition modes comparable again.

The results of an OCTAS MARY experiment on FMN/HEWL are shown in Figure 6.12, showing all the data obtained simultaneously from the PMT detectors. The

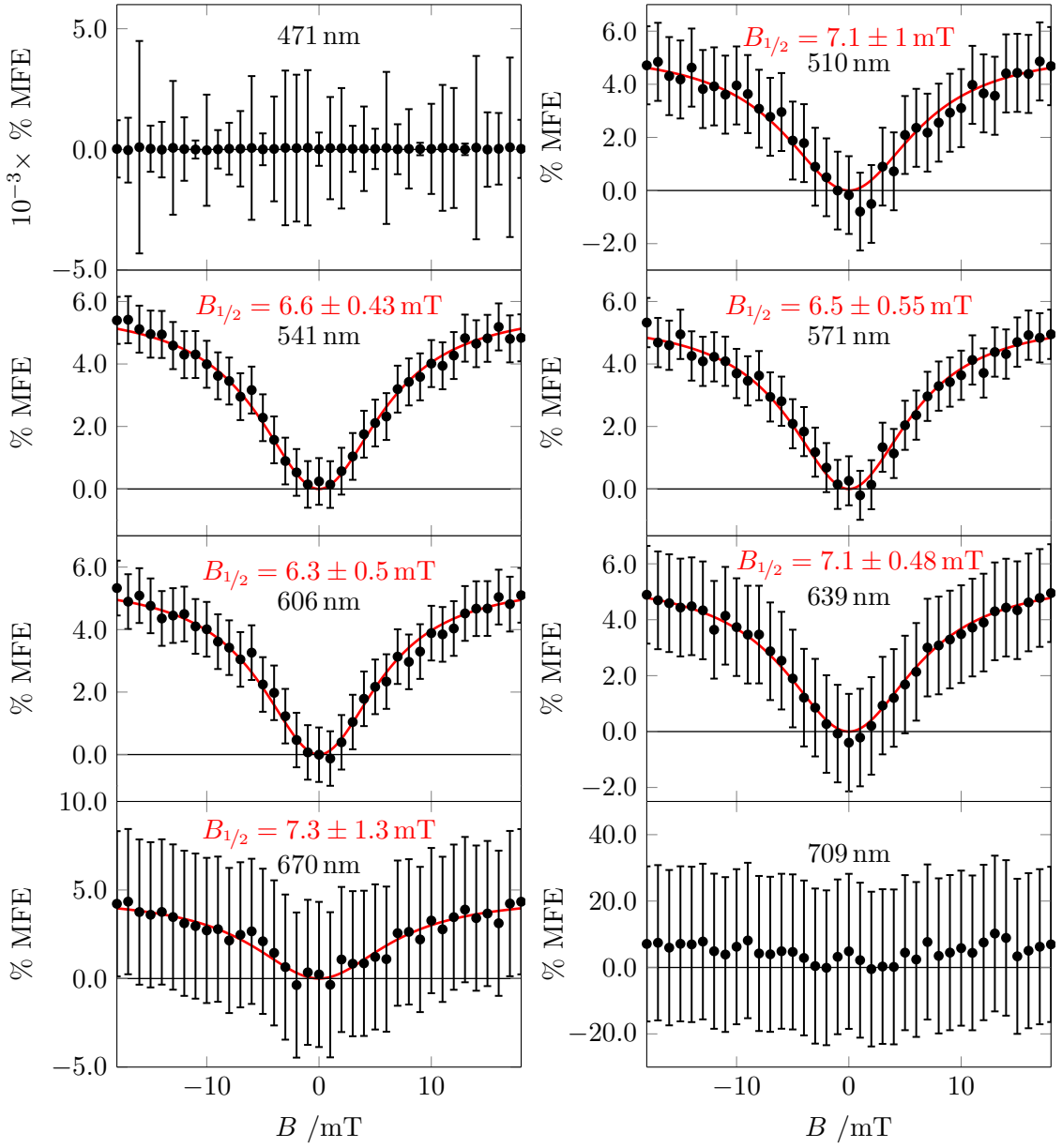


Figure 6.12: MARY curves for FMN/HEWL measured by OCTAS (averaged $5 - 10\,\mu s$) for each channel, corresponding central wavelengths indicated on plots. The huge uncertainty in the 471 nm data is due to the virtually complete lack of light in this region and this data is only shown for completeness. In contrast, the large uncertainty in the 709 nm data is due to the small $\Delta A(t)$ in this region. All error bars represent the SEM of 500 measurements at each field strength.

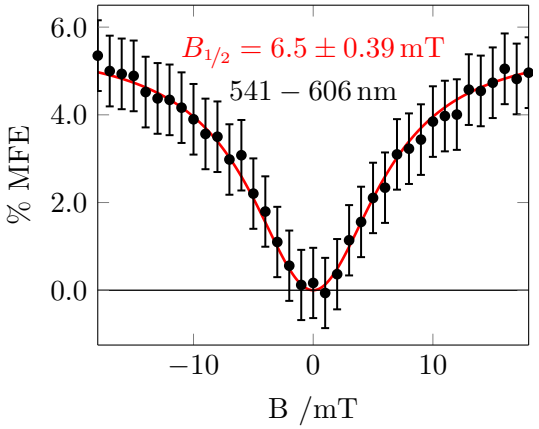


Figure 6.13: MARY curve for the FMN/HEWL system averaged over the radical band (5–10 µs), by combining the data from 541 nm, 571 nm and 606 nm shown in Figure 6.12. Error bars show the SEM of 500 measurements.

data shown at 471 nm is essentially just the result of dividing zero by zero as there is effectively no light reaching the detector in this wavelength region. With the current set-up there are only seven functioning channels, but the instrument is ready to detect at all wavelengths if the blue light transmission can be sufficiently increased. In contrast, the large uncertainties at 709 nm are due to the lack of triplet absorbance after 5 µs rather than a lack of light.

This is not a particularly efficient way in which to display the OCTAS MARY results. However, only showing the results from one channel entails discarding information obtained at no additional experimental time. Therefore, following a similar approach to analysis of the BBCEAS data, the MARY curves can be averaged over the absorbance region of the radical species. The data in Figure 6.12 exhibiting the clearest MFE on the radical absorbance (541 nm, 571 nm and 606 nm) is averaged and displayed in Figure 6.13. While the uncertainties in the measurement are larger than corresponding BBCEAS data (1% vs 0.1%), they are comparable with CRDS, and a MARY response is still clear. A Lorentzian can be fitted to the data, and a $B_{1/2}$ of 6.5 ± 0.4 mT extracted, which is in good agreement with those determined by the other techniques.

These sections have demonstrated the powerful capabilities of OCTAS in combining

the advantages of CRDS and BBCEAS detection to extract data of comparable quality from a single instrument. Due to their shared pulsed nature of photoexcitation, it might be expected that the MFE of a system recorded by both OCTAS and CRDS would be in close agreement. To confirm whether this is the case, the effect of varying photoexcitation power is examined in the next section. The conclusion is that for a pulsed technique the MFE is only determined by the identity of the radical pair being studied (assuming temperature and sample viscosity are held constant). This contrasts with the effects of continuous illumination on MFEs measured by BBCEAS studied in Section 5.4.

6.3.4 Power dependence of the FMN/HEWL MFE

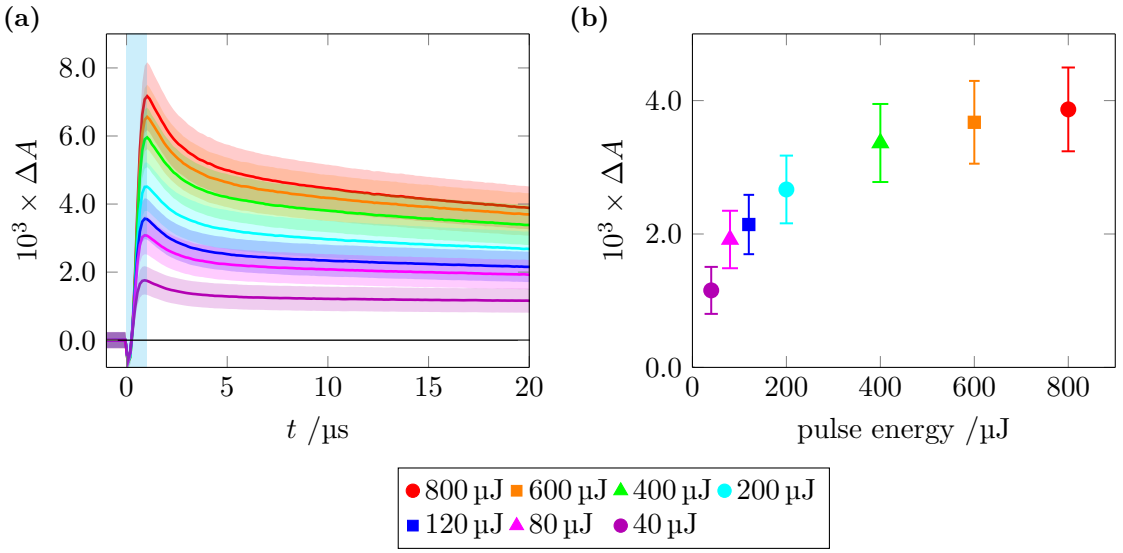


Figure 6.14: Power dependence of $\Delta A(t)$ in the FMN/HEWL radical absorbance region (520–600 nm). a) the full decay profiles, and b) averaged 5–40 µs. The shaded region and error bars represent the standard deviation of 1000 measurements.

The effects of varying the photoexcitation pulse energy on the MFE of FMN/HEWL were investigated using OCTAS. The experiment was repeated at different dye laser powers, varied using a ND filter in the beam path. To maximise the dynamic range and hence the number of data points, the FMN concentration was increased to 100 µM to ensure that a large enough ΔA signal was produced at the lowest powers to observe a detectable MFE.

Figure 6.14 shows the ΔA on photoexcitation as a function of a) time and b) laser power, both averaged over the radical absorbance band. The colours of the decay profiles correspond to the range of photoexcitation powers shown in the legend. The characteristic biphasic decay behaviour due to overlapping triplet and free radical absorbances is clear, the magnitude of which increases with laser power as expected. The radical population seems to be approaching saturation but is still increasing at the highest pulse energies studied here (800 µJ).

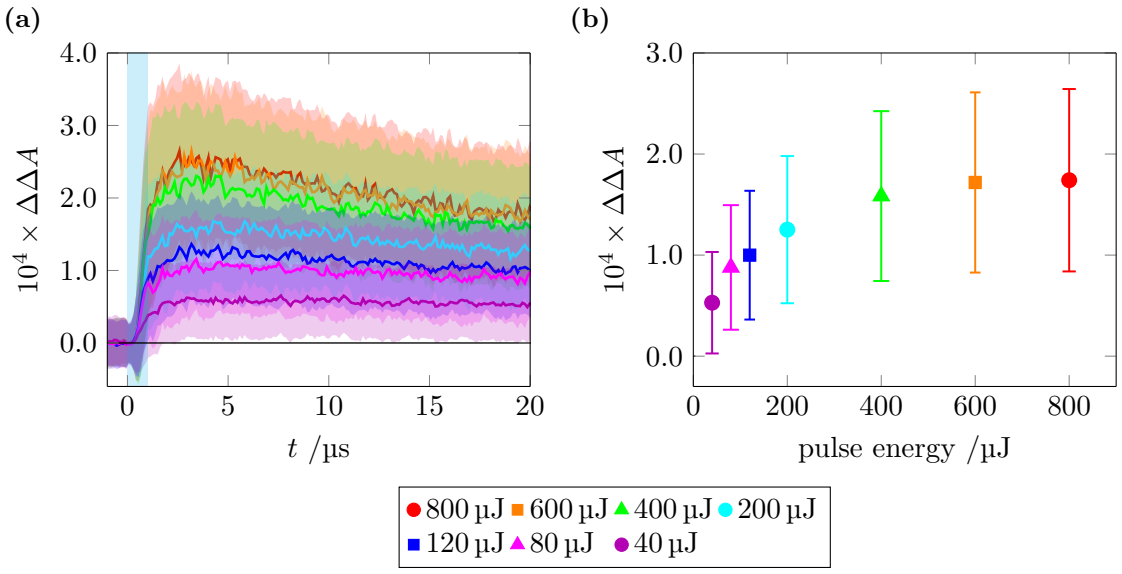


Figure 6.15: Power dependence of $\Delta\Delta A(t)$ in the FMN/HEWL radical absorbance region (520–600 nm). a) the full decay profiles, and b) averaged 5–40 µs. The shaded region and error bars represent the SEM of 1000 measurements.

The $\Delta\Delta A$ observed on application of a 18 mT field is shown in Figure 6.15 as a function of a) time and b) laser power. The same range of laser powers is used (see legend for details), showing a general increase in the magnitude of the field effect, matching the trend shown for the difference spectra in Figure 6.14.

Calculation of the MFE power dependence is achieved by dividing the data in Figure 6.15 by that shown in Figure 6.14 ($\Delta\Delta A/\Delta A$). The result is plotted in Figure 6.16. In contrast to the same study performed by BBCEAS in Section 5.4, in which the MFE

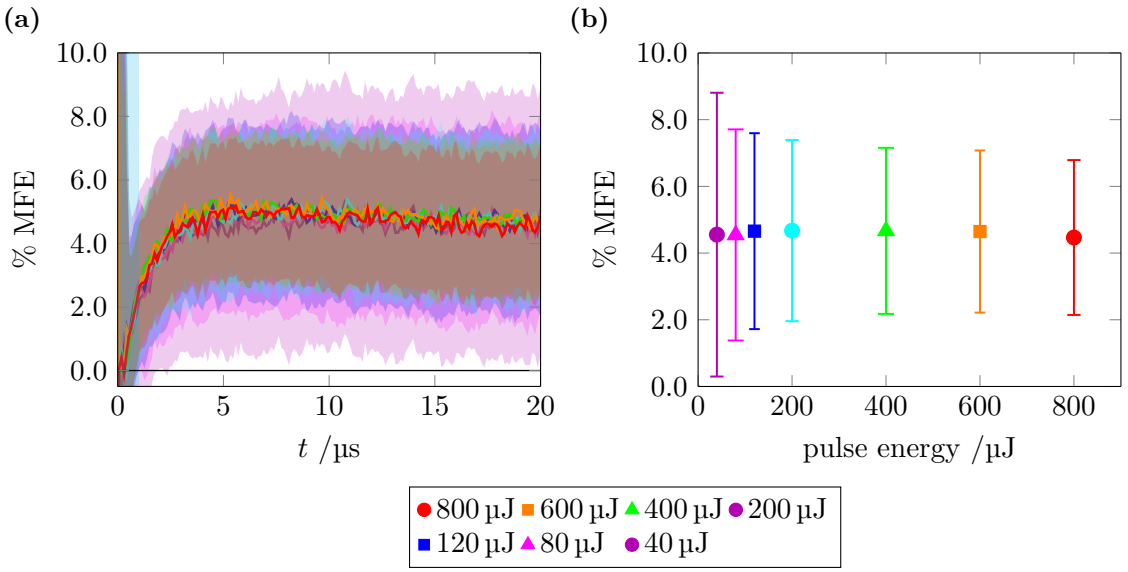


Figure 6.16: Power dependence of the percentage MFE of FMN/HEWL, averaged over the radical absorbance region (520–600 nm). a) the full decay profiles, and b) averaged 5–40 µs. The shaded region and error bars represent the SEM of 1000 measurements. As expected for a pump-probe experiment no power dependence of the MFE is seen.

showed a substantial power dependence, no such effect is seen here. The MFE value is constant around 4.5% for a 20-fold increase in pulse energy. This is an expected result as in a pulsed experiment a single excited population is sent around the photocycle. In a continuous illumination method such as BBCEAS, an equilibrium can be reached in which the ground state is continually replenished and depleted at rates dependent on the photoexcitation. The only effect seen here is the increase in uncertainty as the pulse energy is dropped and MFEs are recorded on successively smaller ΔA signals.

Due to the substantial uncertainty of the measured MFE values ($\pm 2\%$) this lack of power dependence is not conclusive (the power dependence recorded by the more sensitive BBCEAS was only a change of 3%), but the close agreement of the mean values is a convincing indication. Comparison between MFEs measured by the pulsed CRDS and OCTAS techniques should therefore be valid under different photoexcitation conditions (but which are identical in this work), provided other sample conditions that would affect the competition between rate constants (e.g. temperature and viscosity) are held constant.

6.4 OCTAS MFE Studies of FAD and FAD/W

The $\Delta A(t)$ profiles for FAD and FAD/W are shown in Figure 6.17a) and b), respectively. The OCTAS data is presented averaged over regions corresponding to free radical absorption (black) and triplet absorption (red), which both exhibit positive responses to an applied magnetic field (13.5 mT) in the intramolecular SCRP system. The triplet absorbance dominates the FAD spectrum at all wavelengths, and monoexponential fits to both decay traces in a) give the same time constant of 0.76 µs (orange and grey dashed lines), which is in agreement with the lifetime extracted from CRDS.

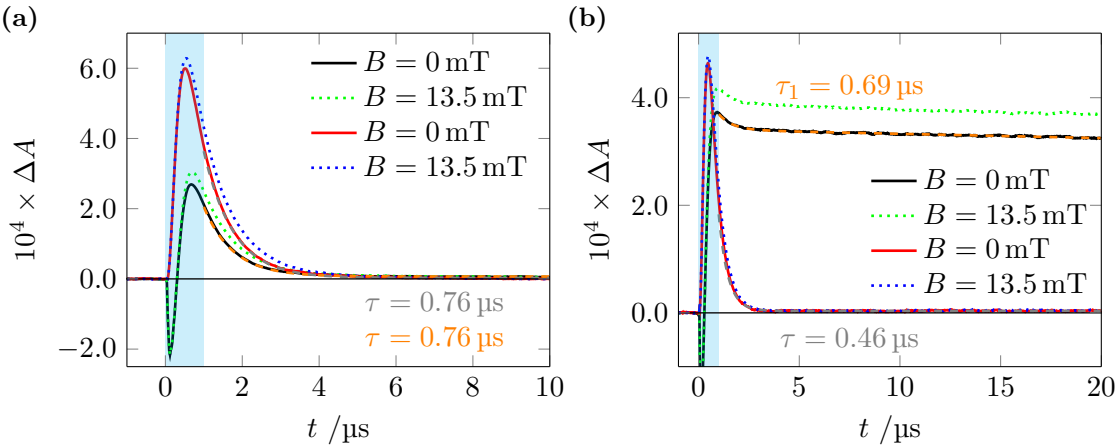


Figure 6.17: $\Delta A(t)$ decay profiles for a) 10 µM FAD (pH 2.2) and b) 10 µM FAD 500 µM W. In each case, the data is presented averaged over i) primarily the radical absorbance band (520–600 nm, black) and ii) the pure triplet absorption band (700–730 nm, red). The dotted lines show the response to an applied 13.5 mT magnetic field, namely an increase in the radical region indicating a triplet-born SCRP. Due to the equilibrium between triplet and SCRP, a MFE is seen on the triplet population in these systems as well. Data is the average of 1000 measurements. Dashed orange and grey lines are fits to the radical and triplet decays, respectively. The fit is biexponential in the case of the FAD/W radical absorbance, and monoexponential otherwise.

As demonstrated in preceding chapters, addition of an electron donor in the shape of the amino acid tryptophan (W) leads to the formation of intermolecular radical pairs with FAD, alongside the existing intramolecular RPs. The result is a system which combines the characteristics of FMN/HEWL and FAD i.e. a long-lived signal due to freely diffusing

radicals, and a magnetically sensitive triplet absorption which extends beyond 700 nm.

The reduced magnitude of the triplet absorbance in comparison with Figure 6.17a) for pure FAD is indicative of quenching by electron transfer from the tryptophan.[247] A monoexponential fit to the triplet $\Delta A(t)$ decay profile (dashed grey line) supports this interpretation, as the time constant is reduced in comparison with the free FAD case ($\tau = 0.46\,\mu s$ vs $0.76\,\mu s$). This is in good agreement with the respective fits performed on the CRDS data in Section 4.3.2. The fast component of the biexponential fit to the radical region (dashed orange line), however, gives only a slightly reduced time constant, $\tau_1 = 0.69\,\mu s$, although the fit in this case is less accurate. A satisfactory fit was not possible on the CRDS data in this region either.

The magnetic responses of each system are shown more clearly as $\Delta\Delta A(t)$ plots in Figure 6.18. The time-resolved magnetic response in pure FAD in a) decays away within 5 µs, matching the lifetime of the triplet state and the data measured by CRDS (Figure 4.8). The addition of tryptophan prolongs the lifetime of the magnetic response in the radical region due to the increased formation of free radical products via the intermolecular RP pathway. The shorter lifetime and reduced magnitude of the magnetic response of the FAD triplet state due to quenching by tryptophan are shown more clearly in red in Figure 6.18b).

Surface plots demonstrating the temporal and spectral response of a) FAD and b) FAD/W to photoexcitation, $\Delta A(\lambda, t)$, are shown in Figure 6.19. The broad extent of the triplet absorbance band, as well as its increased intensity to longer wavelengths, is evident in both plots. For pure FAD, in the absence of any external electron donors, the photochemistry is over in a matter of microseconds due to the short-lived nature of the intramolecular radical pair. The covalent attachment of both components eliminates any possibility of diffusion apart to form long-lived free radical species, which are clearly present in the case of FAD/W (500–650 nm).

Figure 6.20a) shows the effect of applying a 13.5 mT magnetic field on FAD absorbance

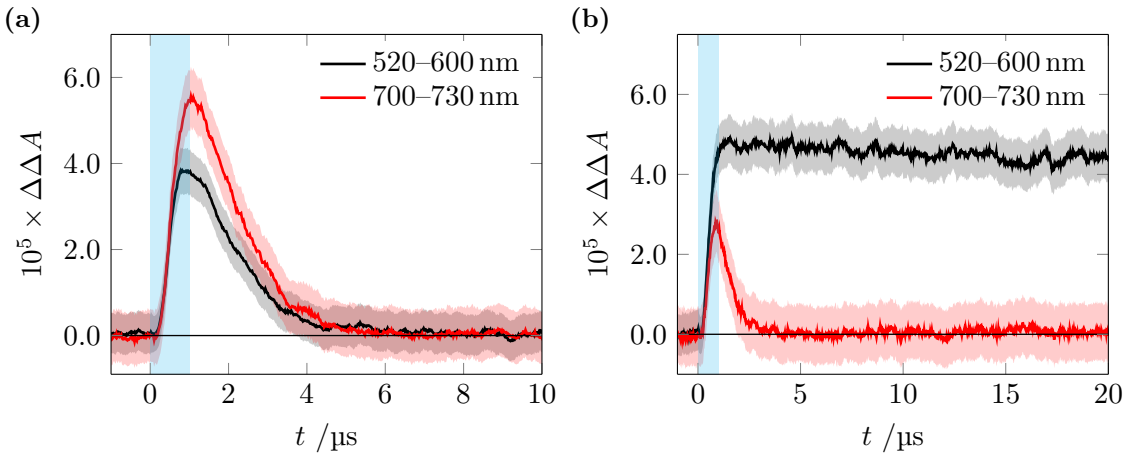


Figure 6.18: $\Delta\Delta A(t)$ decay profiles for a) FAD and b) FAD/W, averaged over the radical absorbance band (black) and the triplet absorption band (red). All species show a magnetic response in these systems due to the equilibrium between the triplet and intramolecular RP that can be formed by the FAD. In FAD/W the magnitude and lifetime of the triplet signal is quenched by electron transfer from tryptophan. The shaded regions in both plots represent the SEM of 1000 measurements.

as a $\Delta\Delta A(\lambda, t)$ surface plot. The characteristic short-lived response of FAD is exhibited across its entire absorbance band (note the shorter timebase). The equivalent data for FAD/W is plotted in Figure 6.20b), emphasising the long-lived magnetic sensitivity of the free radical species. The short-lived signal extending beyond 650 nm, which cannot be explained by a change in free radical absorbance, is instead due to the FAD triplet, albeit with a reduced response compared to free FAD.

The time-dependence of the percentage MFE at an applied field of 13.5 mT in each system is calculated as before, and plotted in Figure 6.21 and Figure 6.22 for the radical region (black) and the triplet region (red), respectively. For FAD, shown in a) in both figures, the percentage MFE increases up to a maximum around 3 µs, after which it begins to decay back to zero and the noise on the signal increases dramatically as both $\Delta A(t)$ and $\Delta\Delta A(t)$ approach zero. As it is not seen in the triplet detection region, the discontinuity in the radical data below 1 µs is likely caused by the fluorescence spike from the FAD. The temporal behaviour of the percentage MFE is very similar in both regions for FAD,

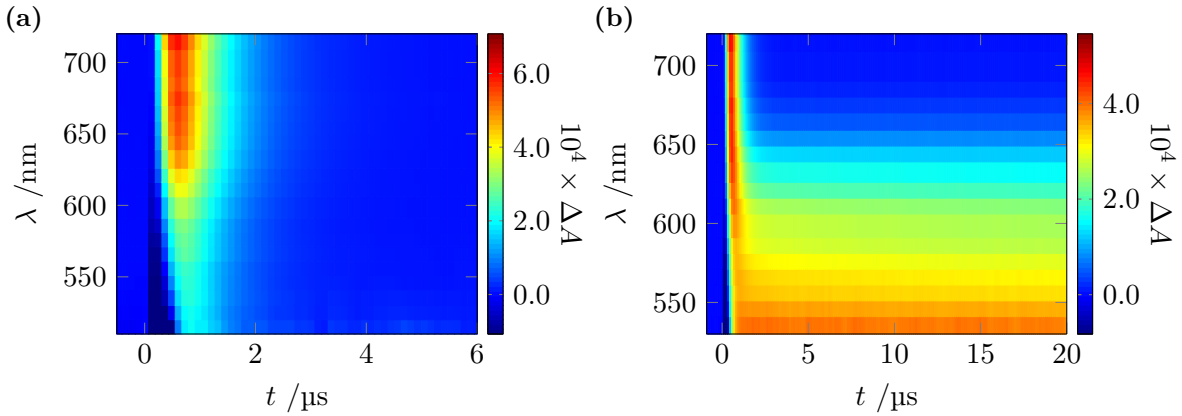


Figure 6.19: $\Delta A(\lambda, t)$ surface plots for a) FAD and b) FAD/W, obtained by combining the multiple decay traces recorded by individual PMT channels on the oscilloscope. In FAD, the broad absorption band of the short-lived triplet state dominates and on this scale there is no indication of the long-lived radical species surviving (500–650 nm). In the case of FAD/W the presence of long-lived radical species is very clear alongside the fast-decaying triplet state (> 650 nm).

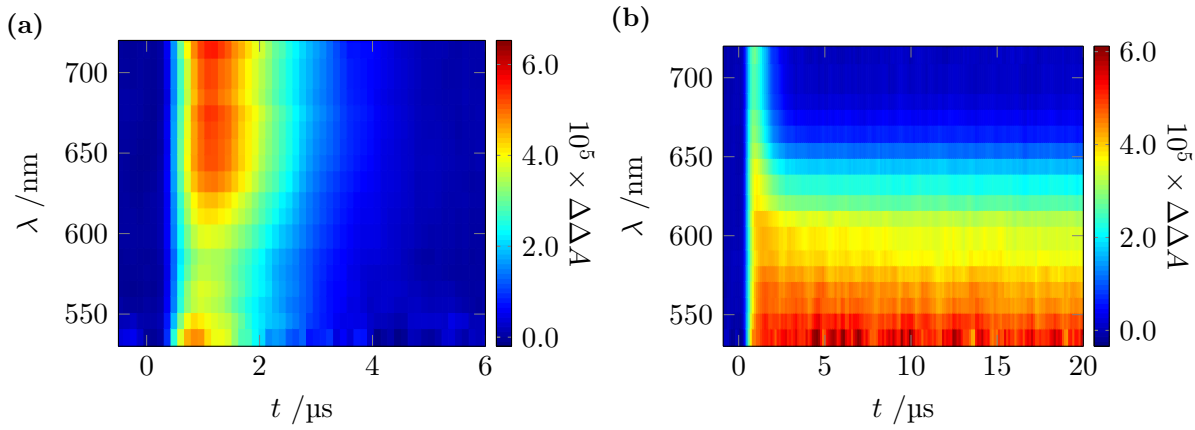


Figure 6.20: $\Delta\Delta A(\lambda, t)$ surface plots for a) FAD and b) FAD/W, showing the spectral and temporal response to a 13.5 mT magnetic field. In both cases the triplet region exhibits a short-lived MFE, the magnitude of which is quenched by electron transfer from the tryptophan in b). The long-lived component of the magnetic response in FAD/W is due to diffusion of the free radical species. In both plots the data is the average of 1000 measurements and is smoothed by a 5-point moving average in the wavelength dimension (*ca.* 50 nm).

confirming that an equilibrium is established between the radical and triplet by rapid BET from the SCRP. There is less noise in Figure 6.22a) due to the more intense triplet absorbance in this region.

The MFE(t) profiles for FAD/W ($B = 13.5\,\mathrm{mT}$) are shown in Figure 6.21b) and Figure 6.22b) for the radical region (black) and triplet region (red), respectively. On comparison of the radical regions in Figure 6.21, the long-lived response of the FAD/W system is clear, with the magnetic field effect surviving well over 20 µs. The percentage MFE for the FAD/W free radicals (*ca.* 14%) is larger than that seen for the FMN/HEWL system, which has tentatively been explained by a feedback mechanism working between the inter- and intra-molecular radical pairs present in the system. Other than its larger magnitude, its temporal behaviour is very similar to FMN/HEWL, rapidly rising to a saturated value (within 3 µs) and then remaining approximately constant on the timescale of the experiment. The triplet region of FAD/W shows a similar temporal profile to that of pure FAD in Figure 6.22a), although it is slightly shorter lived due to the quenching of the triplet-state by electron transfer.

The data recorded for the radical regions using OCTAS in Figure 6.21) are overlaid with the CRDS-measured percentage MFEs at 540 nm, using the data shown in Figure 4.7 for FAD and FAD/W. As with the FMN/HEWL data in the previous section, the agreement is good beyond 2 µs. However, the FAD data at earlier times differs significantly. This is likely to be for the same reasons as suggested in the FMN/HEWL case and is emphasised here by the short-lived nature of the FAD signal. Additionally, the different applied fields (13.5 mT OCTAS vs 19 mT CRDS) will also account for some of the difference, but this is not expected to be a large effect. The MARY curves measured by CRDS (Figure 4.13) indicate little difference in the percentage effect between the two fields (which are similar within error). However, the time dependence of the MARY curve measured by OCTAS has not been examined.

The MARY curve measured for FAD by OCTAS is shown in Figure 6.23a). Due to

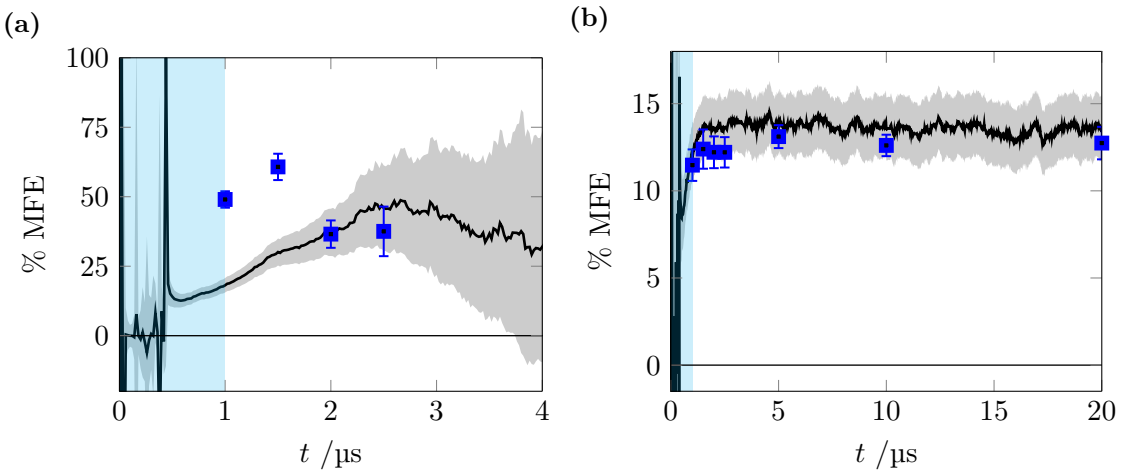


Figure 6.21: The time-dependence of the percentage MFE for a) FAD and b) FAD/W, averaged over the radical absorbance region (520–600 nm). In FAD, the effect increases rapidly up to 2.5 µs, where it reaches a maximum value (*ca.* 50%) after which it starts to decay back to zero and noise begins to dominate the reading due to the fast decay of the triplet species. The contrasting long-lived behaviour of the FAD/W system is clear. The blue points are the corresponding values measured by CRDS, calculated from the data shown in Figure 4.7. The shaded regions indicate the SEM of 1000 acquisitions.

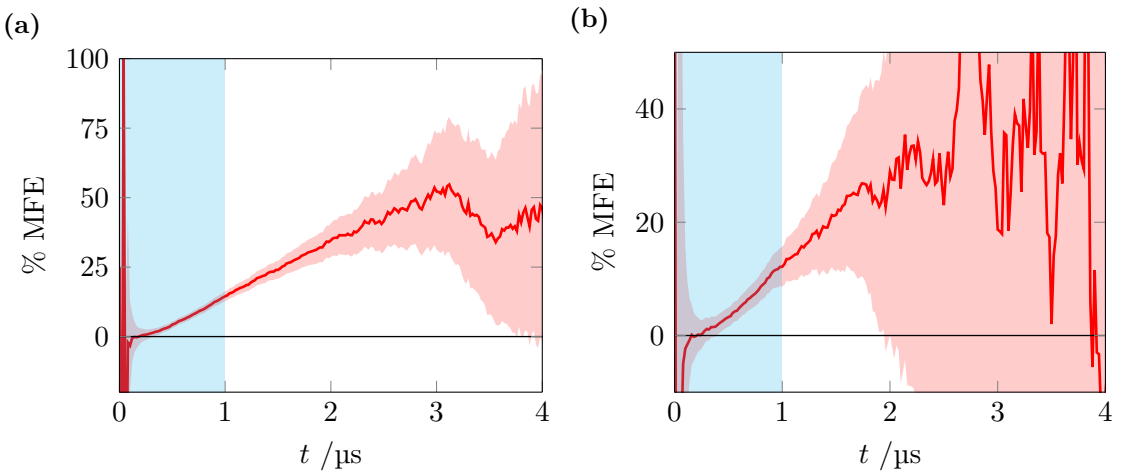


Figure 6.22: The time-dependence of the percentage MFE for a) FAD and b) FAD/W, averaged over the purely triplet absorbance region (700–730 nm). In both plots, the signal drops below the noise level above 3 µs, corresponding to a region of the spectrum where both $\Delta A(t)$ and $\Delta\Delta A(t)$ approach zero (Figures 6.17 and 6.18). The FAD/W effect has a shorter lifetime due to quenching by electron transfer. The shaded regions indicate the SEM of 1000 acquisitions.

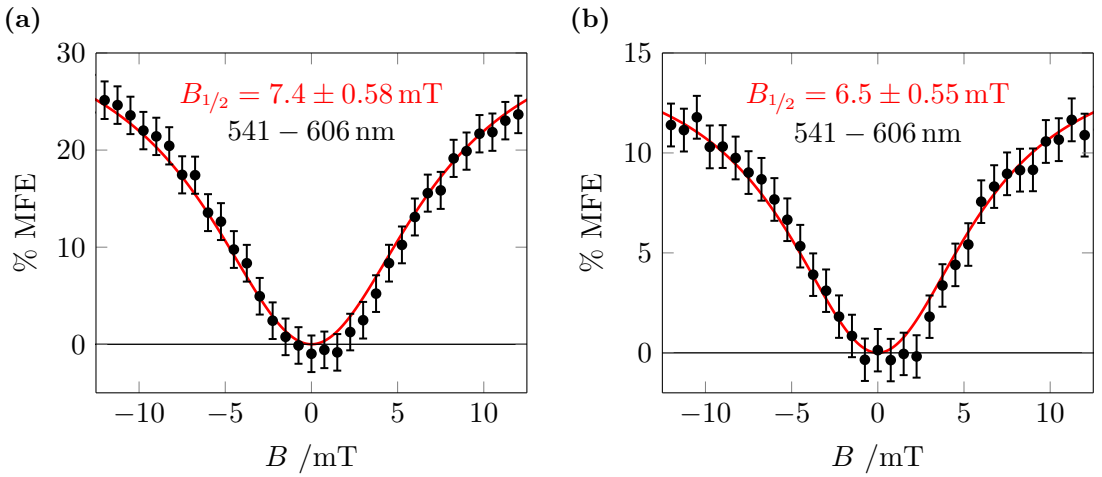


Figure 6.23: MARY curves measured by OCTAS for a) FAD and b) FAD/W, averaged over the radical absorbance region (541–606 nm). Decay profiles averaged over a) 1–2 µs and b) 5–10 µs. The red lines are Lorentzian fits and the extracted $B_{1/2}$ values of 7.4 ± 0.58 mT and 6.5 ± 0.55 mT are in good agreement with those measured by the other techniques. In both cases there appears to be a slight (≈ 0.5 mT) field offset from zero. Error bars show the SEM of 500 measurements.

the short lifetime of the magnetically sensitive species, the decay profiles were averaged over 1–2 µs at each field strength to provide a MFE value. The large percentage MFE in this system at early times leads to the comparatively smaller uncertainties in this data, making OCTAS particularly suitable for the study of short-lived MFEs. For instance, it compares favourably with the relative high uncertainties in the steady-state BBCEAS MARY curve shown in Figure 5.18c).

The equivalent MARY curve for FAD/W is shown in Figure 6.23b). As for the FMN/HEWL system, the response is long-lived enough to average over the 5–10 µs window. In future, the time-dependence of the MFE should be examined, and if there is little temporal change then averaging long-lived species over the entire 40 µs decay should provide a noticeable increase in SNR.

In both experiments, all 8 channels were recorded concurrently, and for comparability with the FMN/HEWL system the data recorded at 541 nm, 571 nm and 606 nm were averaged together to produce the final MARY plots shown here.

In this data, as well as in some of the individual channel data for the FAD system, there is a tantalising hint of a LFE. However, nothing can be confidently assigned on the current noise levels, and upon fitting a Lorentzian curve it appears as though there is a small (*ca.* 0.5 mT) offset from zero-field, which could be the origin of these effects. If the sensitivity of the OCTAS technique can be further optimised in future (probably by increasing light throughput onto the detectors) then its capabilities should be focused on the LFE regions of model systems, as well as those of cryptochrome proteins.

The results presented so far demonstrate the capabilities of OCTAS to perform successful MFE studies on flavin model systems, including the recording of action spectra and MARY curves with high SNR. In the final results section, this powerful new instrument is applied to the study of the *Xl*Cry protein system and its suitability for biological MFE detection is assessed.

6.5 OCTAS MFE Study of *Xenopus laevis* Cryptochrome

As a cavity-based spectroscopic technique, OCTAS is plagued by the same issues that make protein studies so challenging using BBCEAS and CRDS. The low temperature required to protect protein solutions from aggregation causes condensation to form on the surface of the cell windows. This leads to an unacceptable level of scatter, significantly reducing the cavity finesse and rendering the sensitivity of a cavity 'enhanced' technique worse than that of a corresponding single-pass measurement. In order to avoid this issue air is blown at the cell surfaces, but in its current design this leads to mechanical noise due to vibrations of the cell window.

Once this problem has been overcome the sample has some inherent limitations of its own. Protein molecules are sufficiently large to scatter light themselves, so centrifugation to remove the largest particulates from the solution can only reduce scattering rather than completely eliminating it. The use of (often high) concentrations of glycerol to further stabilise the protein and maintain the solution phase at low temperatures also contributes

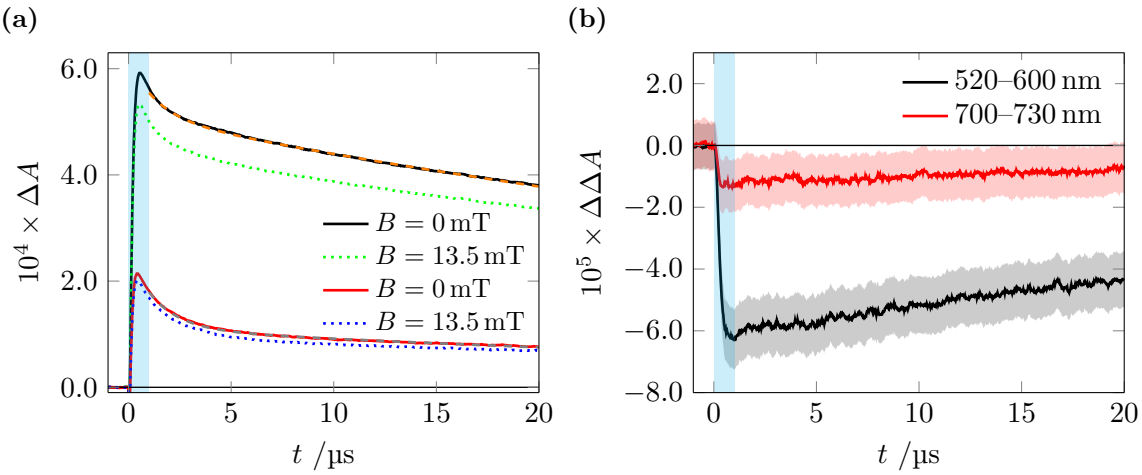


Figure 6.24: a) $\Delta A(t)$ decay profiles for the *Xl*Cry protein upon 150 µJ, 450 nm photoexcitation, averaged over i) primarily the radical absorbance band (520–600 nm, black) and ii) the region corresponding to the pure triplet absorption band in free FAD (700–730 nm, red). The dotted lines show the response to an applied 13.5 mT magnetic field, namely a decrease in the absorbance indicating a singlet-born SCRP. The dashed grey and orange lines are biexponential fits to the data, see text for time constants. b) $\Delta\Delta A(t)$ decay profiles for the *Xl*Cry protein, averaged over the same wavelength regions as a). All data is the average of 1000 acquisitions and the shaded regions in b) represent the SEM.

to scatter within the sample cell. The tiny volumes of sample available for study mean that sample flow is impracticable, leading to the build-up of scattering photodegradation products throughout the course of an experiment.

Despite these numerous challenges, OCTAS has been successfully used to reproduce the same negative MFE observed in *Xl*Cry using CRDS. With further optimisation in future, it appears to be the optical technique with the best chance of detecting a biological low field effect out of those currently available.

The $\Delta A(t)$ and $\Delta\Delta A(t)$ decay profiles for two spectral regions of the *Xl*Cry protein are shown in Figure 6.24a) and b) respectively. The kinetic profiles are almost identical across the whole visible region, with the only apparent difference in their magnitudes. Both are described well by the same biexponential decay (dashed orange/grey lines) with rate constants $\tau_1 = 1.37\,\mu s$ and $\tau_2 = 66.5\,\mu s$. In model systems the slow component of the decay has a time constant in the hundreds of microseconds range, but as in this case it is

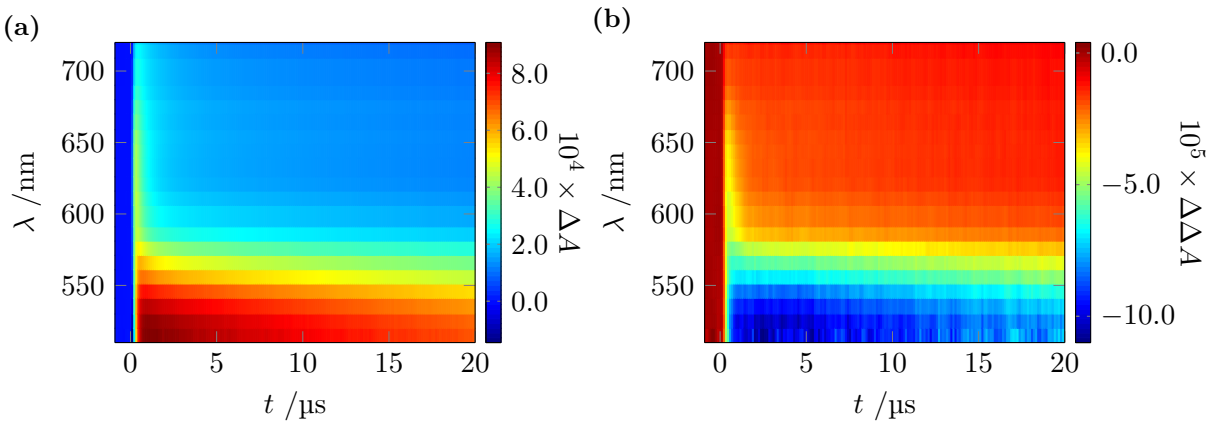


Figure 6.25: a) $\Delta A(\lambda, t)$ surface plot for *Xl*Cry showing the long-lived radical species (500–550 nm) and $TrpH^{\bullet+}$ radical deprotonation (> 580 nm) are both visible. b) $\Delta\Delta A(\lambda, t)$ surface plot for *Xl*Cry, demonstrating the negative effect of a 13.5 mT magnetic field on the RP2 absorbance. All data is the average of 1000 measurements and a 5-point moving average is applied to smooth in the wavelength dimension.

only 50% longer than the timescale of the experiment it is of more relevance.

The magnetic response seen beyond 700 nm is likely due to the wide spectral region detected by each optical fibre. The very large MFE of this system means that any trace of the RP1 or RP2 absorbance detected in channel 8 will give the appearance of a MFE at that wavelength.

Figure 6.25 shows a) $\Delta A(\lambda, t)$ and b) $\Delta\Delta A(\lambda, t)$ surface plots obtained by ordering the *Xl*Cry decay traces recorded by OCTAS by wavelength. Here, the narrow absorbance band of the long-lived RP2 state is very clear between $500 < \lambda < 560$ nm, and there is some evidence of the fast deprotonation of the $TrpH^{\bullet+}$ radical to longer wavelengths. Particularly clear in Figure 6.25b) is the high field sensitivity in the RP2 absorbance, which dwarfs signals from any other spectral region. The spectral agreement between these surface plots recorded by OCTAS, and those recorded by CRDS (Figure 4.14), is very convincing. It also demonstrates the improvement in the data offered by OCTAS. The $\Delta\Delta A(\lambda, t)$ profile in particular has much higher definition in the OCTAS study. The only processing performed on the data is averaging of multiple acquisitions and a 5-point smoothing applied in the wavelength direction.

The OCTAS experiment takes *ca.* 45 min to acquire the data, a substantial improvement on the *ca.* 2 h CRDS experiment, which only provides 20 averages. The benefits of OCTAS are two-fold: i) time delays do not need to be scanned as the oscilloscope records the whole trace in one shot, at a resolution determined by the user, and ii) there is an automatic eight-fold increase in wavelength resolution due to the simultaneous acquisition by the array of eight PMT detectors. These gains can be used to increase the amount of averaging by at least an order of magnitude, while reducing the experimental time by more than half. These are crucial considerations when it comes to exposing a light-sensitive sample to photoexcitation. For comparability, these studies were run at the same repetition rate of 3.33 Hz. The reduced OCTAS experimental time is therefore not due to taking the same number of readings more quickly. The OCTAS data reported here involved subjecting the sample to 6000 photoexcitation pulses, each of 150 µJ. The CRDS surfaces plotted in Figure 4.14 by comparison, required 24000 laser shots of comparable intensity, for 50 times fewer averages at each data point. A comprehensive tabulated comparison is provided in the final chapter of this thesis as part of the summary.

The *Xl*Cry MFE as a function of time is plotted in Figure 6.26a), showing similar behaviour to the FAD/W model system but of opposite phase. The rise of the field effect is rapid and it reaches a maximum value of *ca.* 11% within 2 µs, after which it saturates and remains constant on the experimental timescale due to the long-lived nature of the RP2 state. The system exhibits behaviour comparable to that of a free-radical system, although here it is the need for the $Trp^{\bullet}$ radical to be re-protonated before recombination back to the ground state can occur that is the origin of the extended lifetime. As for the model systems, the blue points indicate the MFE on *Xl*Cry measured by CRDS. Within the (substantial) uncertainty on both datasets the agreement is gratifyingly close, a considerable achievement for such challenging studies.

Figure 6.26b) shows the *Xl*Cry MARY curve measured by OCTAS. The negative MFE characteristic of the singlet-born RP1 is present at all field strengths, but the elusive

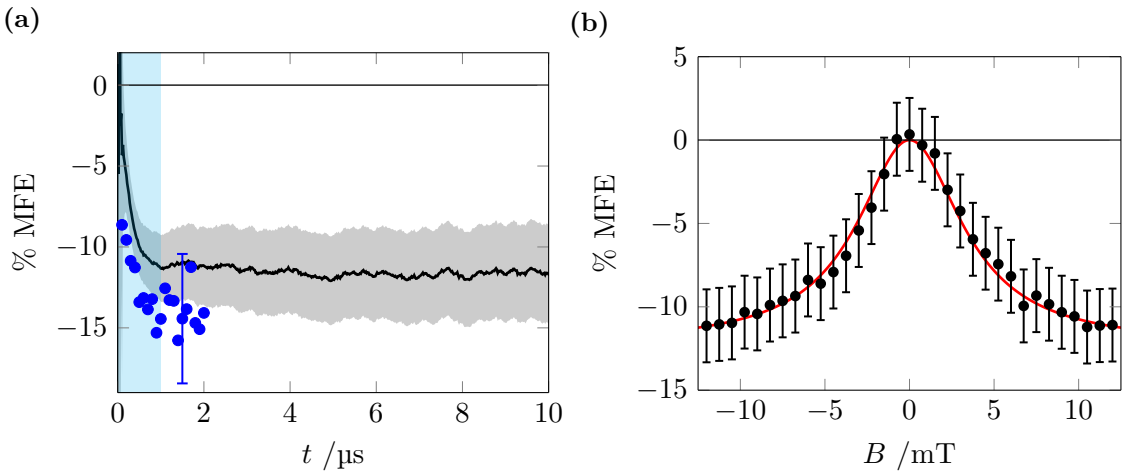


Figure 6.26: a) Time dependence of the MFE in *Xl*Cry, averaged over the radical absorbance region (520–600 nm). The effect grows in rapidly up to 1.5 µs, where it reaches a maximum value (*ca.* 11%) after which it remains constant on the timescale of the experiment. The shaded region represents the SEM of 1000 measurements. The blue data is the MFE measured by CRDS, calculated from the data shown in Figure 4.15 and they agree within the sizeable uncertainty, however the magnitude of the CRDS MFE is larger as it was recorded at 19 mT. b) The MARY curve of *Xl*Cry measured by OCTAS, averaged 5–10 µs over channels 3–5 (i.e. 541 nm, 571 nm and 606 nm). Error bars represent the SEM of 500 measurements.

biological LFE still evades detection under these conditions.

6.6 Conclusions and Future Directions

A new cavity-based instrument, OCTAS, has been developed with the aim of combining the microsecond time resolution of CRDS (Chapter 4) and the simultaneous broadband detection of BBCEAS (Chapter 5) for MFE detection in chemical and biological systems. The studies reported in this chapter have demonstrated the success of the new technique – field effects have been resolved in all systems studied at microsecond time resolution. The extracted kinetic parameters have agreed well with those obtained by the existing CRDS instrument, indicating a comparable time response. The increased spectral resolution, achieved by simultaneous monitoring with eight separate detectors connected to the same high resolution oscilloscope, has significantly reduced experimental time, and therefore

demands made of the sample and cavity alignment.

While the spectral resolution will never be as good as that obtained by dispersal onto a CCD camera, 10 nm resolution is demonstrated to be high enough to identify the important components of our photochemical systems by their broad spectral signatures. If processes occurring on the sub-microsecond timescale need to be resolved in future there is scope to improve the time resolution of the instrument by using gated PMTs to remove the scattered light from the photoexcitation pulse and the sample fluorescence. Pushing the time response to its limit will require the consideration of deconvolution effects of the light circulating in the optical cavity with the decaying absorbances, similar to that performed for CRDS in Section 4.3.4. However, only examining data $\geq 1\,\mu s$ has meant this has not been required in this work.

OCTAS has been shown to offer data of competitive, if not better, quality than that obtained from the existing cavity techniques available to the group. However, there are other ways in which this data could be obtained. The use of a gated CCD camera was trialled, but the data was not deemed to be of sufficient quality. With the amount of time since invested in the PMT detection perhaps it would offer similar SNR at a comparable cost. The other alternative is the use of a streak camera, which can measure microsecond kinetics at a CCD-level of spectral resolution. These specifications come at a high cost (currently an order of magnitude higher than the combined cost of the PMT detectors and oscilloscope), and due to the prohibitive expense were not considered for these studies.

This chapter has demonstrated the ability to combine two previously separate cavity-based techniques into a single, powerful instrument, capable of replacing either technique with little disadvantage. The newly developed OCTAS experiment is capable of following MFEs as they develop on a microsecond timescale, across multiple excited states of interest simultaneously. In time it should establish itself as the technique of choice for photochemical MFE studies in the group, and focus now should be on the final improvements that will ultimately permit a biological LFE to be detected.

Chapter 7

Summary and Outlook

This thesis has reported on the development of cavity-enhanced spectroscopic techniques for the condensed-phase study of radical pair recombination reactions in chemical and biological systems, and their associated magnetic field effects. Existing CRDS and BBCEAS techniques have been improved and optimised and a powerful new OCTAS instrument developed, combining their respective advantages and capabilities.

The context within which this work finds relevance is provided in Chapter 1, where the broad area of Spin Chemistry is introduced, along with the radical pair mechanism hypothesis of animal magnetoreception. This remains one of the two surviving hypotheses (the other involving magnetite) to explain the ability of some animals to use the Earth's small magnetic field as a navigational cue during long-distance migrations. Attention is focused on the cryptochrome family of proteins, which is currently under scrutiny as the potential carrier of this magnetic sense. Current methods for the detection of biological magnetic field effects and their associated limitations are summarised, with the conclusion that new approaches are required to provide the necessary sensitivity. Optical cavities are proposed as one solution.

Chapter 2 introduces the concept of an optical cavity as the extreme variant of multipassing spectroscopic techniques, whereby the sensitivity of a measurement can be im-

proved by increasing the effective optical pathlength through an absorbing sample. It is noted that optical cavities, however, owe their sensitivity to the suppression of measurement noise. The principles of CRDS and (BB)CEAS are introduced, with particular focus on their application to the condensed phase, where background losses from the sample and intracavity cell pose additional challenges. An approach to quantify these effects and permit the selection of the optimum mirror reflectivity and cavity geometry for a particular application is summarised. The choice of light source and detector is considered as part of a brief overview of existing cavity-based literature, with particular focus on previous studies performed in the condensed phase.

The experimental apparatus used in this work is summarised in Chapter 3, including details of the cavity light sources (a supercontinuum white light source and a tunable OPO), photoexcitation sources (a CW diode laser and a pulsed Nd:YAG-pumped dye laser), photodetectors (a CCD camera and PMTs) and the intracavity cell. For absolute absorbance values to be determined from CEAS-based techniques the CEF must be known, and a successful calibration procedure relevant to the BBCEAS and OCTAS studies is presented. The spectrally resolved cavity mirror reflectivity profile is studied in detail and features are successfully matched to those recorded in the CEF spectrum. The stability of the SCR source is characterised by the results of Allan deviation studies performed under different conditions, from which an optimum CCD integration time and sample flow rate can be extracted for use in later chapters. These are chosen to provide the best compromise between reduction of white noise on averaging while avoiding systematic long-term drift. The simple introduction of a syringe filter into the set-up is also demonstrated to significantly reduce measurement noise.

Chapter 4 reports the results of MFE studies performed on flavin model systems and an animal cryptochrome, *Xl*Cry, using a pump-probe (BB)CRDS instrument employing a tunable OPO laser as its probe beam. Scanning the OPO frequency permits the acquisition of broadband spectral information, while varying the delay time provides sub-microsecond

temporal resolution. The magnetic field effects of radical pair reactions in FMN/HEWL, FAD and FAD/W have been characterised in terms of their magnitude and kinetics. More challenging MFE studies on a biological sample, *Xl*Cry, were also successfully performed. The effect of studying an absorbance decaying on a comparable timescale to the ring-down time was noted, and a deconvolution procedure demonstrated to improve the accuracy of measured absorbance values. However, the impact on the measured kinetics was not found to be significant.

While the BBCRDS instrument has been shown to be powerful in elucidating MFEs, it is not a truly broadband technique as the spectrum must be obtained in a stepwise fashion. To address this issue, Chapter 5 introduces another cavity-based instrument, BBCEAS, which combines the broad spectral coverage and high irradiance of a SCR source with a spectrograph and CCD detector. This permits the simultaneous acquisition of the entire visible absorption spectra of systems, and its high sensitivity allows MFEs to be spectrally resolved with high SNR. MFEs in a range of systems have been characterised, with SNR that enables the effects of photoexcitation power, Coulombic interactions, viscosity, ionic strength and low hyperfine interactions (resulting in LFEs) to be distinguished. Successful MFE studies have also been performed on the related *Ec*PL and *Dm*Cry proteins, the latter of which is the subject of a new communication (to be submitted) reporting on the first detected *in vitro* response of an animal cryptochrome to an external magnetic field.

Although the use of an integrating CCD camera reduces the time resolution considerably (minimum exposure time = 3.66 ms), behaviour on slow timescales (milliseconds to seconds) can still be monitored by the BBCEAS instrument. This is exemplified by detection of enhanced-MFEs and related effects on TTL-modulation of the diode laser photoexcitation. A new modulated-BBCEAS variant and associated analysis is also introduced, with the advantage that the ground state absorption spectrum can be monitored throughout the experiment.

The gain in true broadband coverage offered by BBCEAS comes at the expense of

the microsecond time resolution available in CRDS detection so crucial in understanding the magnetically sensitive photochemistry of cryptochrome proteins. In an effort to combine these two powerful capabilities, Chapter 6 of this thesis reports on the new OCTAS instrument, which utilises the SCR broadband source and spectrograph of the BBCEAS instrument coupled with the fast detection capabilities of PMTs used in CRDS. To benefit from the wide spectral coverage of the probe beam, an array of PMT detectors has been coupled with a high resolution (12-bit) oscilloscope to monitor microsecond kinetics over eight wavelength regions simultaneously. The OCTAS instrument has been used to obtain proof-of-principle MFE results on the same systems as previously studied by CRDS, namely FMN/HEWL, FAD and FAD/W, as well as the *Xl*Cry protein. The satisfying agreement between the MFEs and kinetics measured by the two different techniques is demonstrated by the close match upon overlaying of the data.

In order to further demonstrate the success of the new technique, Tables 7.1 and 7.2 include the experimental parameters for typical cryptochrome MFE studies performed using each instrument. The minimum detectable absorbance values (A_{min}) quoted in the final row are based on the work reported in the relevant chapters of this thesis. In cryptochrome studies they are typically an order of magnitude higher than in the model systems, due to increased background losses from sample scatter and noise resulting from operating at low temperatures (vibrations of and condensation on the cell window surfaces). Furthermore, lower laser powers must be used to prevent photodegradation, resulting in a lower radical population on which to detect a magnetic field effect.

Table 7.1 assesses the suitability of each technique for MARY studies, where the change in reaction yield is monitored as a function of applied magnetic field strength. BBCEAS is shown to be the most sensitive, not least due to its multiplexing advantages where 100 nm absorbance bands are routinely averaged over to increase the already high SNR on the CCD detector. It can also be run at a higher repetition rate, determined by the total of acquisition and field delay times (here taken to be 50 ms each). This results in a shorter

	CRDS	BBCEAS	OCTAS
Photoexcitation	150 µJ /pulse	0.5 mW	150 µJ /pulse
Acquisition rate	3.33 Hz	10 Hz	3.33 Hz
Time resolution	N/A	N/A	sub µs (1 to 40 µs)
Wavelength resolution	N/A	*ca.* 0.6 nm (480–730 nm)	*ca.* 30 nm (500–730 nm)
Field points (±15 mT, 1 mT resolution)	31	31	31
Averages	500	500	500
Total acquisitons	15,500	15,500	15,500
Experimental duration	78 min	26 min	78 min
Total pump energy	2.33 J	0.78 J	2.33 J
Total no. photons ($\lambda = 450$ nm)	5.27×10^{18}	1.76×10^{18}	5.27×10^{18}
$\boldsymbol{A_{\mathrm{min}}}$	1.45×10^{-5}	1×10^{-6}	1×10^{-5}

Table 7.1: Parameters for typical MARY studies on cryptochrome proteins performed in this thesis. The number of photons does not include those incident from the probe beam, as these can be removed by spectral filtering without any loss of information > 500 nm. For the model systems, A_{min} is typically an order of magnitude smaller in each case due to the lower background losses *cf.* the protein studies that are subject to sample scatter and vibrations from the air flow required to avoid condensation forming.

experimental duration than CRDS or OCTAS, which are restricted by the recovery time of the sample and the repetition rate of the dye laser. Consequently, the sample conditions are gentler in a BBCEAS experiment, requiring only a third of the number of photons to be incident on the sample compared to an equivalent OCTAS or CRDS measurement. Furthermore, shorter experiments are advantageous for maintaining good cavity alignment at low temperatures.

The sensitivity of OCTAS is limited by the poorer light transmission onto the detectors. However, full decay traces at eight wavelengths are recorded automatically for the same experimental duration as a monochromatic CRDS measurement at a fixed delay time.

This information can be used to investigate the time-dependence of the MARY plot. If there is no time evolution, the signal can be averaged over the large number of time points, offering a temporal equivalent of multiplexing.

OCTAS and CRDS can also be compared on their acquisition of 2-D time-resolved spectra. From Table 7.2 the advantage of OCTAS is clear: per photoexcitation pulse the entire temporal decay is recorded (with resolution determined by the oscilloscope settings) at eight wavelengths simultaneously. CRDS, in contrast, must scan through each wavelength point and time delay individually to build up spectral and temporal resolution. For the typical example shown, OCTAS can record and average ten times more data than CRDS in just over 20% of the experimental time. It combines double the wavelength resolution with much improved time resolution, while maintaining comparable SNR. Consequently, the light sensitive protein sample is exposed to fewer than 25% of the high energy photons than in a comparable CRDS experiment.

Due to its universal capabilities, future effort should be focused on the optimisation of the new OCTAS instrument. Currently, the light coupling from the cavity to the PMT array is inefficient and SNR suffers due to the high amount of detector noise on the PMTs operated at high gain voltages. Minimum detectable absorbances of 1×10^{-7}, comparable to the BBCEAS instrument, should be achievable as PMTs are at least as sensitive as CCD cameras provided there is sufficient light intensity.

In addition to improving the collection optics, light transmission can also be increased by reducing the reflectivity of the broadband mirrors used. The background losses have been calculated for this cavity set-up as 1×10^{-3}, suggesting that reducing R to between 0.998–0.999 should increase the transmission, and therefore the SNR, without adversely impacting the cavity enhancement.

Employing a dual-beam variant to monitor and correct for long-term drift in the SCR output intensity would be of great benefit to both BBCEAS and OCTAS due to the significant intensity fluctuations in the shared probe light source. A similar approach

	CRDS	OCTAS
Photoexcitation	150 µJ /pulse	150 µJ /pulse
Acquisition rate	3.33 Hz	3.33 Hz
Time resolution	1 µs (−2 to 10 µs)	sub-µs (1 to 40 µs)
Time points	13	> 10000
Wavelength resolution	20 nm* (500–700 nm)	*ca.* 10 nm (500–730 nm)
Wavelength steps	11	3
Field points (0 mT & 15 mT)	2	2
Averages	50	500
Total acquisitons	14,300	3,000
Experimental duration	72 min	15 min
Total pump energy	2.15 J	0.45 J
Total no. photons	4.86×10^{18}	1.02×10^{18}
$\boldsymbol{A_{\min}}$	2.2×10^{-5}	1×10^{-5}

Table 7.2: Parameters for typical 2-D time-resolved spectra of cryptochromes in this thesis, recorded by CRDS and OCTAS. The temporal and spectral resolution can be varied with associated implications for experimental duration. The photons incident from the probe beam in each case are ignored, as these are only important for studies including the ground state. *the physical limit is determined by the probe laser linewidth but at the expense of vastly increased experimental time.

has been employed to great effect in recent work, coupled with field modulation in an instrument which has been able to very accurately record MFEs without the need for optical cavity enhancement (including discerning a LFE in FAD).[248] The comparatively high shot-to-shot fluctuations in the dye laser used for OCTAS and CRDS could also be monitored in a similar way to correct for variations in the ΔA signal.

Following the proof-of-principle studies reported here, the new modulated variant of the BBCEAS experiment should be applied to MFE measurements of cryptochrome pro-

teins. Its continuous monitoring of the ground state population throughout the experiment allows accurate percentage MFE values to be calculated, and could also be used as a self-referencing reading.

The chemical environment of a radical pair has been shown to have a great influence on its associated MFE, in terms of the viscosity and dielectric constant of solution. If such reactions are harnessed by animals for magnetic field sensing, then their cellular environment must have had such properties fine-tuned by evolution. Work is soon to be performed on cells containing *Dm*Cry protein, using an ultra sensitive fluorescence method developed concurrently within the group. The range of cavity-enhanced techniques reported in this thesis are now also well-suited for these investigations.

To be truly relevant to magnetoreception, the magnetic field effects measured in this project need to exhibit directionally dependent responses to an applied field. An evanescent-wave variant of the BBCEAS instrument is currently in development in the group, and efforts are under way to align proteins on the surface of the intracavity prism. If they can successfully be shown to exhibit preferential response to the direction of an applied field this would be strong evidence in support of the radical pair hypothesis.

Following the success of the MFE studies reported here, the BBCRDS pump-probe instrument has since been harnessed for the study of artificial "maquette" flavoproteins, whose structure (and therefore photochemistry) can be tuned by synthetic chemists. These maquettes can be created with flavin and tryptophan molecules bound at separations mimicking those found in natural cryptochrome proteins. Their fast kinetics and complicated spectral profiles emphasise the importance of deconvolution procedures, both in terms of the ring-down time and spectral global analysis (similar to that demonstrated for OCTAS in this work).

The OCTAS technique is well-suited to the further investigation of these maquette systems due to its advantages over CRDS as set out above. However, it is currently unable to monitor kinetic processes occurring under 1 µs due to the blinding effect of pump

beam scatter and sample fluorescence. Gated PMTs would be required to circumvent this issue. Owing to its rare combination of high sensitivity, microsecond time resolution, and broadband spectral coverage, OCTAS is ideally positioned for the study of animal cryptochrome proteins and assessing the potential impact of the fourth tryptophan residue on the radical pair hypothesis of avian magnetoreception.

Chapter 8

Bibliography

[1] H. Mouritsen & T. Ritz, "Magnetoreception and its use in bird navigation", *Current Opinion in Neurobiology*, **15**, 406–414 (2005).

[2] S. Johnsen & K. J. Lohmann, "The physics and neurobiology of magnetoreception", *Nature Reviews Neuroscience*, **6**, 703–712 (2005).

[3] K. J. Lohmann, "Q&A Animal Behaviour: Magnetic-field perception", *Nature*, **464**, 1140–1142 (2010).

[4] H. Mouritsen, *Magnetoreception in Birds and Its Use for Long-Distance Migration*, Sturkie's Avian Physiology, 6th Edition, Academic Press Ltd-Elsevier Science Ltd, London (2015).

[5] P. J. Hore & H. Mouritsen, "The Radical-Pair Mechanism of Magnetoreception", *Annual Review of Biophysics* (2016).

[6] A. Ahlbom, N. Day, M. Feychting, E. Roman, J. Skinner, J. Dockerty, M. Linet, M. McBride, J. Michaelis, J. H. Olsen, T. Tynes & P. K. Verkasalo, "A pooled analysis of magnetic fields and childhood leukaemia", *British Journal of Cancer*, **83**, 692–698 (2000).

[7] I. W. G. on the Evaluation of Carcinogenic Risks to Humans, W. H. Organization & I. A. for Research on Cancer, *Non-ionizing Radiation: Static and Extremely Low-frequency (ELF) Electric and Magnetic Fields*, volume 80, World Health Organization (2002).

[8] I. Lagroye, Y. Percherancier, J. Juutilainen, F. P. De Gannes & B. Veyret, "ELF magnetic fields: Animal studies, mechanisms of action", *Progress in Biophysics & Molecular Biology*, **107**, 369–373 (2011).

[9] J. L. Kirschvink & J. L. Gould, "Biogenic magnetite as a basis for magnetic field detection in animals", *Biosystems*, **13**, 181–201 (1981).

[10] J. L. Kirschvink, M. M. Walker & C. E. Diebel, "Magnetite-based magnetoreception", *Current Opinion in Neurobiology*, **11**, 462–467 (2001).

[11] A. F. Davila, G. Fleissner, M. Winklhofer & N. Petersen, "A new model for a magnetoreceptor in homing pigeons based on interacting clusters of superparamagnetic magnetite", *Physics and Chemistry of the Earth*, **28**, 647–652 (2003).

[12] J. L. Kirschvink, D. S. Jones & B. J. MacFadden, *Magnetite Biomineralization and Magnetoreception in Organisms: A New Biomagnetism*, volume 5, Springer Science & Business Media (2013).

[13] R. Kaptein & J. L. Oosterhoff, "Chemically induced dynamic nuclear polarization II - (Relation with anomalous ESR spectra)", *Chemical Physics Letters*, **4**, 195–197 (1969).

[14] G. L. Closs, "A mechanism explaining nuclear spin polarizations in radical combination reactions", *Journal of the American Chemical Society*, **91**, 4552–4554 (1969).

[15] U. E. Steiner & T. Ulrich, "Magnetic-field effects in chemical kinetics and related phenomena", *Chemical Reviews*, **89**, 51–147 (1989).

[16] T. Ritz, S. Adem & K. Schulten, "A Model for Photoreceptor-Based Magnetoreception in Birds", *Biophysical Journal*, **78**, 707–718 (2000).

[17] C. A. Dodson, P. J. Hore & M. I. Wallace, "A radical sense of direction: signalling and mechanism in cryptochrome magnetoreception", *Trends in Biochemical Sciences*, **38**, 435–446 (2013).

[18] S. R. T. Neil, K. Maeda, K. B. Henbest, M. Goez, R. Hemmens, C. R. Timmel & S. R. Mackenzie, "Cavity enhanced detection methods for probing the dynamics of spin correlated radical pairs in solution", *Molecular Physics*, **108**, 993–1003 (2010).

[19] K. Maeda, S. R. T. Neil, K. B. Henbest, S. Weber, E. Schleicher, P. J. Hore, S. R. Mackenzie & C. R. Timmel, "Following radical pair reactions in solution: A step change in sensitivity using cavity ring-down detection", *Journal of the American Chemical Society*, **133**, 17807–17815 (2011).

[20] P. A. M. Dirac, "The quantum theory of the electron", in *Proceedings of the Royal Society of London A: Mathematical, Physical and Engineering Sciences*, volume 117, pages 610–624, The Royal Society (1928).

[21] P. A. M. Dirac, "The quantum theory of the electron. Part II", in *Proceedings of the Royal Society of London A: Mathematical, Physical and Engineering Sciences*, volume 118, pages 351–361, The Royal Society (1928).

[22] P. W. Atkins & J. De Paula, *Atkins' Physical Chemistry*, Oxford University Press (2006), ISBN 0716787598.

[23] P. W. Atkins & R. S. Friedman, *Molecular Quantum Mechanics*, Oxford University Press (2011), ISBN 0199541426.

[24] N. J. B. Green, *Quantum Mechanics 1: Foundations*, volume 2, Oxford University Press on Demand (1997).

[25] N. J. B. Green, *Quantum Mechanics 2: The Toolkit*, volume 2, Oxford University Press on Demand (1998).

[26] W. Gerlach & O. Stern, "Der experimentelle nachweis der richtungsquantelung im magnetfeld", *Zeitschrift für Physik A Hadrons and Nuclei*, **9**, 349–352 (1922).

[27] J. A. Syage, "A vector model for CIDEP - the role of the exchange interaction", *Chemical Physics Letters*, **91**, 378–382 (1982).

[28] O. Efimova & P. J. Hore, "Role of exchange and dipolar interactions in the radical pair model of the avian magnetic compass", *Biophysical Journal*, **94**, 1565–1574 (2008).

[29] P. A. M. Dirac, "Quantum mechanics of many-electron systems", in *Proceedings of the Royal Society of London A: Mathematical, Physical and Engineering Sciences*, volume 123, pages 714–733, The Royal Society (1929).

[30] C. T. Rodgers, "Magnetic field effects in chemical systems", *Pure and Applied Chemistry*, **81**, 19–43 (2009).

[31] F. J. J. Dekanter, J. A. Denhollander, A. H. Huizer & R. Kaptein, "Biradical CIDNP and dynamics of polymethylene chains", *Molecular Physics*, **34**, 857–874 (1977).

[32] Y. Salikov, R. Sagdeev & A. Buchachenko, *Spin Polarisation and Magnetic Field Effects in Radical Reactions*, Elsevier, Amsterdam (1984).

[33] C. T. Rodgers & P. J. Hore, "Chemical magnetoreception in birds: The radical pair mechanism", *Proceedings of the National Academy of Sciences*, **106**, 353–360 (2009).

[34] S. Nagakura, H. Hayashi, T. Azumi et al., *Dynamic Spin Chemistry*, Kodansha; Wiley (1998).

[35] A. R. O'Dea, A. F. Curtis, N. J. B. Green, C. R. Timmel & P. J. Hore, "Influence of

dipolar interactions on radical pair recombination reactions subject to weak magnetic fields", *Journal of Physical Chemistry A*, **109**, 869–873 (2005).

[36] C. T. Rodgers, S. A. Norman, K. B. Henbest, C. R. Timmel & P. J. Hore, "Determination of Radical Re-encounter Probability Distributions from Magnetic Field Effects on Reaction Yields", *Journal of the American Chemical Society*, **129**, 6746–6755 (2007).

[37] D. R. Kattnig, E. W. Evans, V. Dejean, C. A. Dodson, M. I. Wallace, S. R. Mackenzie, C. R. Timmel & P. J. Hore, "Chemical amplification of magnetic field effects relevant to avian magnetoreception", *Nature Chemistry*, **8**, 384–391 (2016).

[38] B. Brocklehurst, "Spin correlation in geminate recombination of radical ions in hydrocarbons: Part 1 - theory of the magnetic-field effect", *Journal of the Chemical Society-Faraday Transactions II*, **72**, 1869–1884 (1976).

[39] C. R. Timmel, U. Till, B. Brocklehurst, K. A. McLauchlan & P. J. Hore, "Effects of weak magnetic fields on free radical recombination reactions", *Molecular Physics*, **95**, 71–89 (1998).

[40] C. R. Timmel, F. Cintolesi, B. Brocklehurst & P. J. Hore, "Model calculations of magnetic field effects on the recombination reactions of radicals with anisotropic hyperfine interactions", *Chemical Physics Letters*, **334**, 387–395 (2001).

[41] U. Till, C. Timmel, B. Brocklehurst & P. J. Hore, "The influence of very small magnetic fields on radical recombination reactions in the limit of slow recombination", *Chemical Physics Letters*, **298**, 7–14 (1998).

[42] H. Hayashi & S. Nagakura, "Theoretical study of relaxation mechanisms in magnetic-field effects on chemical reactions", *Bulletin of the Chemical Society of Japan*, **57**, 322–328 (1984).

[43] S. R. T. Neil, *Development of Novel Cavity-Based Spectroscopic Techniques for use in Probing Condensed Phase and Interfacial Systems*, DPhil. Thesis, University of Oxford (2012).

[44] P. Valberg, R. Kavet & C. Rafferty, "Can low-level 50/60 Hz electric and magnetic fields cause biological effects?", *Radiation Research*, **148**, 2–21 (1997).

[45] C. J. Portier & M. S. Wolfe, "Assessment of health effects from exposure to power-line frequency electric and magnetic fields", *NIH Publication*, **98**, 3981 (1998).

[46] M. Havas, "Biological effects of non-ionizing electromagnetic energy: A critical review of the reports by the US National Research Council and the US National Institute of Environmental Health Sciences as they relate to the broad realm of EMF bioeffects", *Environmental Reviews*, **8**, 173–253 (2000).

[47] Z. Sienkiewicz & C. Kowalczuk, *A Summary of Recent Reports on Mobile Phones and Health (2000-2004)*, National Radiological Protection Board (2005).

[48] D. Wartenberg, "Residential magnetic fields and childhood leukemia: a meta-analysis", *American Journal of Public Health*, **88**, 1787–1794 (1998).

[49] K. K. Cheng, N. Day, R. Cartwright, A. Craft, J. M. Birch, O. B. Eden, P. A. McKinney, J. Peto, V. Beral, E. Roman, P. Elwood, F. E. Alexander, C. E. D. Chilvers, R. Doll, C. M. Taylor, M. Greaves, D. Goodhead, F. A. Fry, G. Adams, S. G. Allen, M. P. Maslanyj, T. J. Mee, E. Gilman, J. Skinner, D. Williams, J. Deacon, J. Peto, V. Beral, E. Roman, P. Elwood, F. E. Alexander, M. Mott, K. Muir, G. Law, J. Simpson & U. K. C. C. S. Investigators, "Exposure to power-frequency magnetic fields and the risk of childhood cancer", *Lancet*, **354**, 1925–1931 (1999).

[50] J. R. Woodward, T. J. Foster, A. R. Jones, A. T. Salaoru & N. S. Scrutton, "Time-resolved studies of radical pairs", *Biochemical Society Transactions*, **37**, 358–362 (2009).

[51] C. T. Lin & D. Shalitin, "Cryptochrome structure and signal transduction", *Annual Review of Plant Biology*, **54**, 469–496 (2003).

[52] C. T. Lin & T. Todo, "The cryptochromes", *Genome Biology*, **6** (2005).

[53] A. J. Hoff, "Magnetic-field effects on photosynthetic reactions", *Quarterly Reviews of Biophysics*, **14**, 599–665 (1981).

[54] R. Haberkorn & M. E. Michelbeyerle, "Mechanism of magnetic-field effects in bacterial photosynthesis", *Biophysical Journal*, **26**, 489–498 (1979).

[55] Y. Liu, R. Edge, K. Henbest, C. R. Timmel, P. J. Hore & P. Gast, "Magnetic field effect on singlet oxygen production in a biochemical system", *Chemical Communications*, pages 174–176 (2005).

[56] M. Ahmad, P. Galland, T. Ritz, R. Wiltschko & W. Wiltschko, "Magnetic intensity affects cryptochrome-dependent responses in Arabidopsis thaliana", *Planta*, **225**, 615–624 (2007).

[57] S.-R. Harris, K. B. Henbest, K. Maeda, J. R. Pannell, C. R. Timmel, P. J. Hore & H. Okamoto, "Effect of magnetic fields on cryptochrome-dependent responses in Arabidopsis thaliana", *Journal of The Royal Society Interface*, pages rsif–2008 (2009).

[58] H. Mouritsen, "The magnetic sense(s) of birds: recent molecular and physiological evidence", *Journal of Ornithology*, **147**, 73–73 (2006).

[59] H. Mouritsen & P. J. Hore, "The magnetic retina: light-dependent and trigeminal magnetoreception in migratory birds", *Current Opinion in Neurobiology*, **22**, 343–52 (2012).

[60] H. Mouritsen, D. Heyers & O. Gunturkun, *The Neural Basis of Long-Distance Nav-*

igation in Birds, volume 78 of *Annual Review of Physiology*, pages 133–154, Annual Reviews, Palo Alto (2016).

[61] P. J. Hore, "Are biochemical reactions affected by weak magnetic fields?", *Proceedings of the National Academy of Sciences of the United States of America*, **109**, 1357–1358 (2012).

[62] W. Wiltschko & R. Wiltschko, "Magnetic compass of European robins", *Science*, **176**, 62–64 (1972).

[63] W. Wiltschko & R. Wiltschko, "Magnetic compass orientation in birds and its physiological basis", *Naturwissenschaften*, **89**, 445–452 (2002).

[64] R. Wiltschko & W. Wiltschko, "Avian magnetic compass: Its functional properties and physical basis", *Current Zoology*, **56**, 265–276 (2010).

[65] W. Wiltschko, R. Wiltschko & T. Ritz, *The Mechanism of the Avian Magnetic Compass*, volume 3 of *Procedia Chemistry*, Elsevier Science Bv, Amsterdam (2011).

[66] T. P. Quinn, R. T. Merrill & E. L. Brannon, "Magnetic field detection in sockeye salmon", *Journal of Experimental Zoology*, **217**, 137–142 (1981).

[67] D. Shcherbakov, M. Winklhofer, N. Petersen, J. Steidle, R. Hilbig & M. Blum, "Magnetosensation in zebrafish", *Current Biology*, **15**, R161–R162 (2005).

[68] P. Light, M. Salmon & K. J. Lohmann, "Geomagnetic orientation of loggerhead sea turtles: evidence for an inclination compass", *Journal of Experimental Biology*, **182**, 1–10 (1993).

[69] J. B. Phillips, "Two magnetoreception pathways in a migratory salamander", *Science*, **233**, 765–767 (1986).

[70] R. Wehner & T. Labhart, "Perception of the geomagnetic field in the fly Drosophila melanogaster", *Experientia*, **26**, 967–968 (1970).

[71] R. J. Gegear, L. E. Foley, A. Casselman & S. M. Reppert, "Animal cryptochromes mediate magnetoreception by an unconventional photochemical mechanism", *Nature*, **463**, 804–807 (2010).

[72] P. Němec, J. Altmann, S. Marhold, H. Burda & H. H. Oelschläger, "Neuroanatomy of magnetoreception: the superior colliculus involved in magnetic orientation in a mammal", *Science*, **294**, 366–368 (2001).

[73] S. Marhold, W. Wiltschko & H. Burda, "A magnetic polarity compass for direction finding in a subterranean mammal", *Naturwissenschaften*, **84**, 421–423 (1997).

[74] W. Wiltschko & R. Wiltschko, "Magnetoreception in birds: two receptors for two different tasks", *Journal of Ornithology*, **148**, S61–S76 (2007).

[75] Y. Harada, M. Taniguchi, H. Namatame & A. Iida, "Magnetic materials in otoliths of bird and fish lagena and their function", *Acta Oto-Laryngologica*, **121**, 590–595 (2001).

[76] Y. Harada, "The relation between the migration function of birds and fishes and their lagenal function", *Acta Oto-Laryngologica*, **128**, 432–439 (2008).

[77] Y. Zhao, Y. N. Huang, L. Shi & L. Chen, "Analysis of magnetic elements in otoliths of the macula lagena in homing pigeons with inductively coupled plasma mass spectrometry", *Neuroscience Bulletin*, **25**, 101–108 (2009).

[78] L. Q. Wu & J. D. Dickman, "Magnetoreception in an avian brain in part mediated by inner ear lagena", *Current Biology*, **21**, 418–423 (2011).

[79] R. Beason, N. Dussourd & M. Deutschlander, "Behavioural evidence for the use of magnetic material in magnetoreception by a migratory bird", *Journal of Experimental Biology*, **198**, 141–146 (1995).

[80] M. N. Williams & J. M. Wild, "Trigeminally innervated iron-containing structures in the beak of homing pigeons, and other birds", *Brain Research*, **889**, 243–246 (2001).

[81] G. Fleissner, E. Holtkamp-Rotzler, M. Hanzlik, M. Winklhofer, G. Fleissner, N. Petersen & W. Wiltschko, "Ultrastructural analysis of a putative magnetoreceptor in the beak of homing pigeons", *Journal of Comparative Neurology*, **458**, 350–360 (2003).

[82] G. Falkenberg, G. Fleissner, K. Schuchardt, M. Kuehbacher, P. Thalau, H. Mouritsen, D. Heyers, G. Wellenreuther & G. Fleissner, "Avian magnetoreception: Elaborate iron mineral containing dendrites in the upper beak seem to be a common feature of birds", *PloS one*, **5**, e9231 (2010).

[83] C. V. Mora, M. Davison, J. M. Wild & M. M. Walker, "Magnetoreception and its trigeminal mediation in the homing pigeon", *Nature*, **432**, 508–511 (2004).

[84] D. Heyers, M. Zapka, M. Hoffmeister, J. M. Wild & H. Mouritsen, "Magnetic field changes activate the trigeminal brainstem complex in a migratory bird", *Proceedings of the National Academy of Sciences of the United States of America*, **107**, 9394–9399 (2010).

[85] M. Zapka, D. Heyers, C. M. Hein, S. Engels, N. L. Schneider, J. Hans, S. Weiler, D. Dreyer, D. Kishkinev, J. M. Wild & H. Mouritsen, "Visual but not trigeminal mediation of magnetic compass information in a migratory bird", *Nature*, **461**, 1274–1277 (2009).

[86] C. D. Treiber, M. C. Salzer, J. Riegler, N. Edelman, C. Sugar, M. Breuss, P. Pichler, H. Cadiou, M. Saunders, M. Lythgoe, J. Shaw & D. A. Keays, "Clusters of iron-rich cells in the upper beak of pigeons are macrophages not magnetosensitive neurons", *Nature*, **484**, 367–370 (2012).

[87] C. E. Diebel, R. Proksch, C. R. Green, P. Neilson & M. M. Walker, "Magnetite defines a vertebrate magnetoreceptor", *Nature*, **406**, 299–302 (2000).

[88] S. H. Eder, H. Cadiou, A. Muhamad, P. A. McNaughton, J. L. Kirschvink & M. Winklhofer, "Magnetic characterization of isolated candidate vertebrate magnetoreceptor cells", *Proceedings of the National Academy of Sciences*, **109**, 12022–12027 (2012).

[89] P. Thalau, T. Ritz, H. Burda, R. E. Wegner & R. Wiltschko, "The magnetic compass mechanisms of birds and rodents are based on different physical principles", *Journal of the Royal Society Interface*, **3**, 583–587 (2006).

[90] T. Ritz, P. Thalau, J. B. Phillips, R. Wiltschko & W. Wiltschko, "Resonance effects indicate a radical-pair mechanism for avian magnetic compass", *Nature*, **429**, 177–180 (2004).

[91] H. Mouritsen, G. Feenders, M. Liedvogel & W. Kropp, "Migratory birds use head scans to detect the direction of the Earth's magnetic field", *Current Biology*, **14**, 1946–1949 (2004).

[92] M. Liedvogel, K. Maeda, K. Henbest, E. Schleicher, T. Simon, C. R. Timmel, P. J. Hore & H. Mouritsen, "Chemical magnetoreception: Bird cryptochrome 1a is excited by blue light and forms long-lived radical-pairs", *PloS one*, **2**, e1106 (2007).

[93] K. Maeda, K. B. Henbest, F. Cintolesi, I. Kuprov, C. T. Rodgers, P. A. Liddell, D. Gust, C. R. Timmel & P. J. Hore, "Chemical compass model of avian magnetoreception", *Nature*, **453**, 387–390 (2008).

[94] T. Ritz, R. Wiltschko, P. J. Hore, C. T. Rodgers, K. Stapput, P. Thalau, C. R. Timmel & W. Wiltschko, "Magnetic compass of birds is based on a molecule with optimal directional sensitivity", *Biophysical Journal*, **96**, 3451–3457 (2009).

[95] C. Jianming, G. G. Guerreschi & H. J. Briegel, "Quantum control and entanglement in a chemical compass", *Physical Review Letters*, **104**, 220502 (2010).

[96] K. Maeda, A. J. Robinson, K. B. Henbest, H. J. Hogben, T. Biskup, M. Ahmad, E. Schleicher, S. Weber, C. R. Timmel & P. J. Hore, "Magnetically sensitive light-induced reactions in cryptochrome are consistent with its proposed role as a magnetoreceptor", *Proceedings of the National Academy of Sciences of the United States of America*, **109**, 4774–4779 (2012).

[97] W. Wiltschko & R. Wiltschko, "Light-dependent magnetoreception in birds: the behaviour of European robins, Erithacus rubecula, under monochromatic light of various wavelengths and intensities", *Journal of Experimental Biology*, **204**, 3295–3302 (2001).

[98] R. Muheim, J. Bäckman & S. Åkesson, "Magnetic compass orientation in European robins is dependent on both wavelength and intensity of light", *Journal of Experimental Biology*, **205**, 3845–3856 (2002).

[99] C. Niessner, S. Denzau, K. Stapput, M. Ahmad, L. Peichl, W. Wiltschko & R. Wiltschko, "Magnetoreception: activated cryptochrome 1a concurs with magnetic orientation in birds", *Journal of The Royal Society Interface*, **10**, 20130638 (2013).

[100] P. Thalau, T. Ritz, K. Stapput, R. Wiltschko & W. Wiltschko, "Magnetic compass orientation of migratory birds in the presence of a 1.315 MHz oscillating field", *Naturwissenschaften*, **92**, 86–90 (2005).

[101] S. Engels, N. L. Schneider, N. Lefeldt, C. M. Hein, M. Zapka, A. Michalik, D. Elbers, A. Kittel, P. J. Hore & H. Mouritsen, "Anthropogenic electromagnetic noise disrupts magnetic compass orientation in a migratory bird", *Nature*, **509**, 353–356 (2014).

[102] R. Wiltschko, P. Thalau, D. Gehring, C. Niessner, T. Ritz & W. Wiltschko, "Magnetoreception in birds: the effect of radio-frequency fields", *Journal of the Royal Society Interface*, **12**, 20141103 (2015).

[103] K. Schulten, C. E. Swenberg & A. Weller, "Biomagnetic sensory mechanism based on magnetic-field modulated coherent electron-spin motion", *Zeitschrift Fur Physikalische Chemie-Frankfurt*, **111**, 1–5 (1978).

[104] A. Moeller, S. Sagasser, W. Wiltschko & B. Schierwater, "Retinal cryptochrome in a migratory passerine bird: a possible transducer for the avian magnetic compass", *Naturwissenschaften*, **91**, 585–588 (2004).

[105] M. Liedvogel & H. Mouritsen, "Cryptochromes – a potential magnetoreceptor: what do we know and what do we want to know?", *Journal of the Royal Society Interface*, **7**, S147–S162 (2010).

[106] C. Niessner, S. Denzau, J. C. Gross, L. Peichl, H. J. Bischof, G. Fleissner, W. Wiltschko & R. Wiltschko, "Avian ultraviolet/violet cones identified as probable magnetoreceptors", *PloS one*, **6**, e20091 (2011).

[107] M. Ahmad & A. R. Cashmore, "HY4 gene of A-thaliana encodes a protein with characteristics of a blue-light photoreceptor", *Nature*, **366**, 162–166 (1993).

[108] A. R. Cashmore, J. A. Jarillo, Y. J. Wu & D. M. Liu, "Cryptochromes: Blue light receptors for plants and animals", *Science*, **284**, 760–765 (1999).

[109] A. R. Cashmore, "Cryptochromes: Enabling plants and animals to determine circadian time", *Cell*, **114**, 537–543 (2003).

[110] A. Sancar, "Structure and function of DNA photolyase and cryptochrome blue-light photoreceptors", *Chemical Reviews*, **103**, 2203–2237 (2003).

[111] A. Sancar, "Structure and function of DNA photolyase", *Biochemistry*, **33**, 2–9 (1994).

[112] C. Aubert, M. H. Vos, P. Mathis, A. P. M. Eker & K. Brettel, "Intraprotein radical transfer during photoactivation of DNA photolyase", *Nature*, **405**, 586–590 (2000).

[113] B. D. Zoltowski, A. T. Vaidya, D. Top, J. Widom, M. W. Young & B. R. Crane, "Structure of full-length Drosophila cryptochrome", *Nature*, **480**, 396–399 (2011).

[114] A. Lukacs, A. P. M. Eker, M. Byrdin, K. Brettel & M. H. Vos, "Electron hopping through the 15 angstrom triple tryptophan molecular wire in DNA photolyase occurs within 30 ps", *Journal of the American Chemical Society*, **130**, 14394–14395 (2008).

[115] B. Paulus, C. Bajzath, F. Melin, L. Heidinger, V. Kromm, C. Herkersdorf, U. Benz, L. Mann, P. Stehle, P. Hellwig, S. Weber & E. Schleicher, "Spectroscopic characterization of radicals and radical pairs in fruit fly cryptochrome-protonated and nonprotonated flavin radical-states", *Febs Journal*, **282**, 3175–3189 (2015).

[116] P. Müller, J. Yamamoto, R. Martin, S. Iwai & K. Brettel, "Discovery and functional analysis of a 4th electron-transferring tryptophan conserved exclusively in animal cryptochromes and (6-4) photolyases", *Chemical Communications*, **51**, 15502–15505 (2015).

[117] Y. M. Gindt, E. Vollenbroek, K. Westphal, H. Sackett, A. Sancar & G. T. Babcock, "Origin of the transient electron paramagnetic resonance signals in DNA photolyase", *Biochemistry*, **38**, 3857–3866 (1999).

[118] T. Biskup, E. Schleicher, A. Okafuji, G. Link, K. Hitomi, E. D. Getzoff & S. Weber, "Direct observation of a photoinduced radical pair in a cryptochrome blue-light photoreceptor", *Angewandte Chemie-International Edition*, **48**, 404–407 (2009).

[119] S. Weber, C. W. M. Kay, H. Mogling, K. Mobius, K. Hitomi & T. Todo, "Photoactivation of the flavin cofactor in Xenopus laevis (6-4) photolyase: Observation of

a transient tyrosyl radical by time-resolved electron paramagnetic resonance", *Proceedings of the National Academy of Sciences of the United States of America*, **99**, 1319–1322 (2002).

[120] S. Weber, T. Biskup, A. Okafuji, A. R. Marino, T. Berthold, G. Link, K. Hitomi, E. D. Getzoff, E. Schleicher & J. R. Norris, "Origin of light-induced spin-correlated radical pairs in cryptochrome", *Journal of Physical Chemistry B*, **114**, 14745–14754 (2010).

[121] T. Biskup, B. Paulus, A. Okafuji, K. Hitomi, E. D. Getzoff, S. Weber & E. Schleicher, "Variable electron transfer pathways in an amphibian cryptochrome: Tryptophan vs tyrosine-based radical pairs", *Journal of Biological Chemistry*, **288**, 9249–9260 (2013).

[122] I. A. Solov'yov & K. Schulten, "Reaction kinetics and mechanism of magnetic field effects in cryptochrome", *Journal of Physical Chemistry B*, **116**, 1089–1099 (2012).

[123] I. A. Solov'yov, T. Ritz, K. Schulten & P. J. Hore, "A chemical compass for bird navigation", *Quantum Effects in Biology*, pages 218–236 (2014).

[124] R. J. Gegear, A. Casselman, S. Waddell & S. M. Reppert, "Cryptochrome mediates light-dependent magnetosensitivity in Drosophila", *Nature*, **454**, 1014–1018 (2008).

[125] L. E. Foley, R. J. Gegear & S. M. Reppert, "Human cryptochrome exhibits light-dependent magnetosensitivity", *Nature Communications*, **2**, 356 (2011).

[126] S. Qin, H. Yin, C. Yang, Y. Dou, Z. Liu, P. Zhang, H. Yu, Y. Huang, J. Feng, J. Hao et al., "A magnetic protein biocompass", *Nature Materials*, **15**, 217–226 (2016).

[127] T. Ritz, M. Ahmad, H. Mouritsen, R. Wiltschko & W. Wiltschko, "Photoreceptor-based magnetoreception: optimal design of receptor molecules, cells, and neuronal processing", *Journal of the Royal Society Interface*, **7**, S135–S146 (2010).

[128] K. B. Henbest, K. Maeda, P. J. Hore, M. Joshi, A. Bacher, R. Bittl, S. Weber, C. R. Timmel & E. Schleicher, "Magnetic-field effect on the photoactivation reaction of Escherichia coli DNA photolyase", *Proceedings of the National Academy of Sciences*, **105**, 14395–14399 (2008).

[129] J. R. Woodward, C. R. Timmel, K. A. McLauchlan & P. J. Hore, "Radio frequency magnetic field effects on electron-hole recombination", *Physical Review Letters*, **87**, 077602/1–077602/4 (2001).

[130] B. Brocklehurst, "Magnetic fields and radical reactions: recent developments and their role in nature", *Chemical Society Reviews*, **31**, 301–311 (2002).

[131] J. R. Woodward, "Radical pairs in solution", *Progress in Reaction Kinetics and Mechanism*, **27**, 165–207 (2002).

[132] C. R. Timmel & K. B. Henbest, "A study of spin chemistry in weak magnetic fields", *Philosophical Transactions of the Royal Society of London Series A: Mathematical Physical and Engineering Sciences*, **362**, 2573–2589 (2004).

[133] E. W. Evans, C. A. Dodson, K. Maeda, T. Biskup, C. J. Wedge & C. R. Timmel, "Magnetic field effects in flavoproteins and related systems", *Interface Focus*, **3**, 20130037 (2013).

[134] E. W. Evans, J. Li, J. G. Storey, K. Maeda, K. B. Henbest, C. A. Dodson, P. J. Hore, S. R. Mackenzie & C. R. Timmel, "Sensitive fluorescence-based detection of magnetic field effects in photoreactions of flavins", *Physical Chemistry Chemical Physics*, **17**, 18456–18463 (2015).

[135] M. Horiuchi, K. Maeda & T. Arai, "Magnetic field effect on electron transfer reactions of flavin derivatives associated with micelles", *Applied Magnetic Resonance*, **23**, 309–318 (2003).

[136] M. Murakami, K. Maeda & T. Arai, "Dynamics of intramolecular electron transfer reaction of FAD studied by magnetic field effects on transient absorption spectra", *Journal of Physical Chemistry A*, **109**, 5793–5800 (2005).

[137] B. Brocklehurst & K. A. McLauchlan, "Free radical mechanism for the effects of environmental electromagnetic fields on biological systems", *International Journal of Radiation Biology*, **69**, 3–24 (1996).

[138] A. Weller, F. Nolting & H. Staerk, "A quantitative interpretation of the magnetic-field effect on hyperfine-coupling-induced triplet formation from radical ion-pairs", *Chemical Physics Letters*, **96**, 24–27 (1983).

[139] K. Schulten, H. Staerk, A. Weller, H.-J. Werner & B. Nickel, "Magnetic field dependence of the geminate recombination of radical ion pairs in polar solvents", *Zeitschrift für Physikalische Chemie*, **101**, 371–390 (1976).

[140] F. Cintolesi, T. Ritz, C. W. M. Kay, C. R. Timmel & P. J. Hore, "Anisotropic recombination of an immobilized photoinduced radical pair in a 50-μT magnetic field: A model avian photomagnetoreceptor", *Chemical Physics*, **294**, 385–399 (2003).

[141] F. Himo, A. Graslund & L. A. Eriksson, "Density functional calculations on model tyrosyl radicals", *Biophysical Journal*, **72**, 1556–1567 (1997).

[142] S. R. T. Neil, J. Li, D. M. W. Sheppard, J. Storey, K. Maeda, K. B. Henbest, P. J. Hore, C. R. Timmel & S. R. Mackenzie, "Broadband cavity-enhanced detection of magnetic field effects in chemical models of a cryptochrome magnetoreceptor", *Journal of Physical Chemistry B*, **118**, 4177–4184 (2014).

[143] E. Frankland & J. Lockyer, "Researches on gaseous spectra in relation to the physical constitution of the sun, stars, and nebulae – second note", *Proceedings of the Royal Society of London*, pages 453–454 (1868).

[144] P. Bouguer, *Essai d'Optique sur la Gradation de la Lumière*, Jombert (1729).

[145] J. Lambert, *Photometria sive de Mensura et Gradibus Luminus, Colorum et Umbrae* (1892).

[146] A. Beer, "Bestimmung der Absorption des rothen Lichts in farbigen Flüssigkeiten", *Annalen der Physik und Chemie*, **86**, 78–88 (1852).

[147] J. U. White, "Long optical paths of large aperture", *JOSA*, **32**, 285–288 (1942).

[148] D. Herriott, R. Kompfner & H. Kogelnik, "Off-axis paths in spherical mirror interferometers", *Applied Optics*, **3**, 523–526 (1964).

[149] B. Abbott, R. Abbott, T. Abbott, M. Abernathy, F. Acernese, K. Ackley, C. Adams, T. Adams, P. Addesso, R. Adhikari et al., "Observation of gravitational waves from a binary black hole merger", *Physical Review Letters*, **116**, 061102 (2016).

[150] A. Einstein, "Approximative integration of the field equations of gravitation", *Sitzungsber. Preuss. Akad. Wiss. Berlin (Math. Phys.)*, **688** (1916).

[151] G. Hernández, *Fabry-perot Interferometers*, Cambridge University Press (1988).

[152] M. Mazurenka, A. J. Orr-Ewing, R. Peverall & G. A. D. Ritchie, "Cavity ring-down and cavity enhanced spectroscopy using diode lasers", *Annual Reports on the Progress of Chemistry, Vol 101, Section C, Physical Chemistry*, **101**, 100–142 (2005).

[153] H. Kogelnik & T. Li, "Laser beams and resonators", *Applied Optics*, **5**, 1550–1567 (1966).

[154] J. M. Herbelin & J. A. McKay, "Development of laser mirrors of very high reflectivity using the cavity-attenuated phase-shift method", *Applied Optics*, **20**, 3341–3344 (1981).

[155] M. A. Kwok, J. M. Herbelin & R. H. Ueunten, "Cavity phase-shift method for high reflectance measurements at mid-infrared wavelengths", *Optical Engineering*, **21**, 979–982 (1982).

[156] A. O'Keefe & D. A. G. Deacon, "Cavity ring-down optical spectrometer for absorption measurements using pulsed laser sources", *Review of Scientific Instruments*, **59**, 2544–2551 (1988).

[157] G. Berden, R. Peeters & G. Meijer, "Cavity ring-down spectroscopy: Experimental schemes and applications", *International Reviews in Physical Chemistry*, **19**, 565–607 (2000).

[158] G. Berden & R. Engeln, *Cavity Ring-Down Spectroscopy: Techniques and Applications*, Wiley-Blackwell (2009).

[159] C. Vallance, "Innovations in cavity ringdown spectroscopy", *New Journal of Chemistry*, **29**, 867–874 (2005).

[160] G. Gagliardi & H.-P. Loock, *Cavity-Enhanced Spectroscopy and Sensing*, Springer (2014).

[161] R. Engeln, G. Berden, R. Peeters & G. Meijer, "Cavity enhanced absorption and cavity enhanced magnetic rotation spectroscopy", *Review of Scientific Instruments*, **69**, 3763–3769 (1998).

[162] A. O'Keefe, "Integrated cavity output analysis of ultra-weak absorption", *Chemical Physics Letters*, **293**, 331–336 (1998).

[163] S. E. Fiedler, A. Hese & A. A. Ruth, "Incoherent broad-band cavity-enhanced absorption spectroscopy", *Chemical Physics Letters*, **371**, 284–294 (2003).

[164] S. E. Fiedler, A. Hese & A. A. Ruth, "Incoherent broad-band cavity-enhanced absorption spectroscopy of liquids", *Review of Scientific Instruments*, **76**, 023107 (2005).

[165] S. E. Fiedler, A. Hese & U. Heitmann, "Influence of the cavity parameters on the

output intensity in incoherent broadband cavity-enhanced absorption spectroscopy", *Review of Scientific Instruments*, **78**, 073104 (2007).

[166] B. Ouyang & R. L. Jones, "Understanding the sensitivity of cavity-enhanced absorption spectroscopy: pathlength enhancement versus noise suppression", *Applied Physics B: Lasers and Optics*, **109**, 581–591 (2012).

[167] M. D. Wheeler, S. M. Newman, A. J. Orr-Ewing & M. N. R. Ashfold, "Cavity ringdown spectroscopy", *Journal of the Chemical Society, Faraday Transactions*, **94**, 337–351 (1998).

[168] J. T. Hodges, J. P. Looney & R. D. van Zee, "Response of a ring-down cavity to an arbitrary excitation", *The Journal of Chemical Physics*, **105**, 10278–10288 (1996).

[169] D. Romanini, A. A. Kachanov, N. Sadeghi & F. Stoeckel, "CW cavity ring down spectroscopy", *Chemical Physics Letters*, **264**, 316–322 (1997).

[170] D. Romanini, A. A. Kachanov & F. Stoeckel, "Diode laser cavity ring down spectroscopy", *Chemical Physics Letters*, **270**, 538–545 (1997).

[171] B. A. Paldus, C. C. Harb, T. G. Spence, B. Wilke, J. Xie, J. S. Harris & R. N. Zare, "Cavity-locked ring-down spectroscopy", *Journal of Applied Physics*, **83**, 3991–3997 (1998).

[172] J. Morville, D. Romanini, A. A. Kachanov & M. Chenevier, "Two schemes for trace detection using cavity ringdown spectroscopy", *Applied Physics B: Lasers and Optics*, **78**, 465–476 (2004).

[173] J. Ye & J. L. Hall, "Cavity ringdown heterodyne spectroscopy: High sensitivity with microwatt light power", *Physical Review A*, **61**, 061802 (2000).

[174] M. Schnippering, H. V. Powell, M. Q. Zhang, J. V. Macpherson, P. R. Unwin, M. Mazurenka & S. R. Mackenzie, "Surface assembly and redox dissolution of sil-

ver nanoparticles monitored by evanescent wave cavity ring-down spectroscopy", *Journal of Physical Chemistry C*, **112**, 15274–15280 (2008).

[175] H. V. Powell, M. Schnippering, M. Mazurenka, J. V. Macpherson, S. R. Mackenzie & P. R. Unwin, "Evanescent wave cavity ring-down spectroscopy as a probe of interfacial adsorption: Interaction of tris(2,2 '-bipyridine)ruthenium(II) with silica surfaces and polyelectrolyte films", *Langmuir*, **25**, 248–255 (2009).

[176] M. Schnippering, H. V. Powell, S. R. Mackenzie & P. R. Unwin, "Real-time monitoring of polyaniline nanoparticle formation on surfaces", *The Journal of Physical Chemistry C*, **113**, 20221–20227 (2009).

[177] M. Mazurenka, S. M. Hamilton, P. R. Unwin & S. R. Mackenzie, "In-situ measurement of colloidal gold adsorption on functionalized silica surfaces", *The Journal of Physical Chemistry C*, **112**, 6462–6468 (2008).

[178] M. Mazurenka, L. Wilkins, J. V. Macpherson, P. R. Unwin & S. R. Mackenzie, "Evanescent wave cavity ring-down spectroscopy in a thin-layer electrochemical cell", *Analytical Chemistry*, **78**, 6833–6839 (2006).

[179] K. K. Lehmann & D. Romanini, "The superposition principle and cavity ring-down spectroscopy", *The Journal of Chemical Physics*, **105**, 10263–10277 (1996).

[180] S. M. Ball, I. M. Povey, E. G. Norton & R. L. Jones, "Broadband cavity ringdown spectroscopy of the NO3 radical", *Chemical Physics Letters*, **342**, 113–120 (2001).

[181] S. M. Ball & R. L. Jones, "Broad-band cavity ring-down spectroscopy", *Chemical Reviews*, **103**, 5239–5262 (2003).

[182] J. M. Langridge, S. M. Ball & R. L. Jones, "A compact broadband cavity enhanced absorption spectrometer for detection of atmospheric NO2 using light emitting diodes", *Analyst*, **131**, 916–922 (2006).

[183] S. M. Ball, J. M. Langridge & R. L. Jones, "Broadband cavity enhanced absorption spectroscopy using light emitting diodes", *Chemical Physics Letters*, **398**, 68–74 (2004).

[184] M. Islam, L. N. Seetohul & Z. Ali, "Liquid-phase broadband cavity-enhanced absorption spectroscopy measurements in a 2 mm cuvette", *Applied Spectroscopy*, **61**, 649–658 (2007).

[185] L. N. Seetohul, Z. Ali & M. Islam, "Broadband cavity enhanced absorption spectroscopy as a detector for HPLC", *Analytical Chemistry*, **81**, 4106–4112 (2009).

[186] L. N. Seetohul, Z. Ali & M. Islam, "Liquid-phase broadband cavity enhanced absorption spectroscopy (BBCEAS) studies in a 20 cm cell", *Analyst*, **134**, 1887–1895 (2009).

[187] L. van der Sneppen, G. Hancock, C. Kaminski, T. Laurila, S. R. Mackenzie, S. R. T. Neil, R. Peverall, G. A. D. Ritchie, M. Schnippering & P. R. Unwin, "Following interfacial kinetics in real time using broadband evanescent wave cavity-enhanced absorption spectroscopy: a comparison of light-emitting diodes and supercontinuum sources", *Analyst*, **135**, 133–139 (2010).

[188] C. F. Kaminski, R. S. Watt, A. D. Elder, J. H. Frank & J. Hult, "Supercontinuum radiation for applications in chemical sensing and microscopy", *Applied Physics B: Lasers and Optics*, **92**, 367–378 (2008).

[189] M. Schnippering, P. R. Unwin, J. Hult, T. Laurila, C. F. Kaminski, J. M. Langridge, R. L. Jones, M. Mazurenka & S. R. Mackenzie, "Evanescent wave broadband cavity enhanced absorption spectroscopy using supercontinuum radiation: A new probe of electrochemical processes", *Electrochemistry Communications*, **10**, 1827–1830 (2008).

[190] S.-S. Kiwanuka, T. Laurila & C. F. Kaminski, "Sensitive method for the kinetic measurement of trace species in liquids using cavity enhanced absorption spectroscopy with broad bandwidth supercontinuum radiation", *Analytical Chemistry*, **82**, 7498–7501 (2010).

[191] S. R. T. Neil, C. M. Rushworth, C. Vallance & S. R. Mackenzie, "Broadband cavity-enhanced absorption spectroscopy for real time, in situ spectral analysis of microfluidic droplets", *Lab on a Chip*, **11**, 3953–3955 (2011).

[192] M. Schnippering, S. R. T. Neil, S. R. Mackenzie & P. R. Unwin, "Evanescent wave cavity-based spectroscopic techniques as probes of interfacial processes", *Chemical Society Reviews*, **40**, 207–220 (2011).

[193] S. S. Kiwanuka, T. K. Laurila, J. H. Frank, A. Esposito, K. B. von der Geest, L. Pancheri, D. Stoppa & C. F. Kaminski, "Development of broadband cavity ring-down spectroscopy for biomedical diagnostics of liquid analytes", *Analytical Chemistry*, **84**, 5489–5493 (2012).

[194] A. J. Hallock, E. S. F. Berman & R. N. Zare, "Direct monitoring of absorption in solution by cavity ring-down spectroscopy", *Analytical Chemistry*, **74**, 1741–1743 (2002).

[195] A. J. Hallock, E. S. F. Berman & R. N. Zare, "Ultratrace kinetic measurements of the reduction of methylene blue", *Journal of the American Chemical Society*, **125**, 1158–1159 (2003).

[196] A. J. Hallock, E. S. F. Berman & R. N. Zare, "Use of broadband, continuous-wave diode lasers in cavity ring-down spectroscopy for liquid samples", *Applied Spectroscopy*, **57**, 571–573 (2003).

[197] B. Bahnev, L. van der Sneppen, A. E. Wiskerke, F. Ariese, C. Gooijer & W. Ubachs,

"Miniaturized cavity ring-down detection in a liquid flow cell", *Analytical Chemistry*, **77**, 1188–1191 (2005).

[198] L. van der Sneppen, A. Wiskerke, F. Ariese, C. Gooijer & W. Ubachs, "Improving the sensitivity of HPLC absorption detection by cavity ring-down spectroscopy in a liquid-only cavity", *Analytica Chimica Acta*, **558**, 2–6 (2006).

[199] L. van der Sneppen, A. E. Wiskerke, F. Ariese, C. Gooijer & W. Ubachs, "Cavity ring-down spectroscopy for detection in liquid chromatography: Extension to tunable sources and ultraviolet wavelengths", *Applied Spectroscopy*, **60**, 931–935 (2006).

[200] S. C. Xu, G. H. Sha & J. C. Xie, "Cavity ring-down spectroscopy in the liquid phase", *Review of Scientific Instruments*, **73**, 255–258 (2002).

[201] A. J. Alexander, "Flowing liquid-sheet jet for cavity ring-down absorption measurements", *Analytical Chemistry*, **78**, 5597–5600 (2006).

[202] M. Vogelsang, T. Welsch & H. Jones, "A free-flowing soap film combined with cavity ring-down spectroscopy as a detection system for liquid chromatography", *Journal of Chromatography A*, **1217**, 3316–3320 (2010).

[203] M. Gupta, H. Jiao & A. O'Keefe, "Cavity-enhanced spectroscopy in optical fibers", *Optics Letters*, **27**, 1878–1880 (2002).

[204] R. S. Brown, I. Kozin, Z. Tong, R. D. Oleschuk & H. P. Loock, "Fiber-loop ring-down spectroscopy", *Journal of Chemical Physics*, **117**, 10444–10447 (2002).

[205] Z. G. Tong, M. Jakubinek, A. Wright, A. Gillies & H. P. Loock, "Fiber-loop ring-down spectroscopy: A sensitive absorption technique for small liquid samples", *Review of Scientific Instruments*, **74**, 4818–4826 (2003).

[206] H. Waechter, J. Litman, A. H. Cheung, J. A. Barnes & H. P. Loock, "Chemical sensing using fiber cavity ring-down spectroscopy", *Sensors*, **10**, 1716–1742 (2010).

[207] C. M. Rushworth, D. James, J. W. L. Lee & C. Vallance, "Top notch design for fiber-loop cavity ring-down spectroscopy", *Analytical Chemistry*, **83**, 8492–8500 (2011).

[208] C. M. Rushworth, J. Davies, J. T. Cabral, P. R. Dolan, J. M. Smith & C. Vallance, "Cavity-enhanced optical methods for online microfluidic analysis", *Chemical Physics Letters*, **554**, 1–14 (2012).

[209] D. James, B. Oag, C. M. Rushworth, J. W. Lee, J. Davies, J. T. Cabral & C. Vallance, "High-sensitivity online detection for microfluidics via cavity ringdown spectroscopy", *RSC Advances*, **2**, 5376–5384 (2012).

[210] A. L. Gomez, R. F. Renzi, J. A. Fruetel & R. P. Bambha, "Integrated fiber optic incoherent broadband cavity enhanced absorption spectroscopy detector for near-IR absorption measurements of nanoliter samples", *Applied Optics*, **51**, 2532–2540 (2012).

[211] S. Stob, J. Kemmink & R. Kaptein, "Intramolecular electron-transfer in flavin adenine-dinucleotide - photochemically induced dynamic nuclear-polarization studcy at high and low magnetic-fields", *Journal of the American Chemical Society*, **111**, 7036–7042 (1989).

[212] M. S. Jorns, B. Y. Wang, S. P. Jordan & L. P. Chanderkar, "Chromophore function and interaction in Escherichia coli DNA photolyase – reconstitution of the apoenzyme with pterin and or flavin derivatives", *Biochemistry*, **29**, 552–561 (1990).

[213] E. Schleicher, B. Hessling, V. Illarionova, A. Bacher, S. Weber, G. Richter & K. Gerwert, "Light-induced reactions of Escherichia coli DNA photolyase monitored by Fourier transform infrared spectroscopy", *Febs Journal*, **272**, 1855–1866 (2005).

[214] R. Brudler, K. Hitomi, H. Daiyasu, H. Toh, K.-i. Kucho, M. Ishiura, M. Kanehisa, V. A. Roberts, T. Todo, J. A. Tainer & E. D. Getzoff, "Identification of a new

cryptochrome class: Structure, function, and evolution", *Molecular Cell*, **11**, 59–67 (2003).

[215] B. Liu, H. T. Liu, D. P. Zhong & C. T. Lin, "Searching for a photocycle of the cryptochrome photoreceptors", *Current Opinion in Plant Biology*, **13**, 578–586 (2010).

[216] T. Miura, K. Maeda & T. Arai, "Effect of coulomb interaction on the dynamics of the radical pair in the system of flavin mononucleotide and hen egg-white lysozyme (HEWL) studied by a magnetic field effect", *The Journal of Physical Chemistry B*, **107**, 6474–6478 (2003).

[217] P. J. Hore & R. Kaptein, "Proton nuclear magnetic-resonance assignments and surface accessibility of tryptophan residues in lysozyme using photochemically induced dynamic nuclear-polarization spectroscopy", *Biochemistry*, **22**, 1906–1911 (1983).

[218] A. S. Kiryutin, O. B. Morozova, L. T. Kuhn, A. V. Yurkovskaya & P. J. Hore, "1H and 13C hyperfine coupling constants of the tryptophanyl cation radical in aqueous solution from microsecond time-resolved CIDNP", *The Journal of Physical Chemistry B*, **111**, 11221–11227 (2007).

[219] M. Murakami, K. Maeda & T. Arai, "Structure and kinetics of the intermediate biradicals generated from intramolecular electron transfer reaction of FAD studied by an action spectrum of the magnetic field effect", *Chemical Physics Letters*, **362**, 123–129 (2002).

[220] M. Murakami, Master's thesis, University of Tsukuba (2004).

[221] D. Nohr, S. Franz, R. Rodriguez, B. Paulus, L.-O. Essen, S. Weber & E. Schleicher, "Extended electron-transfer in animal cryptochromes mediated by a tetrad of aromatic amino acids", *Biophysical Journal*, **111**, 301–311 (2016).

[222] F. Cailliez, P. Müller, T. Firmino, P. Pernot & A. de la Lande, "Energetics of

photoinduced charge migration within the tryptophan tetrad of an animal (6–4) photolyase", *Journal of the American Chemical Society*, **138**, 1904–1915 (2016).

[223] C. Aubert, P. Mathis, A. P. M. Eker & K. Brettel, "Intraprotein electron transfer between tyrosine and tryptophan in DNA photolyase from Anacystis nidulans", *Proceedings of the National Academy of Sciences of the United States of America*, **96**, 5423–5427 (1999).

[224] J. K. Ranka, R. S. Windeler & A. J. Stentz, "Visible continuum generation in air-silica microstructure optical fibers with anomalous dispersion at 800 nm", *Optics Letters*, **25**, 25–27 (2000).

[225] J. C. Knight, "Photonic crystal fibres", *Nature*, **424**, 847–851 (2003).

[226] P. Russell, "Photonic crystal fibers", *Science*, **299**, 358–362 (2003).

[227] J. Li, *Applications of Optical-Cavity-Based Spectroscopic Techniques in the Condensed Phase*, DPhil. Thesis, University of Oxford (2013).

[228] D. W. Allan, "Statistics of atomic frequency standards", *Proceedings of the Institute of Electrical and Electronics Engineers*, **54**, 221–230 (1966).

[229] A. J. Alexander, "Reaction kinetics of nitrate radicals with terpenes in solution studied by cavity ring-down spectroscopy", *Chemical Physics Letters*, **393**, 138–142 (2004).

[230] T. Yu & M. C. Lin, "Kinetics of phenyl radical reactions studied by the cavity-ring-down method", *Journal of the American Chemical Society*, **115**, 4371–4372 (1993).

[231] K. Maeda, A. J. Robinson, K. B. Henbest, E. J. Dell & C. R. Timmel, "Protein surface interactions probed by magnetic field effects on chemical reactions", *Journal of the American Chemical Society*, **132**, 1466–1467 (2010).

[232] F. Mueller, M. Bruestlein, P. Hemmerich, V. Massey & W. H. Walker, "Light absorption studies on neutral flavin radicals", *European Journal of Biochemistry*, **25**, 573–580 (1972).

[233] M. S. Grodowski, B. Veyret & K. Weiss, "Photochemistry of flavins II: Photophysical properites of alloxazines and isoalloxazines", *Photochemistry and Photobiology*, **26**, 341–352 (1977).

[234] M. Sakai & H. Takahashi, "One-electron photoreduction of flavin mononucleotide: Time-resolved resonance Raman and absorption study", *Journal of Molecular Structure*, **379**, 9–18 (1996).

[235] S. S. Brown, A. R. Ravishankara & H. Stark, "Simultaneous kinetics and ringdown: Rate coefficients from single cavity loss temporal profiles", *Journal of Physical Chemistry A*, **104**, 7044–7052 (2000).

[236] Z. C. Qu, J. Engstrom, D. Wong, M. Islam & C. F. Kaminski, "High sensitivity liquid phase measurements using broadband cavity enhanced absorption spectroscopy (BBCEAS) featuring a low cost webcam based prism spectrometer", *Analyst*, **138**, 6372–6379 (2013).

[237] K. Buckton, *Magnetic Field Effects in Protein-Based Model Systems of Cryptochromes*, Master's thesis, University of Oxford (2015).

[238] W. Holzer, A. Penzkofer, M. Fuhrmann & P. Hegemann, "Spectroscopic characterization of flavin mononucleotide bound to the LOV1 domain of Phot1 from Chlamydomonas reinhardtii", *Photochemistry and Photobiology*, **75**, 479–487 (2002).

[239] A. Losi, E. Polverini, B. Quest & W. Gärtner, "First evidence for phototropin-related blue-light receptors in prokaryotes", *Biophysical Journal*, **82**, 2627–2634 (2002).

[240] E. Evans, *A Study of Magnetic Field Effects on Chemical Compass Model Systems Using Optical Spectroscopy Methods*, Master's thesis, University of Oxford (2012).

[241] Y. P. Tsentalovich, J. J. Lopez, P. J. Hore & R. Z. Sagdeev, "Mechanisms of reactions of flavin mononucleotide triplet with aromatic amino acids", *Spectrochimica Acta Part A: Molecular and Biomolecular Spectroscopy*, **58**, 2043–2050 (2002).

[242] V. Massey, "Activation of molecular oxygen by flavins and flavoproteins.", *The Journal of Biological Chemistry*, **269**, 22459–22462 (1994).

[243] K. Maeda, T. Miura & T. Arai, "A practical simulation and a novel insight to the magnetic field effect on a radical pair in a micelle", *Molecular Physics: An International Journal at the Interface Between Chemistry and Physics*, **104**, 1779 (2006).

[244] R. Leenders, M. Kooijman, A. Hoek, C. Veeger & A. J. Visser, "Flavin dynamics in reduced flavodoxins", *European Journal of Biochemistry*, **211**, 37–45 (1993).

[245] T. Kouyama, K. Kinosita & A. Ikegami, "Correlation between internal motion and emission kinetics of tryptophan residues in proteins", *European Journal of Biochemistry*, **182**, 517–521 (1989).

[246] P. F. Heelis, "The photophysical and photochemical properties of flavins (isoalloxazines)", *Chemical Society Reviews*, **11**, 15–39 (1982).

[247] C. A. Dodson, C. J. Wedge, M. Murakami, K. Maeda, M. I. Wallace & P. J. Hore, "Fluorescence-detected magnetic field effects on radical pair reactions from femtolitre volumes", *Chemical Communications*, **51**, 8023–8026 (2015).

[248] J. P. Beardmore, L. M. Antill & J. R. Woodward, "Optical absorption and magnetic field effect based imaging of transient radicals", *Angewandte Chemie – International Edition*, **54**, 8494–8497 (2015).

[249] A. A. Lee, J. C. S. Lau, H. J. Hogben, T. Biskup, D. R. Kattnig & P. J. Hore, "Alternative radical pairs for cryptochrome-based magnetoreception", *Journal of the Royal Society Interface*, **11**, 20131063 (2014).

[250] G. Puxty, M. Maeder & K. Hungerbühler, "Tutorial on the fitting of kinetics models to multivariate spectroscopic measurements with non-linear least-squares regression", *Chemometrics and Intelligent Laboratory Systems*, **81**, 149–164 (2006).